EXPERIMENTAL STUDIES OF LIQUID INJECTOR RESPONSE AND WALL HEAT FLUX IN A ROTATING DETONATION ROCKET ENGINE

A Dissertation

Submitted to the Faculty

of

Purdue University

by

Dasheng Lim

In Partial Fulfillment of the

Requirements for the Degree

of

Doctor of Philosophy

December 2019

Purdue University

West Lafayette, Indiana

THE PURDUE UNIVERSITY GRADUATE SCHOOL
STATEMENT OF DISSERTATION APPROVAL

Dr. Stephen D. Heister, Chair

School of Aeronautics and Astronautics

Dr. William E. Anderson

School of Aeronautics and Astronautics

Dr. Timothée L. Pourpoint

School of Aeronautics and Astronautics

Dr. Carson D. Slabaugh

School of Aeronautics and Astronautics

Approved by:

Dr. Gregory A. Blaisdell

Head of the School Graduate Program

To my parents, for their unconditional support every step of the way.

ACKNOWLEDGMENTS

I'm extremely grateful of my advisor, Professor Stephen D. Heister for presenting me with the opportunity to undertake this exciting project, and for his active guidance towards my research efforts. I'd also like to express my gratitude to Professors Timothée L. Pourpoint and Carson D. Slabaugh for graciously sharing some of the equipment that made this work possible. Scott Meyer, Michael Bedard, and Rohan Gejji deserve recognition for their invaluable technical knowledge and advice in the design and execution of my experiments. Sincere thanks to my colleagues David Stechmann, Brandon Kan, Wesly Anderson, Kota Mikoshiba, Hasan F. Celebi, Jenna Humble, Alexis Harroun, Stephen Kubicki, Silas Meriam, Timo Buschhagen, and many others for their assistance and advice, and also for adding to the wonderful experience of working at Zucrow Labs. Special mention goes to Tristan Fuller not just for talking me into tripling the number of thermocouple probes used on the RDE, but also for the wealth of knowledge, advice, and conversation topics that he so generously dispensed. I'm also indebted to our machinists Rob McGuire, Toby Lamb, and Gerald Hahn for their expertise and seemingly miraculous ability to fulfil my machining requests that were oftentimes made in short notice. Last but not least, I would like to thank the Air Force Office of Scientific Research for their financial support.

TABLE OF CONTENTS

Page

Page

LIST OF TABLES

Table Page

LIST OF FIGURES

Figure Page

Figure Page

Figure Page

Figure Page

Figure Page

Figure Page

ABSTRACT

Lim, Dasheng PhD, Purdue University, December 2019. Experimental Studies of Liquid Injector Response and Wall Heat Flux in a Rotating Detonation Rocket Engine. Major Professor: Stephen D. Heister.

The results of two experimental studies are presented in this document. The first is an investigation on the transient response of plain orifice liquid injectors to transverse detonation waves at elevated pressures of 414, 690, and 1,030 kPa (60, 100, and 150 psia). Detonations were produced using a predetonator which utilized hydrogen and oxygen or ethylene and oxygen as reactants. For injectors of identical diameter, an increase in length correlated with a decrease in the maximum back-flow distance. A preliminary study using an injector of larger diameter suggested that for injectors of the same length under the same pressure drop, the larger injector was more resistant to back-flow. Refill time of the injectors was found to be inversely-proportional to detonation pressure ratio and injector stiffness, and a curve fit was produced to relate the three parameters.

The second experimental campaign was the hotfire testing of an RP-2-GOX rotating detonation engine. Total engine mass flow rates ranged from 0.8 to 3.5 kg/s (1.7 to 7.7 lbm/s) and static chamber pressures between 316 and 1,780 kPa (46 and 258 psia) were produced. In a majority of tests, between four and six co-rotating detonation waves were observed. Using an array of 36 embedded thermocouple probes, chamber outer wall heat fluxes between 2.8 and 8.3 MW/m^2 were estimated using an inverse heat transfer method of calculation. Performance of the RP-2 injector was assessed by relating to the information obtained in the prior injector response study.

1. INTRODUCTION

1.1 Background

Pressure-gain combustion has been studied for several decades, motivated by the potential to improve thermodynamic performance of aerospace and ground-based powerplants. The theoretical benefits of this mode of combustion stem from the reduced entropy gains by enabling combustion at higher pressures than a comparable constant-pressure Brayton cycle combustion device [1]. Detonations have been investigated fundamentally for various combinations of reactant mixtures [2, 3], but the technology to harness the energy released by detonations is still in its nascent stage.

In his 1940 journal paper, Zeldovich claimed that detonation combustion was unlikely to be practical in energy production due to the low theoretical gain in efficiency. Nevertheless, the community continued to pursue this approach as efficiency gains of up to 10% over constant-pressure combustion have been estimated from basic thermodynamic cycle considerations [1]. In a world where even a 0.1% improvement in efficiency is sought, the potential benefits of pressure-gain combustion are tremendous. A fair amount of work has since been done on pulse detonation engines (PDEs), but the low operating frequency, mechanical complexity, and requirement for repeated ignitions have made the concept disadvantageous.

Researchers first began experimenting on annular detonation chambers in the 1960s [4, 5] and were able to capture photographic evidence of rotating detonations. Unlike PDEs, this alternate form of pressure-gain combustion promised higher operating frequencies while requiring only a single ignition. This is highly advantageous as it eliminates the need for timed valve actuations and ignitions as is needed in a typical PDE. However, the idea seemed to have fallen by the wayside soon after its conception.

During this time, research institutes and the industries continued to improve constant-pressure combustion technology, using it in both air-breathing and rocket applications. Presently, constant-pressure combustion has reached the point where it is limited by thermodynamic laws rather than design. For several decades now, constant-pressure devices have been operating at over 99% combustion efficiency (e.g. SSME [6]), and further gain is extremely marginal. Consequently, current commercial efforts in improving these engines and increasing profitability lie mainly in developing reusable systems that utilize propellants that are less harmful to the environment [7,8].

In the mid to late 2000s, research activity in annular detonation chambers was revived. Several research institutes began to conduct experiments on annular rocket and airbreathing engines [9–11] and these devices were given the names *continuous spin detonation*, *continuous detonation wave*, or *rotating detonation* engines – in this document, the term *rotating detonation engine* (RDE) will be used to refer to the technology. Since then, the propulsion community has taken keen interest in the subject. The number of entities conducting research on RDEs has been growing at an increasing rate, and papers related to RDEs now make up a significant portion of conference proceedings. One of the most prominent researchers on rocket RDEs is Bykovskii of the Lavrentyev Institute of Hydrodyamics, who has conducted extensive experiments and established the foundation on which numerous groups, Purdue included, are now building upon. In his 2006 paper [12], he proposed guidelines for achieving sustained detonations based on the cell size of propellant mixtures.

In 2014, researchers at Purdue University's Zucrow Labs officially began conducting research on RDEs. The group focused on two main objectives simultaneously: building a functional RDE, and understanding injector dynamics. The motivation behind the decision to study injector dynamics finds its roots in the more conventional constant-pressure engine design. In a constant-pressure engine, the injector plays a critical role in ensuring the stable and efficient operation of the combustor. Chamber instabilities are closely coupled with the propellant injection dynamics and self-excited resonant modes have been known to lead to hardware failure. For this

reason, rocket injectors typically undergo many design and testing iterations. Just as importantly, the injector is responsible for atomizing and mixing propellants in a way that supports efficient combustion. Coaxial swirl injectors, impinging jet injectors, and pintle injectors are some examples of injection and mixing technology most commonly used today.

It was understood from the beginning that the injector in an RDE operates in a vastly different environment, but there is still reason to believe that it is a critical component in the successful operation of the engine since rotating detonations need to be sustained by an adequate supply of propellants. The difference here lies in the cyclic, steep-fronted and high-amplitude pressure waves that each injector element will encounter during engine operation.

According to literature [2] and NASA CEA [13], gaseous phase detonations can produce pressure ratios greater than 20 depending on propellant combination. In addition, current lab-scale RDEs operate with frequencies of several kilohertz at the minimum, and can easily reach tens of kilohertz with multiple detonation waves propagating simultaneously. Therefore, it becomes apparent that these injectors will be subject to highly-dynamic downstream conditions. While the injectors for constant-pressure engines have been well-studied with various design guidelines [14], little open literature is available for transient injection systems. Most transient fluid studies pertain to low-amplitude instabilities in constant-pressure combustors or water hammer effects in pipes.

A prototype RDE was built and tested during the period of 2015 through 2017 by Stechmann [15] at Purdue University's Zucrow Labs. The initial propellants chosen were gaseous oxygen and gaseous hydrogen for the combination's high detonability. Liquid oxygen was first reacted with hydrogen at very high mixture ratios in an oxidizer-rich preburner before being injected into the RDE. He discovered from these experiments that the combination of high temperature and pressure was causing the hydrogen-oxygen mixture to ignite and flamehold in the direct vicinity of the hydrogen injectors, depleting propellants before detonations could establish.

The experiments were subsequently modified to utilize oxygen and gaseous methane instead, for their slower reaction kinetics. The experiments showed thrust produced by the prototype RDE residing predominantly between 85 and 95% of a theoretical equivalent constant-pressure engine operating at 100% efficiency. The experiments were a success in demonstrating the operability of the prototype. Ultimately, there is a strong case to be made for operating the RDE on liquid propellants for practical reasons. The elimination of preburners represents the most ideal scenario since preburners count for additional combustion devices that add to the complexity of the system.

1.2 Literature Review

At present, there exists a dearth of literature on the transient response of liquid injection systems and heat flux studies relevant to RDEs. Much of the current open literature on *experimental* RDEs feature gas-gas systems, with a large portion of the studies focusing on hydrogen-oxygen or hydrogen-air detonations. Some of the groups investigating hydrogen-oxygen RDEs include the Lavrentyev Institute of Hydrodynamics (LIH) and Peking University [12, 16], while those studying hydrogen-air RDEs include the Air Force Research Laboratory (AFRL), Air Force Institute of Technology (AFIT), LIH, Nanjing University of Science and Technology, University of Cincinnati, and University of Michigan [11, 17–21].

Evidently, gaseous hydrogen RDEs are currently the most well-studied. On the other hand, systems that employ at least one liquid propellant are still uncommon. At the time of writing, the only published literature on RDE experiments with liquid propellants were from LIH (liquid oxygen with kerosene and acetone) [12], Warsaw University of Technology (air with kerosene) [22], National University of Singapore (air with Jet A-1) [23], and Purdue University (hydrogen peroxide with triglyme) [24]. Understandably, gas-gas platforms provide a more conducive environment for investigating the fundamental phenomena in RDEs by avoiding complexities associated with

two-phase flows. Nonetheless, the author expects increased attention on liquid-gas and liquid-liquid RDEs when the demand for information becomes driven by practical applications.

While an appreciable number of operational RDE prototypes have been constructed, there is still very little known about the highly-transient injection systems, and even more so when it comes to liquid propellant RDEs. Some relevant fundamental fluid dynamics studies that were conducted under similar conditions as liquid RDEs are discussed below, followed by a handful of experiments that included heat transfer analysis.

Nicholls [5] performed experiments to investigate the droplet breakup times of 250 to 1000-micron droplets. According to their tests, "considerable breakup" was attainable in as little as 12 μs through a shattering mechanism as opposed to evaporation. This figure is roughly 10 to 30% of wave separation intervals seen in earlier tests performed by Stechmann [15] and suggests that heterogeneous detonations are possible given that the initial droplet sizes are sufficiently small.

As motivated primarily by injector response during combustion instabilities, the liquid injector community has developed classical treatments for transfer functions that relate the amplitude and phase lag of injection massflow characteristics to a low-amplitude, sinusoidal pressure disturbance [25, 26]. More recent nonlinear models have been applied to this problem [27], which also uncovered natural tones produced in the injector itself due to oscillations in the vena-contracta anchored to the inlet lip. While these efforts provide some level of understanding, they did not consider the very steep-fronted, high amplitude waveforms that modulate the injection process in an RDE.

Richards et al. [28] conducted fundamental cavitation studies in a water column by setting off a detonation in the gas pocket above the column. The events that occur in their experiments were similar to those in the present study – a steep-fronted pressure wave impacts one end of a column of water. The main difference is that the water column in their experiment is stationary, while the water column in this

study moves with the expanding gas. Nonetheless, the phenomena that occur in the water column are largely similar, as will be discussed further alongside the analysis of results obtained in the liquid injector response experiments.

Benusiglio et al. [29] studied the cavities formed by explosions on the surface of water. They recorded the growth rates and shapes of the cavities and compared the results with a potential flow model. Of particular interest were their experiments in which the explosions of various strengths were confined using a submerged transparent tube. They found that regardless of the strength of the explosion tested, the gaseous cavity only ever grew to the full length of the tube; never past it. They explained that it becomes increasingly easy for the constant pressure force at the end of the tube to decelerate the mass of water getting expelled by the expanding cavity. Eventually, as the cavity fills the tube, the mass of water reaches zero and the deceleration effectively becomes infinitely high and prevents any further growth of the cavity. Their finding is of some relevance to the present study of injector dynamics due to the similarities between the physical geometry and nature of the perturbance on the liquid. While the potential flow model was able to capture flow behavior with appreciable accuracy, it was of limited use as an injector design tool due to its input requirements.

Aside from the engine hotfire experiments utilizing hydrogen peroxide and triglyme, Anderson also performed an investigation on the behavior of a liquid jet in supersonic crossflow driven by two detonation pulses spaced roughly 100 µs apart [30]. He discovered that the high-speed flow of gas following a detonation wave atomized the liquid jet in such a way that core flow maintained a near-constant length for a duration of several hundred microseconds. This length was strongly influenced by the momentum ratio of the liquid jet to the gaseous crossflow. More importantly, jet penetration distance was extremely limited within the duration that separated the two detonation pulses, suggesting that detonation-augmented mixing could be an important mixing mechanism in RDEs.

The most recent work on liquid injector response to detonation waves was performed by Celebi [31, 32]. The experiments were performed on angled and tapered

injectors using the same pressure vessel platform developed for the present study and compared with perpendicular plain orifices. The results revealed that a constant-area injector that was angled towards the direction of detonation recovered in a shorter time and *vice-versa*, with the caveat being the unpredictability of wave direction in an RDE. Most importantly, using tapered injectors significantly reduced refill time. Correlations for injector refill time as a function of chamber and manifold pressures were also formulated for the tapered injectors.

Several experiments that measured wall heat flux in RDEs were conducted by Bykovskii, ISSI/AFRL, and a collaborative effort among universities and industrial partners in Japan. In 1991, Bykovskii [33] tested a propane-oxygen RDE with a diameter of 40 mm (1.6 in). It was instrumented with four thermocouple probes and heat flux was calculated by curve-fitting the temperature history. The combustor was operated in both detonative and deflagrative modes, and the author found that heat flux was lower in the former. Reported peak heat flux values at the chamber head were between 20 and 30 MW/m^2 in detonative mode and between 40 and 50 MW/m^2 in deflagrative mode.

In 2009, Bykovskii and Vedernikov [34] published a study conducted on a 306 mm air-breathing RDE that utilized acetylene and hydrogen as fuels. Two different chamber profiles were investigated: One with a constant annular area, and the other with a 15° internal expansion. The instrumentation for temperature measurement appeared to be similar to those used in the prior study and were also flush-mounted to the outer chamber wall. Reported chamber head-end heat fluxes were very similar across all fuel and chamber gemoetry combinations and peak values were between 2 and 3 MW/m^2.

In 2014 and 2015 Theuerkauf et al. published experiments on a 152 mm (6 in) water-cooled hydrogen-air RDE at ARFL where heat flux was measured both calorimetrically and using thin-film heat flux gauges [35,36]. The gauges were mounted directly on the wall surface inside the combustion chamber. The high-frequency gauges were sampled at 100 kHz and were able to capture the heat flux profile of individual

detonation waves. It was revealed that the walls experienced short-duration heat flux spikes very much like the pressure spikes associated with detonation waves, during which heat flux values reached peaks approaching 6 MW/m^2. In the expansion region following the detonation front, little to no heat flux was measured. Time-averaged heat flux in the reported single-wave case was 390 kW/m^2.

Stevens et al. published findings in 2018 and 2019 on the calorimetrically-measured heat flux of a similar water-cooled RDE at steady-state operation [37, 38]. In their tests, the hardware was allowed to reach steady-state by holding conditions for at least 90 s before taking measurements. The average heat flux during each test was determined through a lumped-parameter analysis that iterated on material properties that were temperature-dependent. In their tests, average heat fluxes up to 1.5 MW/m^2 were obtained.

The study by Ishihara et al. [39] was conducted on a 78-mm (3.1-in) engine utilizing ethylene and oxygen as propellants. The combustion chamber's inner and outer walls were made of carbon composite and the outer wall was instrumented with thermocouples at depths of 1 and 2 mm (0.039 and 0.079 in) along several axial stations. Their method of determining heat flux was not explicitly stated, but most likely calculated from temperature gradients. A peak heat flux value of 7 MW/m^2 was reported near the combuster exit during the shutdown transients for one of the tests. Considerable erosion of the carbon-composite inner wall within 2 cm of the head-end was also documented.

A summary of the operating parameters and reported heat fluxes of the literature discussed above is presented in Table 1.1.

Table 1.1. Summary of reported RDE heat fluxes in open literature.

Author(s)	Propellants	Chamber Pressure [kPa (psia)]	Reported Heat Flux [MW/m2]
Bykovskii [33]	Propane-oxygen	230 (33)	20–30 (peak)
Bykovskii and Vedernikov [34]	Acetylene-air, hydrogen-air	130 (19)	2–3 (peak)
Theuerkauf et al. [35, 36]	Hydrogen-air	Not reported	0.39 (time-averaged)
Stevens et al. [37, 38]	Hydrogen-air	Not reported	1.5 (time-averaged)
Ishihara et al. [39]	Ethylene-oxygen	350 (51)	7 (peak)

1.3 Research Objectives

A study of liquid injector response was initiated by the author in 2014 in contribution to the goal of building a functional liquid-liquid or liquid-gas RDE at Zucrow Labs. In [40], the first series of experiments were conducted at atmospheric pressure. The test articles were plain orifice injectors machined from clear acrylic. As a detonation wave traveled along a rectangular channel, it traversed the injector face, causing the liquid flow (water in these experiments) to be perturbed. Using a high-speed camera, the response of the water column was captured and analyzed. Taking the injector's centerline as the basis of measurement, the maximum distance back-flowed by the water and time required for the injector to refill were recorded. The measured results were compared with a one-dimensional numerical model developed to predict liquid injector response when given a set of operating parameters.

The model's prediction of back-flow distance appeared to improve with injection pressure, but refill time prediction lacked accuracy and did not seem to show any improvement nor worsening with increased injection pressure. The inability of the

model to predict refill time to an acceptable degree of accuracy was attributed to the dynamic manifold pressure following the passage of the pressure wave. Compression and expansion waves were expected to cause numerous reflections within the internal passages of the injector and feed line assembly, which could affect the response. Without a high-speed pressure measurement in the manifold, it was difficult to ascertain the cause of the model's inaccuracy.

In addition, the detonation waves produced by the setup were weak (typical pressure ratio of 3–5) and the response of the injectors was rather mild. The weakness of the detonations also meant that the injectors stopped showing bulk response at injector pressure drop (ΔP) as low as 3 psi. Clearly, the range of conditions was unsatisfactory and did not make a convincing case for the predictive capability of the numerical model. While these experiments were not representative of actual rocket conditions, they provided an introductory glimpse into the highly-dynamic and chaotic nature of these injectors.

Naturally, the next step was to perform the same experiments at elevated pressures, so a pressure vessel was designed and built to house the test article. The goal of this project was to investigate the transient response of liquid injectors at conditions that better approximate those that actual rocket systems – and the kerosene-GOX RDE – would encounter, so that phenomena that might otherwise not manifest at low pressures could be observed. With the increased initial pressure, higher injector ΔP could be achieved, extending the range of response data significantly to lend more weight to the findings.

Since detonation cell size is inversely-proportional to initial pressure, the smaller cell sizes in this research campaign resulted in stronger detonations that better matched Chapman-Jouguet (C-J) predictions. Coupled with the fact that detonation pressure scales with initial pressure, very high amplitude pressure disturbances that drove large responses in the liquid column were produced. For an RDE to be competitive with constant-pressure engines, the benefits it brings have to outweigh its shortcomings. In [12] and [24], the injector ΔP employed were several times higher

than the average chamber pressure. While the laboratory setting permits the application of feed pressures far above practical levels, flight-weight systems do not afford the same luxury. Therefore, understanding the response time of an injector is critical for the path forward.

It should be readily apparent that the turbopump and thrust chamber structural mass will increase with manifold pressure, which decreases engine trust-to-weight ratio. In doing so, the potential benefits of pressure-gain combustion become eroded. Instead, the goal should be to investigate the injector design space to determine features that are beneficial for the dynamic environment in RDEs. It was the hope of the injector response experiments to shed some light on high-level design parameters such as injector geometry, manifold pressures, sustainable wave count, etc.

The other major objective of the current research was to assess the general performance of a kerosene-GOX RDE in a series of hotfire tests. These tests served three main purposes:

1. Primarily, as a proof of operability. Once established, the base design of the system will be able to serve as a platform for further tests, including but not limited to injector design, nozzle design, and cooling strategy studies.

2. The combustion characteristics of the tests were used to infer the response characteristics of the kerosene injectors. Specifically, whether or not the engine was capable of sustaining rotating detonations at any given injector ΔP served as an indicator of the injector's recovery time. The findings were tied in with the more fundamental injector response studies outlined above.

3. The outer chamber wall was instrumented with thermocouples to estimate the average heat flux produced in an RDE chamber. Little is known about thermal characteristics in RDEs and even less so about optimal cooling strategies. The data generated by this test campaign will be valuable for designing cooling systems for similar engines.

The subsequent chapters will cover the test facilities and setup for both the injector response and RDE hotfire experiments, followed by a discussion of their results. Finally, the document will conclude with a recommendation of future studies that will benefit the development of rotating detonation technology.

2. FACILITIES AND HARDWARE

The research work covered in this document was performed on two different test facilities: Liquid injector response testing was carried out in a pressure vessel test platform residing in Test Cell C of the Maurice J. Zucrow Laboratories Building ZL2 while the RDE hotfire tests made use of the 10,000 lbf thrust stand (10k Stand) located in the Rocket Cell of Building ZL3. The facilities and hardware, data interpretation methodology, and uncertainty quantification will be divided according to test campaign and presented in each section.

2.1 Injector Response Test Platform

The test platform consisted of a pressure vessel, a detonation channel assembly, modular injectors, and a predetonator (henceforth referred to as "predet"). Bulk nitrogen was supplied at up to 34 MPa (5,000 psia) from tube trailers located at the High Pressure Lab (HPL or ZL3) and distributed to the various lines in the test cell through a central regulator panel. The nitrogen was used to pressurize the water tank, pressure vessel, and purge the predet propellant lines. Substantial effort was involved in the development of Test Cell C in the ZL2 building before injector response experiments could be conducted. To accomodate the operation of the pressure vessel, additional fluid lines and pressure regulators were connected to the existing facility. This was jointly accomplished with another colleague, Dr. Wesly Anderson.

2.1.1 Pressure Vessel

The pressure vessel shown in Fig. 2.1 was designed for operation at pressures up to 2.1 MPa (300 psig). It featured three 89 mm (3.5 in) quartz windows, two

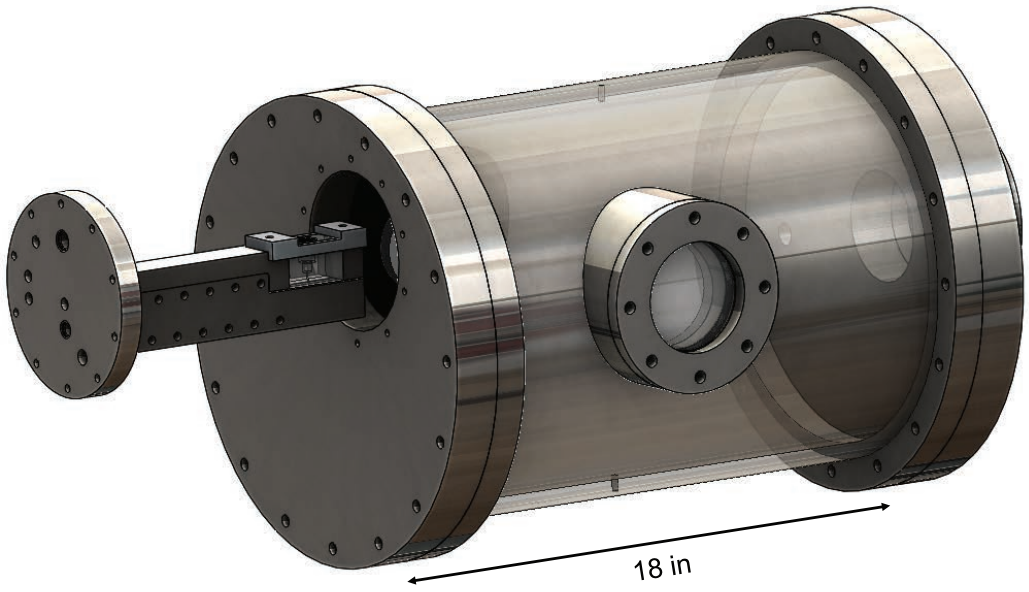

Figure 2.1. Pressure vessel with body rendered translucent to show interior volume.

of which were located on the sides to allow direct view and backlighting of the test article and injector near-exit region. The third window was positioned on the back end lid directly across from the test article mount. While unsused in this study, future projects may find use for the additional viewing angle provided.

The vessel body was built from a 460 mm (18 in) section of Schedule 80S stainless steel pipe with a 300 mm (11.75 in) nominal inner diameter and 13 mm (0.50 in) wall thickness. Stainless steel flanges with O-ring grooves were machined and full-penetration-welded onto each end of the pipe section to permit mounting of end lids. The two window mounts on the vessel body were CNC-machined to follow the contour of the cylindrical surface and full-penetration-welded to the body. The quartz window panes were secured by 13 mm-thick retainers and sealed on both the internal and external surfaces using 1.6 mm (0.0625 in) graphite gaskets compressed by 40%, which have been used extensively and successfully in numerous setups at Zucrow Labs.

The pressure vessel's internal volume was chosen such that the expansion of gases from the detonation would result in less than a 5% rise in pressure. On the front lid, a 127 mm (5.0 in) port sealed using an O-ring enabled the vessel to be used for different modular experiments. The vessel was built with a safety factor of at least 4 in all of the steel structure, and a safety factor of 2 in the quartz windows. A pressure relief valve rated at 2.5 MPa (360 psig) and a rupture disc rated at 2.7 MPa (385 psig) served as the primary safety system. Both components were sized to handle the over-pressure flow rate equivalent to all pressure regulators leading into the pressure vessel failing in the fully-open position. The windows were intentionally designed with a lower factor of safety to minimize the possibility of failure in the steel components, which would carry much more destructive potential in the event of an explosion.

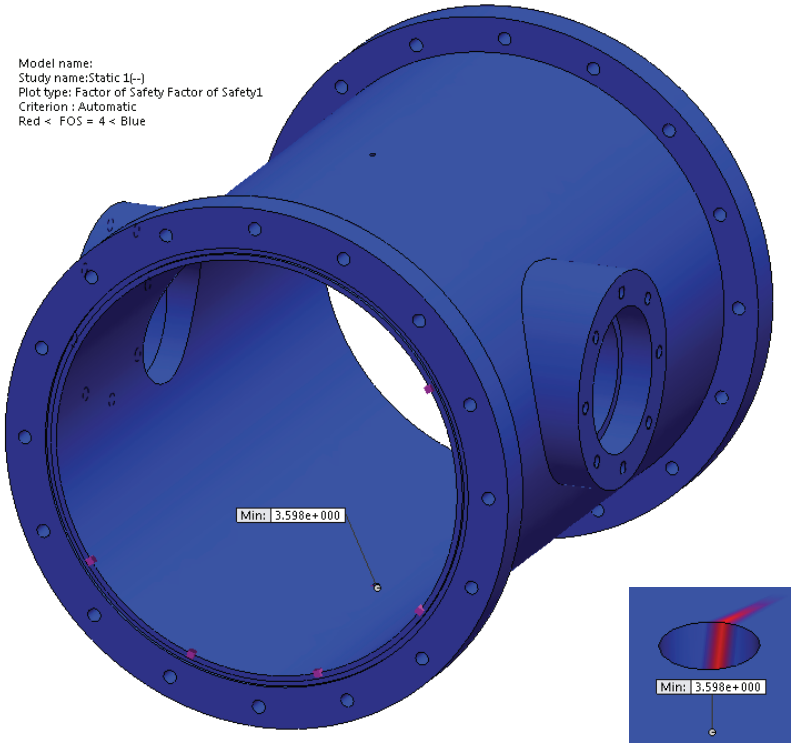

Figure 2.2. Factor of safety distribution of the pressure vessel body showing at least a factor of safety of 4 throughout the vessel.

Safety factors were calculated using Roark's Formulas for Stress and Strain [41] for the simple geometries (flanges, lids, and viewports) and the built-in stress analysis tool in Solidworks® for the pressure vessel body. Fixed boundaries were prescribed on both flange faces, and an internal pressure of 2.1 MPa (300 psi) was applied to produce the resulting stress. The factor of safety (FOS) distribution of the pressure vessel body is shown in Fig 2.2. The minimum FOS criterion was set to 4, with areas passing the criterion colored blue and areas that failed colored red. Two areas of failure were identified; both were located around the 4.6 mm (0.18 in) pressurization and drainage ports on the top and bottom of the vessel. The inlay at the bottom right of the figure shows a close-up view of one of these ports. It is most likely that these were numerical artifacts resulting from the combination of a coarse mesh, sharp edges, and small radius of curvature rather than real physical stress concentrations since these small ports were expected to be at a lower stress than the larger features such as the viewports.

To date, the pressure vessel has been hydrostatically tested to 2.3 MPa (340 psig), allowing manned operation up to 1.4 MPa (200 psig). The hydrostatic tests were intended to be performed in two stages, the first (completed) at 2.3 MPa and the second (to be completed before testing above 1.4 MPa, or 200 psig) at 3.4 MPa (500 psig), with the intention of ensuring that data could be collected in the very least at 1.4 MPa should the weaker windows fail the 3.4 MPa hydrostatic test. While the pressure vessel has been rated for manned operation, test operators remained in the control room during the ramp-up of internal pressure, and did not enter the test cell while the vessel was pressurized unless absolutely necessary. Such an instance includes adjusting the manual drain valve to allow trickling flow of nitrogen through the pressure vessel to help alleviate the problem of fogging. However, this was only done when the vessel was below 345 kPa (50 psia) – well below the designed limit.

2.1.2 Detonation Channel Assembly

A detonation channel block assembly similar to that used in [40] was machined from stainless steel to withstand the extremely high detonation pressures that will be produced at these elevated initial ambient pressures. The detonation channel (annotated by the yellow arrow in Fig. 2.3) began with a 5.1×5.1 mm (0.2×0.2 in) square cross-section that diverged on the top and bottom faces at a 5° half-angle into a 15.7×5.1 mm (0.62×0.2 in) rectangular straight channel. The straight section of the channel ran for approximately 104 mm (4.1 in) before the lower wall opened away to produce a lateral relief effect similar to that in an RDE. To create this channel profile, the detonation channel block was manufactured in two parts – a main block and a channel closeout. The injection site was located 25.4 mm (1 in) downstream from the edge of the bottom wall and the injector block was secured using a bracket in a slot cut out of the detonation channel block, labeled "optical path" in the figure.

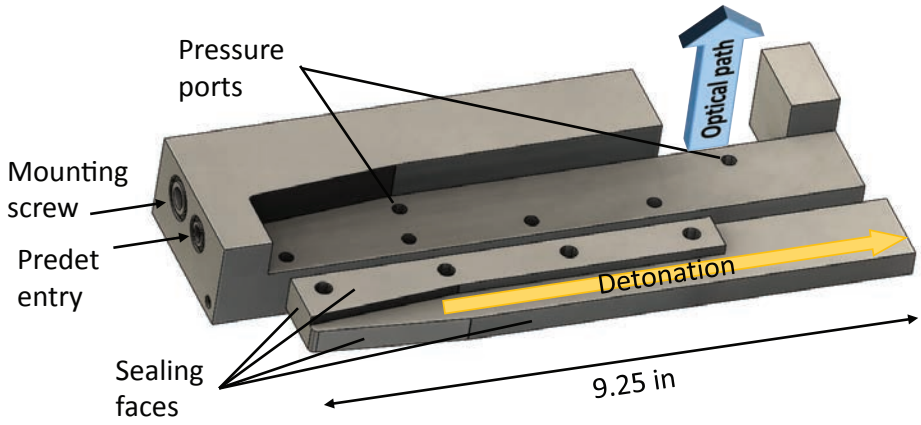

Figure 2.3. Disassembled Version 1.0 channel block showing internal features that form detonation channel.

At the time of writing, the channel block assembly had undergone four design iterations. In version 1.0 (Fig. 2.3) of the channel block design, the channel closeout was sealed against the main block using only room-temperature vulcanization (RTV)

sealant. Four $\frac{1}{4}$-28 alloy steel screws were used to compress the sealant and fasten the closeout. It was quickly discovered that the RTV sealant did not possess sufficient structural and adhesive strength, and portions were ejected from the top mating surface (parallel to cylindrical axis of the screws) after multiple firings. A consequence of the loss of sealing was the decrease in peak pressure of the detonation as the pressurized detonation products were able to escape upstream through the resulting gaps. In a series of tests with ethylene (otherwise known as ethene, C_2H_4) and oxygen, the higher detonation pressures (close to 28 MPa or 4000 psia) due to ethylene's higher detonation pressure ratio (DPR) exerted sufficient force to plastically-deform the four screws used to secure the channel closeout.

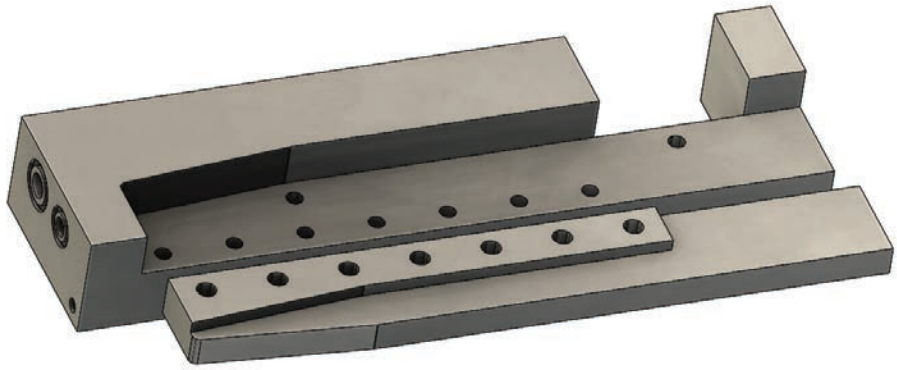

Figure 2.4. Version 1.1 channel block with additional fasteners for structural support.

Version 1.1 (Fig. 2.4) of the assembly added three more screws to help distribute the bending force that was produced by the detonations. To alleviate the sealing problem, the channel closeout had two of its faces machined down by 0.038 in to accommodate graphite gaskets. The graphite gaskets were expected to be more rigid and maintain their seal more effectively than RTV sealant. This version was an interim design that allowed testing of more injectors with minimal downtime while the channel closeout of version 1.2 (Fig. 2.5) was being fabricated. Unfortunately, the channel closeout required gasket compression in two perpendicular directions while

the screws fastening the channel closeout were only able to provide significant compression in one direction. As a result, the graphite gasket failed where compression was inadequate (again, along the faces parallel to the screws) after only several firings.

Version 1.2 of the channel block assembly relocated the sealing surfaces such that most of the required gasket compression was perpendicular to the fasteners. A small amount of off-axis sealing was unavoidable, but the effects of loss of sealing were expected to be small. The off-axis sealing was achieved using a combination of graphite gaskets and RTV sealant. As shown in Fig. 2.5, the channel closeout was now fastened on both sides of the channel, and the load on the screws was almost purely axial. More than 300 tests utilizing hydrogen and oxygen as propellants were performed using this version of the detonation channel block with good results.

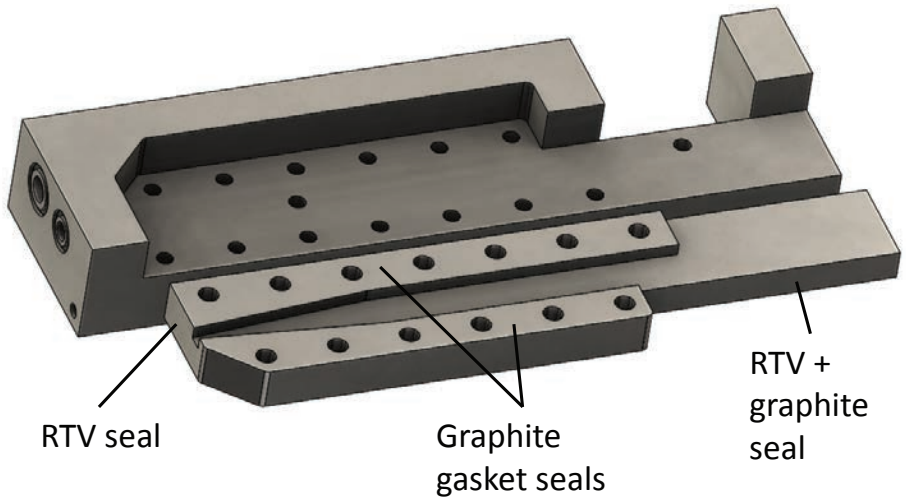

Figure 2.5. Version 1.2 channel block with fasteners on both sides of the channel, and majority of sealing surfaces on the same plane.

While version 1.2 of the assembly stood up to the hydrogen-oxygen detonations, further difficulties with sealing between the injector module and channel closeout surfaced when ethylene was used as fuel instead of hydrogen. The increased detonation pressure was high enough to overcome the compressive force holding the gasket, causing it to dislodge within a couple of tests. The final iteration of the assembly involved

the addition of a retaining step on the outboard side of the sealing surface, shown in Fig. 2.6. The purpose of the step was to provide additional mechanical support to prevent the graphite gasket from dislodging outwards. Over 250 tests were conducted using ethylene and oxygen using the version 1.3 design with acceptable gasket performance; gasket replacement frequency decreased, but the extreme pressure still did occasionally push the gasket out of position. A redesign is recommended to improve seal longevity for future testing.

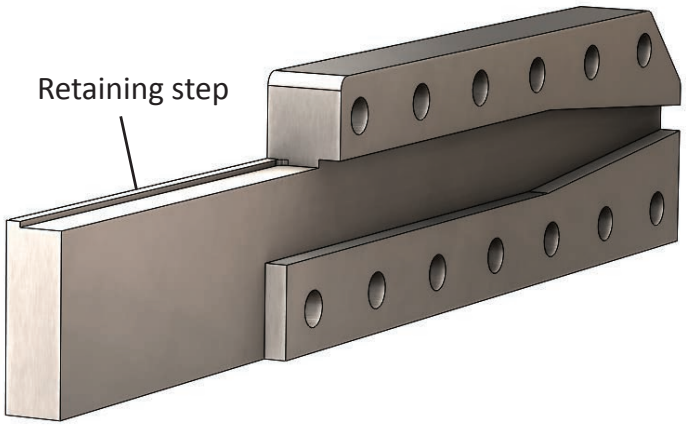

Figure 2.6. Version 1.3 channel closeout with graphite gasket retaining step.

2.1.3 Predetonator

A predet similar in design to the one used in [40] is shown in Fig. 2.7. This device was used to generate a detonation wave using oxygen and either hydrogen or ethylene as propellants. It was redesigned from an earlier version [11] by Andrei Anghelus (now graduated) at Zucrow Labs, to be more durable than the original unit. Solenoid valves (Parker® 009-0172-900) were chosen as propellant run valves for their fast response (<5 ms). Propellants were fed to the predet chamber through 1.59 mm (0.0625 in) tubing. The hot components comprise a mixing and ignition chamber and

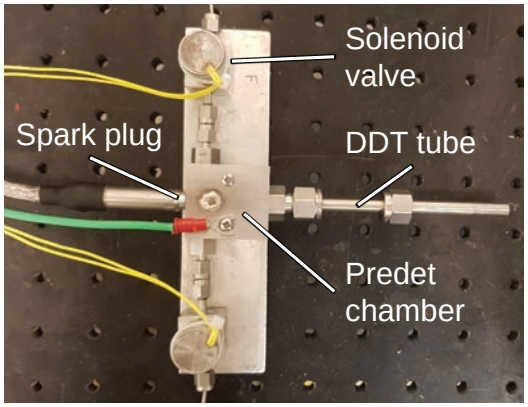

Figure 2.7. Predetonator used to initiate detonation.

a deflagration-to-detonation transition (DDT) tube. At the head end of the chamber, a spark plug (NGK^{TM} ME-8) was used as the ignition source.

Once the mixture was ignited, it expanded through the DDT tube, which was constructed using a 6.35 mm (0.25 in) stainless steel tube tapped internally with a 10-32 thread. The threads acted similarly to a Shchelkin spiral, which is commonly used to promote transition of the combustion from deflagration to detonation. The DDT tube passed through the test article mounting lid via a Swagelok® compression fitting into the detonation channel block. Propellant mass flow rates were not metered; they were estimated by assuming choked flow in the feed lines.

It was found during testing that humidity inside the pressure vessel was extremely high due to production of steam during combustion and evaporation of injected water into the warm environment. As a result, condensation within the predet chamber often caused it to fail to ignite. Another problem that surfaced from the presence of excess moisture was the irregularity of detonation, which will be elaborated on in Section 3.1.1. Since purge gas was fed through the same 1.59 mm (0.0625 in) tubing that supply propellants, flow rate was severely limited and insuficient for ejecting condensate from the predet.

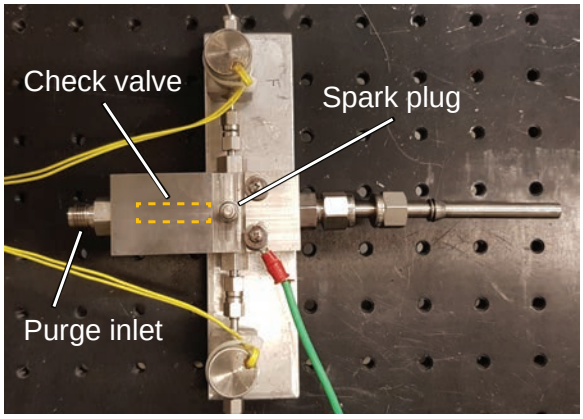

Figure 2.8. Version 2 of predetonator with extended body for housing check valve.

After the conclusion of tests using hydrogen and oxygen, the predet's design was modified. A dedicated purge port was introduced to allow increased volumetric flow. The predet body was extended to accommodate installation of a LeeCo® miniature check valve (CHFA2506501A); this was necessary for minimizing residual volume adjacent to the combustion chamber. The new predet design proved to be very effective: 100% ignition was achieved, and detonation pressure profiles were consistent and repeatable.

Figure 2.9 provides a side-by-side comparison of the peak pressures recorded in each test, normalized by each propellant combination's respective C-J pressure ratio. In Fig. 2.9(a) the large scatter in obtained peak pressures is apparent; values greater than 1.6 were caused by unstable and overdriven detonations believed to have been caused by excessive condensation obstructing detonation wave passage. The data in 2.9(b) shows a stark difference in scatter; grouping is much tighter and overdriven detonations had been eliminated. The reader may notice that average normalized peak pressures are lower; this was possibly due to under-filling of the detonation channel. However, their absolute amplitudes were more than sufficient for the purpose of the study.

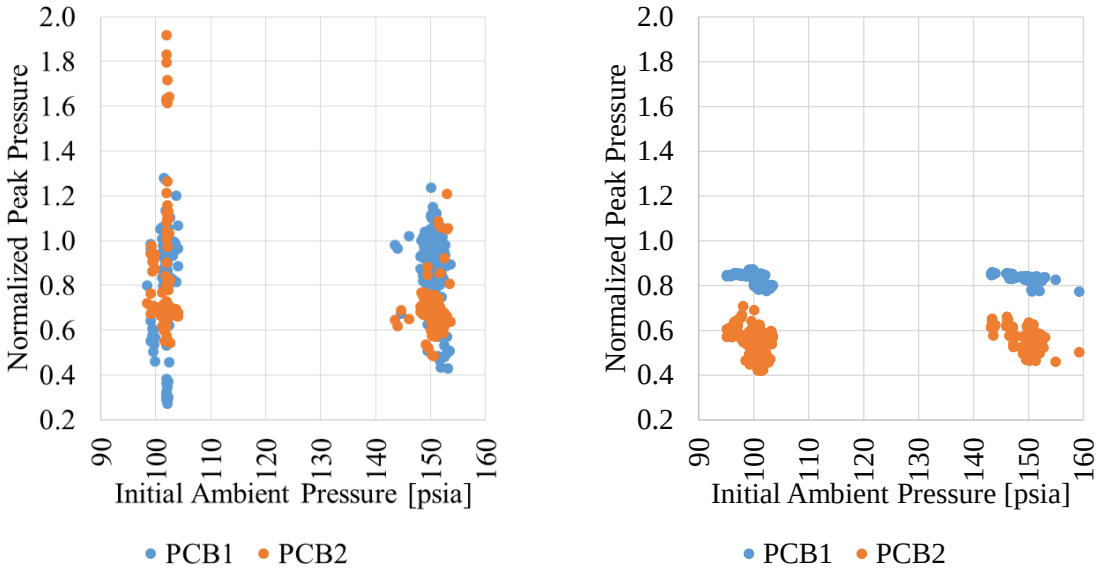

(a) Old predet design (H_2-O_2)

(b) New predet design (C_2H_4-O_2)

Figure 2.9. Normalized detonation pressure ratio vs. initial ambient pressure. Vertical axes have been set to the same range for better comparison.

2.1.4 Injector Modules

The injector modules were machined from clear acrylic to provide optical access to the injector passages. The baseline injector inner diameter was designed to 0.033 in (0.84 mm). Four injector designs were tested for this study: Three of the same baseline diameter at different length-to-diameter ratios and one of a larger diameter to investigate the effects of geometrical scaling. Their nominal major geometrical parameters are tabulated in Table 2.1, and Fig. 2.10 depicts the internal geometry of the injector modules. To facilitate reference and discussion, these injectors will be referred to as the *LD6-1.5S*, *LD10*, *LD6*, and *LD4* injectors according to the table.

The LD6 injector was chosen for scaling by 1.5 times to give the LD6-1.5S configuration because the resultant length ends up being similar to that of the LD10 injector, providing another dimension for comparison. The ports seen in the plenum area immediately upstream of the injector passage are pressure ports; these were

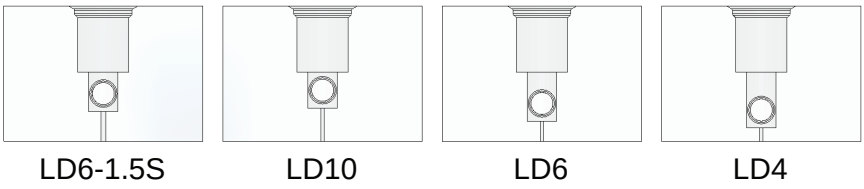

Figure 2.10. Drawings of injectors showing internal geometry.

Table 2.1. Geometrical parameters of injectors tested.

Injector designation	Nominal diameter, D [mm (in)]	Nominal L/D	Max. deviation in L/D [%]	Injection Angle [°]
LD6-1.5S	1.26 (0.050)	6	+3.8, -1.7	0
LD10	0.84 (0.033)	10	+4.7, -1.5	0
LD6	0.84 (0.033)	6	+5.7, -2.5	0
LD4	0.84 (0.033)	4	+7.0, -3.8	0

present only for the second test series utilizing ethylene and oxygen. In the initial configuration, the pressure port was located upstream of the injector module (Fig. 2.12). Reason for the change will be explained in Section 3.3.4.

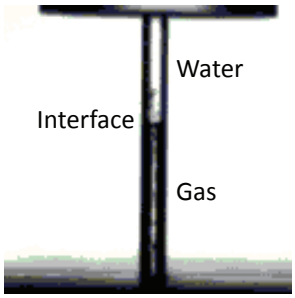

Figure 2.11. Visual example of the distinction between injector volumes occupied by liquid and gas phases.

Due to the injector's cylindrical surface and refractive indices of acrylic and different phases of fluids in the injector passage, the volume occupied by water appears bright and sharp when backlit while the gaseous volume appears much darker and with thicker edges along the wall. Figure 2.11 is an image taken during back-flow of gases into the injector following the passage of a detonation wave. The liquid phase is easily distinguishable from the gas phase. Due to adhesion, a film of water remains on the passage wall in the region occupied by the gas phase. The turbulence of high-speed flow distorts the surface of the film causing dark shadows to be formed from the shadowgraphic effect of the backlight.

2.1.5 Data Acquisition and Instrumentation

Two National Instruments™ data acquisition (DAQ) systems were employed. The first was a standard DAQ system with a maximum sampling rate of 1 kHz, which was used to control valves and electronic pressure regulators, and to acquire pressure data from the water manifold and pressure vessel transducers. A second high-speed mobile DAQ cart capable of sampling at 2 MHz was used to record data from three PCB® high-frequency pressure sensors located at various points on the test article, and also to trigger the high-speed camera.

Two high-frequency pressure sensors (PCB® 113B22), one located at the injection site and the other 130 mm (5.1 in) upstream in the detonation channel, were used to capture the pressure profile of the detonation waves and calculate the average detonation wave speed. Output from these sensors is analyzed to assess the strength of the detonation by comparing the peak pressures and wave speeds to their respective C-J values.

It is worth clarifying at this point that it was not a goal in these experiments to achieve C-J values; any coupled detonation with consistent strength and steep-fronted pressure profiles will suffice. Realistically, one should not expect to consistently obtain peak pressures close to C-J values due to the fact that C-J calculations are based on

steady one-dimensional detonations. However, it is still possible to achieve peak pressures greater than C-J theory when over-driven detonations occur.

Initially, the elbow fitting installed on the injector module was modified to permit installation of a third pressure transducer that measured the transient manifold pressure approximately 53 mm (2.1 in) upstream of the injector. All three high-frequency pressure sensors were flush-mounted to manufacturer specifications so as to capture high-frequency content with minimal attenuation. In [40], it was deduced that the transient pressure fluctuations within the manifold resulting from the reflections of compression and expansion waves could potentially affect the recovery rate of the injector. Therefore, this high-frequency pressure measurement could be utilized as inflow boundary conditions for numerical modeling of the injection dynamics. In addition, manifold pressure amplitudes can also be compared with those measured at the injection site to examine how the acoustic waves attenuate as they travel up the manifold.

Since the test article was contained within the pressure vessel, instrumentation cables and fluid feed lines had to be passed through the mounting lid with appropriate sealing. Tubing for water and predet were passed through the lid using bored-through Swagelok® compression fittings. Conax® hermetic feedthroughs were used for the PCB® sensor cables. As a word of caution, the nut responsible for compressing instrumentation cable feedthroughs should be tightened gently since excessive compression of the soft sealing components could result in the complete severance of the fine cables over time.

A 575 W theatre light (ETC® PARNel-A) fitted with a gel diffusion sheet was used to provide diffused backlight for the experiments. The high-speed camera (Vision Research® Phantom V2512) was used with a 200 mm lens to provide magnified high-speed images of the dynamic events during testing. Since the high-frequency pressure transducers only measured dynamic pressure, a 2.1 MPa (300 psia) (GE® Druck PMP1260) and a 4.1 MPa (600 psia) (GE® Unik 5000) pressure sensors were used to provide absolute reference pressures for the vessel and feed line respectively. A

picture of the assembled test article is shown in Fig. 2.12 and the full plumbing and instrumentation diagram (P&ID) of the setup can be found in Appendix B.

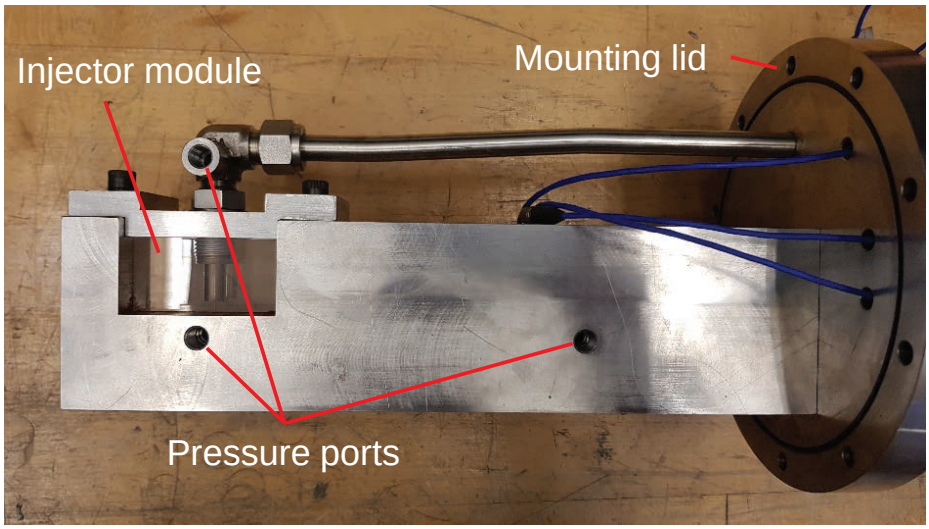

Figure 2.12. Assembled test article showing high-frequency pressure port locations and various feedthrough ports.

2.1.6 Methodology

Due to the high-powered lighting and combustion, the interior of the pressure vessel became warm and evaporation of the injected water was promoted. Since steam was also a major product of combustion, the vessel became saturated with water vapor very quickly and image quality degraded as a thick fog obscured the optical path. This problem was exacerbated as operating pressure increased because of the increased gas density and decrease in water solubility with increased pressure.

Dr. Wesly Anderson used the same test facility [30, 42] and also observed that flooding was a problem associated with long predet DDT tubes; the predet failed to function after every two to four tests. Aside from failure of the spark plug to discharge, the water also hindered the flow of propellants through the tube. It was quickly realized that the pressure vessel's drain valve should be left partially open so

that the excess water and moisture could be purged with an active nitrogen flow from the vessel's pressurization line. While visibility improved very significantly, predet flooding remained a problem. When this occurred, the predet purge had to be run for several minutes to dry its internal components before resuming operation. This problem was later solved by the modification to the predet per Section 2.1.3.

To minimize test duration, the initial pressure drop was set to 10 psig for every injector and tested once. The extent of back-flow was noted, and pressure drop was increased by another 69 kPa (10 psi) until the injector just barely back-flowed completely. This pressure drop was then taken as the first test condition and four more tests were performed at the same condition. Subsequently, pressure drop was raised by approximately 10 psi (dependent on response of pressure regulator) until each injector began to show limited back-flow. Each injector was tested five times per condition to verify that results were consistent and to help identify outliers. To obtain the high-speed images, a Phantom® V2512 camera which was capable of recording at 400,000 fps at a resolution of 128×128 pixels was used.

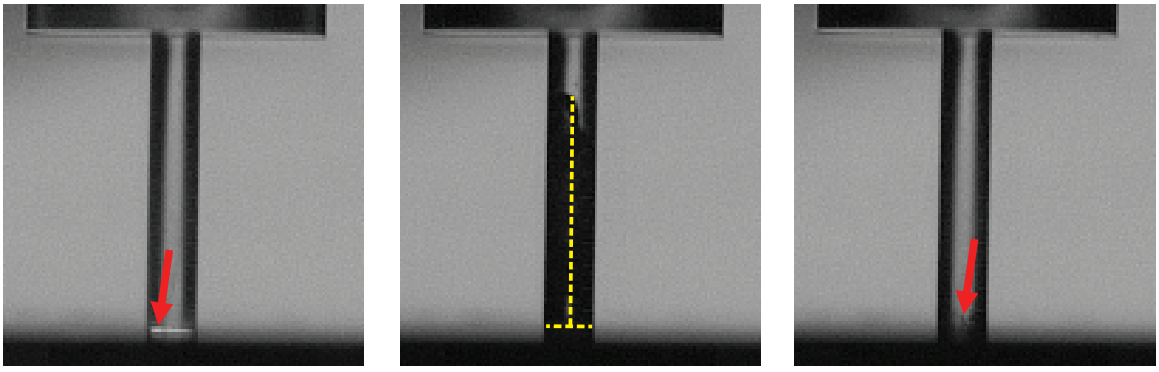

Figure 2.13. Visualization of measurement standards for back-flow distance and refill time, Left: Start of refill time measurement, center: maximum back-flow, right: end of refill time measurement.

Through the Vision Research® Cine Viewer software, injector back-flow distance and refill time measurements could be made from the raw video data. Both measurements were taken using the injector centerline as basis since the liquid-gas interface

was rarely perpendicular to the injector's cylindrical axis. Refill time was defined as the time from the first visible evidence of back-flow to the instant at which the centerline was once again occupied by the liquid phase.

Figure 2.13 provides a visual reference of the standard employed when taking measurements. In the left image, a small pocket of gas had just become visible in the corner of the injector exit, indicated by the red arrow – refill time measurement starts at this frame. Just as importantly, the bright horizontal line caused by light emission from the detonation sets the refrence point for back-flow distance measurements. The reader may notice that it is not collinear with the dark horizontal shadow in the foreground which appears to be the injection plane, but the effect is solely due to the injection plane being non-perpendicular to the focal plane. The center image demonstrates that even though the free surface may be highly-tilted, measurement is taken only along the centerline indicated by the vertical yellow dashed line. Finally, the image on the right marks the end of refill time measurement. A red arrow points at the existence of some dispersed gas bubbles; these are regarded as negligible gas volumes. These measurements were used to evaluate the accuracy of the 1-D numerical model developed in [40].

2.1.7 Uncertainty Quantification

Basic uncertainty quantification was carried out on the data obtained from the experiments. Table 2.2 shows the base uncertainties of instruments and measurement methods employed in the study. Subsequently, statistical error propagation was applied to obtain the final uncertainty ranges associated with the derived quantities: back-flow distance, refill time, and injector stiffness.

For the most part, the uncertainty values associated with the high-speed images are small; due to the high magnification afforded by the lens and high frame rate, length measurements were limited by pixel count (± 1 pixel) and refill time measurements could be made within two frames of accuracy (± 5 μs). Compared to the scales

Table 2.2. Uncertainties of base parameters associated with injector response hardware and instrumentation.

Parameter	Uncertainty
Video pixel resolution	.05 to .07 mm/pix (.002 to .003 in/pix) by case - see Appendix A
Video temporal resolution	±2.5 μs
On-screen point placement	±1 pixel
Determination of start of back-flow	±2.5 μs (1 frame)
Determination of completion of refill	±7.5 μs (3 frames)
PCB113B22 pressure sensor output	≤ ±50 psi (348 kPa)
Vessel pressure	±.75 psi (5 kPa)
Water manifold pressure	±.24 psi (2 kPa)
Injector diameter (pin gauge)	±.0005 in (.01 mm)
Injector length (machining specification)	±.005 in (.1 mm)

of the actual measurements, these are small, and attempts to include error bars on the plots resulted in error bars whose spans were smaller than the size of the markers themselves. Consequently, error bars have been omitted from the plots. However, resolution and uncertainty values are tabulated and shown in Tables A.1 through A.18 in Appendix A. Propagation of uncertainties for derived quantities was calculated according to the following equations most commonly used in the calculation of standard deviation [43]:

$$\Delta\left(x \pm y\right) = \sqrt{\left(\Delta x\right)^2 + \left(\Delta y\right)^2} \tag{2.1}$$

$$\frac{\Delta\left(x/y\right)}{\left(x/y\right)} = \frac{\Delta\left(xy\right)}{\left(xy\right)} = \sqrt{\left(\frac{\Delta x}{x}\right)^2 + \left(\frac{\Delta y}{y}\right)^2} \tag{2.2}$$

In these equations, x and y represent variables in a function and the Δ terms represent the uncertainties associated with the corresponding variables. Eq. (2.1) states that the *absolute* uncertainty of a function involving the sum of variables x and y is equal to the square root of the summed squares of the independent uncertainties. Eq. (2.2) is pertinent to functions involving division or multiplication of variables. Here, the *relative* uncertainty of the function is the square root of the sum summed squares of the independent relative uncertainties. For example, in the calculation of back-flow distance, two points are selected on the image - one at the injector exit, and one at the surface of the water. Because of the low pixel count, it is trivial to achieve one pixel of accuracy at each point. Subtraction of the coordinates at each point gives the distance, so the first equation is employed. The case is the same for refill time measurements. As for injector stiffness, the first equation is required to determine the uncertainty in ΔP and the second equation accounts for the division by initial pressure.

Table 2.3 summarizes the resultant minimum and maximum uncertainty ranges for the derived quantities of interest to the study after computing error propagation: back-flow distance, refill time, and injector stiffness. Since high-speed videos were taken at the same frame rate every time, the uncertainty in refill time is constant in all tests. However, the uncertainties for back-flow distance and injector stiffness vary by test and therefore it is impractical to present detailed information here, but are tabulated in Appendix A.

Table 2.3. Minimum and maximum uncertainties of derived injector response parameters.

Derived Parameter	Min. Uncertainty	Max. Uncertainty
Injector stiffness, $\Delta P/P_{min}$	$\pm.005$	$\pm.025$
Max. back-flow distance [mm (in)]	$\pm.08$ (.003)	$\pm.14$ (.005)
Refill time [μs]	±8	

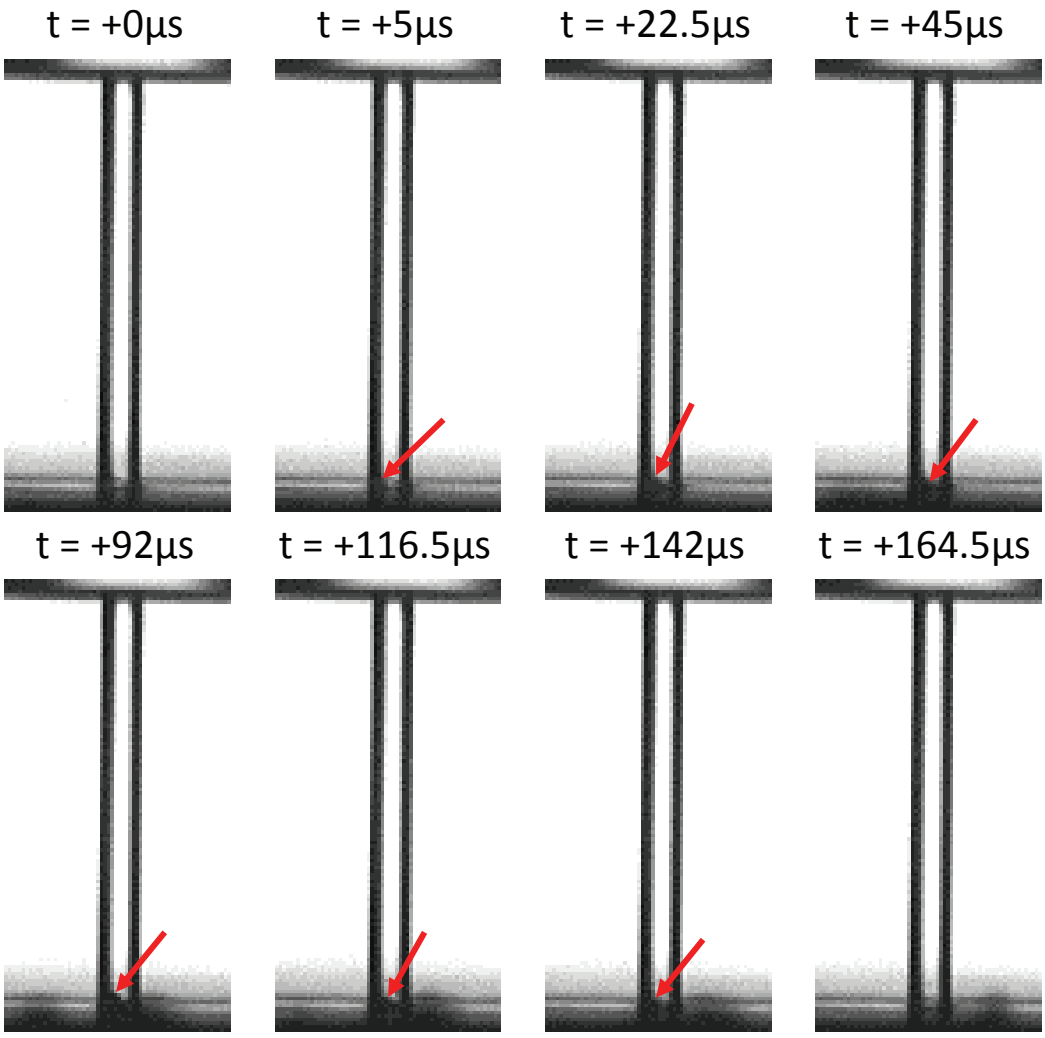

Figure 2.14. Images showing a gas pocket's evolution during limited backflow. Red arrows point at the free surface in an approximately normal direction to magnify the undulating behavior of the surface. Injector: LD10, fuel: hydrogen, vessel pressure: 1,030 kPa (150 psia), ΔP: 731 kPa (106 psi). Images captured at 400,000 fps and a resolution of 128×128 pixels.

In the cases bordering on limited backflow, the largest source of uncertainty came not from the accuracy of the data, but from the backflow event itself. The reason is as such: The diameter of the injector orifice is large compared to the thickness of the detonation front. As the shock front traverses the orifice, the water column

does not respond as a whole; instead, the upwind edge recedes first, and so a slanted free surface forms. This free surface undulates even at the short time scale of the experiments. Since this waviness is not apparent in still images, red arrows have been used in Fig. 2.14 to point at the free surface in an approximately normal direction such that the undulating behavior is amplified.

The highly-skewed pocket of gas sometimes crosses the centerline to a greater extent than others, and in doing so introduces an element of randomness that is difficult to quantify. In the figure, the pocket of gas initiating from the upwind edge of the orifice expanded laterally partway across the orifice and was eventually expelled completely from the passage. Throughout the back-flow and refill phases, the free surface remained tilted in the same direction. While the abovementioned uncertainty has not been accounted for in the above calculations, it should be noted that the right-hand end of each set of data should be expected to contain larger random error than the rest.

2.2 GOX-RP-2 RDE Facility

A large majority of the RDE main chamber design work was done by Dr. David Stechmann [15], and modified for additional instrumentation and to operate with a liquid fuel. The full engine system contained four combustion devices: preburner, main chamber, and two torch igniters. It was mounted on the 10k Stand at the High Pressure Lab, which contained the supporting infrastructure necessary for conducting test operations.

Bulk nitrogen is supplied at up to 41.4 MPa (6,000 psia) and was used to pressurize the RP-2 and LOX run tanks, as well as provide purge gas for the combustion devices at various stages of operation. The facility RP-2 run tank was designed to a maximum operating pressure of 34.5 MPa (5,000 psia) and holds 56.6 liters (15 US gallons) of kerosene-based fuel. LOX is stored in a low-pressure bulk tank and transferred into a run tank prior to engine operation. The LOX run tank has a maximum operating

pressure of 34.5 MPa and capacity of 238 liters (63 US gallons). Both propellant run tanks are pressurized through computer-controlled pressure regulators to permit safe propellant loading from the control room.

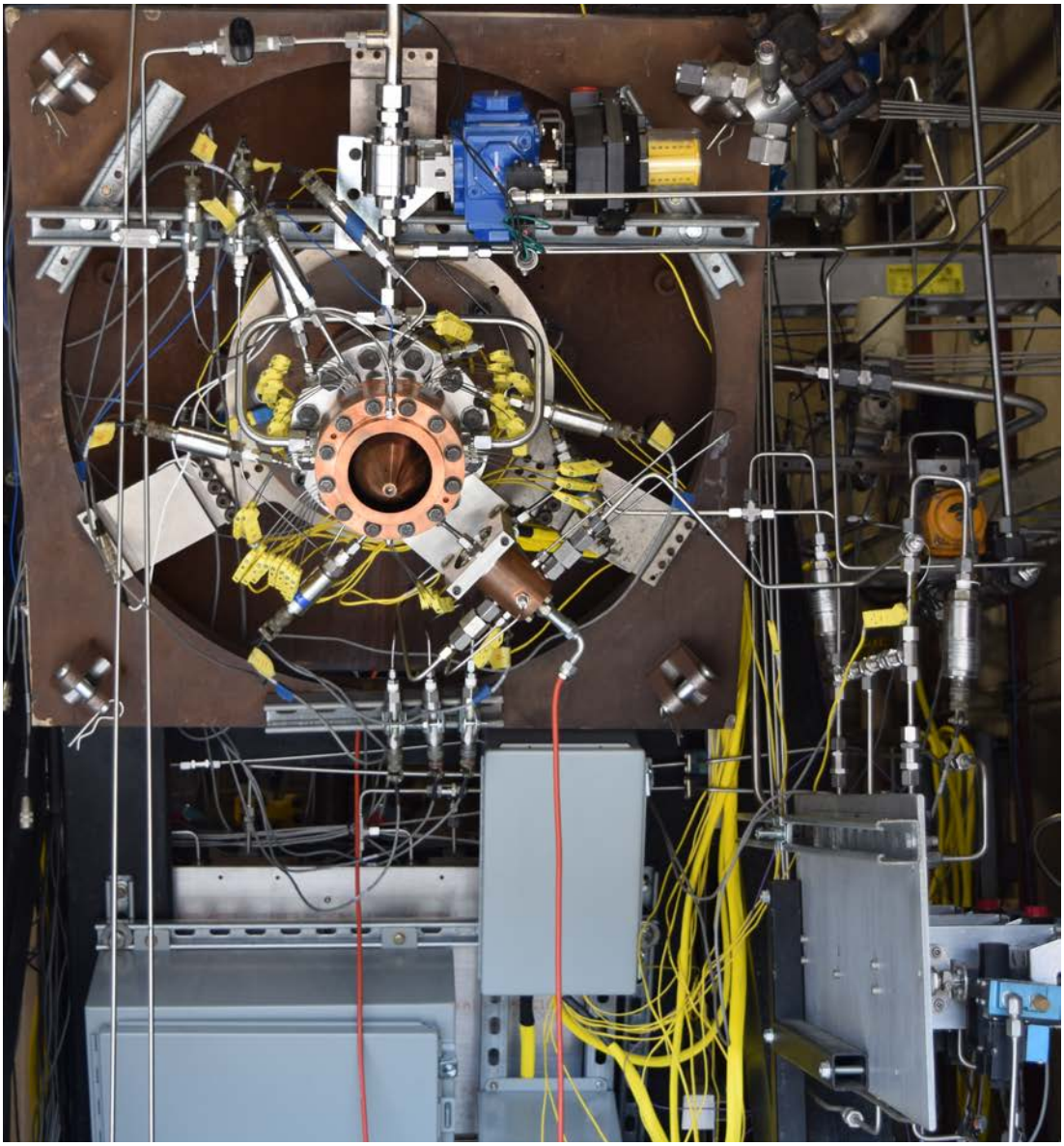

Figure 2.15. Full RDE v1.4 assembly mounted on the 10k Stand at the High Pressure Lab, Maurice J. Zucrow Laboratories. Photograph courtesy of Jenna Humble.

2.2.1 Preburner

An oxidizer-rich preburner installed upstream of the RDE chamber was used to generate GOX for use in the RDE. The preburner operates by burning LOX and hydrogen in a very lean mixture ratio resulting in a mixture of GOX and water. It is capable of operating at a wide range of temperatures; in Stechmann's tests, GOX outlet temperatures ranged from 223 to 466 K (-40 to 380 °F) [15]. In the majority of the current test cases, the preburner's mixture ratio was between 230 and 240, resulting in GOX temperatures in the vicinity of 400 K (260 °F). As these gases accelerate to the chamber from this nearly-stagnant combustion condition, their static temperature drops to values near room temperature as the stream interacts with fuel in the combustion chamber. Throughout the test campaign, the largest distribution plate was utilized such that the preburner outlet was un-choked relative to the RDE's GOX manifold. Mass flow rate into the main combustor was controlled by the LOX and hydrogen venturis feeding the preburner. The GOX is allowed to mix and homogenize in a plenum downstream of the chamber exit before passing into the RDE's GOX manifold.

2.2.2 Main Chamber

The main combustion chamber was a constant-area annulus with outer and inner diameters of 98.6 and 83.3 mm (3.88 and 3.28 in) respectively. In its most basic configuration, it comprised six components: Fuel injector housing, fuel injector insert, outer chamber igniter ring, outer chamber extension, injector centerbody, and inner chamber centerbody. An aerospike nozzle could also be installed to the combustor exit as an additional attachment for nozzle studies. However, nozzle performance is out of the scope of this document.

The fuel injector housing contained the fuel manifold and its inner wall separated the fuel manifold from the GOX manifold. The fuel injector insert was clamped between the fuel injector housing and outer chamber igniter ring, which was a 19 mm

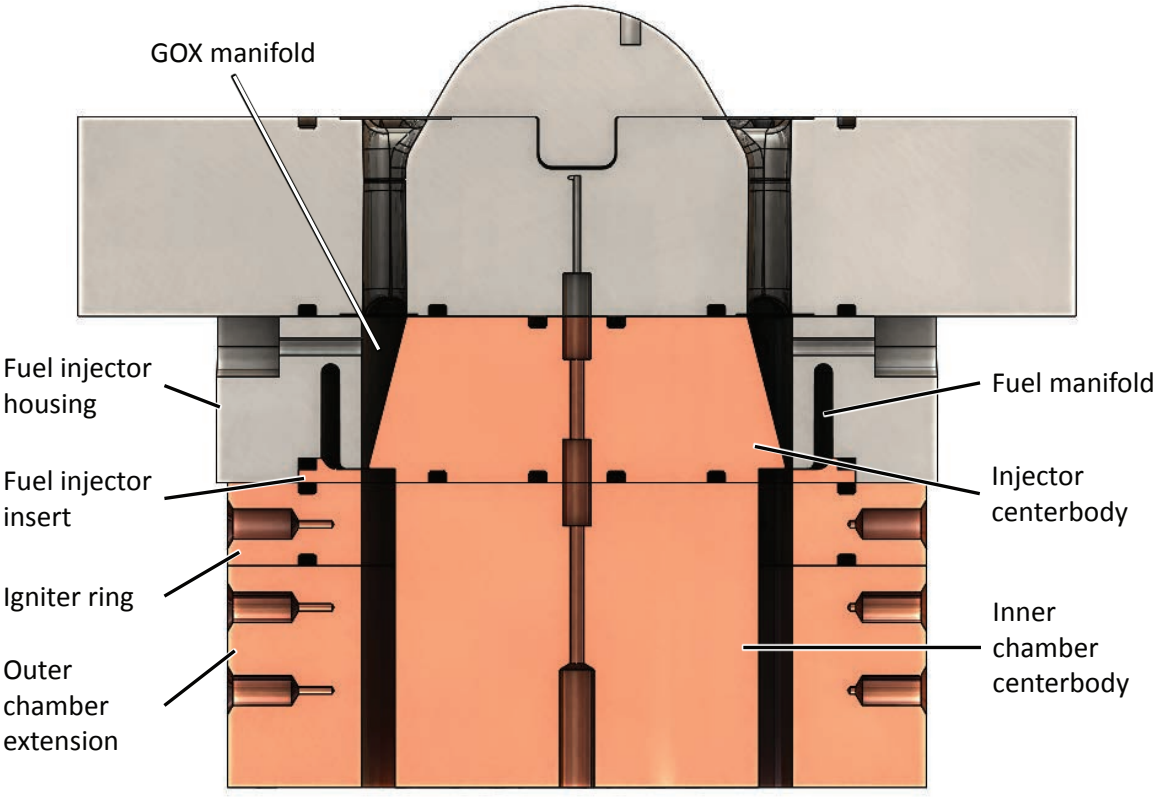

Figure 2.16. Longitudinal section of RDE v1.4 showing major components.

(0.75 in) thick copper section that contained an igniter torch port through which hot combustion products from a hydrogen-oxygen torch igniter were injected. The next component was a 50.8 mm (2 in) outer chamber extension that extended the overall chamber length and hence increased chamber residence time.

The contraction ratio of the GOX manifold was set by the injector centerbody, which took the form of a cone frustum that formed a converging flow path with the fuel injector housing. The base diameter of the centerbody used was 97 mm (3.82 in) and was kept constant throughout the test campaign. The resulting GOX injection annulus had a width of 0.76 mm (0.030 in) and contraction ratio of 12. The inner chamber centerbody was 83.3 mm in diameter and set the combustion chamber's

width. This was also kept fixed in all tests. A longitudinal section of the main combustor is shown in Fig. 2.16.

2.2.3 Injector Inserts

Figure 2.17. CAD render of injector insert with 120 injectors, groove width 0.38 mm (0.015 in).

A total of five different injector configurations were tested. The injector inserts were flat copper rings into which grooves were machined using ball end mills of various diameters. When the insert was seated in the injector housing, the lands between the milled grooves were pressed against the fuel manifold inner wall forming semicircular orifices. Sealing between the passages relied on metal-to-metal contact achieved through compression of the engine stack. The outboard side of the fuel injector and manifold was sealed using O-rings. Table 2.4 shows the major dimensions associated with each injector configuration and Fig. 2.17 is a CAD render of the 015×120 injector insert.

Prior to testing, two of the injectors (configs. 008×120 and 011×120) were imaged using a microscope to record their pre-test surface condition. This was done based on the findings of the injector dynamic response experiments where cavitation was observed within the injector passages following the passage of detonation waves. Post-test microscope images were also taken and results will be discussed in Section 4.8.

Table 2.4. Geometrical parameters of slot injectors tested.

Injector designation	Groove width, W [mm (in)]	Groove depth, d [mm (in)]	No. of grooves
008×120	0.20 (0.008)	0.10 (0.004)	120
011×120	0.28 (0.011)	0.15 (0.006)	120
015×120	0.38 (0.015)	0.20 (0.008)	120
011×180	0.28 (0.011)	0.15 (0.006)	180
015×180	0.38 (0.015)	0.20 (0.008)	180

2.2.4 Data Acquisition and Instrumentation

The standard DAQ system for the 10k Stand made use of the National Instruments™ platform and included 64 thermocouple (48 Type-K and 16 Type-E), 104 analog input, 32 analog output, and 32 digital output channels, allowing for valve control and feedback, pressure regulation, and temperature and pressure measurements at up to 5 kHz. For high-frequency instrumentation such as pressure sensors and load cells, a second high-speed DAQ system was used to record data at up to 2 MHz.

The RDE main chamber section was instrumented with a total of 36 Omega™ Type-K exposed-junction thermocouples, two Kulite® XTM-190 and a PCB® 113B22 high-frequency transducers, and nine Honeywell® and GE® standard-frequency pressure transducers. The 10k Stand also features three load cells from which thrust was recorded, but will not be discussed by the author due to ITAR restrictions. Lastly, a Vision Research® Phantom V2512 high-speed camera was used to capture aft-end views of the RDE.

To facilitate discussion in the document, the thermocouple probes have been grouped numerically from 1 through 13. Figure 2.18 shows a plot of the locations of all 36 thermocouple probes on the z-θ plane while Figs. 2.19 and 2.20 provide visual

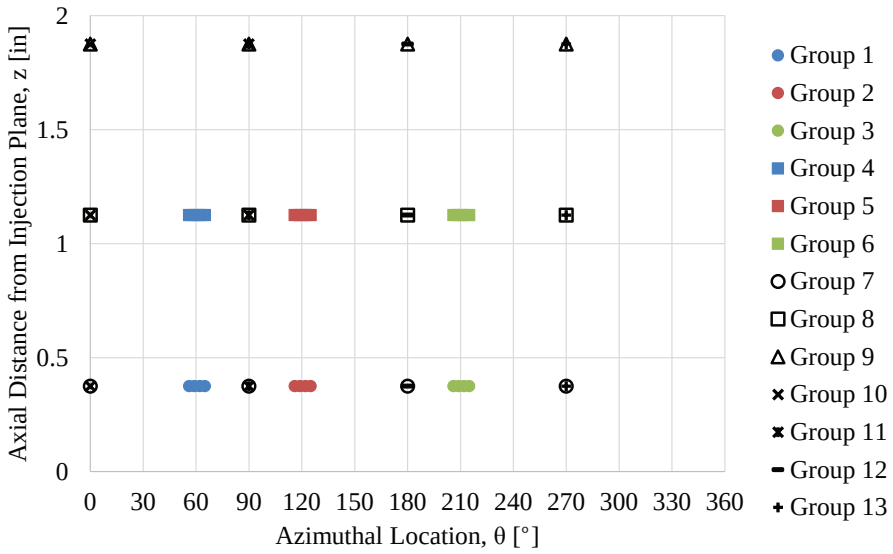

Figure 2.18. Location map of embedded thermocouple probes in the chamber outer wall (depths not indicated).

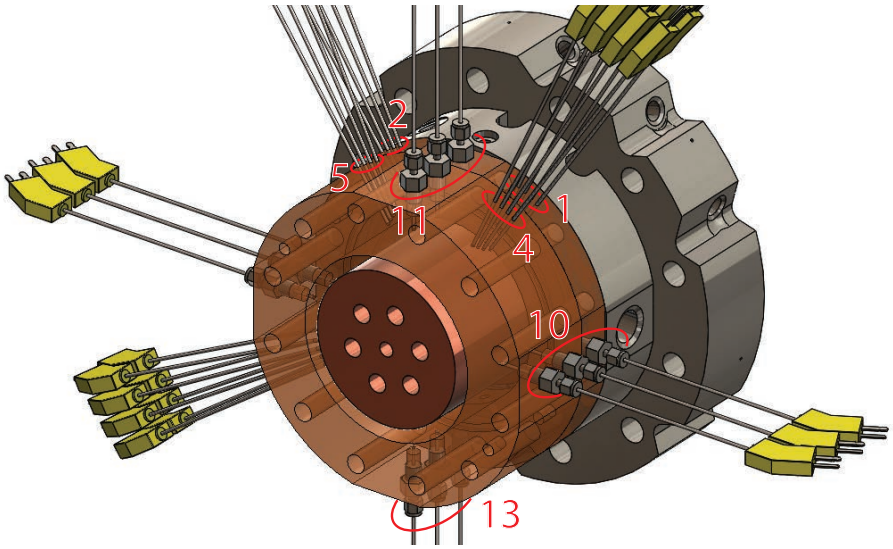

Figure 2.19. Angled view (from right) of chamber exterior indicating groups of thermocouple probes. Copper external wall rendered translucent to show probe positions.

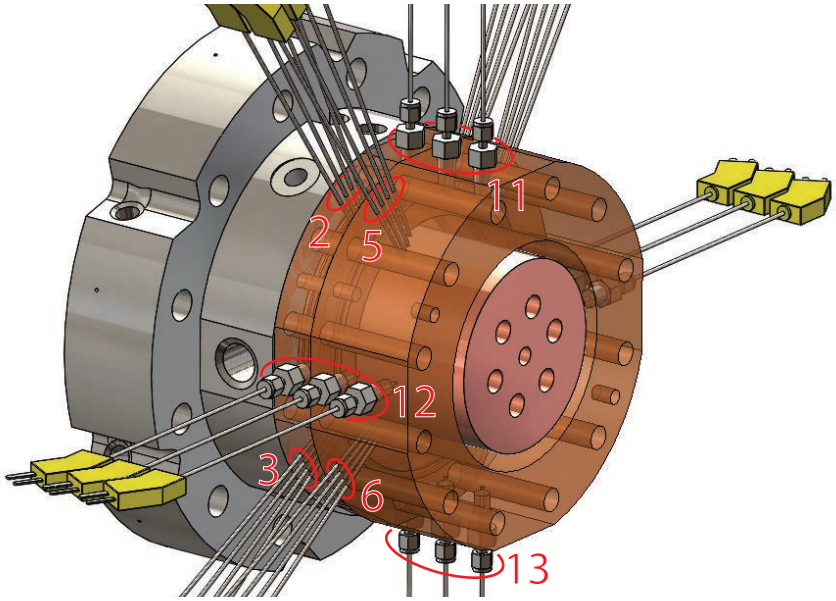

Figure 2.20. Angled view (from left) of chamber exterior indicating groups of thermocouple probes.

references of the locations relative to the engine. Note that due to clutter, groups 7, 8, and 9 have not been labeled; these include the same thermocouple probes in groups 10 through 13, but divided according to axial instead of azimuthal station. Group 8 comprises the four thermocouples closest to the chamber head, group 9 the ones in the middle, and group 10 being the aftmost. The thermocouple probes were installed dry based on the high wall temperatures expected; thermal compounds could degrade over tests and result in drifts in readings. The azimuthal and axial (from chamber head) locations, and depths (distances from chamber surface) of all 36 thermocouples are tabulated in Appendix D.

The chamber outer wall components were originally machined with only 12 thermocouple ports (groups 10 through 13) arranged in four rows of three, spaced 90° apart. The groups were aligned with the longitudinal axis of the engine and spaced 19 mm (0.75 in) apart. The port depths were constant at each azimuthal station,

with the deepest ports at the 0° (3 o'clock) position and decreasing in depth in the counter-clockwise direction.

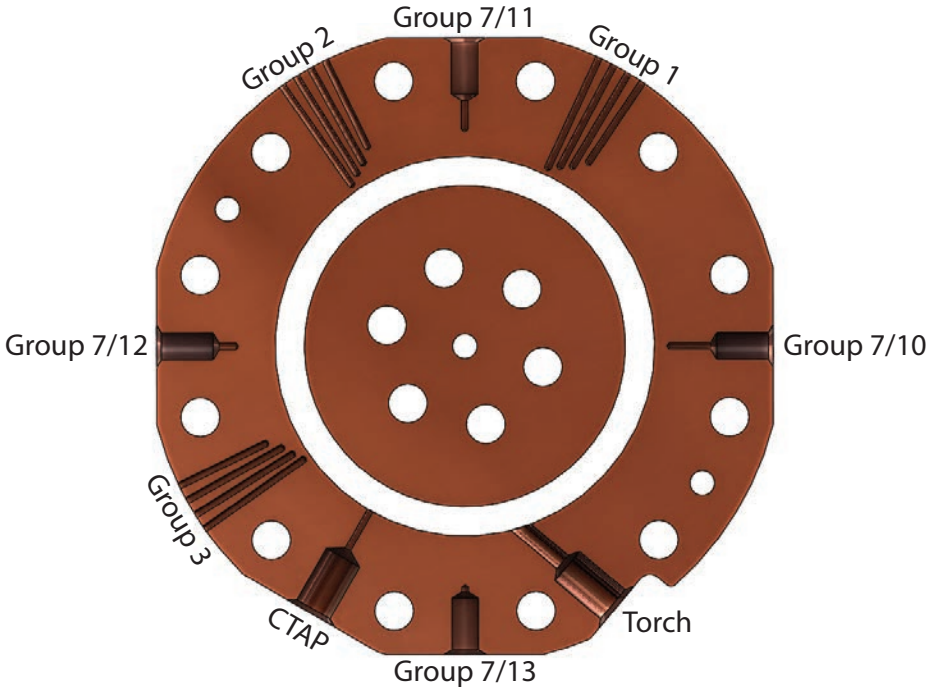

Figure 2.21. Section view of outer chamber igniter ring showing thermocouple probe locations in relation to igniter torch port.

This arrangement was influenced by the position of the torch port and its direction bias. Figure 2.21 depicts a section view of the outer chamber igniter ring which reveals the locations of the numerous ports that have been machined into the component. The torch exit can be found at approximately 285° (lower right) and canted off-radial towards the clockwise direction. The thermocouple ports were made shallowest at the 270° station to minimize the amount of distortion in wall temperature profile caused by torch ignition. The arrangement of this thermocouple array assumes that the heat flux in the chamber is axisymmetric to estimate the average heat flux of the full annulus.

24 additional thermocouple ports (groups 1 through 6) were later machined into the outer wall as alternative methods of measurement; 12 in the igniter ring and 12

in the chamber extension at approximately the 1, 8, and 11 o'clock positions. Four were located at each azimuthal station at different depths. The four thermocouples were separated 3° apart and the wall temperature profile they measured were treated as purely radial for simplicity; it was understood that the intrusive instrumentation would inevitably alter the conduction pathway. These thermocouples were used to resolve heat flux at six different locations in the chamber without having to assume axisymmetric distribution.

The initial 12 thermcouples were held in place using 0.0625-inch Swagelok® compression fittings with through bores. As the nut was tightened to compress the ferrules against the thermocouple sheath, the thermocouple probe was drawn further into the port by friction against the ferrules. Due to the fineness of the thermocouple wires, impingement of the exposed junction on a solid surface usually caused them to buckle. The buckling, while not necessarily damaging, ccould result in improper contact between the junction and the surface. With this in consideration alongside the small separation between the group 1–6 thermocouples, an adhesive was used to affix them.

The thermocouple sheaths and chamber wall surface were roughened with sandpaper and JB Weld® Extreme Heat putty was applied generously to the external surfaces. Contact of probe junction and wall surface was determined by tactile feedback and verified via application of heat on the chamber wall using a heat gun. It was found later that the probes could loosen from the torque applied while being bent to facilitate attachment of connecting cables because of the extremely small bonded surface area. Due to difficulties in maintaining good probe junction contact with either method of fixture, some loss of measurement was expected.

2.2.5 Methodology

One of the objectives of the test campaign was to sweep through several equivalent ratios for a range of mass flow rates to build an operating map. The initial targets were equivalent ratios between 1 and 1.6, with intermediate cases. The benchmark

performance was that of a theoretical constant-pressure combustor whose throat area was equal to the RDE's annular area. The following mass flow rate ($\dot{m}$) equation was used with characteristic velocity values calculated using CEA for the various equivalence ratios and arbitrary chamber pressure targets of 0.689, 1.03, 1.38, 2.07, and 2.76 MPa (100, 150, 200, 300, and 400 psia):

$$\dot{m} = \frac{P_c A_t}{c^*} \tag{2.3}$$

where P_c is the chamber stagnation pressure, A_t is the nozzle throat area, and c^* is the propellant's characteristic velocity. Since pressure regulators are subject to up- and downstream pressure fluctuations, the achieved mass flow rates were never exactly equal to target values. A post-test computation of theoretical constant-pressure combustor P_c was performed (courtesy of Jenna Humble) to obtain the corrected benchmark values to compare to experiments.

Initial tests made use of the 008×120 injector at extremely high stiffness settings and low flow rates as a precaution against back-flow of detonation products into the fuel manifold. Subsequently, larger injectors with lower pressure drops were utilized at higher fuel mass flow rates to obtain higher chamber pressures. Burn time was limited to approximately 1 second due to limitations imposed by the engine's heat sink design.

Pressure, temperature, and video data were windowed between 16.5 and 16.7 seconds on the autosequence coordinate. This window was chosen to exclude electrical noise originating from the main chamber spark plug – which unfortunately overlapped with engine startup – and ran for the duration of operation for which measured CTAP was relatively steady. Pressure and temperature from propellant circuits were used alongside cavitating or sonic venturis for flow metering.

High-speed videos were used to assess wave topology and stability during operation, both of which served as important metrics of detonation quality for the discussion to follow. All videos were captured at 200,000 fps and 256×256 pixels resolution. Temperatures recorded from the probe array in the outer chamber wall were vital to

the computation of heat flux produced in the chamber via the inverse heat transfer method, which is discussed in the following subsection.

2.2.6 Heat Flux Quantification

Problem Formulation

Heat flux into the chamber outer wall was computed in the form of a numerical inverse heat transfer problem utilizing an optimization algorithm. The numerical formulation of the problem begins by modeling the problem as 1-D radial conduction with forced and free convection on the chamber-side and external surfaces respectively. The heat diffusion equation in cylindrical coordinates according to [44] is

$$\rho c_p \frac{\partial T}{\partial t} = \frac{1}{r}\frac{\partial}{\partial r}\left(kr\frac{\partial T}{\partial r}\right) + \frac{1}{r^2}\frac{\partial}{\partial \theta}\left(k\frac{\partial T}{\partial \theta}\right) + \frac{\partial}{\partial z}\left(k\frac{\partial T}{\partial z}\right) + \dot{q} \tag{2.4}$$

where T is temperature, t is time, $\dot{q}$ is heat flux, and ρ, c_p, and k are the material's density, specific heat capacity, and thermal conductivity respectively. r, θ, and z represent the radial, azimuthal, and axial coordinates. The heat flux analysis presented in this document will only be concerned with 1-D diffusion in the radial direction. Together with the fact that there is no heat generation within the chamber wall, the terms in θ and z, as well as $\dot{q}$, are removed. The heat diffusion equation in the chamber wall can therefore be reduced from 2.4 to

$$\rho c_p \frac{\partial T}{\partial t} = \frac{1}{r}\frac{\partial}{\partial r}\left(kr\frac{\partial T}{\partial r}\right) \tag{2.5}$$

At the chamber wall surface, a convective boundary condition is imposed. Generally the convective heat flux term takes the form $h_g \Delta T$ where h_g is the heat transfer coefficient and ΔT is the temperature difference between the free stream flow and wall surface. Determining the value of h_g is not trivial and is typically estimated through use of empirical correlations such as the Bartz relation [14]. Both the combustion gas and wall surface temperature are also difficult measurements: Flame temperature routinely exceeds 3,000 K (4,900 °F) in rocket combustors and no thermocouple probe known to the author is capable of withstanding such harsh conditions.

Alternatively, laser diagnostics can be applied. However, that is a discipline on its own and requires expensive equipment and specialized training. The wall surface temperature may appear to be a simple measurement at first, but further consideration reveals its true challenges: Firstly, ignoring radiative effects, surface temperature is influenced by the gas in direct contact; mounting any sensor on the surface effectively changes its heat transfer characteristics such that the measurement no longer represents the quantity sought. Additionally, the sensor would need to survive the chamber environment. Placing a subsurface thermocouple probe from the external surface results in the same alteration of heat diffusion path. In short, invasive measurement techniques are both challenging and likely to produce inaccurate data. Again, laser diagnostics could potentially be used here. Consequently, the convective heat flux will simply be treated as a single heat flux term and solved as such.

On the external surface of the engine, a free convection boundary condition was applied. Given that the combustion chamber section of the engine was a short cylinder that was in surface contact with stainless steel on one side and open to ambient air on the other, it did not resemble any of the canonical shapes for which free convection relations exist. Therefore, treatment as a sphere and horizontal cylinder were both considered. Since the wall was almost thick enough to be considered a semi-infinite solid, it was subsequently found that the solution was for all intents and purposes insensitive to the type of geometry assumed here. The free convection equations used are as follows [44]:

$$Gr = \frac{g\beta\left(T_s - T_\infty\right)D^3}{\nu^2} \tag{2.6}$$

$$Ra_D = GrPr \tag{2.7}$$

$$\overline{Nu}_D = 2 + \frac{0.589Ra_D^{\frac{1}{4}}}{\left[1 + \left(\frac{0.469}{Pr}\right)^{\frac{9}{16}}\right]^{\frac{4}{9}}} \tag{2.8a}$$

$$\overline{Nu}_D = \left\{0.60 + \frac{0.387Ra_D^{\frac{1}{6}}}{\left[1 + \left(\frac{0.559}{Pr}\right)^{\frac{9}{16}}\right]^{\frac{8}{27}}}\right\}^2 \tag{2.8b}$$

$$h_\infty = \frac{\overline{Nu}_D D}{k_\infty} \tag{2.9}$$

Gr, Ra_D, $\overline{Nu}_D$, and h_∞ are the Grashof number, Rayleigh number, Nusselt number, and heat transfer coefficient respectively. β is the volumetric expansion coefficient of air, T_s is the wall's external surface temperature, T_∞ is ambient temperature, D is the diameter of the sphere or long cylinder, ν, Pr, and k_∞ are the kinematic viscosity, Prandtl number, and thermal conductivity of ambient air. The Nusselt number used in Eq. 2.9 depends on whether the engine is approximated as a sphere or cylinder; Eq. 2.8a for sphere and Eq. 2.8b for cylinder. The heat flux at the external wall surface is the product of the heat transfer coefficient and temperature difference between the wall surface and ambient air:

$$\dot{q}_\infty = h_\infty (T_s - T_\infty) \tag{2.10}$$

However, it has been found that the effects of free convection are negligible at the short time scales associated with engine hotfire.

Discretization

The wall was divided into $M-1$ equal radial segments using M nodes. The equations that represent the heat transfer problem were discretized as follows for computation. At the chamber surface boundary,

$$T_m^{p+1} = T_m^p + \frac{2\Delta t}{\rho_s c_{p,s} \Delta r}\dot{q} + \frac{2\alpha_s \Delta t}{\Delta r^2}\left(T_2^p - T_1^p\right) \tag{2.11}$$

For the wall internal nodes,

$$T_m^{p+1} = T_m^p + \frac{\alpha_s \Delta t}{r}\left(\frac{T_{m+1}^p - T_{m-1}^p}{2\Delta r} + r\frac{T_{m+1}^p - 2T_m^p + T_{m-1}^p}{\Delta r^2}\right) \tag{2.12}$$

And for the exterior surface boundary,

$$T_M^{p+1} = T_M^p - \frac{2h_\infty \Delta t}{\rho_s c_{p,s} \Delta r}\left(T_M^p - T_\infty\right) - \frac{2\alpha_s \Delta t}{\Delta r^2}\left(T_M^p - T_{M-1}^p\right) \tag{2.13}$$

where thermal diffusivity $\alpha = \frac{k}{\rho c_p}$. The superscript p and subscript m on the T terms denote the indices for the temporal (t) and spatial (r) coordinates respectively for

the current calculation step. The subscript s indicates that the properties are for the solid material.

The time step and mesh size chosen were $\Delta t = 1E-4$ s and $\Delta r = 0.0158$ mm (0.0062 in) using 211 nodes ($M = 211$) respectively to fulfil the cell Fourier number criterion for numerical stability [44]

$$Fo = \frac{\alpha t}{\Delta r^2} \leq 0.5 \tag{2.14}$$

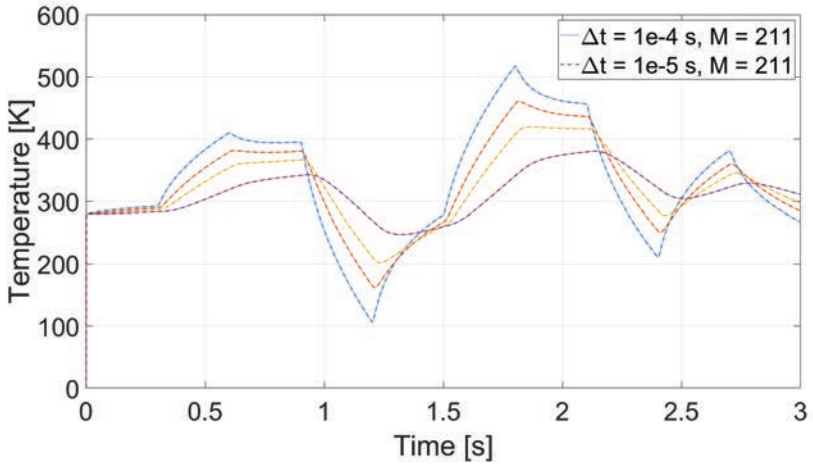

Figure 2.22. Time step convergence study of the transient 1-D conduction model. Solid lines represent baseline grid and dashed lines represent refined grid.

A time step and mesh size convergence study was performed to ensure that solutions computed were independent of either parameter. Figures 2.22 and 2.23 depict wall temperature profiles, produced by imposing a series of step changes in heat flux, at depths of 1.6, 3.2, 4.8, and 8.0 mm (0.063, 0.126, 0.189, and 0.314 in) corresponding to Group 1 probe locations. Solid lines represent solutions obtained using the chosen parameters, and dashed lines represent solutions from refined parameters. In Fig. 2.22, the time step was refined by a factor of ten to produce overlapping solutions. Both mesh size and time step (to fulfil stability criterion) were refined in Fig. 2.23. Similarly, solutions overlapped with baseline computations. Therefore, the

above-mentioned parameters have been proven to be insensitive to further grid size refinement and will be used to minimize computational time.

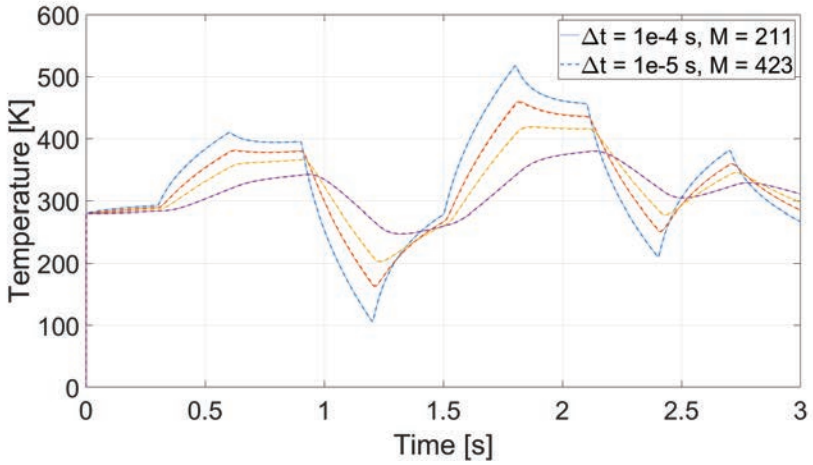

Figure 2.23. Mesh size convergence study of the transient 1-D conduction model. Solid lines represent baseline grid and dashed lines represent refined grid.

Inverse Heat Transfer Problem

A commonly-used numerical method of solving the inverse heat transfer problems is through numerical optimization [45]. In the current scenario, combustion in the chamber produces an unknown heat flux profile that causes the chamber wall's temperature to change with time. Given properties of the wall material, equations 2.11 through 2.13 can be used to compute wall temperature based on the heat flux from the gas. By taking the sum squared error (SSE) between measurement and computation as the cost function, a convex optimization problem is formed. MATLAB®'s optimization function *fminunc* [46] is a simple algorithm that uses the gradient method to seek the minimum value of a function. The discretized ideal conduction equations were written as a function that was called by *fminunc*, with the chamber heat flux

as the variable and SSE as cost function. The flow of the optimization process is as follows:

1. Initialize wall temperature by curve-fitting based on recorded wall temperature data

2. At each time interval, run the optimization function at a finer temporal resolution to find the heat flux value that results in a wall temperature profile that most closely matches data at the next time interval. Save the value of heat flux.

3. For the same time interval, run ideal conduction function a second time using heat flux found in the previous step to compute the new wall temperature profile. This profile will be used as the initial condition for the next time interval.

4. Repeat steps 2 and 3 until the end of the stipulated duration

Note that the duplicate run of the ideal conduction function in step 3 is necessary because the optimization function was programmed with a specific set of outputs that does not include the actual wall temperature profile.

Due to the finite rate of heat diffusion, large wall thickness, and long thermocouple response time, it should be expected of the wall temperature profile to lag the combustion significantly. The heat diffusion timescale $\frac{L^2}{\alpha_s}$ for the shallowest probe location is 0.02 s, therefore computational interval was set to a greater value to avoid numerical instability.

The greatest difficulty in accurately determining the heat flux produced in these short-duration tests stems from the long response time of thermocouple probes. According to documentation provided by Omega$^{\text{TM}}$, the exposed-junction probes utilized in the experiments, which contain wires 0.2 mm (0.008 in) in width, have a time constant (time to reach 63.2% of the value of a step-change in temperature) of approximately 0.19 s. In other words, given that hotfire duration was approximately 1 s, the thermocouple would only register 63.2% of any temperature change after a fifth of the total duration. Compounding the fact that wall temperature was changing

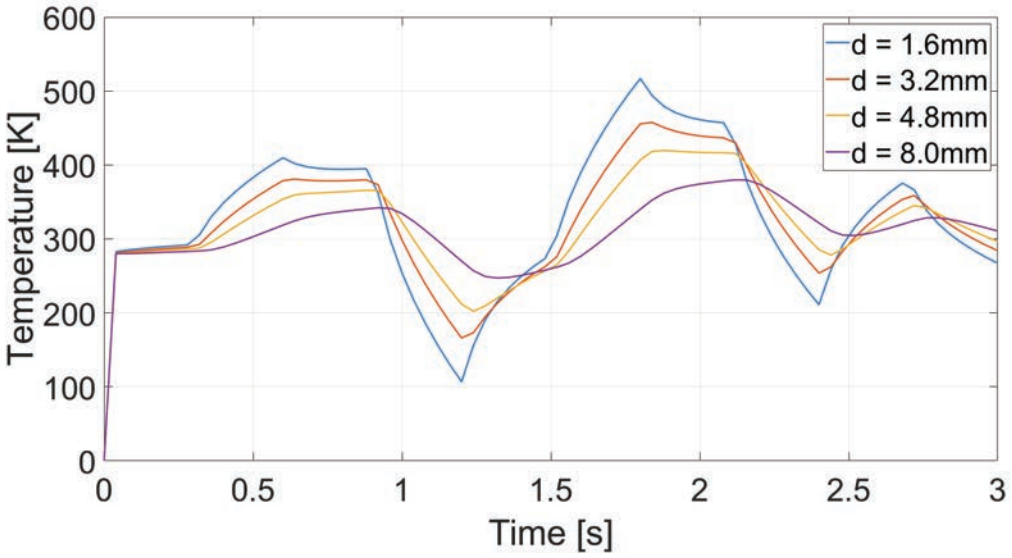

(a) Wall temperature target

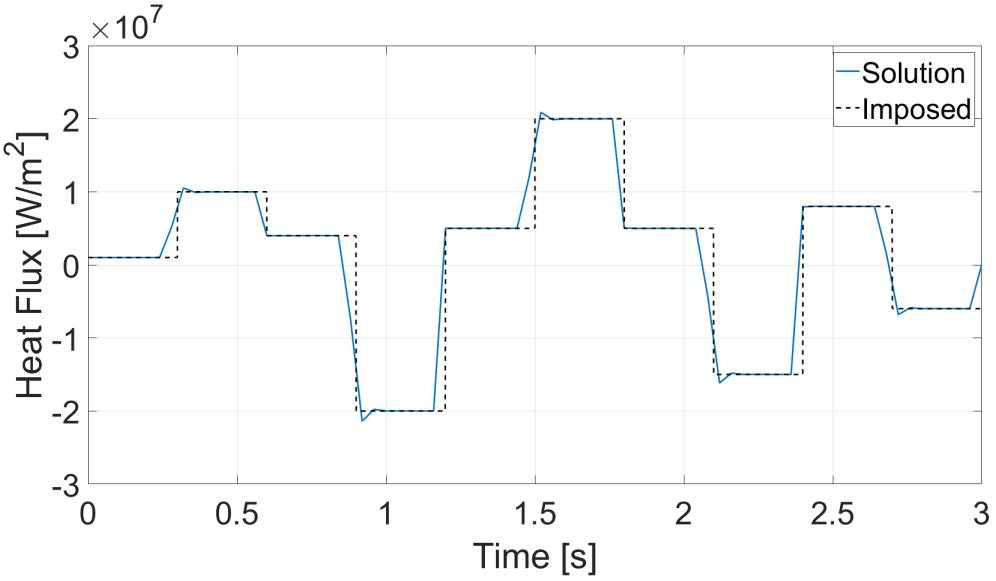

(b) Heat flux profile

Figure 2.24. Test case with step-changes in heat flux.

continuously, the readings always contained substantial error and lag. Rather than artificially correcting for thermocouple transient response, temperature data were

used unaltered and all heat flux values reported in this document are *uncorrected*, i.e., actual heat flux is expected to be higher than reported.

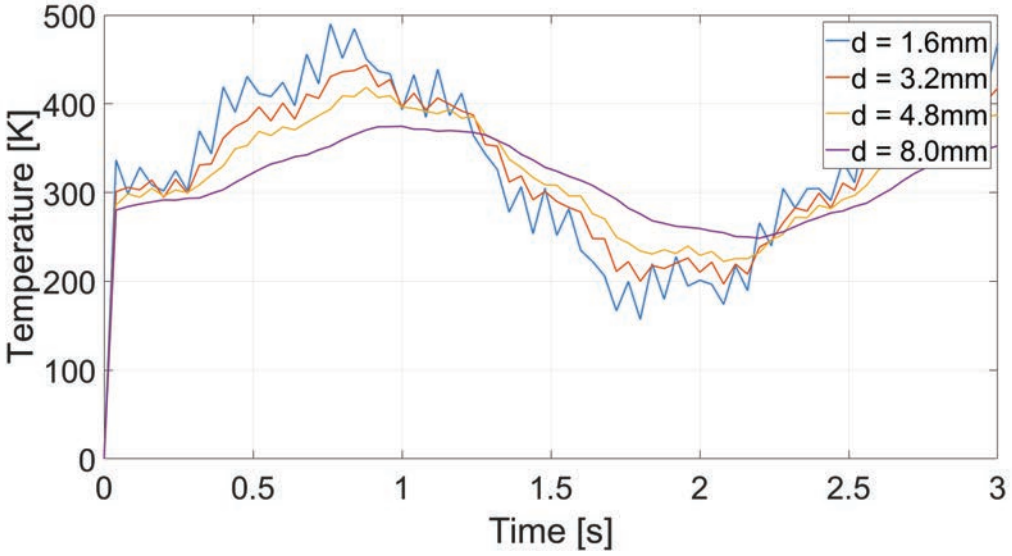

(a) Wall temperature target

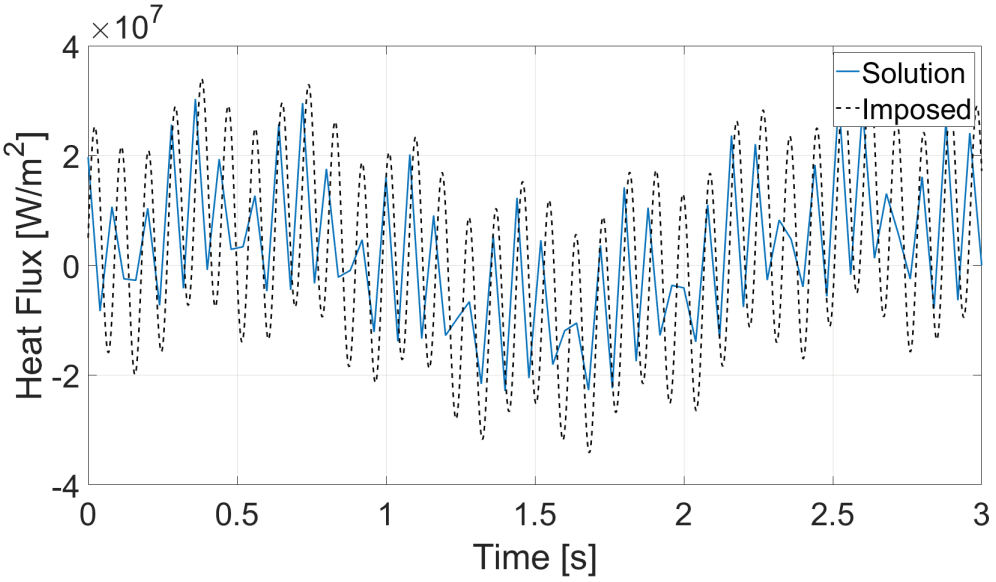

(b) Heat flux profile

Figure 2.25. Test case with superimposed sinusoidal heat flux.

Before the heat flux solver was used on experimental data, it was tested on artificial wall temperature profiles shown in Figs. 2.24(a) and 2.25(a) which were created by imposing heat fluxes shown in Figs. 2.24(b) and 2.25(b) composed of step-changes and superimposed sinusoids of various frequencies respectively. The artificial temperature profiles were created with a time step size of 1E-4 s to represent a continuous "true" profile. Subsequently, four point measurements downsampled from the "true" temperature data were fed to the inverse heat transfer solver.

The corresponding heat flux solutions produced by the sovler have been plotted on the same axes as the original heat flux boundary conditions in Figs. 2.24(b) and 2.25(b). In the case of the low-frequency step-changes, rise time of the solution was limited by the size of the time steps used in the optimization routine. However, after the initial overshoot following each step-change, the solution converged with the imposed value within two time steps.

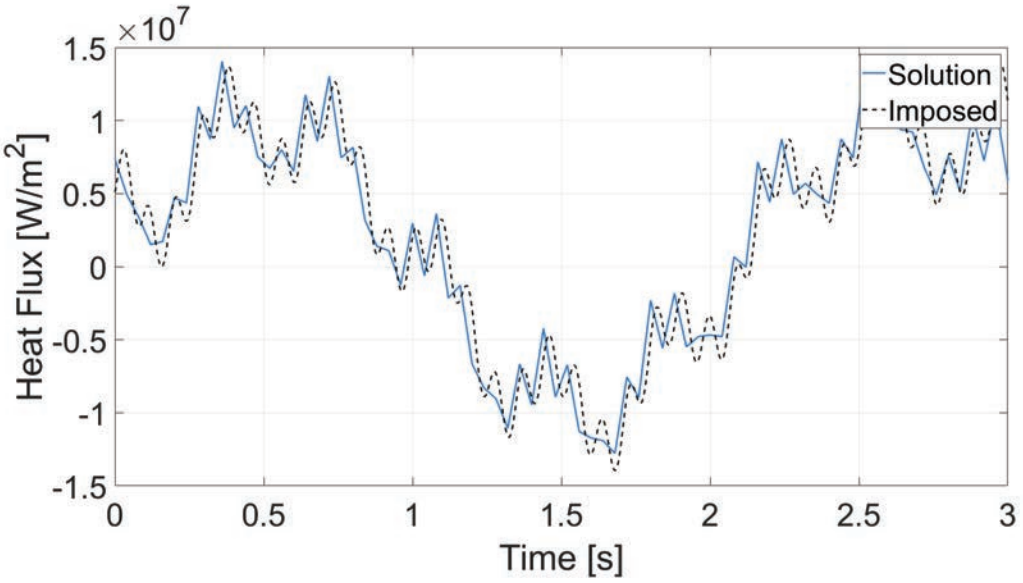

Figure 2.26. Moving average of heat flux in solution and imposed condition.

The theoretical maximum frequency resolution of the solver is $\frac{1}{2\Delta t}$, corresponding to 25 Hz ($\Delta t = 0.04s$) for the chosen time step for group 1 through 6 thermocouples,

and 12.5 Hz ($\Delta t = 0.08s$) for group 7 through 13. The second test case utilizing a superimposed sinusoidal heat flux profile contains frequency content up to 70 Hz. Clearly, the solver was not expected to reproduce the original signal's frequency content. Nonetheless, the moving average over five time steps of the solver (0.2 s), shown in Fig. 2.26, demonstrates that average heat flux can nonetheless be resolved with considerable accuracy. As a disclaimer, a time step convergence study was not performed for this solver since the solution sought was heat flux, which is a function of the rate of change of temperature. Therefore, the solution is expected to vary with time step selection. Instead, the optimization time steps were simply chosen to be as small as numerical stability permitted.

2.2.7 Uncertainty Quantification

Similar to uncertainty quantification for the injector response study, the base uncertainties of instruments and measurement methods were first considered (Table 2.5) and statistical error propagation was applied to obtain the final uncertainty ranges associated with derived quantities using equations 2.1 and 2.2. The derived parameters of interest for the RDE v1.4 hotfire test include detonation wave speed, injector stiffness, mass flow rate, and heat flux.

However, unlike injector stiffness in the injector response experiments which calculated using direct measurements, determining stiffness for the RDE injector involved the use of estimated detonation pressure ratios owing to the lack of a high-frequency pressure measurement in the main chamber. For the same reason, the minimum chamber pressure, which is required for stiffness calculation, was also unknown. It was estimated using chamber CTAP and estimated detonation pressure ratio under copious assumptions (discussed in more detail at the beginning of Section 4). Therefore, uncertainty quantification will not be performed on injector stiffness because the resulting values will not be meaningful due to the unknown uncertainties of the assumptions.

Table 2.5. Uncertainties of base parameters associated with RDE v1.4 hardware and instrumentation.

Parameter	Uncertainty
HS video temporal resolution	± 5 μs
Main chamber CTAP	± 34 kPa (5 psi)
RP manifold HF pressure	$\leq \pm 348$ kPa (50 psi)
RP venturi pressure	± 17 kPa (2.4 psi)
LOX venturi pressure	± 17 kPa (2.4 psi)
Preburner H_2 venturi pressure	± 34 kPa (5 psi)
RP density	$\pm 0.1\%$ [47]
RP vapor pressure	$\pm 0.5\%$ [47]
LOX density	$\pm 0.1\%$ [48]
LOX vapor pressure	$\pm 0.01\%$ [48, 49]
H_2 density	$\pm 0.04\%$ [50]
H_2 speed of sound	$\pm 0.5\%$ [50]
Venturi diameter	$\pm .0254$ mm (.001 in)
Venturi discharge coefficient	$\pm .5\%$
Type K thermocouple output	greater of $\pm .75\%$ or 2.2 K
Type E thermocouple output	greater of $\pm .5\%$ or 1.7 K

Similarly, the temperature measurements used to derive heat flux in the main chamber were subject to unknown errors due to the large time constant associated with the thermocouple probes, as discussed in Section 2.2.6. Instead, additional numerical simulations were used to estimate heat flux assuming that the maximum recorded temperatures were 63.2% of actual wall values. The heat flux computed via this method resulted in an average difference of 58% above the values computed using raw temperature data. Since temperature measurements always lagged actual wall

temperature, the actual chamber wall heat flux was expected to be at least 58% above the presented values. Due to the data available, further quantification of uncertainty in heat flux estimation was not possible.

Calibration of thermocouple response was initially considered, but for calibration to be useful, the heat source needed to fulfil two criteria: to have a known/controllable heating power, and to be capable of producing sufficient levels of heat flux (of the order of 1 MW/m^2). However, yet another experiment would need to be designed and executed for this purpose. The estimated amount of time and resources necessary were deemed to be too high for the task to be undertaken alongside the hotfire test campaign. Consequently, the calibration work was not performed, but is recommended as a dedicated study in the future.

The calculated uncertainties for average detonation wave speed and engine mass flow rates are summarized in Table 2.6. Detailed uncertainty tables associated with each test can be found in Appendix A.

Table 2.6. Minimum and maximum uncertainties of derived RDE hotfire parameters.

Derived Parameter	Min. Uncertainty	Max. Uncertainty
Detonation wave speed [m/s (ft/s)]	±30 (100)	±96 (320)
RP mass flow rate [kg/s (lbm/s)]	±.007 (.016)	±.017 (.037)
LOX mass flow rate [kg/s (lbm/s)]	±.012 (.026)	±.042 (.092)
H_2 mass flow rate [kg/s (lbm/s)]	±.0001 (.0003)	±.0005 (.001)
Total mass flow rate [kg/s (lbm/s)]	±.020 (.044)	±.059 (.13)
Peak heat flux [%]	Estimated average +58/-0	

3. ANALYSIS OF A LIQUID INJECTOR'S TRANSIENT RESPONSE

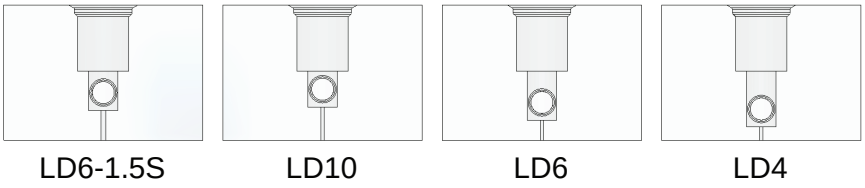

Figure 3.1. Drawings of injectors showing internal geometry (reproduced from Section 2.1.4).

The injector transient response test campaign comprised two test series, each utilizing a different propellant combination. In the initial test series, a total of 255 tests were performed among the three injectors designated LD10, LD6, and LD4, and between two different initial pressures of 690 and 1,030 kPa (100 and 150 psia) using oxygen and hydrogen as propellants. In order to further understand the influence of detonation pressure ratio (DPR) on injector response, the second test series was conducted to include an additional 300 tests that involved the LD10, LD6, LD4, and LD6-1.5S injectors using oxygen and ethylene as propellants.

It was discovered after substantial testing that due to the higher detonation pressure ratio of this propellant combination, data could not be collected for the LD4 injector due to its short length and difficulties associated with cavitation and hydraulic flip [51] (discussed in more detail in the following subsections). Similarly, data could not be obtained for the LD6 injector at the initial pressure of 1,030 kPa (150 psia) for the same reasons. Subsequently, tests were also performed at a lower initial pressure of 414 kPa (60 psia) to provide results generating partial back-flow of detonation gases into the orifice passage.

High-frequency pressure measurements were collected from the detonation channel and injector manifold in addition to high-speed videos. From the videos, maximum back-flow distance and refill time were the primary parameters of interest. These were graphed against various operating parameters in an effort to explore correlations that could potentially be used as design guidelines.

Section 3.1 opens with a presentation of the operating characteristics of the predetonator used to drive injector repsonse using two propellant combinations: hydrogen with oxygen, and ethylene with oxygen. Discussion of test results begins with the description of some common events and flow structures observed in Section 3.2 before delving into the analysis of measured data in Section 3.3. A brief examination of the high-frequency manifold pressure signals will then be presented and followed by Section 3.4, where an evaluation of a 1-D numerical model developed by the author in [40] is made.

3.1 Predetonator Functionality

Before the present study, the predet had neither been operated above atmospheric pressure, nor had it been used in an enclosed vessel. Therefore, functionality tests had to be performed for two reasons: To confirm spark discharge capability at elevated pressure due to increased breakdown voltage requirement [52], and to determine the shortest possible propellant fill time that produces a coupled detonation so as to prevent over-pressurizing the vessel. Two propellant combinations were used: hydrogen and oxygen for the first test series, and ethylene and oxygen for the second.

3.1.1 Oxygen and Hydrogen as Propellants

Figure 3.2 shows a typical pressure profile for a hydrogen-oxygen detonation with the initial pressure set to 690 kPa (100 psia). Compared to the ambient pressure profile obtained in the M.S. studies [40] reproduced here in Fig. 3.3, the differences are stark. Firstly, the double pressure peaks observed in Fig. 3.3 were absent with

the elevated initial pressure. The other difference is that the pressure ratio of the peak had increased from approximately 3 at atmospheric pressure to 13 at 690 kPa. Hence, the power of the detonation events is vastly increased with operating pressure.

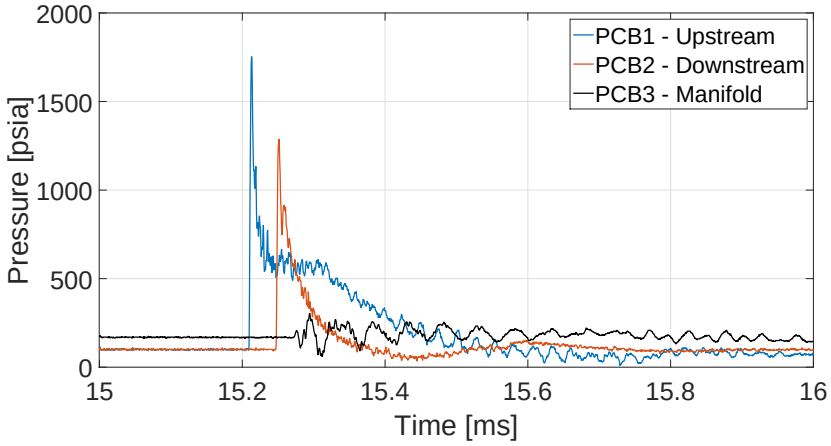

Figure 3.2. High-frequency pressure signals at initial pressure of 687 kPa (99.7 psia) and injector ΔP of 478 kPa (69.3 psi).

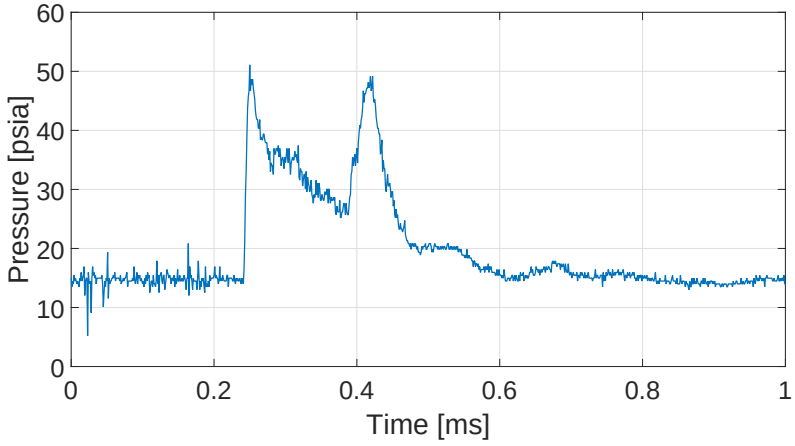

Figure 3.3. High-frequency pressure signal from [40] at initial pressure of 101 kPa (14.7 psia).

The double peaks at atmospheric pressure were most likely to have been caused by the decoupling of the reaction zone from the shock, i.e., the detonation had either decoupled or had not fully developed. At 690 kPa, fully-developed detonations were obtainable and so a single high-amplitude peak was obtained. This behavior is important for accurately representing the dynamic range of conditions experienced by an injector feeding an RDE. The improved performance at high ambient pressure can most likely be attributed to the decrease in detonation cell width with increased initial pressure. For example, stoichiometric H_2/O_2 cell width decreases from 1.4 mm (0.055 in) at 101 kPa (14.7 psia) to 0.21 mm (0.0083 in) at 690 kPa [3].

Another feature to highlight here is the pressure profile recorded by PCB1 (blue line in Fig. 3.2). After the initial spike and decay, the pressure plateaus for approximately 0.1 ms before decaying again towards initial value. This was due to the design of the detonation channel; it was fully-confined by four walls for about 10 cm (4 in) downstream of PCB1's location before the lateral relief allowed blowdown of the combustion products. This feature also leads to some differences between the cold flow environments and those in actual operational RDEs by introducing a blowdown crossflow that is not present in the latter.

After numerous rounds of testing at both 690 and 1,030 kPa initial pressures involving the adjustment of supply pressures and fill times, it was determined that the operating parameters for the predet should be as shown in Table 3.1. Theoretical C-J pressures for these operating conditions have been included in the table for reference. The equivalence ratio resulting from the feed pressures was approximately 2; setting equivalence ratio closer to unity did not appear to augment detonation strength significantly. For C-J calculations, the feed lines were assumed to be choked to estimate mass flow rates. NASA CEA [13] was used to compute the corresponding detonation properties.

The pressure profile and velocity of the detonation waves were recorded and compared to their C-J values via the time difference between the two gauges. From Figs. 3.4(a) and 3.4(b), the peak pressures recorded at the injector's location (PCB2) were

Table 3.1. Predetonator operating parameters for oxygen and hydrogen.

Initial pressure [kPa (psia)]	H_2 feed pressure [kPa (psia)]	O_2 feed pressure [kPa (psia)]	Fill time [ms]	C-J pressure [kPa (psia)]
690 (100)	2,070 (300)	2,070 (300)	250	12,900 (1,870)
1,030 (150)	2,760 (400)	2,760 (400)	250	19,400 (2,820)

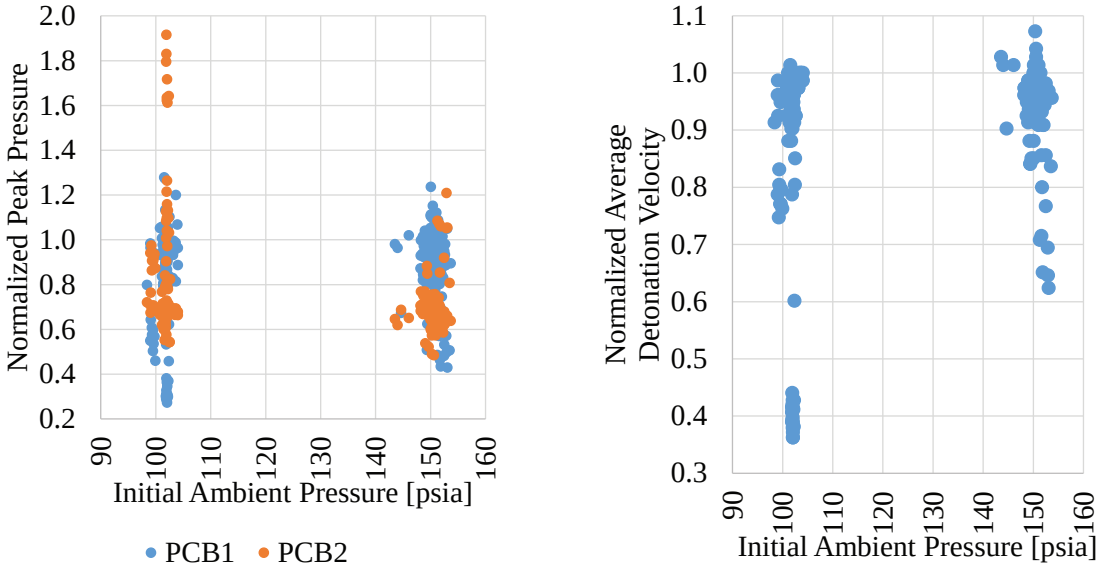

(a) (b)

Figure 3.4. Detonation (a) peak pressure and (b) average velocity of hydrogen and oxygen normalized with their respective C-J values.

predominantly above 60% of the C-J value, while normalized detonation velocities were above 90%. As mentioned before, it is expected of the pressure to be somewhat lower than C-J value because of the lateral relief.

A small fraction of the experiments carried out at 100 psia also exhibited normalized peak pressures above 1.6 with corresponding normalized velocities between 0.25 and 0.35. The inverted relationship between pressure and velocity for these data sug-

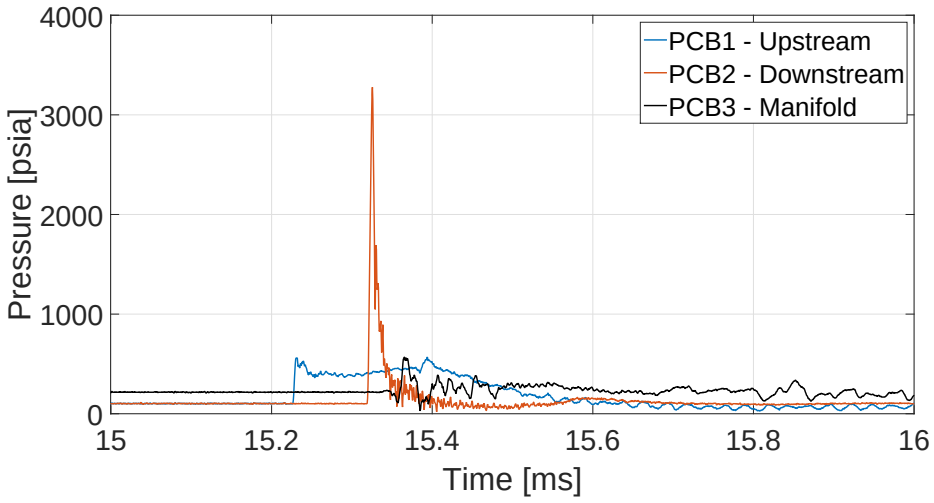

Figure 3.5. High-frequency pressure traces of an unstable hydrogen-oxygen detonation at an initial ambient pressure of 690 kPa (100 psia).

gests that the detonations were either not fully-developed or disrupted in the predet. Figure 3.5 shows a typical plot of pressure profiles corresponding to such an event. It is evident that the detonation channel upstream pressure (PCB1) is several factors lower than that at the injector (PCB2). In this case, even though the upstream pressure profile shows a steep front, its peak was merely 29% of C-J value. On the other hand, the downstream pressure shows a very large spike 172% of C-J value.

Clearly, the detonation event that produced these measurements was of a different nature from the typical detonation seen in the large majority of the tests – it was unstable. Since close to 40 tests had been run before the unstable detonation first occurred, accumulation of condensed water vapor was suspected to be its cause. Following the hypothesis, the predet was allowed to purge with nitrogen for several minutes to dry the predet after each occurrence of unstable detonation. This process produced stable detonation after each purge, but only for less than a handful of tests before it became unstable again. Due to the unusually-high peak pressures produced in these over-driven detonations, the injector responses produced

were characteristically-different. Therefore, the data from tests with over-driven detonations were discarded as outliers.

3.1.2 Oxygen and Ethylene as Propellants

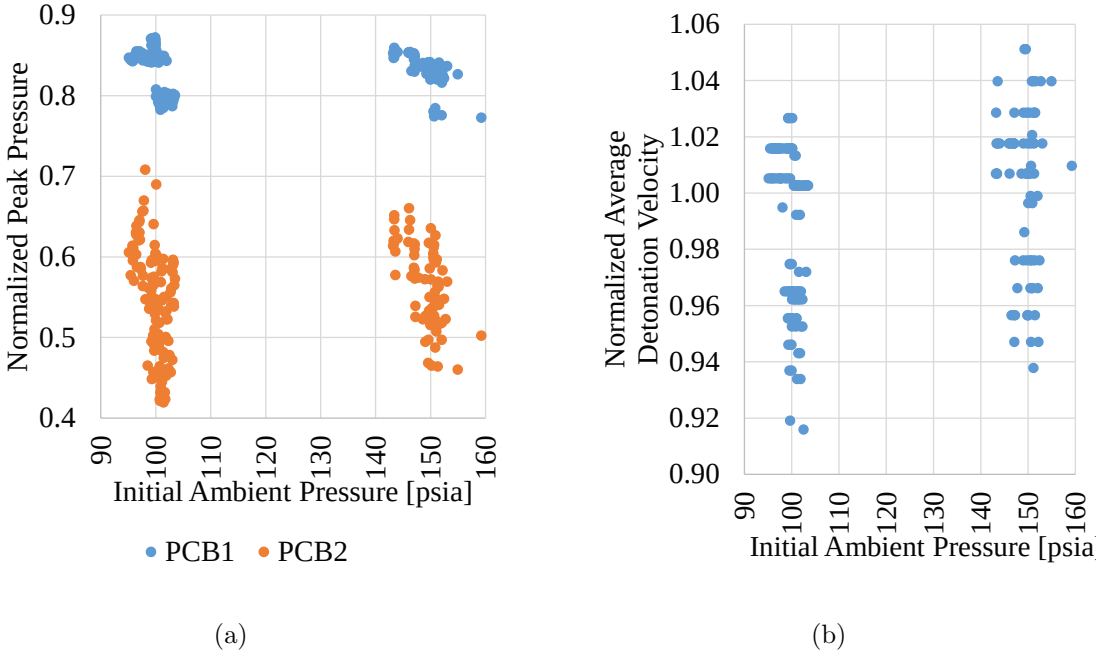

(a) (b)

Figure 3.6. Detonation (a) peak pressure and (b) average velocity of ethylene and oxygen normalized with their respective C-J values.

As discussed in Section 2.1.3, the predet was rebuilt to incorporate a high-flow purge port that enabled consistent production of stable detonations. Detonation characteristics of the predet were again evaluated with ethylene fuel. Since ethylene is far denser than hydrogen and has a lower speed of sound, new feed parameters were required. Ethylene's fill time needed to be longer because of the decreased volumetric flowrate compared to hydrogen; more fuel was necessary to pre-fill the detonation channel. For the tests, feed pressures were swept until detonation peak pressures were sufficiently different from those obtained with oxygen and hydrogen.

The threshold for peak pressure ratio was arbitrary; the highest possible value was not sought because of difficulties in keeping the various gasket seals intact.

Table 3.2. Predetonator operating parameters for oxygen and ethylene.

Initial pressure [kPa (psia)]	C_2H_4 feed pressure [kPa (psia)]	O_2 feed pressure [kPa (psia)]	Fill time [ms]	C-J pressure [kPa (psia)]
414 (60)	1,170 (170)	2,340 (340)	350	18,100 (2,620)
690 (100)	1,720 (250)	3,450 (500)	350	30,900 (4,480)
1,030 (150)	2,410 (350)	4,830 (700)	350	47,500 (6,890)

Figures 3.6(a) and 3.6(b) show normalized peak pressures and velocities recorded in the tests. The reduced vertical scatter in either plot compared to that in Fig. 3.4 is indicative of the efficacy of the predet modification. The reduced water vapor mole fraction in the ethylene-oxygen combustion products is the main explanation for the improved performance. The poor solubility of water at high pressure makes ethylene a superior fuel relative to condensation processes that impact predet performance at these more arduous conditions. The propellant feed parameters that were deemed appropriate are listed in Table 3.2. In the rightmost column, the extremely high C-J pressure values hint at the difficulties that would be faced in the collection of data.

3.1.3 Test Conditions

To reiterate on the methodology employed, the injectors were tested at initial pressures of 414, 690, and 1,030 kPa (60, 100, and 150 psia) across a range of injector ΔP. Tests performed with oxygen and hydrogen were limited to 690 and 1,030 kPa initial pressures as the decision to test at 414 kPa was made only during the second test series utilizing oxygen and ethylene. When oxygen and ethylene were used as propellants, only the LD10 injector was of sufficient length to be tested with 1,030 kPa

initial pressure; the shorter injectors required higher ΔP such that they entered the hydraulic flip regime before complete back-flow could be prevented.

Table 3.3. Summary of test conditions for oxygen-hydrogen detonations.

Injectors tested	Initial pressure [kPa (psia)]	Injector ΔP [kPa (psia)]	Initial Reynolds number
LD10, LD6, LD4	690 (100)	121 to 1,020 (17.5 to 148)	14,600 to 42,300
LD10, LD6, LD4	1,030 (150)	194 to 1,520 (28.2 to 220)	18,500 to 51,700

Table 3.4. Summary of test conditions for oxygen-ethylene detonations.

Injectors tested	Initial pressure [kPa (psia)]	Injector ΔP [kPa (psia)]	Initial Reynolds number
LD10, LD6, LD6-1.5S	414 (60)	82.0 to 917 (11.9 to 133)	15,500 to 60,200
LD10, LD6, LD6-1.5S	690 (100)	352 to 1,680 (51.0 to 244)	22,000 to 76,800
LD10, LD6-1.5S	1,030 (150)	550 to 2,000 (79.7 to 290)	31,100 to 58,800

The increment in ΔP was kept between 69 and 138 kPa (10 and 20 psi) to provide good resolution in the collective data. The accuracy of each increment was ultimately dependent on the fineness afforded by the pressure regulator's adjustment knob and responsiveness of the pressure gauge. Injector ΔP was increased until each injector ceased to show significant or measurable back-flow. In total, approximately 600 tests were performed across both propellant combinations to produce the results to be discussed in the following sections; this excludes exploratory tests performed for each

injector at each initial pressure to determine the starting manifold pressure. Summaries of the sweep of test conditions for the hydrogen-oxygen and ethylene-oxygen test series are shown in Tables 3.3 and 3.4 respectively.

3.2 Visual Observations

3.2.1 Bulk Response

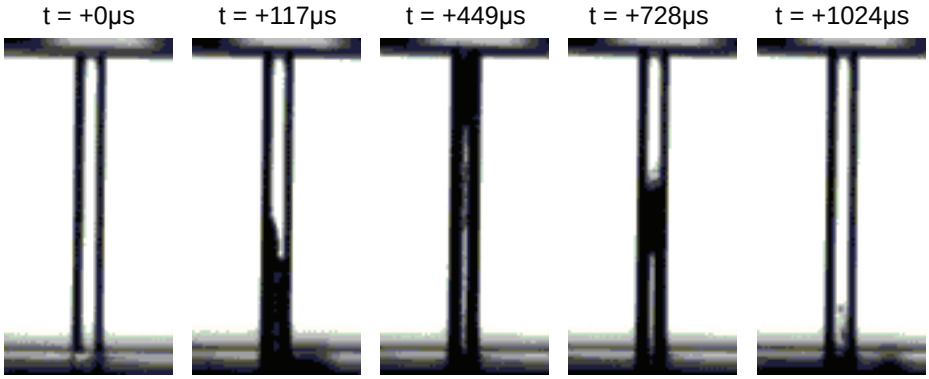

Figure 3.7. Sequential images (cropped) showing complete back-flow of the liquid phase. Fuel: hydrogen, injector: LD10, initial ambient pressure: 1,030 kPa (150 psia), ΔP: 197 kPa (28.6 psi). Images captured at 400,000 fps and a resolution of 128×128 pixels.

To remain consistent with previous work [40], response of the water column was categorized as follows: *complete back-flow*, *partial back-flow*, and *limited back-flow*. In addition, high-speed images presented in this chapter will all follow the same convention: Direction of water injection is top to bottom, and the detonation wave (not visible) travels from left to right. Complete back-flow, depicted in Fig. 3.7, describes situations where the detonation products traveled upstream through the full length of the injector.

For injectors of the same diameter, ΔP required to prevent complete back-flow increased with decreasing injector length; this is to be expected if one were to think from the standpoint of fluid mass (and hence its inertia) contained within the injector

passage. Typical refill times were over 1 ms at these conditions – an order of magnitude larger than the expected duration between detonation waves in an RDE 10 to 15 cm (4 to 6 in) in diameter. The long refill times observed in this coldflow test platform are also partly due to the presence of a transverse blowdown flow originating from the fully-confined section of the detonation channel.

It is unlikely that any rocket RDE system will adopt such low pressure drop values, but the findings were interesting nonetheless, and contribute to the completeness of the study. While these refill times are unlikely to meet the requirements of RDE cycle times, other applications that are not constrained by such short cycle times may find use for this information. For this reason, it is still meaningful to understand the minimum possible pressure drop to inhibit complete back-flow. This condition is typically to be avoided due to potential for combustion in the manifold with its potentially destructive effects.

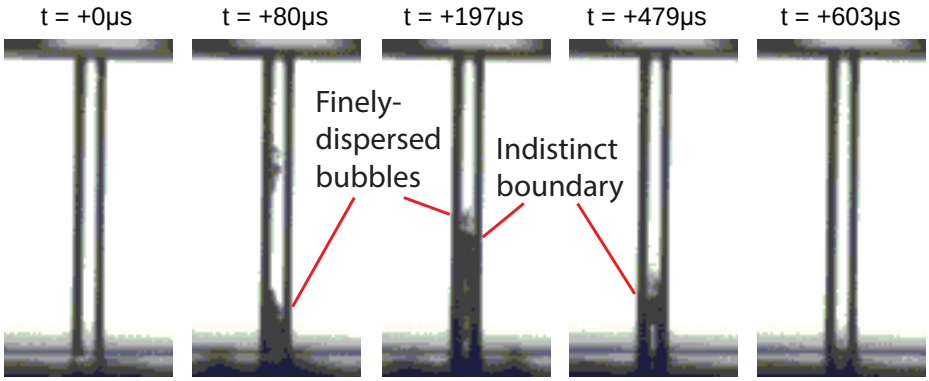

Figure 3.8. Sequential images (cropped) showing partial back-flow. Evidence of cavitation is seen in the upper portion of the injector passage in the second frame. Fuel: hydrogen, injector: LD10, initial ambient pressure: 1,030 kPa (150 psia), ΔP: 339 kPa (49.1 psi). Images captured at 400,000 fps and a resolution of 128×128 pixels.

Partial back-flow is the term used to describe cases where the injector back-flows for a portion of its full length, as depicted Fig. 3.8. Most of the test cases fall under this intermediate category. Finally, limited back-flow occurs when injector ΔP is

sufficiently large such that liquid flow does not cease completely, but merely decreases momentarily and recovers almost immediately. The high-pressure gas still possesses sufficient energy to penetrate into the injector passage along the wall, presumably along the boundary layer, but at no instance does the gaseous cavity extend fully across the entire cross-section to stop flow of the liquid phase. For borderline cases like these, it still takes more than 100 μs for the gas cavity to be completely expelled from the injector passage at the upper bound of pressures tested.

One may see from Figs. 3.7 and 3.8 that the free surface of the water column is neither planar nor distinct. The tremendous force of the detonations invite Rayleigh-Taylor instabilities and presumably wave growth and breaking occurs on the free surface alongside penetration of discrete gas bubbles into the liquid phase; this surface feature was seen across all test conditions. In most cases and also shown in both figures, the free surface also tilted facing upwind with respect to the detonation wave's direction of travel during the back-flow phase, and rotated to face downwind during the recovery phase. This behavior can likely be attributed to the chronology of events; the detonation wave first encounters the upwind edge of the orifice causing the water column to recede starting from the same side. The time history of the pressure distribution also carried through the recovery process: At around the same time that the free surface reached its maximum extent of back-flow, it began to tilt towards the downwind direction.

Figure 3.9 presents an example of the limited back-flow case under high ΔP conditions. The small pocket of gas (indicated by red arrows) that was present in the injector passage can hardly be seen. Under high injection pressures, the liquid possessed sufficient forward momentum to resist the impulse of the detonation wave. Consequently, the high-pressure gas was only able to cause minimal *scalloping* of liquid in the immediate region of the injector face without inducing motion of the entire column. One may picture the liquid being displaced laterally instead of upstream in such a situation. In these limited back-flow cases, the free surface of the liquid often does not have sufficient time to change its direction of tilt before the injector fully

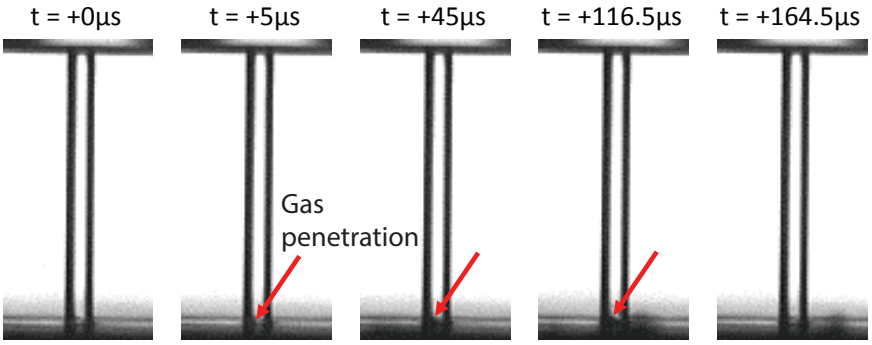

Figure 3.9. Sequential images (cropped) showing limited back-flow. Fuel: hydrogen, injector: LD10, initial ambient pressure: 1,030 kPa (150 psia), ΔP: 731 kPa (106 psi). Images captured at 400,000 fps and a resolution of 128×128 pixels.

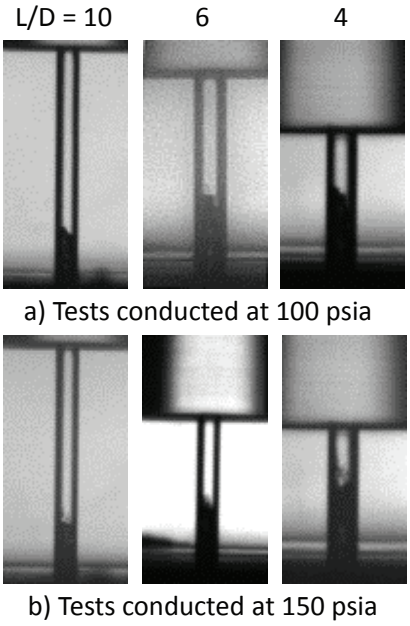

Figure 3.10. Images of injectors at maximum back-flow using hydrogen as fuel, under initial pressures of (a) 690 and (b) 1,030 kPa (100 and 150 psia). Shown back-flow distance between 1.7 and 1.8 mm (0.067 and 0.071 in). Injector L/D from left to right: 10, 6, and 4.

recovers, perhaps due to the liquid's inviscid core possessing sufficient momentum to divert flow of gas following the detonation front.

Figure 3.10 shows a comparison of the different injectors at the point of maximum back-flow at the two different ambient initial pressures tested. In these images, the free surface is sloped and finely-dispersed bubbles can be seen in close proximity. In all except the bottom right image, the free surface was tilted in the upwind direction as the back-flow reached its maximum extent and flipped to tilt facing downwind simultaneously as flow direction reversed. In the bottom right image, the flip had occurred shortly before flow reversal occurred.

3.2.2 Cavitation and Hydraulic Flip

The most significant difference between the present experiments and the ones conducted at atmospheric conditions was the presence of what appear to be cavitation bubbles forming and collapsing along the injector passage in an oscillatory manner. This phenomenon was not observed in atmospheric pressure injection conditions [40], presumably because of the low pressure levels involved. It was noted then that the pressure ratios of the detonation waves at atmospheric pressure were very far below the expected value, and was likely due to the large cell size causing decoupling of the shock and reaction zone in the narrow detonation channel. The lack of cavitation at atmospheric conditions was most likely due to the weak rarefaction waves producing insufficient tension on the water column to incite cavitation.

At elevated initial pressures, detonation cell sizes were much smaller and supported sustained propagation of coupled shock and reaction zones. Consequently, the detonation waves were markedly stronger. The compression and rarefaction waves reflecting off boundaries in the flow passage were hence strong enough to cause cavitation. The phenomenon was observed across all injector pressure drops to varying extents. Figure 3.11 shows cavitation formation and collapse occurring along the injector passage (ΔP of 414 kPa or 60 psi) within 35 μs, even before the column

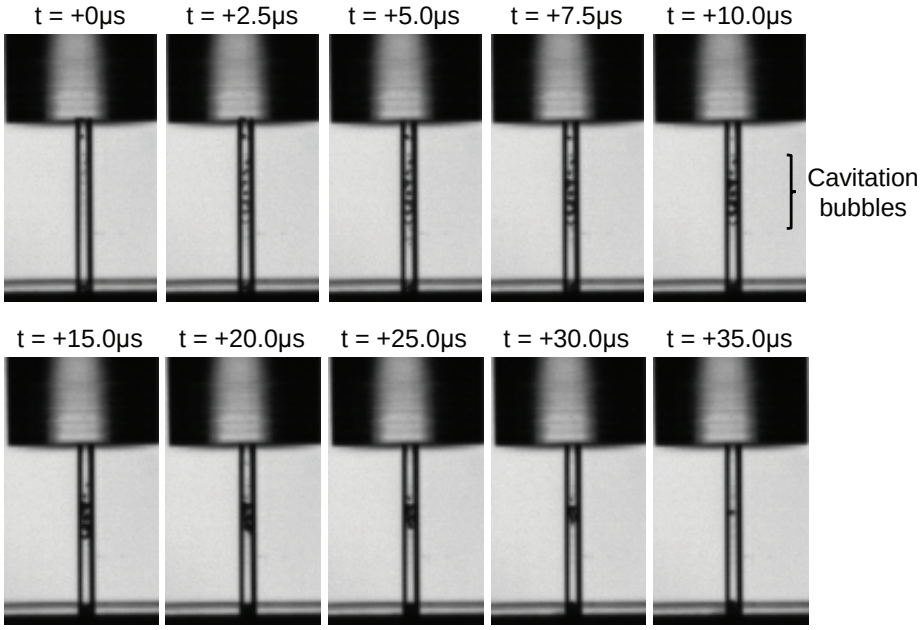

Figure 3.11. Sequential images (cropped) showing the cavitation process within the injector passage. Fuel: hydrogen, injector: LD10, initial ambient pressure: 690 kPa (100 psia), ΔP: 414 kPa (60 psi). Images captured at 400,000 fps and a resolution of 128×128 pixels.

had shown significant bulk response. This was due to the speed of sound in water being two orders of magnitude higher than the bulk motion of the water column. The growth and collapse of cavitation bubbles repeated several more times, with successive occurrences becoming weaker (inferred from the size of cavitation) as the pressure waves attenuated with each reflection. It was discussed in [53] that undissolved gases in the form of microscopic bubbles could exist in water. These, alongside microscopic particulates, can serve as initiation sites for cavitation and is likely to be the case in these experiments since the deionized water used for experiments was untreated.

Attempts to determine a characteristic frequency for the cavitation formation events through means of manual frame counting using imagery from tests with the LD10 injector have failed to uncover such a number; the intervals were irregular. Averaging the frequency by counting instances of maximum bubble size (pressure

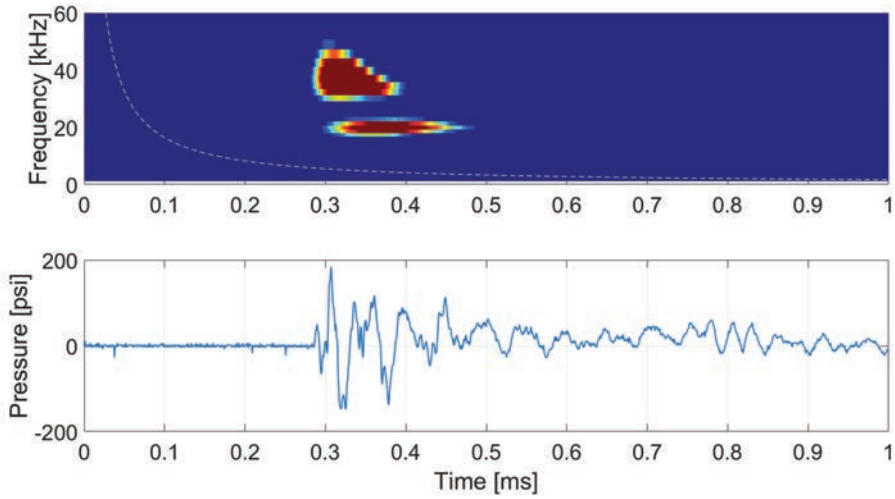

Figure 3.12. Continuous wavelet transform (top) of the high-frequency manifold gauge pressure (bottom) associated with the caviation event shown in Fig. 3.11.

minima) resulted in a value of 30 kHz, far lower than the 1L mode of the orifice length in water, which was 89 kHz in this case. A continuous wavelet transform of the high-frequency manifold pressure data using MATLAB®'s function *cwt* [54] shown in Fig. 3.12 reveals the presence of a strong signal in the 29 to 47 kHz range that lasted approximately 90 μs which could be related to the cavitation event. The white dashed line in the frequency domain delineates the cone of influence of the wavelet transform, to the left of which edge effects due to windowing become significant. Pressure measurement in the upstream plenum region also showed high-amplitude fluctuations with peak-to-peak difference of up to 2.4 MPa (350 psi) during this period. It is very likely that these large pressure perturbations exerted sufficient tensile forces on the water for cavitation to occur.

Figure 3.13 shows another cavitation phenomenon that occurs at very low injector ΔP, which was 103 kPa (15 psi) in this case. Because of the low flow resistance, the column of liquid was expelled at high speed in the reverse direction, causing a strong vortex to form at the inlet. The average speed of the receding free surface was 26 m/s

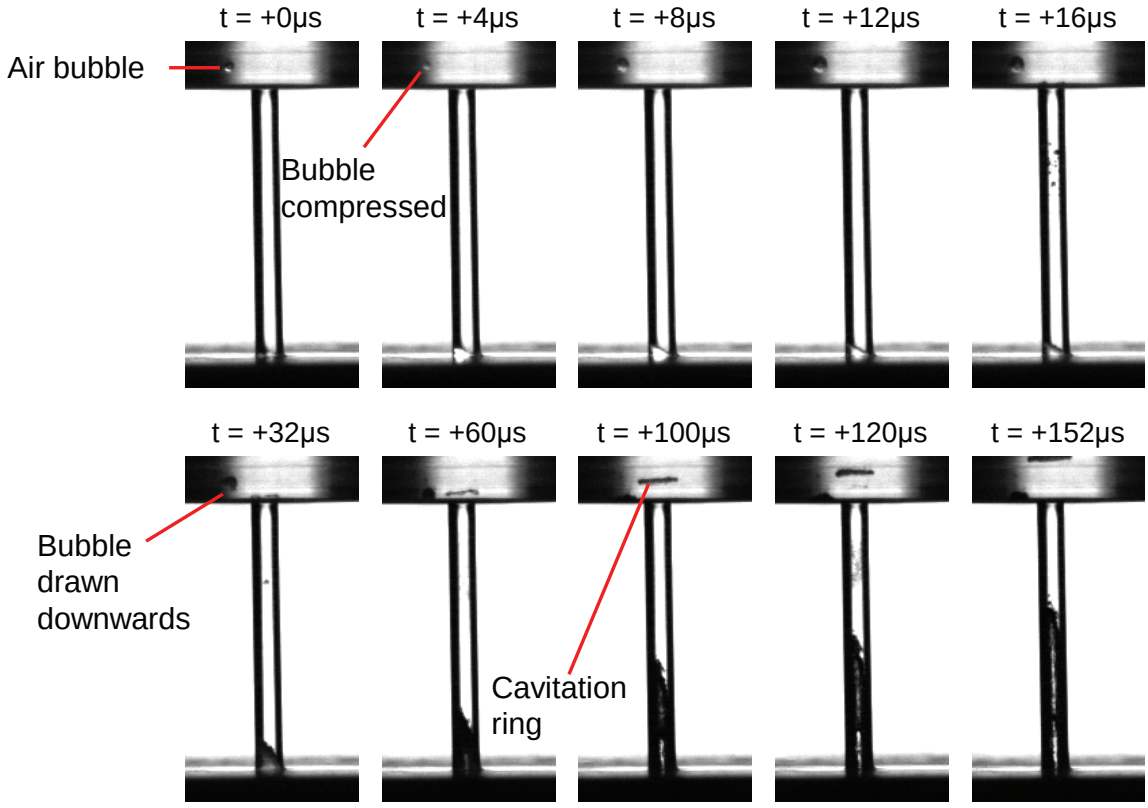

Figure 3.13. Sequential images showing the formation of a cavitation ring structure upstream of the injector inlet. Fuel: hydrogen, injector: LD10, initial ambient pressure: 1,030 kPa (150 psia), ΔP: 103 kPa (15 psi). Images captured at 250,000 fps and a resolution of 128×256 pixels.

(84 ft/s) while the ring structure rose at an average speed of 9 m/s (29 ft/s). The pressure at the vortex core was low enough to manifest as a toroidal cavitation region. The ring was observed to pulsate as it rose. Six instances of maximum toroidal volume were noted within 104 μs, or spaced between 12 and 24 μs apart – irregular intervals, or at an average frequency of 48 kHz. The relatively small manifold size, combined with sharp corner features leads to highly complex wave structures and the existence of myriad frequencies in the manifold hint at the complexity of acoustic interactions and to fully understand them would require dedicated and detailed studies of their own.

One implication of cavitation is the potential damage that injectors may incur from extended operation. Cavitation bubbles collapsing near solid surfaces are known to produce jets directed towards the surface. These jets impinge upon the surface with tremendous pressure that remove small amounts of surface material. Over time, pitting damage results [55]. Cavitation erosion is a problem that is well-known in the marine propulsion and diesel injection community. The high operating frequencies associated with RDEs could represent a problem as millions of cycles can be accumulated over modest engine run times. As the bulk of RDE experiments have been of short duration, the extent to which this may limit injector life is presently unknown.

With regard to injector response, the oscillatory nature of the cavitation events also introduces a great amount of deviation in measurements. During the formation and growth of cavitation bubbles, the volume occupied by the same mass of water increases and pushes the surrounding liquid outward. When confined by the passage walls of an injector, the liquid phase is pushed in both the upstream and downstream directions. As the bubbles collapse, the reverse happens. As a result, instead of a smooth motion taken by the free surface of the liquid phase, it moves in a lurching motion. This would undoubtedly have increased the amount of scatter in the data, or unpredictability by the model.

More fundamentally, under such high-loading conditions, water can no longer be considered incompressible. Not only does that introduce errors to the 1-D model, the presence of rapidly oscillating growth and collapse of the cavitation bubbles also makes it difficult to accurately determine the position of the free surface in many cases. It is unlikely that a reduced-order model would produce predictions of injector response to adequate accuracy and it is most likely that a full 3-D, sophisticated fluid dynamics model capable of resolving multi-phase effects will need to be employed.

Due to the parallel injector passage wall and sharp-edged entrance, the injectors were prone to supercavitation and hydraulic flip above certain ΔP. In these instances the high velocity of water flowing and turning around the sharp inlet causes a continuous cavity to be formed and anchored at the corner. The supercavity extends for

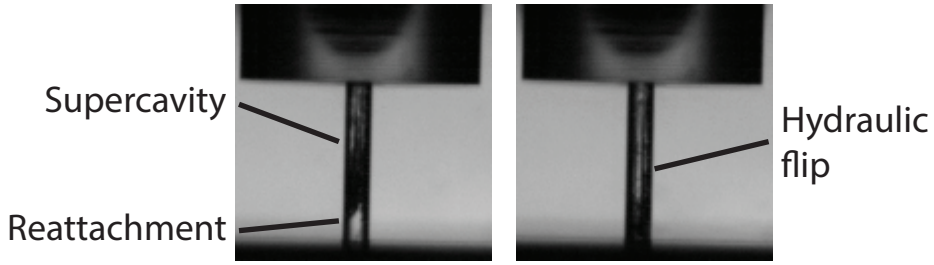

Figure 3.14. Images of supercavitation (left) and hydraulic flip (right) in the LD6 injector before arrival of the detonation wave.

a certain distance before pressure recovers sufficiently for liquid to reattach to the passage wall (Fig. 3.14, left). The length of the supercavity increases with further increase in flow velocity or ΔP until it reaches the exit plane, at which hydraulic flip occurs (Fig. 3.14, right). As Thompson succinctly describes in his Ph.D. dissertation [51], "*... the super-cavitation reaches the exit and the liquid completely separates from the injector wall and ambient air then fills the super-cavitation cavity halting cavitation.*" Hydraulic flip is conventionally avoided in liquid injectors because of its negative impact on spray atomization [56] and orifice discharge characteristics. It may also be an important consideration in RDEs especially because of the short mixing time afforded. As discussed in [31] and [32], hydraulic flip is avoidable through the use of tapered injectors.

3.3 Discussion on Measured Data

The measured quantities that will be discussed in this section are back-flow distance, refill time, and manifold pressure. The maximum back-flow distance and passage refill time were measured from high-speed videos according to the standards laid out in Section 2.1.6 while manifold pressure was recorded using a high-frequency pressure sensor situated upstream of the injector. The reader is reminded that manifold pressure was recorded at different locations in the two test series due to the evolution of knowledge throughout the process of conducting this investigation. Aside

from studying the trends produced, the data will also be compared with predictions computed using a 1-D numerical model developed in [40] in the next section.

In the first three subsections where back-flow distance and refill time are discussed, the following convention will be followed for representing graphical data:

1. Color:
   (a) Hydrogen-oxygen test data are colored blue
   (b) Ethylene-oxygen test data are colored green
2. Shape:
   (a) Injector LD10 data are represented by square markers
   (b) Injector LD6 data are represented by circle markers
   (c) Injector LD4 data are represented by triangle markers
   (d) Injector LD6-1.5S data are represented by diamond markers
3. Fill and border:
   (a) Tests at 690 kPa (100 psia) are represented by filled markers
   (b) Tests at 1,030 kPa (150 psia) are represented by open markers
   (c) Tests at 414 kPa (60 psia) are represented by filled markers with black borders

3.3.1 Back-flow Distance

The back-flow distance is an important parameter due to the potential danger posed by the trapping of hot detonation products in liquid propellant manifolds. Product gases may contain unreacted propellants that could lead to ignition within the manifold with catastrophic results. It has since been determined over the course of the current study that manifold pressures employed in full RDE systems of comparable downstream conditions would be substantially higher than those examined here

for net-positive propellant flow to be possible. Consequently, injectors in actual RDE systems are not expected to undergo complete or even partial back-flow and so the results shall be discussed in brief. However, some of the findings may be of interest to researchers of other applications where detonation frequencies are much lower.

Figure 3.15 presents three plots of normalized back-flow distance against injector stiffness according to their initial pressure settings. The most obvious trend seen across all plots is that for injectors of the same diameter, ability to resist back-flow increases with passage length. This should come as no surprise since a longer passage contains a greater mass of liquid that needs to be decelerated by downstream pressure perturbation acting across the same orifice area. In addition, ethylene-oxygen detonations, that produce higher detonation impulses, resulted in greater amounts of back-flow than the detonations formed by hydrogen and oxygen.

More interestingly, Figs. 3.15(a) and 3.15(c) show that injector LD6-1.5S (diamond markers) possesses greater resistance to back-flow than injector LD10 (square markers) despite being shorter in length. According to the equation for acceleration of an inviscid fluid in a duct of constant area,

$$a = \frac{1}{\rho}\frac{dP}{dx} \tag{3.1}$$

where ρ is the fluid's density and $\frac{dP}{dx}$ is the pressure gradient across the duct. Note here that the momentum balance is independent of duct area. Therefore in the ideal limit, it is expected of shorter injectors to undergo greater deceleration from the detonation impulse due to the steeper pressure gradient imposed, as was the case in the LD6 and LD4 injectors.

The viscosity of water probably plays a significant role in the way that a liquid column responds to steep changes in pressure gradient. The penetration of the high pressure detonation gases is first observed in the windward edge of the orifice – presumably the thickness of the boundary layer could substantially influence the process. In addition, the relative sizes of injector orifice, boundary layer, and detonation wave thickness also likely influence the response of an injector: One can picture an exaggerated configuration where a large orifice 20 mm-wide operates at

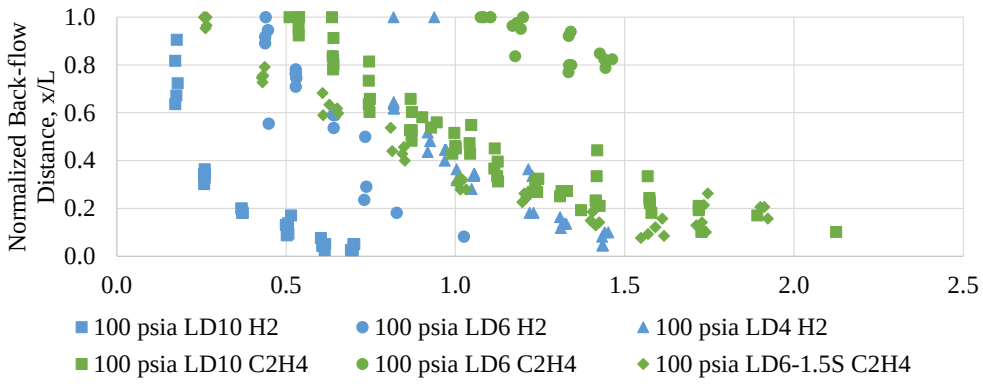

(a)

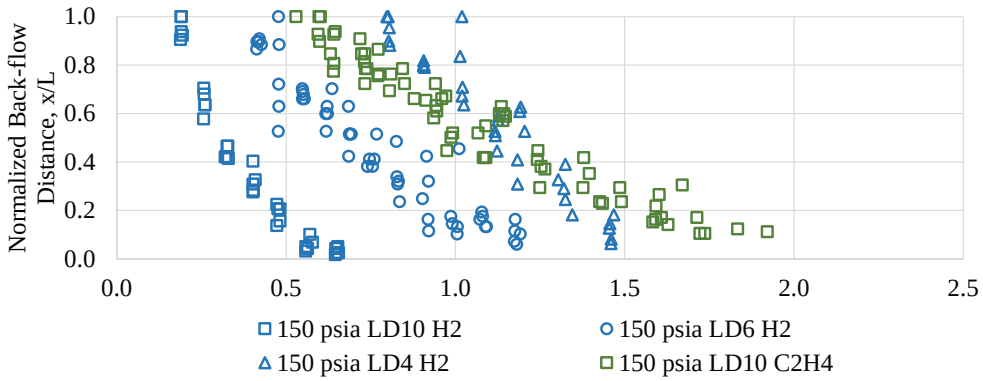

(b)

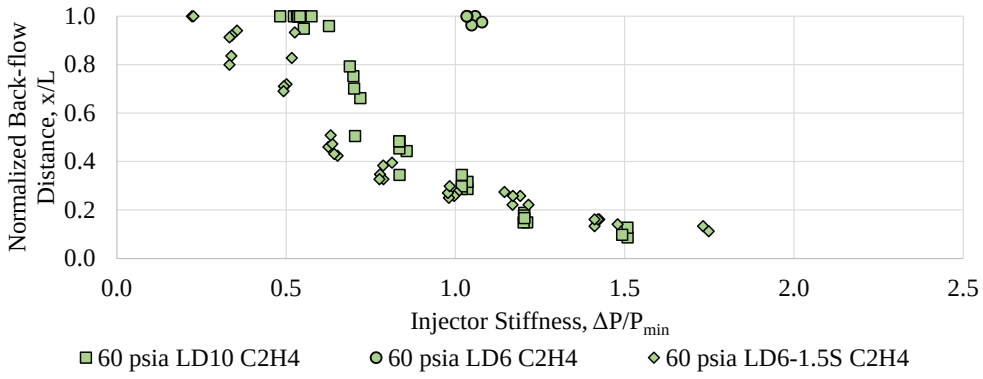

(c)

Figure 3.15. Normalized back-flow distance vs. injector stiffness at (a) 690, (b) 1,030, and (c) 414 kPa (100, 150, 60 psia) initial ambient pressure.

the same conditions. Since the thickness of the detonation front remains unchanged, the high-pressure region acting across the orifice area is now only a small fraction of its total area. The liquid directly adjacent to the detonation wave is allowed to displace laterally resulting in lower axial displacement.

More importantly, the larger column of liquid also acts as an obstacle to the detonation wave since it does not contain a combustible mixture. The detonation wave propagates around the column instead of through it, thus exerting forces only along the lateral directions. As a result, it is possible that an intact liquid core could exist throughout the detonation process. This is consistent with similar observations made during the limited back-flow regime discussed in Section 3.2.1.

3.3.2 Refill Time

The refill time of an injector is of particular importance to RDEs due to their high operational frequencies. To put things in perspective, detonation waves can attain speeds in excess of 2,000 m/s (6,600 ft/s) depending on propellant combination. A single wave at that speed will travel the full circumference of a 30 cm (12 in) annulus, which is within the size range of a 67 kN (15 klbf) engine, in merely 0.5 ms – that is the maximum amount of time within which propellants need to be injected and mixed if rotating detonation is to be sustained.

This length of time reduces if the engine is designed to operate with a larger number of simultaneous detonations – there may be reason to believe that an even number of detonations is desirable when taking thrust symmetry into consideration. If so, feed pressures will have to increase accordingly. Investigations into the effects that the number of detonation waves have on engine performance are still ongoing, but it is foreseeable that an optimum likely exists when factors such as engine mass are taken into consideration. Unlike injectors in conventional engines that flow steadily aside from small deviations, injection in an RDE is a highly-dynamic process where local mass flow rate fluctuates greatly with each passing detonation. It is the goal

of the following discussion to offer some insight into feed pressure requirements in an RDE.

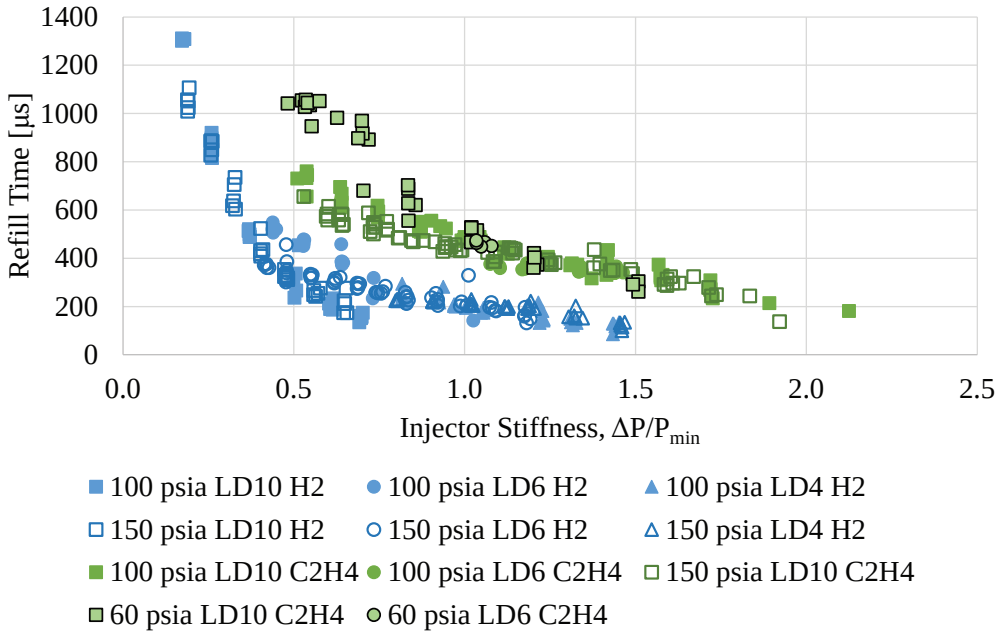

Figure 3.16. Absolute refill time vs. injector stiffness at various initial pressures for the baseline injectors.

Absolute refill time was plotted against injector stiffness in Fig. 3.16. Most apparently, there exists a distinct separation of points from tests performed using hydrogen and those utilizing ethylene as fuel and the reason is logical: Ethylene produces a higher detonation pressure that takes the injector a longer duration to recover from. Data from injector LD6-1.5S have been excluded from the figure due to the injector's geometrical and dynamic dissimilarity and to reduce clutter, but they reside in the intermediate space which separates the blue and green markers. A complete plot including data from injector LD6-1.5S can be found in Appendix C. The data for injector LD10 collected at an initial pressure of 414 kPa (60 psia) between the stiffness range of 0.5 to 1.0 also show large deviation from the data of the other injectors because of its S-shaped profile; the cause of this profile is unclear.

Reynolds numbers and hydraulic entrance lengths were examined for the deviating cases, but appeared to be within the same ranges as those of the other injectors and conditions.

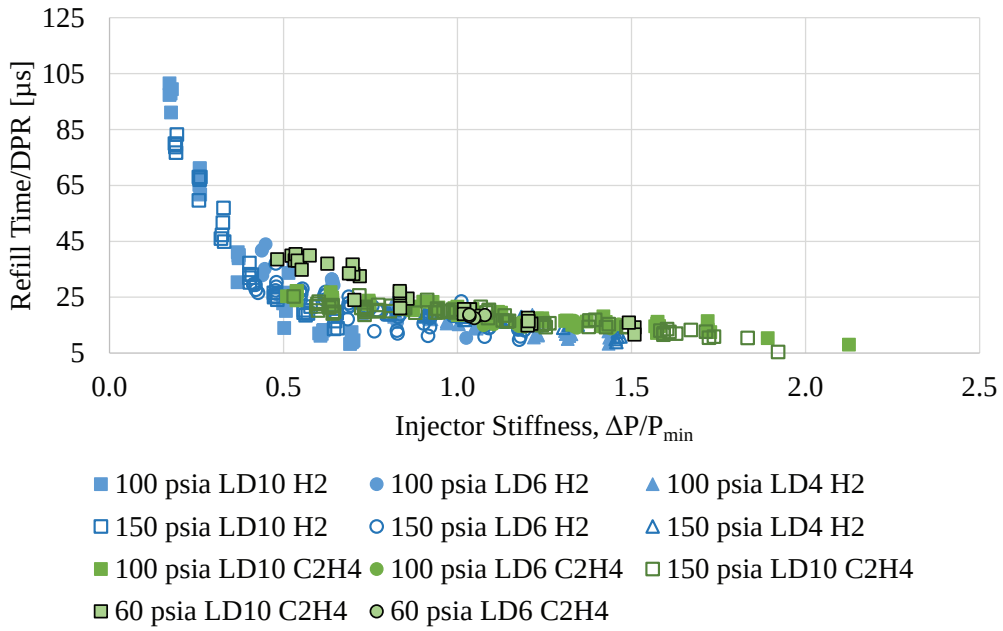

Figure 3.17. Normalized refill time vs. injector stiffness.

What is more interesting is that points in both sets of data appear to fall on their own corresponding curves regardless of injector length. This suggests that injector stiffness was the dominant factor in determining an injector's refill time, while its L/D ratio plays a much weaker role. A further observation that the two different sets of data appear somewhat parallel led to the notion that the data may be collapsible by taking detonation properties of each propellant combination into account. The simplest method of normalization was division by the measured detonation pressure ratio of each fuel since injector response is driven by pressure differences between the chamber and manifold. The result is displayed in Fig. 3.17, where the separation seen in the previous figure has been greatly reduced. Only data from the baseline injectors, which were 0.84 mm (0.033 in) in diameter, have been included on this plot

due to their similarity in geometry and dynamic characteristics. While imperfect, the method is simple and may prove useful for initial estimates of engine requirements.

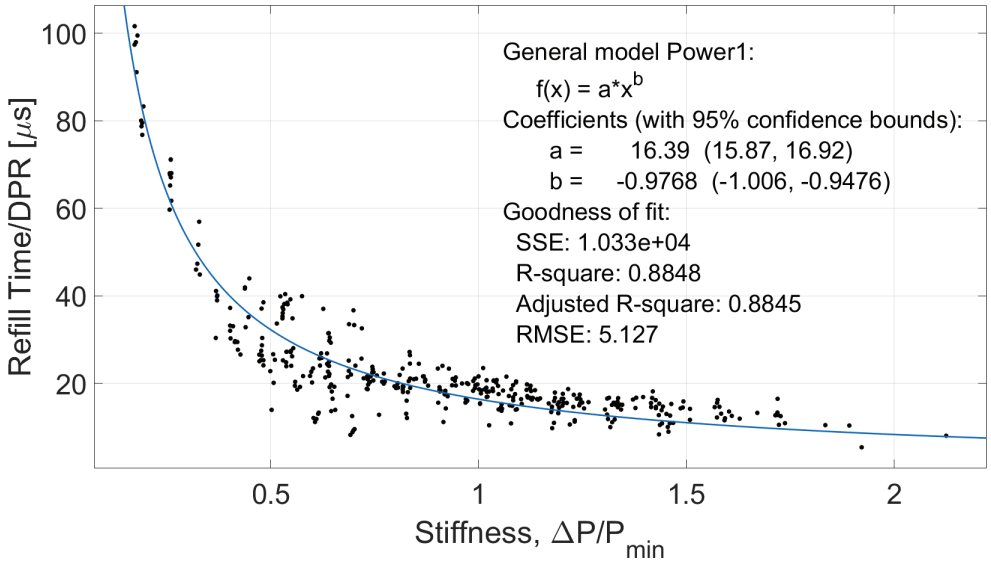

Figure 3.18. Curve fit of normalized refill time as a function of injector stiffness.

A curve fit was applied to the data using the *cftool* [57] function in MATLAB®. The power curve was chosen because of physical representations for this set of axes: As injector stiffness vanishes, i.e. no pressure drop, injector recovery should cease to occur (infinite recovery time). On the opposite end, as injector stiffness approaches infinity, the flow resists any perturbation and recovery should become instantaneous. The equation obtained for the refill time curve is

$$\frac{t_r}{DPR} = 16.39 \left(\frac{\Delta P}{P_{min}} \right)^{-0.9768} \tag{3.2}$$

where t_r is the refill time in microseconds. It was expected of the exponent of injector stiffness to take a value close to -1 since flow acceleration is directly proportional to ΔP, and it is indeed the case here. Note that operating pressure is embedded in the DPR and stiffness terms, hence the equation is generalized and should be applicable to different operating pressures.

The physical representation of the equation is that refill time is inversely-proportional to the pressure differential driving the recovery process. With current information, the lumped coefficient of 16.39 cannot be broken down further into its constituents but is expected to contain information related to properties of the liquid, such as viscosity and density, as well as injector diameter. However it is possible that the effects of propellant viscosity and density may be self-negating during the back-flow and recovery phases, i.e., increased viscosity and density may reduce the amount of time that the injector spends in the back-flow phase but increase the amount of time needed for it to refill.

The conditions covered by the current test campaign were insufficient to ascertain these details and further testing with different working fluids and injector geometries will be necessary. However, by following the assumption that properties such as viscosity and density do not manifest in injector recovery, the curve fit can be applied to actual liquid propellants such as RP-2, which was used in the hotfire experiments discussed in the next chapter. A few other means of normalizing refill time were considered, but it was ultimately found that normalization using DPR provided the most significant amount of collapse across data sets.

3.3.3 Scaling Effects

The range of Reynolds numbers tested was upwards of 15,500 – well into the turbulent flow regime. The turbulent entrance length can be estimated using the equation [58]

$$\frac{L_{h,t}}{D} = 1.359 Re_D^{0.25} \tag{3.3}$$

where $L_{h,t}$ is turbulent entrance length, D is the diameter of the duct, and Re_D is Reynolds number taking diameter as the characteristic length. According to the equation, entrance lengths exceeded injector length in all cases. In other words, the flow velocity profile had not fully-developed, and a boundary layer and inviscid core were present at the point of arrival of the detonation wave.

Low aspect-ratio injectors and high Reynolds numbers are common in rocket applications and it is reasonable to expect flow regimes similar to those studied here. The purpose of the LD6-1.5S injector was to permit a preliminary glimpse into the effects of geometric scaling on injector response. With the change in orifice diameter, the most important differences from the baseline injectors are in the relative flow areas occupied by the core and boundary layer, and the detonation wave thickness in comparison to orifice diameter. To show that geometric scaling results in dynamically-dissimilar flow, consider a constant mass flow rate through two different injectors with the same L/D ratio but different cross sectional areas A_1 and A_2:

$$A_1 v_1 = A_2 v_2 \tag{3.4}$$

$$D_1^2 v_1 = D_2^2 v_2 \Rightarrow D_1 v_1 \neq D_2 v_2 \tag{3.5}$$

therefore

$$Re_{D,1} = \frac{\rho D_1 v_1}{\mu} \neq \frac{\rho D_2 v_2}{\mu} = Re_{D,2} \tag{3.6}$$

for an incompressible liquid. v_1 and v_2 are the Bernoulli velocities of flow through the injectors, ρ is the density of the liquid, and μ is its dynamic viscosity.

Alternatively, the injectors could be subjected to the same ΔP, which implies that the steady-state flow velocities in both cases are equal, in which case $v_1 = v_2$ in Eq. 3.6 and the same inequality holds. Since Reynolds numbers for the two injectors are different in both scenarios according to Eq. 3.3, their entrance lengths will also differ, implying dissimilar velocity distribution across their orifices.

While grossly simplified, the comparisons made here should be able to provide some general indication on the desirable geometric traits of plain orifices. Figure 3.19 presents plots of normalized back-flow distance and refill time graphed against injector stiffness for the LD6 and LD6-1.5S injectors. While the range of conditions tested using injector LD6 had been severely limited by difficulties with hydraulic flip, some obvious differences and similarities are still visible. In Fig. 3.19(a), back-flow distance measured in injector LD6-1.5S was drastically lower, indicating that the larger injector was capable of resisting back-flow more effectively, presumably

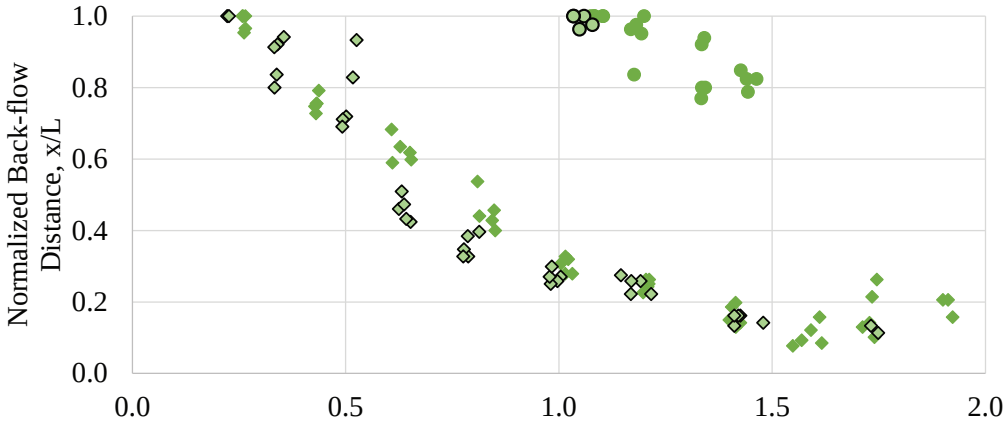

(a)

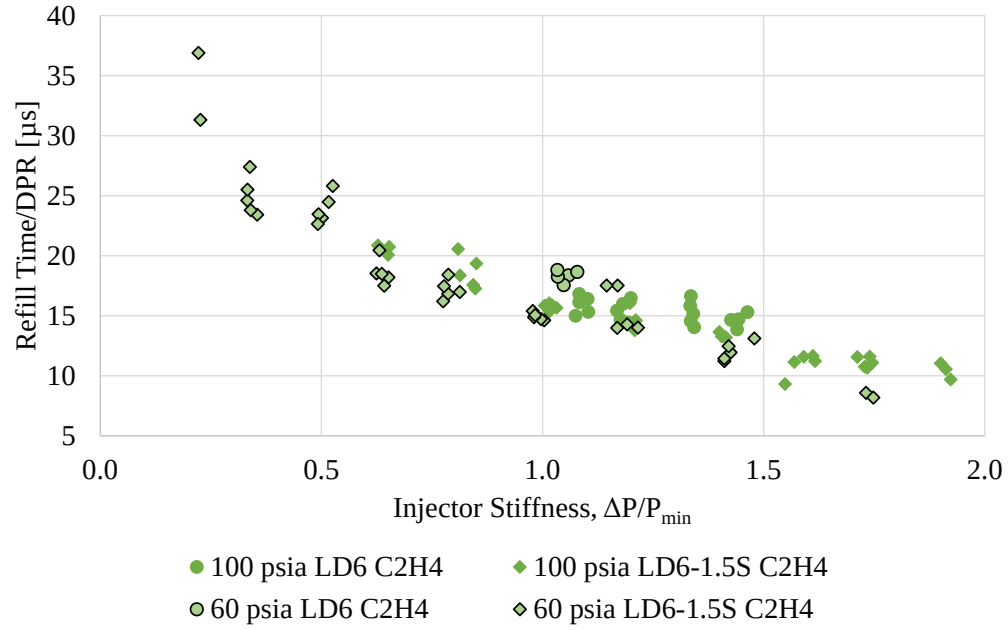

(b)

Figure 3.19. Normalized (a) back-flow distance and (b) refill time vs. injector stiffness for LD6 and LD6-1.5S injectors utilizing ethylene and oxygen as propellants.

because of the expanded inviscid core flow that is more resistant to back-flow than the boundary layer regions. On the other hand, Fig. 3.19(b) only shows a slight

reduction in normalized refill time for the LD6-1.5S injector, suggesting that the refill time is only weakly influenced by geometric scaling.

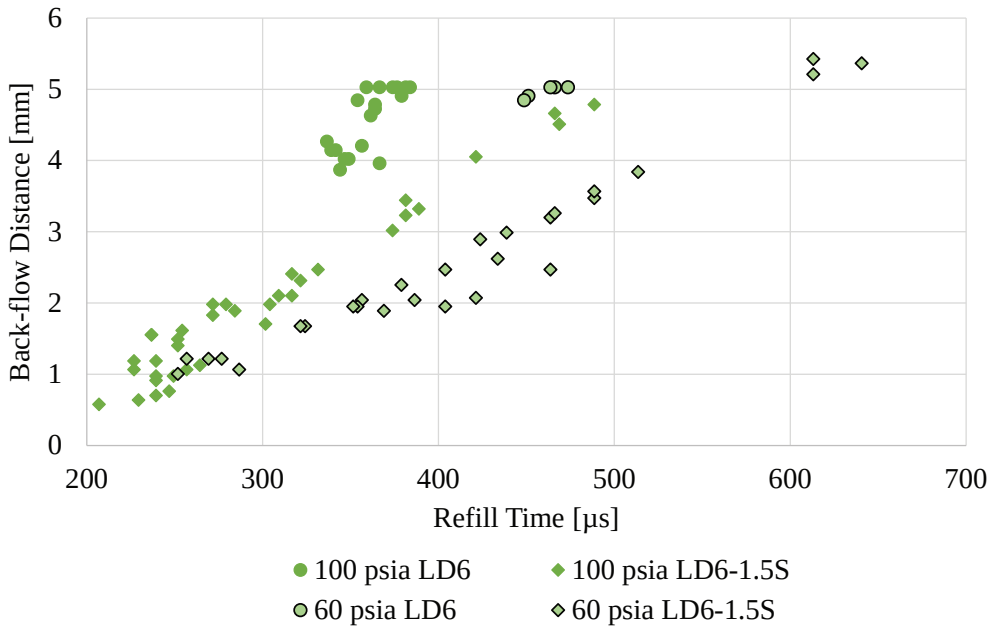

Figure 3.20. Absolute back-flow distance vs. refill time of injectors LD6 and LD6-1.5S utilizing ethylene and oxygen as propellants.

The reason for geometric scaling to affect back-flow distance to a greater extent than refill time is at least partly due to counteracting factors. Figure 3.20 is a plot of absolute back-flow distance against refill time for the two injectors. It is apparent that at the same back-flow distance, injector LD6-1.5S required more time to refill than injector LD6. Injector LD6-1.5S, being the longer injector, encounters gentler pressure gradients than injector LD6 under the same ΔP. Consequently, the liquid within responds more slowly. Therefore, even though it back-flowed to a lesser extent at the same ΔP, the time it took to refill ended being only slightly shorter than that of injector LD6, which had a longer back-flow distance to recover from. The shorter back-flow distance of injector LD6-1.5S was previously discussed in Section 3.3.1.

Since injector stiffness on the horizontal axis is essentially a pressure drop term that dictates injection speed, this finding also suggests that the number of waves present in an engine of a given diameter and mass flow rate may be controllable through geometric scaling of its injectors accompanied by a corresponding adjustment in feed pressure. To elaborate, suppose that operating an engine installed with the LD6 injector at a certain mass flow rate produces five detonation waves. The hypothetical situation can be further simplified by assuming a constant detonation speed (it can be shown through computations in NASA CEA that theoretical detonation wave speed is weakly influenced by mixture ratio or degree of mixedness even though pressure ratio strongly depends on the same parameters).

Suppose that it is the goal of a designer to reduce the number of waves present. In such a case, the LD6-1.5S injector could be used alongside a decrease in pressure drop to maintain the same mass flow rate. Since injector stiffness is reduced in this case, refill time increases such that it is now only capable of sustaining four waves. Alternatively, an existing engine could be scaled in size and still exhibit similar wave characteristics if injector stiffness (and consequently mass flux) were kept constant. This has been demonstrated by Bykovskii et al. in [59], where increasing the combustor's diameter also increased the number of detonation waves for the same chamber mass flux.

3.3.4 High-frequency Manifold Pressure

Prior research at atmospheric pressure conditions [40] did not include a close-coupled manifold pressure measurement which was thought to be crucial in obtaining more accurate numerical predictions of injector response. The test article for the present study was designed to include a high-frequency pressure port upstream of the injector module. Given the limited optical access through the injector, it was challenging to locate a measurement near the orifice inlet plane without compromising optical accessibility.

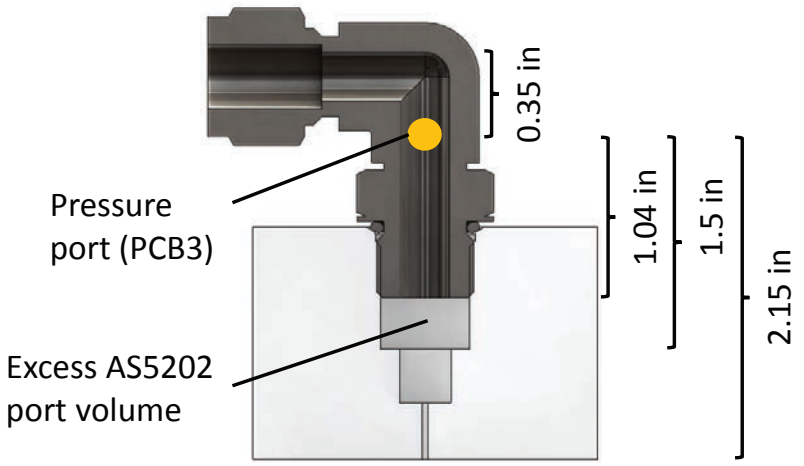

Figure 3.21. Cutaway view of the water flow path (thread engagement depth shown not reflective of actual setup).

Figure 3.21 shows a cutaway view of the second-generation injector module used in the first test series and the 90° elbow fitting that fed the injector. The high-frequency manifold pressure port was installed at the location indicated by the yellow circle. The various distances relative to the pressure port have been labeled on the figure. The distance from the pressure port to the bottom of the injector plenum has not been shown because it was a variable that depended on the injector length; the longer injector had a shorter plenum and vice-versa. The volume labeled "Excess AS5202 port volume" was the result of the standard port cutting tool being significantly longer than the thread length on the elbow fitting; in an ideal situation the fitting would come in contact with the port shoulder such that flow area remained constant up to the injector passage.

The response of the fluid surface in the orifice passage was always non-planar, so it is obvious that there was a non-uniform distribution of pressure across the injector passage at any given point in time. This factor, combined with the three-dimensional wave reflections within the manifold confines creates a complex picture even for the simplest of manifold geometries. Figure 3.22 (shown previously at the beginning of the chapter) depicts the typical manifold response in relation to measured wave

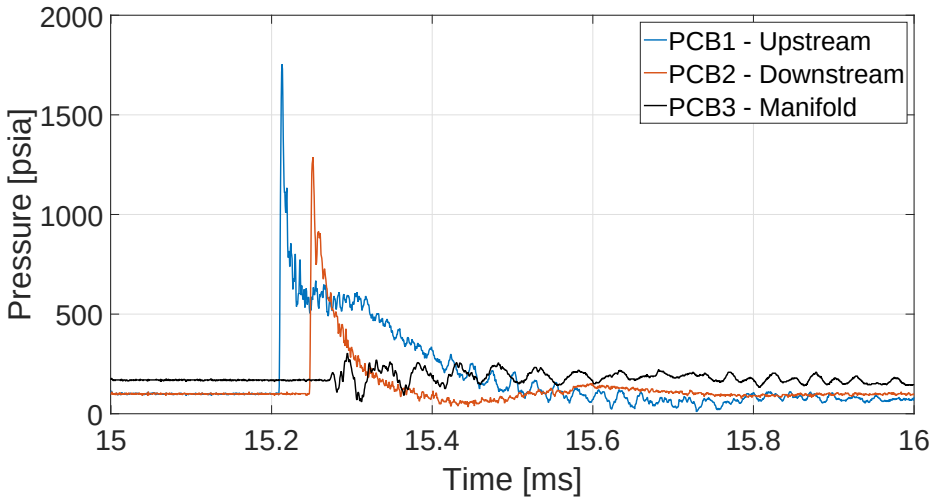

Figure 3.22. High-frequency pressure measurements. Injector: LD10, fuel: hydrogen, initial ambient pressure: 690 kPa (100 psia), ΔP: 478 kPa (69.3 psi).

characteristics in the chamber. The manifold pressure (black line) clearly contains oscillatory content whose peak-to-peak fluctuations could be several times as large as the initial injector ΔP even though the perturbation amplitude had been attenuated greatly through the series of area changes traveling from the injector face to the manifold pressure port. The oscillations continued with almost the same amplitude for about 300 μs.

Keeping in mind that wave intervals in RDEs containing multiple detonations may be as low as tens of microseconds, pressure in an RDE manifold is expected to be in a continuous state of oscillation. Power spectral density (PSD) plots such as the one shown in Fig. 3.23 were made by passing the manifold pressure signals through a Fast Fourier Transform (FFT). For many of the tests, peaks were not as prominent as hoped, but several notable ones around 15, 21, and 131 kHz were observed for the majority of test cases. These peaks appeared regardless of injector L/D ratio, suggesting that the modes were caused by common geometrical features present in all the injectors or the manifold itself. Assuming that the speed of acoustic waves in

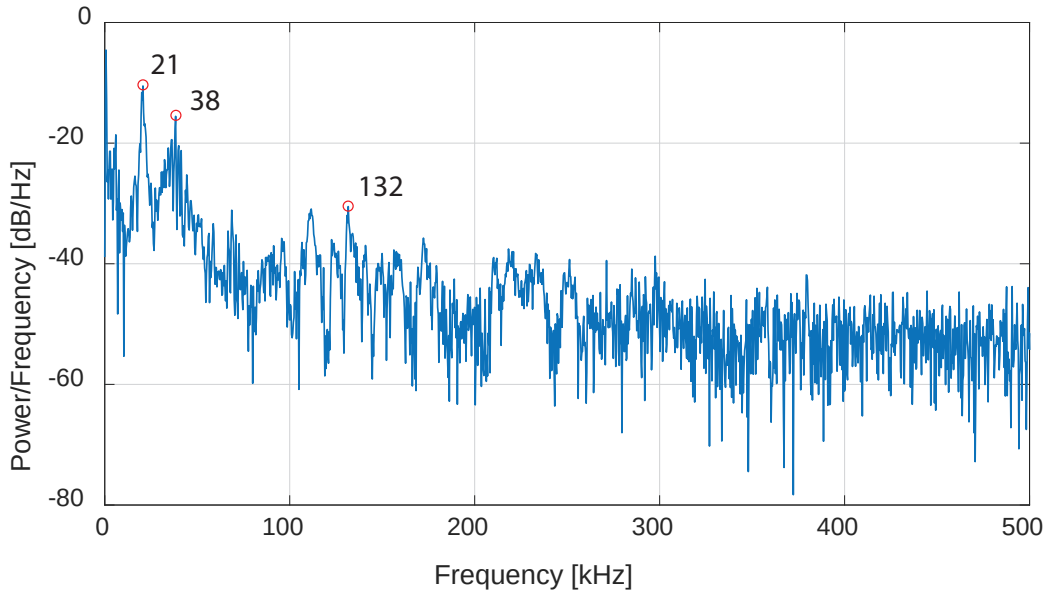

Figure 3.23. Power spectral density corresponding to the manifold pressure shown in Fig. 3.22. Injector: LD10, fuel: hydrogen, initial ambient pressure: 690 kPa (100 psia), ΔP: 478 kPa (69.3 psi).

water is 1,500 m/s (4,920 ft/s), Table 3.5 lists the possible geometrical features that correspond to each peak listed.

Table 3.5. Notable power spectral density peaks in Test Series 1 and the corresponding possible geometrical features that produced them.

Frequency [kHz]	Characteristic length [mm (in)]	Geometric feature
15	51 (2.0)	Top of feedline elbow to bottom of AS5202 port
21	36 (1.4)	Top of feedline elbow to elbow exit
131	5.7 (.23)	Pressure sensor face to opposite wall (transverse)

The pressure boundaries responsible for producing the frequency content measured suggest that the recorded dynamic characteristics may be confined to the volume

further away from the injector orifice. In other words, it is likely that the pressure port had not been placed in the appropriate location required to capture the intended measurement. To address the issue, a third generation of injector modules were designed and manufactured to relocate the high-frequency pressure port into the plenum immediately upstream of the injector passage. It was situated to minimize the distance from the injector inlet plane while ensuring that the footprint of the mounting nut would not obscure the injector passage. Consequently, a large portion of optical access to the plenum region was lost due to the considerable size of the sensor and special attention had to be paid when installing the test article to ensure that the sensor's cable did not fall into the optical path of the injector passage.

A CAD render of the injector is presented in Fig. 3.24. The center of the pressure port was kept at a distance of 4.6 mm (0.18 in) upstream of the injector inlet plane. Its distance from the plenum inlet was variable according to injector length since the plenum's depth was used to set the length of the injector. Simlarly, the port's distance from the injection plane was variable.

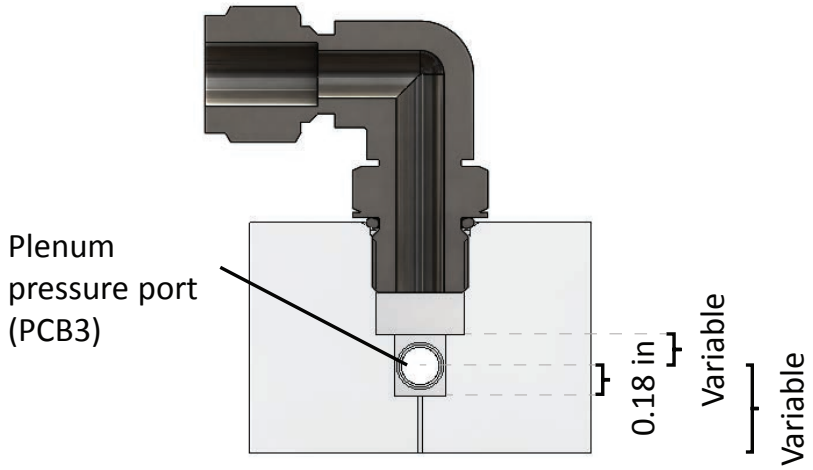

Figure 3.24. CAD render of the third generation injector module showing the location of the manifold pressure port in relation to other geometrical features.

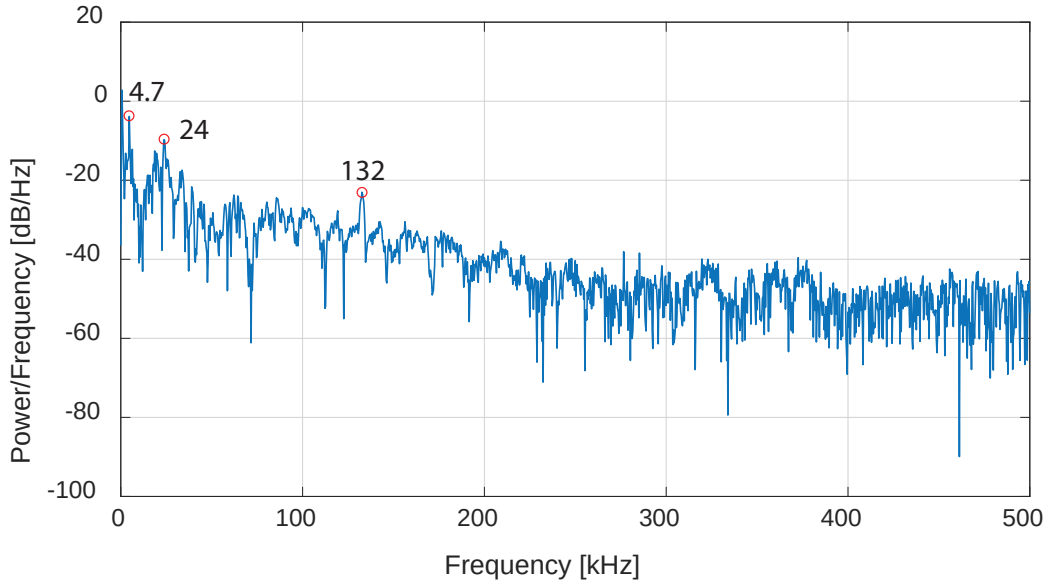

Figure 3.25. Power spectral density of high-frequency manifold pressure measured at new location. Injector: LD10, fuel: ethylene, initial ambient pressure: 689 kPa (100 psia), ΔP: 902 kPa (131 psi).

Manifold pressures recorded from the new port location were once again analyzed for frequency peaks. The PSD plots revealed peaks that were even less distinct than before and repeated tests at the same conditions often produced inconsistent peaks. However, two frequency peaks at 4.7 and 132 kHz common to the majority of tests across all injectors were observed. Figure 3.25 depicts one such example of a typical PSD plot, where the 4.7 and 132 kHz peaks have been labeled. The peak at 4.7 kHz was previously absent in the first test series. Given the high speed of sound of water and small geometrical length scales of the injectors, the signal was unlikely to have been caused by acoustic reflections within the injector. It is believed to have been driven by the longitudinal mode of the detonation channel. The peak at 132 kHz was most likely caused by transverse pressure reflections between the sensor face and plenum wall, similar to the 131 kHz peak seen previously. Surprisingly, the longitudinal modes of the injector plenums corresponding to 82, 60, and 75 kHz for

the LD10, LD6, and LD6-1.5S injectors respectively, were expected but not readily apparent in the data.

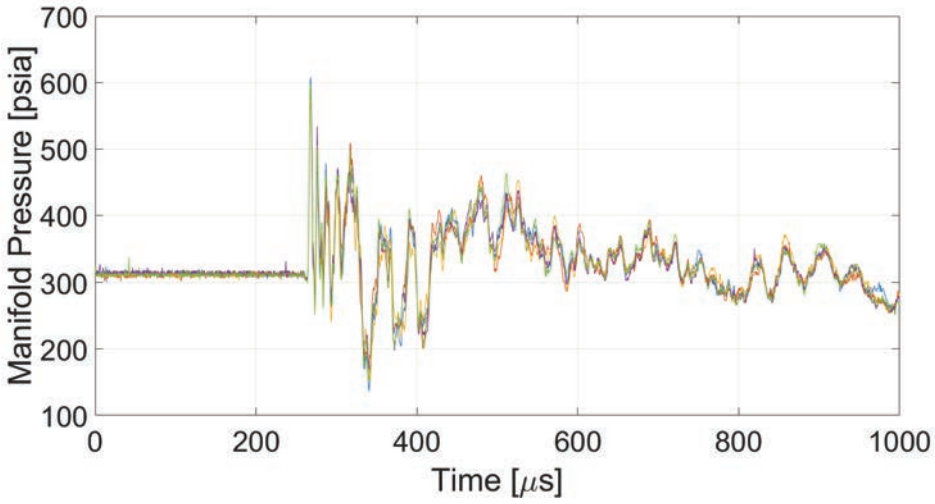

Figure 3.26. Overlay of five manifold pressure measurements demonstrating repeatability of pressure fluctuations. Injector: LD10, fuel: ethylene, initial ambient pressure: 690 kPa (100 psia), ΔP: 1,460 kPa (212 psi).

There is evidently a great amount of variability in the frequency content of the manifold even though the large-scale features were highly repeatable. In Fig. 3.26, five pressure signals recorded at the same conditions are virtually overlapped; most of the differences lie in the small-scale fluctuations at the highest frequencies. The degree of overlap in the seemingly chaotic profile proves that the pressure events are repeatable. Several more selected overlapping plots can be found in Appendix C. From the figure, it is also apparent that there is an absence of any dominant frequency. Clearly, the pressure distribution in the injector plenum is incredibly complex and ephemeral due to the three-dimensional pressure reflections off of the myriad pressure boundaries.

The fleeting nature of the dominant frequencies present in the injector plenum is exemplified in Fig. 3.27, which shows a CWT in the upper plot of a single signal from Fig. 3.26. There is a distinct lack of narrow horizontal bands that indicate the

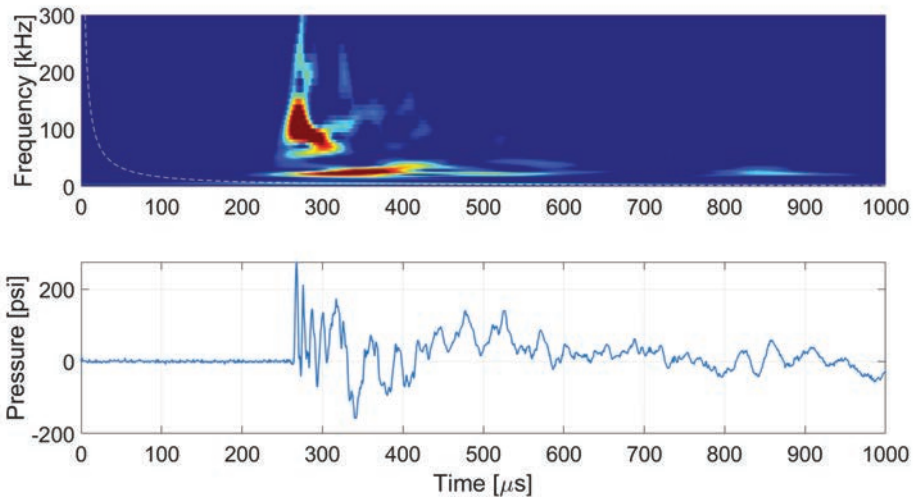

Figure 3.27. Continuous wavelet transform of a single signal (yellow) from Fig. 3.26.

presence of stable frequencies. Instead, multiple strong broadband signals appear for short durations of 100 μs or less. The utility of frequency information in the plenum appears to be limited, but the pressure signals can still find use in evaluating the predictive capability of the 1-D numerical model for injector response, which will be discussed in the following section.

3.4 Evaluation of a 1-D Injector Response Model

To preface the upcoming discussion, the 1-D injector response model in question was conceived by the author in [40]. Its working principle was based on the momentum balance of a one-dimensional, incompressible column of liquid residing in the injector passage. Simply put, as the pressure difference across the injector was varied, as would be the case during the passage of a detonation wave, a net acceleration was applied to the liquid column to augment its motion. In [40], a constant feed pressure was applied to the model resulting in large errors in prediction. The author postulated

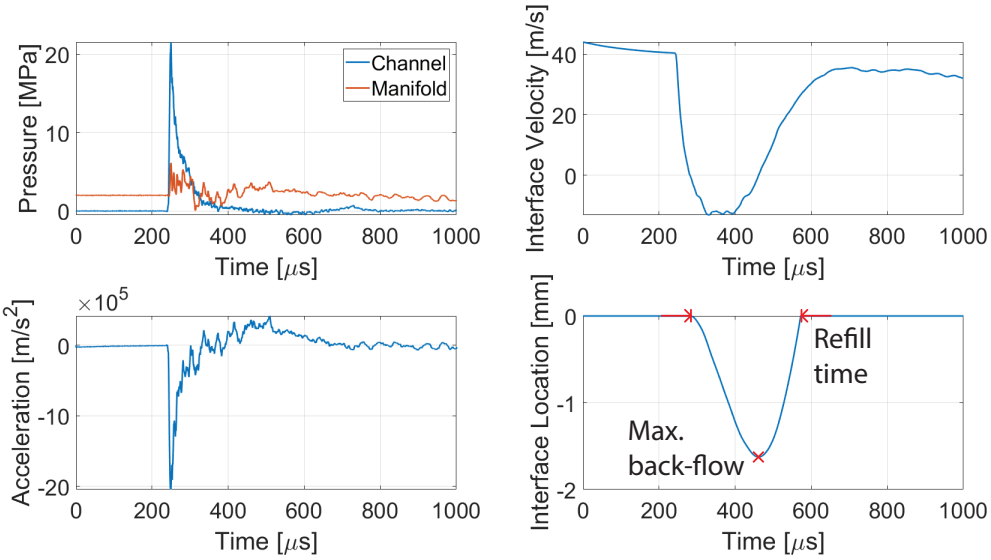

Figure 3.28. Sample output of the 1-D injector response model.

that the utilization of transient feed pressure could improve the predictive accuracy of the model.

An example of the model's output when given the measured dynamic injector feed pressure as input is shown in Fig. 3.28. Maximum back-flow distance and refill time were obtained from the liquid-gas interface location plot in the lower right. Details of the equations utilized in the model can be found in [40, 60].

In this section, only data from the second test series will be examined because of the availability of close-coupled plenum pressure measurements; the measurements taken in the first test series were too far upstream of the injector to be representative of the transient pressure driving injector response. Data associated with the use of dynamic, high-frequency plenum pressure are represented by filled markers while those related with the use of constant plenum pressure are shown as open markers. Marker shapes follow the same convention as the earlier sections, but different colors are used here to improve contrast.

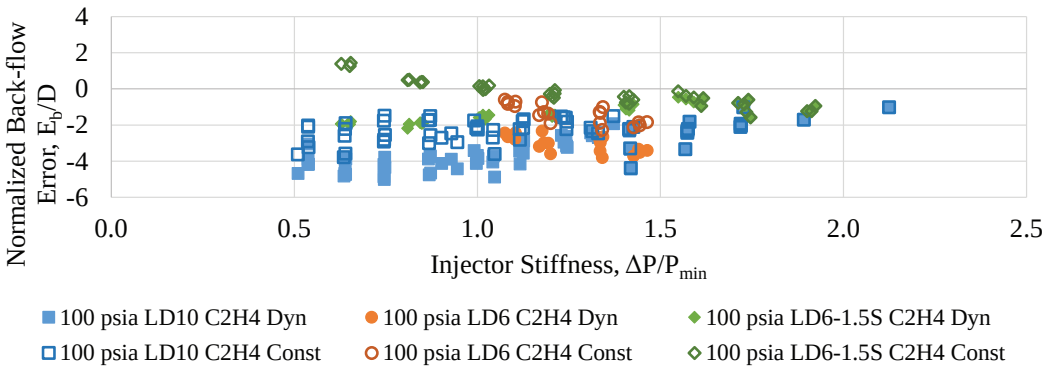

(a)

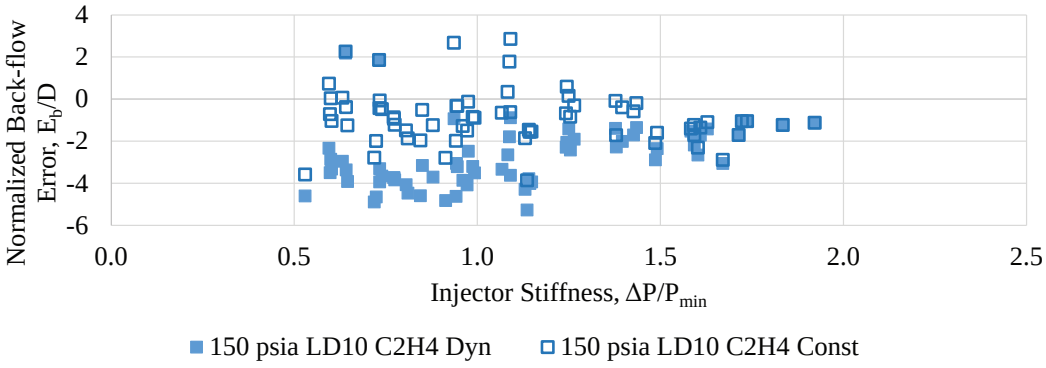

(b)

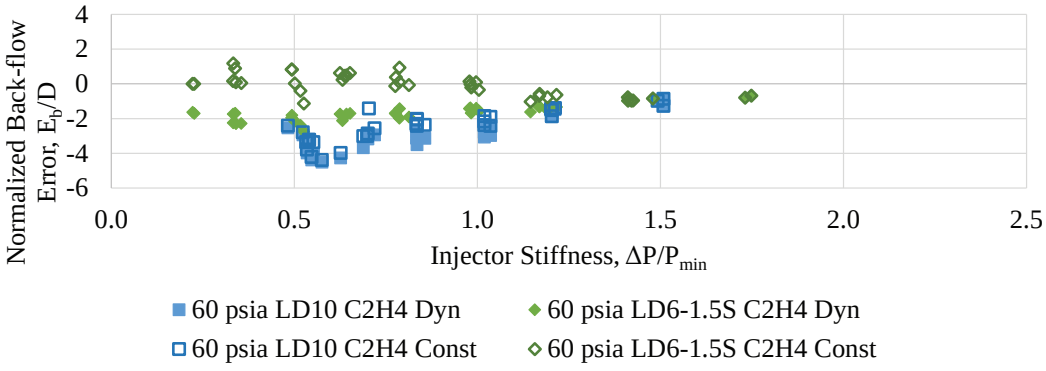

(c)

Figure 3.29. Comparison of normalized back-flow error at (a) 690, (b) 1,030, and (c) 414 kPa (100, 150, and 60 psia) initial ambient pressure using dynamic and constant manifold pressure.

Error E has been defined as the predicted quantity subtracted by measured quantity. Therefore, a negative error value indicates under-prediction by the model and vice-versa. The error for back-flow distance was normalized with injector orifice diameter D while refill time was kept in absolute form to allow comparison with detonation time scales. Both horizontal and vertical axes have been made consistent across plots to facilitate comparison.

Figure 3.29 presents three plots of normalized back-flow distance prediction error categorized by initial ambient pressure. In the upper range of stiffness values, the reader may notice that errors arising from the use of both dynamic and static manifold pressures overlap. This was simply due to both methods predicting zero back-flow distances at those high stiffness settings, leading to the same calculated error values.

In general, error magnitude decreased with increasing injector stiffness for injectors LD10 and LD6-1.5S. In Fig. 3.29(a), injector LD6 displayed the opposite trend – predictions worsened with increasing stiffness. Across the board, scatter of data increased with initial ambient pressure and the use of constant manifold pressure appeared to provide predictions with lower error. In some cases, such as for injector LD6-1.5S in Figs. 3.29(a) and 3.29(c) and for injector LD10 in Fig. 3.29(b), the use of constant manifold pressure also resulted in over-predictions at lower stiffness values. Over-predictions can be considered conservative errors as they serve to steer the designer even further from the potential to trap hot combustion products in the propellant manifolds.

Three plots of absolute refill time prediction error are shown in Fig. 3.30, separated according to initial ambient pressure. Once again, the reader is reminded that overlapping errors between methods in the upper range of stiffness settings is merely the consequence of both methods predicting zero refill times. There is a stark absence of major trend in all three plots; errors neither converge nor deviate from any single value as injector stiffness changes. The accuracy of using either form of manifold pressure varies among injectors and initial pressure conditions: Using a constant feed pressure provided better predictions for injector LD6-1.5S at an initial ambient

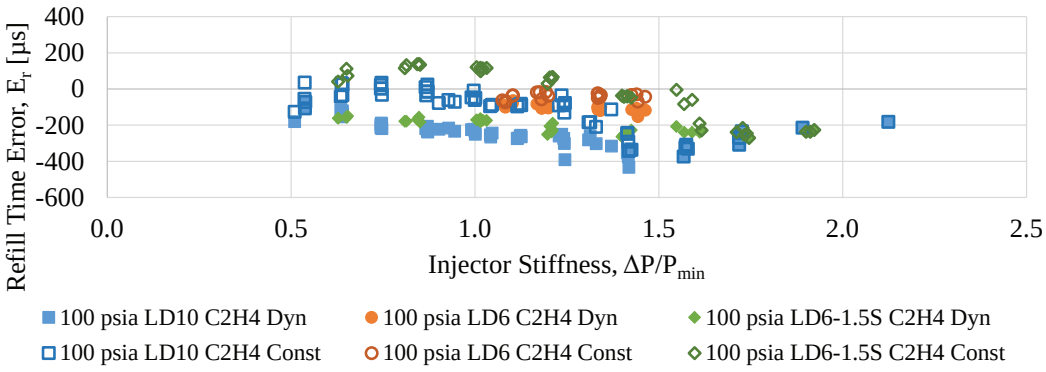

(a)

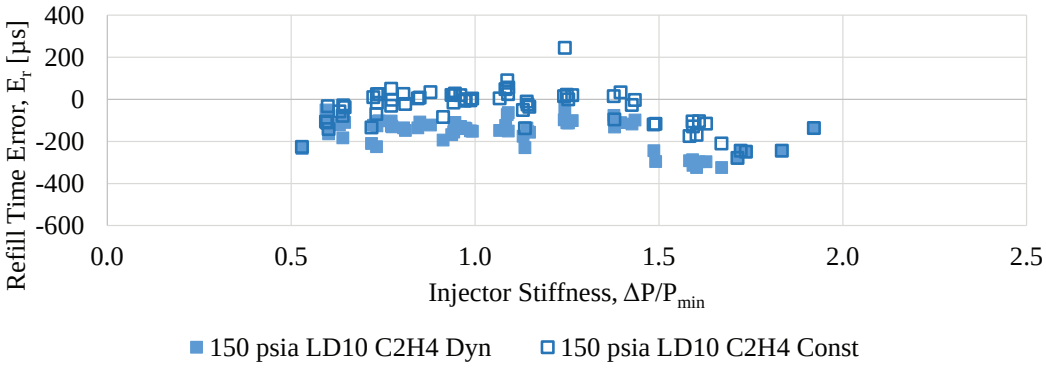

(b)

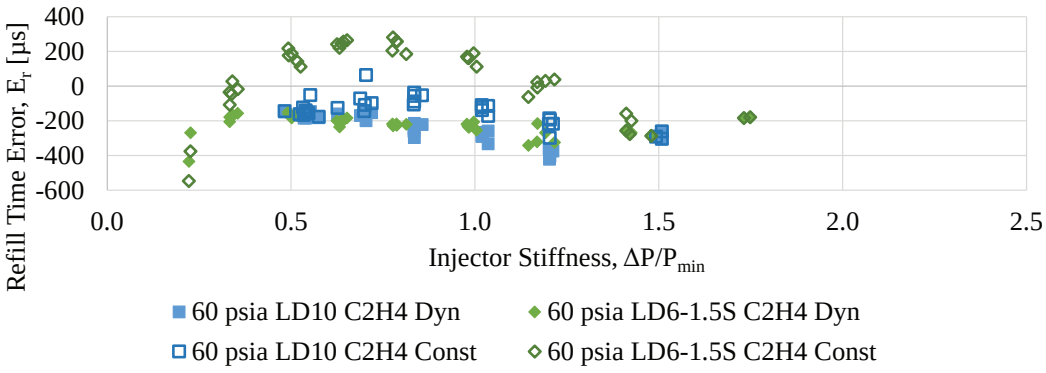

(c)

Figure 3.30. Comparison of refill error at (a) 690, (b) 1,030, and (c) 414 kPa (100, 150, and 60 psia) initial ambient pressure using dynamic and constant manifold pressure.

pressure of 690 kPa (Fig. 3.30(a)), but predictions were worse for the most part at 414 kPa (Fig. 3.30(c)). Remarkably, errors for injector LD10 were very low when the model was used with constant manifold pressure, especially in Fig. 3.30(b), where a large portion of error resided close to zero.

In closing, the magnitudes of errors in both back-flow distance and refill time predictions using the 1-D model are generally large for the range of stiffness values considered. Clearly, the model is extremely simplistic and does not possess the capability of representing the complex physics involved in the injector response process. The model is not recommended for use as a design tool for its lack of consistency. However, as it shall be discussed in the following chapter, injector stiffness settings in real RDE systems are expected to be at least several factors higher than the maximum encountered in these series of tests, in which case back-flow becomes negligible. For the purpose of estimating refill time, the empirical refill time relation given in Eq. 3.2 should be used instead.

4. ANALYSIS OF RDE V1.4 HOTFIRE DATA

Before beginning discussion on the RDE hotfire results, a brief discussion of the definition of injector stiffness (the injector pressure drop as a fraction of the pressure when the detonation arrives) is required. In the injector response test platform [40,60], the initial pressure was known as a single detonation was produced. The initial pressure was first used in the definition of injector stiffness. In the hotfire tests, however, initial pressure was unknown due to the absence of high-frequency pressure measurements. Instead, the average pressure of multiple detonations was measured and it is understood that the average pressure will be substantially higher than the initial pressure.

Ideally an average pressure could be calculated for a single detonation wave and injector stiffness could be redefined, but the caveat lies in the lack of information on how the pressure profile of a detonation wave differs in the case of an isolated detonation and as part of a rotating detonation cycle. For direct comparisons between the injector studies from the previous chapter and injector performance in the hotfire tests in this chapter to be made, details of the detonation pressure waveform in the RDE have to be "reconstructed".

Section 4.1 begins with discussion of the method through which the waveform was reconstructed using the limited information obtained through testing and from literature. A brief summary of the test conditions covered in the test campaign is presented in 4.2, followed by an examination of the various detonation wave topologies observed in Section 4.3, where a rudimentary standard for assessing detonation stability will be introduced and utilized for analysis in later sections. In Section 4.4, a comparison between the static chamber pressure in an RDE and a constant-pressure combustor is made, and a method of correcting for dynamic pressure in RDEs is suggested. Section 4.5 discusses the inferred performance of the injector design employed in RDE v1.4

and highlights a critical structural flaw in the fuel manifold design and its impact on combustion characteristics. Results of the inverse heat transfer computations are examined in Section 4.6 and comparisons are made with throat heat flux levels in equivalent constant-pressure combustors, followed by a short study of the damage incurred by hardware over the course of the test campaign in Section 4.8. Finally, the chapter closes with a suggested liquid propellant mixing mechanism in Section 4.9.

4.1 Waveform Reconstruction

From high-frequency pressure measurements in the injector response experiments [31, 32], it was known that the pressure spike and decay associated with a single detonation wave has a typical duration of 100 to 150 μs. However, from high-speed videos of the hotfire tests, time interval between waves were as low as 40 μs. The results from both experiments imply that a difference in waveform exists between the two operating regimes; clearly the wave form seen in the former tests could not fit within the time scale of the latter while maintaining the same frequency.

Unfortunately, it is unclear how the pressure profile differs due to limitations in instrumentation. One possibility is the temporal compression of the pressure profile such that decay back to the minimum occurs within a shorter duration. The other is the truncation of a preceeding wave's decay phase by the spike and decay of a following wave. However, the latter option would imply an ever-increasing average chamber pressure due to the elimination of the low-pressure phase of the profile and the propellant injectors will eventually fail to replenish the chamber with propellants. Therefore, the former suggestion presents a more realistic mechanism for rotating detonation waves.

Under this assumption, the relationship between initial, peak, and time-averaged pressures from injector response testing were used to provide an estimate of the initial (pre-detonation) pressures in the hotfire tests for the purpose of calculating injector stiffness in a consistent manner. It shall be clarified here that large margins of error

will be associated with these estimates as detonation pressure data for a kerosene-oxygen mixture is scarce in open literature at the time of writing with [61] being the only documentation known to the author. Another method of reconciliation was considered, where injector stiffness was redefined to use average pressure instead of minimum pressure as the baseline. However, it was quickly realized that using this method resulted in negative stiffness values in the injector dynamics experiments.

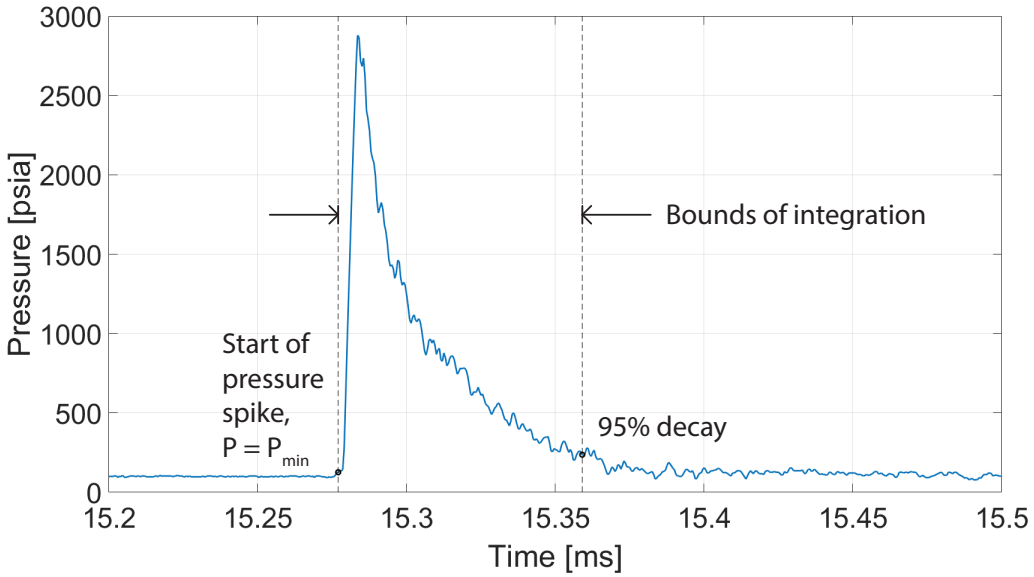

Figure 4.1. Sample plot of detonation pressure profile showing integration boundaries for obtaining average pressure.

Referring to Fig. 4.1, the time-averaged pressure produced by a single detonation wave was calculated by integrating the detonation pressure profile between the initial pressure rise and time at which the pressure had decayed by 95% of the initial increment, and dividing by the corresponding duration. It was discovered that the ratio of average detonation pressure to minimum pressure, or average pressure ratio (APR), lay mostly between 30 and 40% of peak DPR and held true for both propellant combinations, as depicted in Fig. 4.2. The mean APR for hydrogen-oxygen detonations was 0.35×DPR while that of ethylene-oxygen detonations was 0.32×DPR. The mean

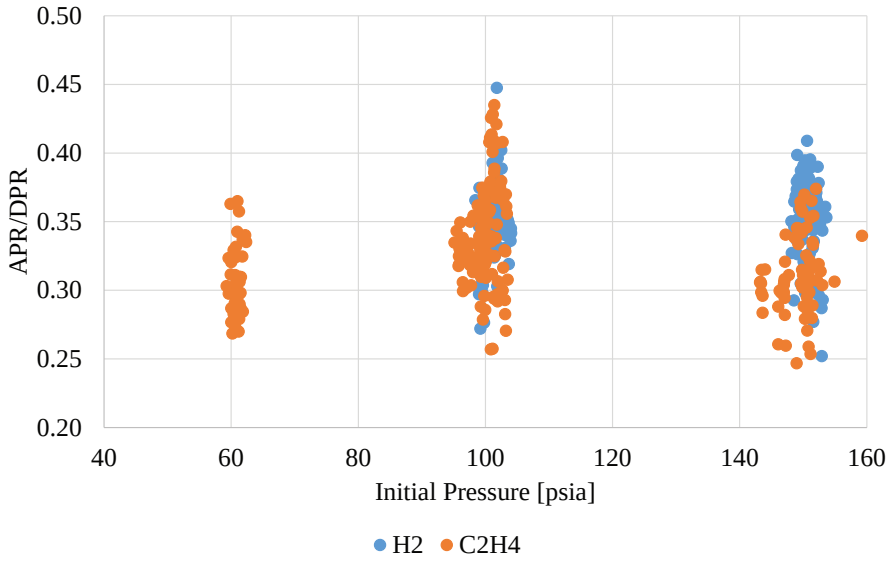

Figure 4.2. Ratio of average to peak detonation pressure ratio collected from injector transient response study.

APR across both propellant combinations was 0.34×DPR. Along with an estimate of detonation pressure ratio (with considerable uncertainty) in the hotfire tests, injector stiffness based on minimum pressure could be calculated and compared with findings from the injector response studies to estimate the maximum number of detonation waves expected. The conversion from measured CTAP to minimum pressure was via the following equation:

$$P_{min} = \frac{P_{avg}}{APR} \approx \frac{P_{avg}}{0.34 \times DPR} \tag{4.1}$$

and injector stiffness was calculated by

$$stiffness = \frac{P_m - P_{min}}{P_{min}} \tag{4.2}$$

where P_m is manifold pressure.

RP-1 and RP-2 are modeled as $C_{11.66}H_{23.32}$ and $C_{11.74}H_{23.40}$ respectively in the NIST database [47] while RP-1 is modeled as $C_1H_{1.95}$ in NASA CEA [13]. Unfortunately, NASA CEA does not feature the capability to compute detonation properties for condensed phase propellants. C-J detonation information for the longest gaseous

hydrocarbon $C_{10}H_{21}$ available in the NASA CEA library, which comes close in length to the surrogate models employed by NIST, shows that stoichiometric detonation produces a DPR of 41 while an equivalence ratio of 1.6 yields a ratio of 53. The variation of DPR with equivalence ratio showed a strong linear relationship as shown by Fig. 4.3. The equation for the linear fit was found to be

$$DPR = 20.071\phi + 20.964 \tag{4.3}$$

Along with the detonation information presented in [61], it was possible to estimate the range of detonation pressure ratios for the tests in question recognizing that both of the cited sources are relevant to 1-D detonations while RDE geometries contain at least two dimensions in which gases can expand. Since CEA computations assume perfect mixing, the P_{min} obtained represents the lower bound of possible values.

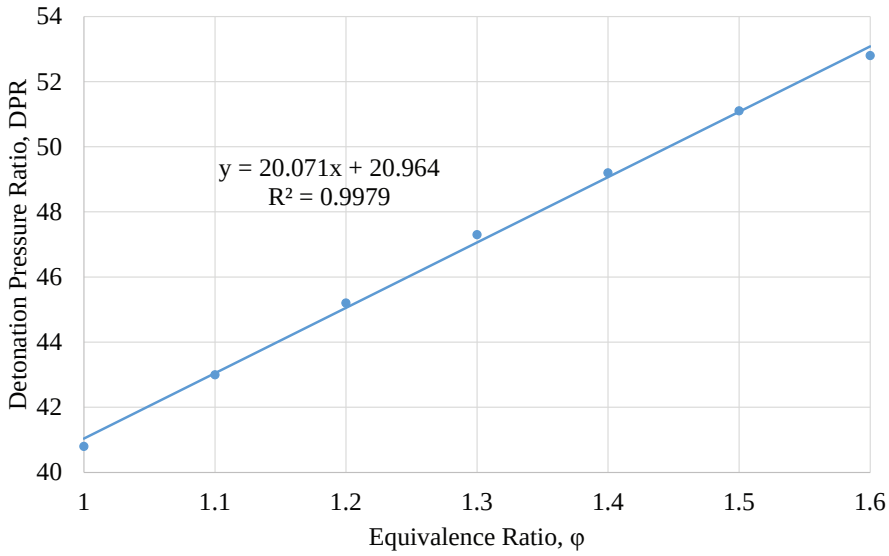

Figure 4.3. Detonation pressure ratio of $C_{10}H_{21}$-O_2 mixtures vs. equivalence ratio.

Peak pressures obtained in the RDE will be somewhat lower due to lateral relief and imperfect mixing, but the resulting difference in refill time calculation is expected

to be minimal by virtue of the negative exponent in the large stiffness term according to the curve fit in Eq. 3.2. From the injector response experiments, DPR measured in the fully-confined section of the detonation channel were typically 75 to 100% of C-J values, decreasing to as low as 50% of C-J in the lateral relief section. To compensate for the lack of information on kerosene-GOX detonation, the DPR term in Eq. 4.1 was reduced by up to 50% to produce a range of stiffness and refill time values in which actual experimental conditions could reside.

4.2 Test Conditions

Version 1.4 of the Purdue RDE was successfully ignited 45 times throughout the test campaign and provided information on bulk operating conditions, chamber heat loads, waveform topologies and speed, manifold behavior, and thrust performance. In this section, relationship among detonation characteristics, heat flux, and fuel feed conditions will be explored. Due to ITAR restrictions, measured thrust will not be discussed by the author.

Table 4.1. Summary of test conditions for RDE v1.4 hotfire tests.

Mass flow rate [kg/s (lbm/s)]	Equivalence ratio, ϕ	Chamber CTAP [kPa (psia)]	Estimated fuel injector stiffness
0.77 to 3.49 (1.70 to 7.67)	0.97 to 1.73	316 to 1,780 (45.9 to 258)	30 to 550 $\pm$ 35%

Injector stiffness in conventional engines is calculated based on the average chamber pressure and is commonly used to quantify the pressure loss of a given injection scheme. However, for sake of comparison with the parameters used in the injector response experiments, injector stiffness based on the minimum chamber pressure has been estimated based on Eq. 4.1. Per prior discussion, an attempt was made to bracket the upper and lower bounds of injector stiffness values encountered in the

hotfire tests. The global range of conditions covered in this test campaign are summarized in Table 4.1.

4.3 Detonation Wave Characteristics

The number of detonation waves obtained during engine operation ranged from one to seven, with five waves being the most common topology. More than two-thirds of all tests produced 4 – 6 co-rotating detonation waves. Surprisingly, while direction of rotation have been known to change mid-test in certain cases, a counter-rotating mode was never observed in RDE v1.4. It is a phenomenon reported by numerous other researchers, including Anderson [24] and Walters [62] at Zucrow Labs, where at least two detonation waves propagated in opposite directions over a sustained duration.

4.3.1 Influence of Mass Flow Rates on Wave Count

Figure 4.4 depicts the average number of detonation waves against total and fuel mass flow rates respectively. Non-integer values on the vertical axes are the result of a change in the number of waves present within the data window. To clarify, the values do *not* take into account the relative durations for which the number of waves persist; their sole purpose is to indicate that the number of waves had varied. On both Figs. 4.4(a) and 4.4(b), the general trend of number of detonation waves increasing with mass flow rate is present, although scatter of data is substantial for the resolution of conditions swept. This trend was not observed in prior gas-gas RDE experiments conducted on the same platform by Stechmann [15] as wave topologies were largely invariant with throttle setting in these experiments.

A comparison of both plots suggests that the number of waves produced was more strongly influenced by the fuel mass flow rate: Trends accounting for injector type are predominantly positive in Fig. 4.4(b) while several instances of wave counts decreasing with increasing total mass flow rate are seen in Fig. 4.4(a). The plot

against GOX flow rate showed an almost identical trend to that of total flow rate and has not been presented here due to spatial constraints, but the interested reader can view it in Appendix E.

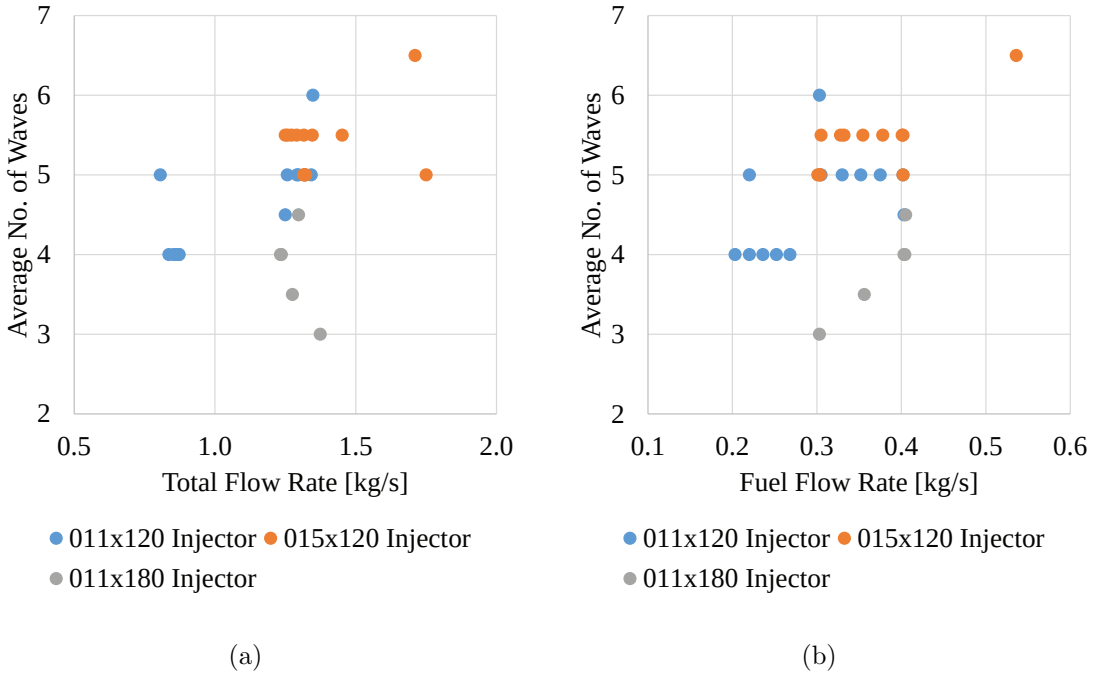

Figure 4.4. Average number of waves vs. (a) total mass flow rate and (b) fuel mass flow rate.

In [12] Bykovskii postulates that a critical fill height exists, below which detonations cannot be sustained. With gaseous reactants using stiff (choked) injection systems, increases in mass flow/throttle setting do not change the fill velocity which remains sonic at all settings. However, for liquid injectants, increases in mass flow lead to corresponding increases in fuel manifold pressures which do affect fuel injection velocity via Bernoulli's equation, $v = \sqrt{\frac{2\Delta P}{\rho}}$. In this case the agility of the fuel circuit increases with throttle setting while the gaseous oxidizer circuit produces roughly the same fill height (albeit with denser gas) as throttle setting is increased. Increases in gas density will translate to improved atomization and shorter droplet lifetimes that can support shorter wave arrival times and hence a larger number of

waves. As the trends in Fig. 4.4 are weak, additional confirmation of this theory is obviously needed.

4.3.2 Qualification of Wave Stability

Due to the lack of instrumentation in the main chamber, one of the indirect ways by which combustion performance was assessed was its apparent waveform stability. Prior gas-gas experiments [15] provided a strong correlation between thrust performance and the observed combustion field as provided by high-speed camera observations of the annular chamber. Paying particular attention to variations in wave spacing and luminosity, bifurcation and extinction events, visual assessments provide an excellent inference of performance. This is a unique advantage particular to RDE combustion and it can presumably streamilne development of engines focusing on this combustion technology. Regular separation between detonation fronts, stable luminosity, and constant wave count are qualities associated with stability and performance.

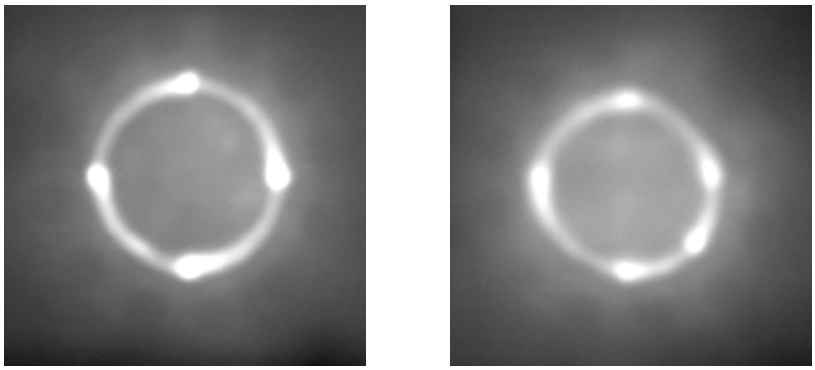

Figure 4.5. Visual comparison of stable (left) and unstable (right) detonation behavior.

Figure 4.5 has been shown as a visual example of the features used to assess stability. Obviously, temporal variations of wave spacing and luminosity, as well as changes in wave count cannot be demonstrated in these still images. Nevertheless,

aside from the number of waves present, it is not hard to see that the two images hold distinct differences:

1. Detonation fronts appear bright and sharp on the left while those on the right are dimmer and do not have well-defined edges

2. Bright spots are uniformly-shaped like tear drops on the left but irregularly-shaped on the right

3. Spacings between detonations are uniform on the left but certainly not so on the right

The blurring of edges around the detonations in the image on the right in Fig. 4.5 may be attritubed to deflagrative afterburning of propellants. When propellants are inadequately-mixed ahead of a detonation, combustion efficiency is likely to decrease. The unconsumed propellant can ignite with a longer delay and manifest itself as a "smeared" light emission. At the same time, with inefficient combustion driving the shock front, the pressure – and therefore density – gradient becomes weaker resulting in a less-distinct leading edge. The non-uniform spacing between waves is a result of waves traveling at different speeds, and is typically associated with the formation or extinction of a detonation wave and overall stability of the combustion process. The image on the right was taken from a case where the number of waves varied between four and five.

The author recognizes the subjectivity in this classification scheme, but a formal standard has yet been established by the rotating detonation community at present. Differences in appearance of the detonation waves are obvious on either end of the stability spectrum, but less so in the middle ground; wave spacing could be regular for the majority of the duration with only isolated instances of uneveness, or luminosity of the detonation fronts might decrease infrequently. Cases like such were placed in a separate classification of *slightly unstable* for the sake of acknowledging the non-duality of operating modes.

4.3.3 Development of Wave Topology

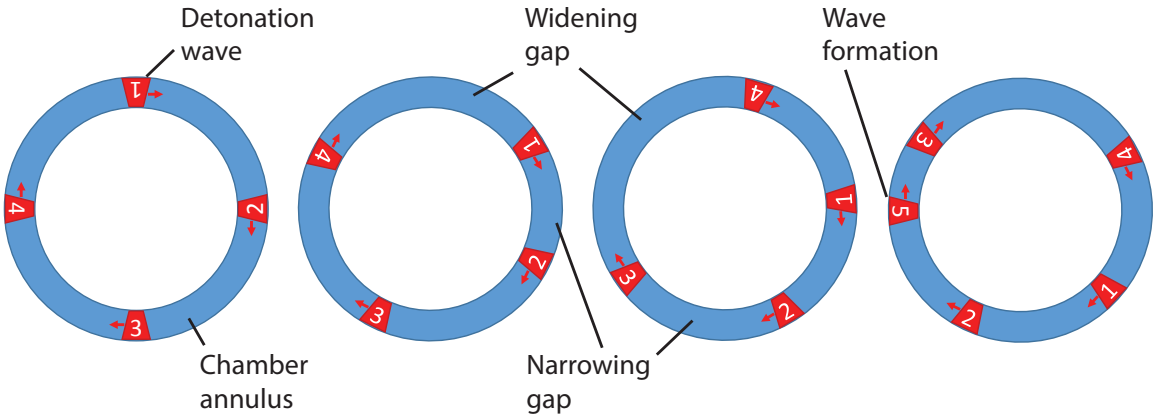

Figure 4.6. Illustration of the wave formation process.

Figure 4.6 is a schematic representation of the process of detonation wave formation observed in high-speed videography, with waves shown traveling in the clockwise direction in the example. A possible mechanism of the wave formation/bifurcation process is as follows:

1. The first image represents the initial condition, where four waves are spaced equally apart.

2. The second image depicts the initiation of the wave formation process: It typically begins with the acceleration of a detonation wave (#1), presumably due to the presence of excess well-mixed propellants. The gap separating it and the trailing wave (#4) widens, resulting in an abundance of propellants in that region.

3. In the third image, wave #4 accelerates towards #1 and the widened gap effectively cascades in the counter-clockwide direction. This cascade can take place multiple times before the next step.

4. In the last image, as wave #3 accelerates towards #4 through the propellant-filled sector, it bifurcates to produce wave #5, which moves at a lower speed. The trigger for the bifurcation event is possibly some form of pressure instability; the exact mechanism is unclear.

The opposite situation has also been observed, where the number of waves was reduced, likely because the dynamic interaction between detonation waves and injectors resulted in inadequate propellant fill. The extinction process happens in reverse: A wave decelerates due to the lack of reactants, and is eventually caught up by the trailing wave, and so on. The narrowed gap cascades, again in the direction opposite to wave travel, until eventually one of the waves becomes weakened to the point where it is consumed by the wave that catches up to it.

4.3.4 Detonation Wave Speed

Detonation speed is a quantity that was also considered and has been used by many as a proctor for performance of RDE chambers. However, it is more related to strength than stability (especially since over-driven detonations, which are unstable, can attain speeds far greater than C-J values) and practical differences exist between an RDe and a classical ideal C-J detonation. Detonation progression in a non-premixed RDE is theorized to be better described as a series of explosive energy-addition events (attributed to each injection site), followed by wave attenuation in the region between successive injection sites. Lateral relief, potential shock reflections off chamber walls, mixing-induced combustion, and the potential for high-pressure gases to back-flow into injector plenums further complicate the analogy between an RDE wave speed and the idealized C-J process. For these reasons, detonation wave speed was not included in the criteria for stability grades. Instead, correlations of engine parameters with wave speed shall be examined as separate subjects.

Average detonation wave speed has been plotted against average number of waves in Fig. 4.7. There appears to be an absence of trend in the data unlike in prior gas-

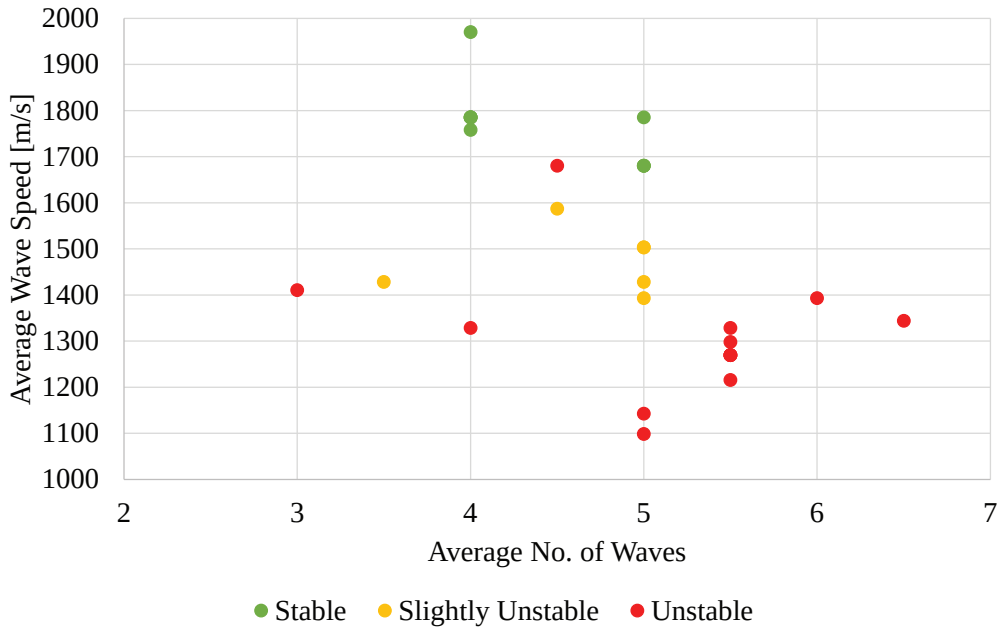

Figure 4.7. Average wave speed vs. average number of waves.

gas experiments on the same platform [15], where an increase in the number of waves was correlated with a decrease in wave speed. However, the stable cases do appear to occupy the upper range of wave speeds while unstable cases appear closer to the bottom of the chart. It may be tempting to suggest that the engine operated most stably with four or five waves from this figure alone, but the picture is incomplete at this point; as discussed in Section 4.5, a design feature in the engine had impacted detonation stability in the majority of tests.

4.4 Chamber Pressure

One of the indicators used to assess performance was capillary tube attenuated pressure (CTAP), which provides a measure of the average chamber pressure by acting as a low-pass filter. The resulting measurement is a *static* pressure of the gas at the CTAP port's location, and the reader should be mindful of its difference from

the conventional P_c used in constant-pressure combustion to represent *stagnation* chamber pressure.

This is primarily due to both the RDE's geometry and mode of combustion. The simplest RDE chamber design, and the topology utilized in the subject test campaign, consists of a constant-area annulus that is choked thermally instead of geometrically. Since the average mass flux is equal at both the head and exit of the chamber, axial velocity is expected to be similar at both locations. The detonation wave travels supersonically with respect to the unburned propellants upstream and its gaseous products travel at near sonic velocity away from the wavefront. While a shock wave on its own carries no momentum, moving gas behind it does. As a result, hot gas downstream of the detonation wave still moves with a high circumferential speed (several hundred m/s) in the laboratory frame of reference.

Axial placement of the capillary opening can expose it to varying degrees of dynamic pressure, and limitations in hardware manufacturing become an issue that in many cases limits the designer substantially. In the v1.4 hardware in question, it appears that the placement was unfortunately in a region where strong detonation waves lie and hence it has been challenging to ascertain/interpret the measurement [15]. In addition, the short run times required for the heat sink hardware necessitated a substantial reduction in the CTAP line length, from a recommended length of 2.7 m (8.9 ft) [63] to a value of 51 cm (20 in) utilized in the test campaign. Data suggest that the CTAP pressure was adequately stabilized in the one second tests with this reduced line volume even though the level of attenuation to the high-amplitude, non-linear pressure fluctuations was low compared to standard CTAP. It becomes apparent now that measured pressure anywhere in an RDE is far from stagnant and should be used with caution in calculations or as a performance metric.

4.4.1 Dynamic Pressure Correction

There is potential for meaningful interpretation of chamber static pressure if it is first corrected with dynamic pressure. While the concept is simple, the difficulty lies in determining the appropriate dynamic pressure (density and flow velocity) to use in the calculation. This is due to the sensitivity of flow properties such as pressure, density, speed, and direction to location relative to the detonation front. If the detonation waves were to pass directly over the CTAP port, it would be expected of a certain volume of detonation products to expand into the capillary tube, stagnate, and result in an increase of measured pressure. For detonations close to but not directly traversing the CTAP port, little to no stagnation pressure recovery would be measured. If the CTAP port were far away from the detonations, such as at the chamber exit, the product gas would have expanded somewhat and thus possess different density and speed compared to the head end.

Hopefully, the elaboration above demonstrates the complexity of the given problem. Since limited information is avilable on flow conditions over the CTAP port, it will be assumed here that the detonations were close to but not directly over the CTAP port. While detonation velocity can be obtained directly from high-speed videos, determining the circumferential *flow* velocity is no menial task due to the lack of flow visualization. It is possible to estimate the local circumferential velocity immediately behind the shock, but its value is expected to decrease non-linearly as the gas expands in the opposite direction with increasing distance from the shock. Additionally, recall that NASA CEA does not currently feature the capability of computing detonations using condensed phase reactants.

This was addressed by performing detonation calculations for a variety of gaseous hydrocarbons and noting their respective sonic-to-detonation velocity ratios, or $\frac{a_2}{v_{det}}$ from Fig. 4.8, where a_2 is the sonic velocity immediately after a detonation wave and v_{det} is the velocity of the detonation wave. In general, it is not recommended to subtract computed sonic velocity from measured detonation velocity to obtain flow

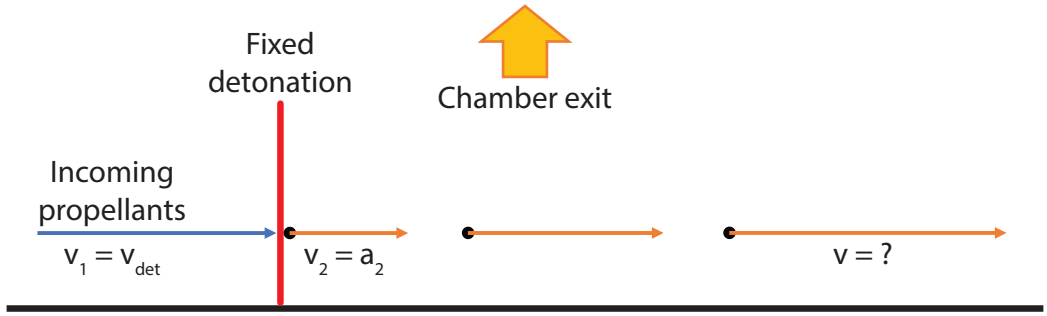

Figure 4.8. Simplified representation of gaseous products expanding azimuthally behind a detonation wave.

speed in the lab-fixed frame of reference. The ideal mixing and complete reaction assumptions in the computation, compounded with non-ideal mixing and incomplete reaction in the actual detonation, lead to a large error in the calculated flow speed. Applying the ratio to measured detonation speed instead reduces the amount error, but is by no means accurate. It is, however, the best available course of action for the analysis here.

Figure 4.9 is a combined plot of $\frac{a_2}{v_{det}}$ against equivalence ratio for the following list of fuels with oxygen: CH_4 (methane), C_2H_4 (ethene/ethylene), C_2H_6 (ethane), C_3H_6 (propene/propylene), C_3H_8 (propane), C_4H_8 (isobutene), C_4H_{10} (isobutane), C_5H_{10} (1-pentene), C_5H_{12} (n-pentane), C_6H_{12} (1-hexene), C_6H_{14} (n-hexane), C_7H_{14} (1-heptene), C_7H_{16} (n-heptane), C_8H_{16} (1-octene), C_8H_{18} (n-octane), and $C_{10}H_{21}$ (n-decyl). The temperature of GOX was set to 400 K, similar to preburner exit temperatures in the hotfire tests. Fuel temperatures used were 280 and 300 K to bracket the range of fuel temperatures encountered during the tests.

According to the figure, the ratio $\frac{a_2}{v_{det}}$ was approximately 0.54 for the listed fuels and varied weakly with equivalence ratio. Therefore, under the assumption that the finding will also be applicable to RP-2, the azimuthal flow velocity can thus be approximated. Unfortunately, the final azimuthal velocity to which the gas expands is unknown. A convenient method is to assume that azimuthal velocity approaches zero

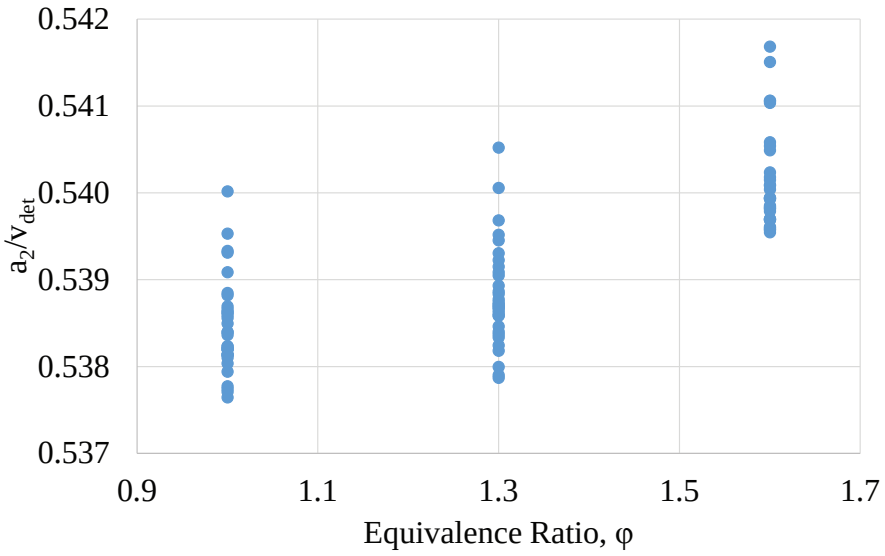

Figure 4.9. Ratio of post-detonation sonic velocity to detonation velocity vs. equivalence ratio for a variety of gaseous hydrocarbons ranging from C_1H_y to $C_{10}H_y$.

at the end of expansion, which at the same time would result in a purely axial flow ahead of the subsequent detonation wave. Next, a velocity decay profile is needed. Theoretically, a non-linear decay profile is expected. However, the information is unavailable and for simplicity, it was assumed as a linear decay. However, it is important to realize that this will result in an *optimistic* estimate of azimuthal flow velocity.

Knowing the total mass flow rate and chamber area, average axial flow velocity could be calculated if gas density were known. However, CFD simulations performed by various researchers have shown that static pressure/density decreases towards the chamber exit [64–66] and is a quantity that cannot be measured directly. Until a high-fidelity numerical simulation of the chamber conditions has been performed, a crude estimate using NASA CEA with measured CTAP as pressure input will have to serve as the next best option.

The detailed process of estimating dynamic pressure at the chamber head is as follows:

1. Axial flow velocity was simply approximated by

$$v_z = \frac{\dot{m}}{\rho A_c} \tag{4.4}$$

where $\dot{m}$ is the measured total mass flow rate, ρ is density of product gas combusted at measured CTAP according to NASA CEA, and A_c is the chamber annular area. Note that it is possible that the CTAP port lies in the propellant fill region for at least part of the detonation cycle, in which case gas density would be higher and dynamic pressure associated with the flow would be significantly reduced. Therefore, this assumption leads to an *optimistic* estimate.

2. Peak azimuthal flow velocity immediately behind the detonation wave was calculated as

$$v_{\theta,max} = v_{det} - a_2 \tag{4.5}$$

where v_{det} is measured detonation wave speed and a_2 is the speed of sound behind the detonation depicted in Fig. 4.8.

3. With increasing distance from the detonation wave, flow was assumed to expand and accelerate in the opposite direction until its azimuthal component vanishes to produce purely axial flow. From lack of information on the expansion profile, it shall be simply estimated to be linear. However, it is important to note that the expansion profile is expected to be asymptotic. Consequently, the linear profile asusmption will result in an *optimistic* dynamic pressure correction.

$$v_\theta = \frac{v_{\theta,max}}{2} \tag{4.6}$$

4. Dynamic pressure was then estimated via

$$q = \frac{1}{2}\rho(v_z^2 + v_\theta^2) \tag{4.7}$$

5. Finally, the estimated total pressure at the chamber head was the summation of CTAP and dynamic pressure

$$P_0 = CTAP + q \tag{4.8}$$

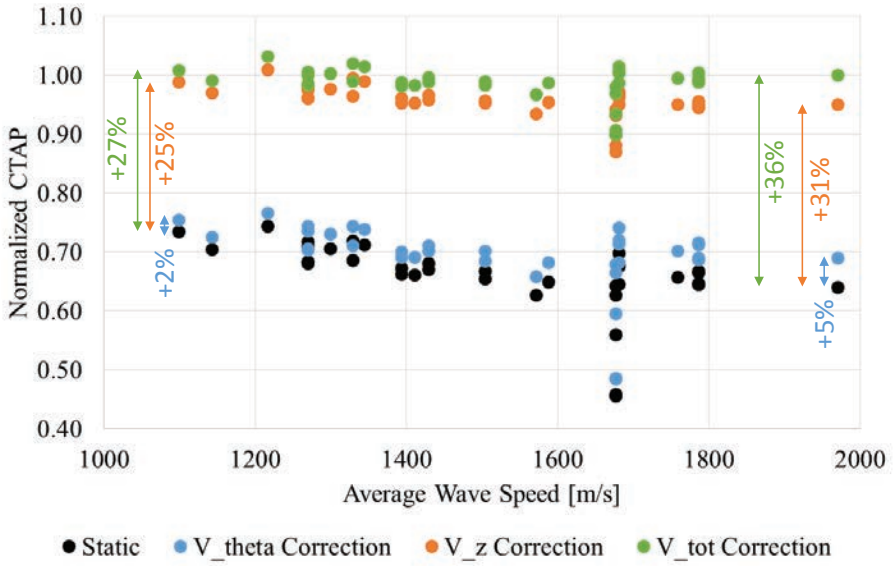

Figure 4.10. Normalized CTAP vs. detonation speed with corrections for dynamic pressure.

Figure 4.10 demonstrates that chamber pressure measurements in RDEs in general should not be treated as analogues to the chamber pressure in constant-pressure combustors. On the vertical axis, measured CTAP has been normalized by the computed ideal chamber pressure in a constant-pressure combustor with equivalent flow rates and whose throat is of the same area as the RDE annulus. Raw CTAP measurements, represented by black circles, show low normalized values and a negative correlation with observed detonation wave speed. The negative correlation was unexpected as high wave velocity has also been associated with stable detonation behavior. However, the application of dynamic pressure correction as outlined above appears to provide an explanation for the observed trend.

The blue circles show the correction for the azimuthal component of dynamic pressure. Between 2 and 5% increments over static CTAP are seen, with greater increments at higher wave speeds. Consequently, the negative trend is slightly reduced. Recall that the method of averaging azimuthal velocity was optimistic, so actual dynamic pressure recovery should be expected to be lower. The axial contribution of

dynamic pressure, shown in orange, is drastically higher, contributing an additional 25 to 31% towards total pressure. Due to the numerous assumptions made in the calculation, this was also an optimistic estimate. Combined, the total dynamic pressure correction brings almost a third of the cases past 100% in normalized value and the slope of the data becomes almost neutral. However, the magnitudes on the vertical axis demand skepticism due to the multitude of assumptions applied in approximating flow speed. Instead, the reader's attention should fall on the potential amount of total pressure that could be missed if chamber flow velocity were unaccounted for.

Results from Stechmann's experiments with RDE v1.3 showed significantly higher CTAP levels with some even surpassing that of an ideal constant-pressure combustor [15]. However, as mentioned previously, CTAP measurements are sensitive to port location relative to the detonation waves. It is possible that the detonation waves passed directly over the CTAP port in the tests, and as the detonation products expanded into the CTAP passage, they eventually reached a stagnation state, therefore resulting in higher measured pressures. As a disclaimer, this is purely a conjecture of the author based on available information and knowledge of the sensitivity of CTAP measurements to port placement. Further verification will be required.

Equation 2.3 can be rearranged as

$$P_c = \frac{c^* \dot{m}}{A_t} \tag{4.9}$$

According to this equation, c^* can be determined by plotting CTAP against mass flux, which is shown in Fig. 4.11. Similar to the previous figure, CTAP with various dynamic pressure corrections have been included. Linear trendlines with y-intercepts fixed at zero to follow the form of Eq. 4.9 have been applied to each set of data, and the slope of each trendline gives the c^* of the corresponding data. Since c^* of a given propellant combination is a function of mixture ratio and pressure, the values obtained from the figure represent only an average across all test conditions. One may also notice that the corrected data sets do not contain as many points of data as the static baseline data, and that is due to the absence of high-speed images for some

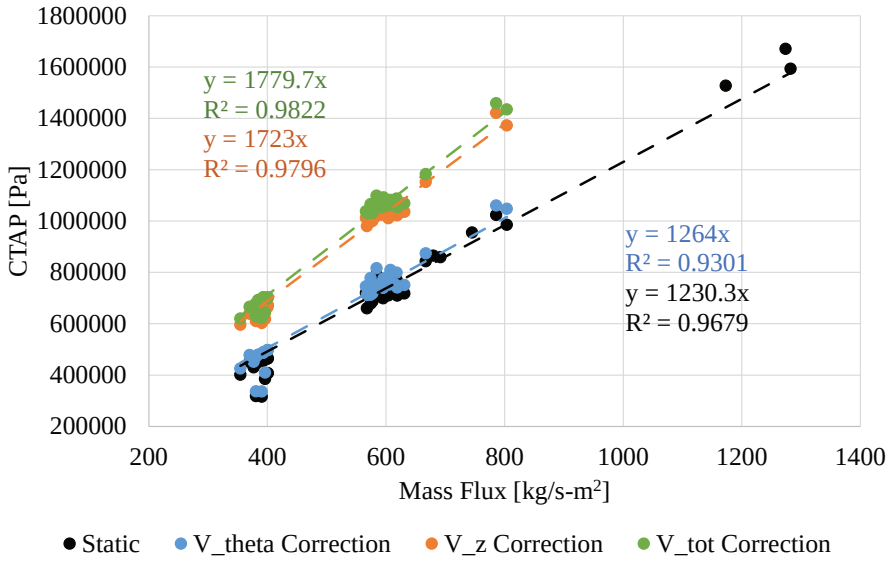

Figure 4.11. CTAP vs. mass flux with corrections for dynamic pressure.

tests from which wave speeds could be measured for correction purposes. Needless to say, c^* also increased when flow velocities were taken into account.

Since the corrections applied to CTAP in this section have required a generous number of assumptions and extrapolations, the corrected results should be regarded as the upper limit that the engine is capable of producing. The massive increments demonstrated in the figures should serve to alert the reader that chamber flow velocities are in no way negligible in RDEs. In closing, the author believes that CTAP measurements in RDEs should not be considered equivalent to chamber pressure measurements in conventional engines. Additionally, CTAP alone does not provide any utility for performance quantification because of the other necessary measurements - local flow speed and density - that are extremely difficult to obtain. Where available, thrust, engine flow rate, and manifold pressures should provide the most direct and accurate means of comparison among different engine types.

4.5 Injector Performance

Combustion characteristics of the engine provided indirect information that could be used to infer injector performance during engine operation. The design of the fuel injectors was highly inflenced by cold flow tests conducted with water and the interpretation of these results was poor given the fact that a real RDE passes the detonation wave over the injector at the minimum pressure in the cycle rather than at an average pressure as imposed in the cold flow rig. Hence, the group was quite surprised by the fact that five detonation waves were present on the very first hotfire test.

The number and apparent stability of detonation waves served as indicators of the injectors' ability to recover from high-amplitude pressure perturbations. From high-speed videos, average detonation wave frequency and speed were calculated. From these, the average time intervals between successive waves were determined. From the injector response experiments with water, the expected recovery times for various injector stiffnesses were estimated for the kerosene injector. With the addition of a fuel jet penetration time based on the calculation of Bernoulli velocity, the expected number of detonation waves was estimated. The estimation is most likely an over-estimate since the actual mixing mechanism has not been considered.

Figure 4.12 shows a section view of the injection region. The RP-2 (red) was injected perpendicularly to the annular GOX flow (blue). It was assumed that the jet penetration distance required for adequate mixing was the 0.76 mm (0.03 in) gap that forms the GOX throat, and that the fuel jets emerged at the Bernoulli velocity corresponding to the injector pressure drop when local chamber pressure was at its *minimum*. The GOX expands supersonically for a short distance before encountering the fuel jets and sudden expansion, and is expected to form complex shocks from the interaction, but that is beyond the scope of discussion. The mixing of propellants likely occurs over some distance, shown in purple (not for scale) in the figure.

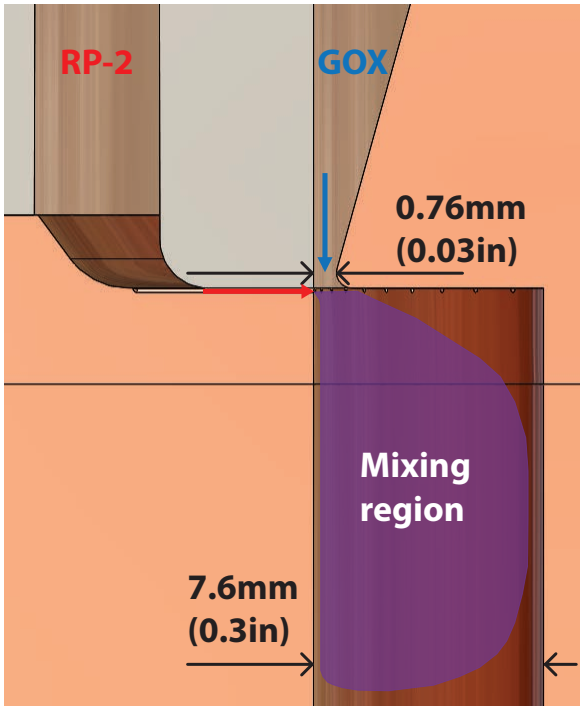

Figure 4.12. Illustration of the formation of the propellant mixing region close to the injection plane.

The process is as follows:

$$t_r = 16.39 \left(\frac{\Delta P}{P_{min}} \right)^{-0.9768} \times DPR \times 10^6 \tag{4.10}$$

$$v_{b,f} = \sqrt{\frac{2\left(P_{m,f} - P_{min}\right)}{\rho_f}} \tag{4.11}$$

$$t_{pen} = \frac{L_{gap}}{v_{b,f}} \tag{4.12}$$

$$N = \frac{\pi D}{v_{det}\left(t_r + t_{pen}\right)} \tag{4.13}$$

where Eq. 4.10 is the fitted equation from Fig. 3.18 modified to give t_r in seconds. $v_{b,f}$ is the Bernoulli velocity of the fuel jet, $P_{m,f}$ is the fuel manifold pressure, P_{min} is the minimum chamber pressure ahead of the detonation, ρ_f is the density of fuel, t_{pen} is the jet penetration time, L_{gap} is the distance of the GOX gap, N is the expected

number of waves, D is the mean diameter of the annulus, and v_{det} is average detonation velocity obtained from high-speed images of hotfire tests.

At the very high injector stiffnesses applied in the hotfire tests, refill times calculated using the fitted equation were highly-insensitive to the inaccuracies of estimating DPR, i.e., differing DPR by 50% led to differences in the total refill and jet penetration time ($t_r + t_{pen}$) of 2% or less. Calculated refill times were very low compared to the observed wave intervals – between 1 and 19 μs. This was unsurprising since manifold pressures employed were factors greater than *average* chamber pressure. Recall from earlier discussion that in the injector response test campaign, manifold pressures were always well below the calculated average detonation pressures. Even so, recovery times had fallen below 200 μs by a stiffness value of 2 (Fig. 3.16). Even accounting for the estimated jet penetration times of between 4 and 11 μs, the actual wave intervals were significantly longer.

According to equations 4.10 through 4.13, between seven and 30 waves could be sustained by the range of injection pressures employed. However, the maximum number of waves observed was only seven. This implies that injection recovery was not the limiting factor in the operating frequency of the engine. Propellant fill height and/or mixing likely also played a major role in dictating the number of sustainable detonations. This hypothesis could also explain the observed increase in number of waves with fuel flow rate: Since fuel would have been injected almost continuously at the high stiffnesses, a layer of fresh propellants would have begun building almost immediately after the detonation. Where the layer's thickness exceeded the critical fill height as suggested by Bykovskii [12] and is sufficiently mixed, a detonation wave could be supported. One can picture a detonation "unit" consisting of a propellant layer of increasing thickness followed by a detonation wave repeating about the circumference of the annulus, as depicted in Fig. 4.13.

In such a scenario, it is more likely than not that the division of annular circumference by arc length of the repeating flow structure does not result in an integer value. Referring to Fig. 4.14, where the data have been colored according to apparent

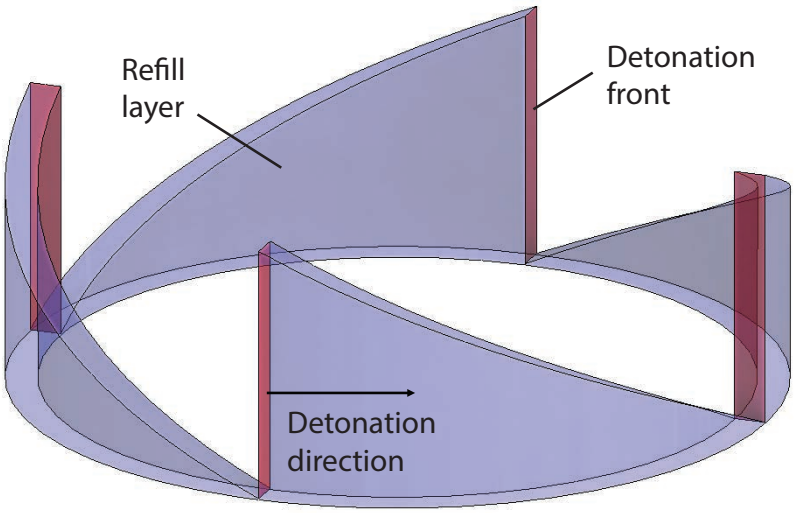

Figure 4.13. Simplified schematic of four detonation units around the annulus (injector refill time neglected for simplicity). Chamber exit towards top of figure.

detonation stability, one may notice that every stable point and all but one slightly unstable points occupy integer values on the vertical axis while non-integer wave numbers are only occupied by cases where waves were unstable or slightly unstable. From this observation, it is perhaps concievable that wave stability was enhanced by injection-detonation interactions that resulted in near-integer numbers of repeated refill layer and detonation units, i.e. $\frac{C}{L_{refill}} \approx N$ where C is the circumference of the annulus, L_{refill} is the arc length of the refill layer and detonation structure, and N is an integer.

To simplify the following discussion, suppose that refill layer thickness increases linearly and that the detonation is perpendicular to the injector face, i.e. the propellant fill and mixing region forms a right triangle. Now cases where $\frac{C}{L_{refill}} \approx N + \frac{1}{2}$ will be considered, taking $N = 4$ as example. In this scenario represented in Fig. 4.15, the circumference contains four full-sized triangular regions and the remaining sector length only permits a fifth refill region that is only half the size. Since this fill height would be unable to support detonation, a larger gap separates detonations

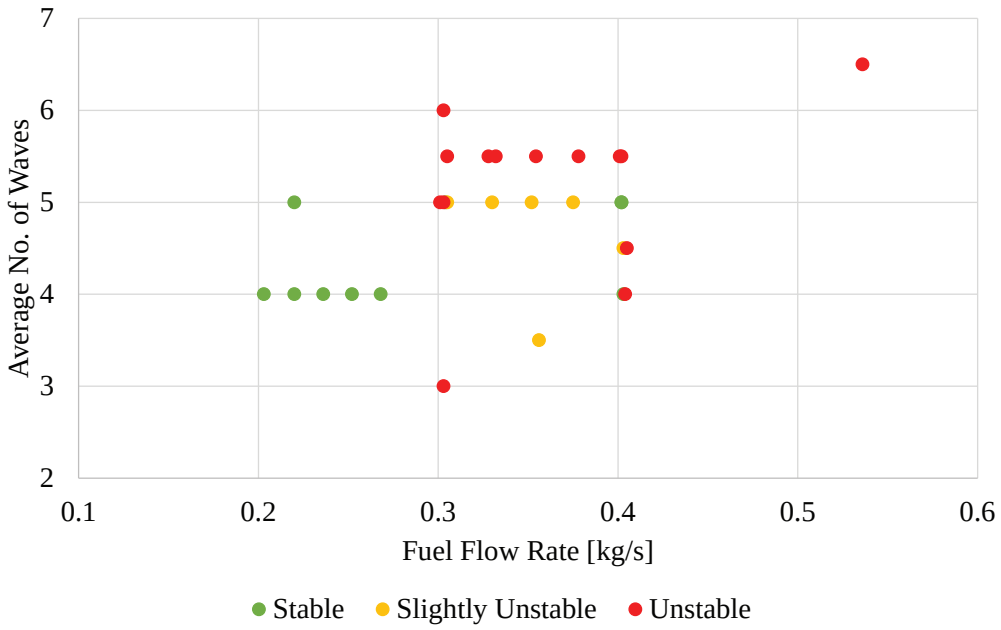

Figure 4.14. Average number of detonation waves vs. fuel mass flow rate, colored by apparent detonation stability.

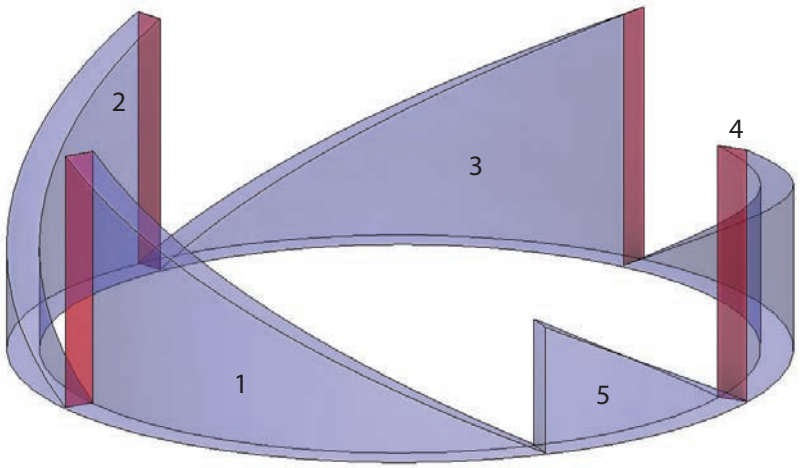

Figure 4.15. Simplified schematic of four and a half detonation units around the annulus (injector refill time neglected for simplicity). Chamber exit towards top of figure.

#1 and #4. The propellants in unit #5 instead add to the refill layer of unit #1 and the extended region of fresh propellants might result in detonation #1 being dimensionally larger than it previously was, causing a greater perturbation to the flow field behind it, possibly interrupting propellant fill for a longer period of time. Consequently, detonation #2 becomes slightly more starved of mixed propellants and the reaction zone begins to decouple from the leading shock. In doing so, its propellant consumption rate decreases such that the refill zone following it contains more unreacted propellants than the nominal flow structure, causing detonation #3 to become stronger.

This chain of events propagates in the opposite direction of the waves and because of the unmatched propellant injection and consumption rates, the dynamics fail to settle at some limit cycle that permits stable detonation behaviour. Per discussion in Section 4.3.3, a number of observations have been made in high-speed videos of unstable detonation behavior where detonation speeds varied and separation was uneven. Detonations separated by large gaps have been seen to accelerate to close the gap, causing a cascade of gap widening and narrowing similar to the prior description. In certain cases the gap separating two detonations even grew large enough that an additional detonation front spontaneously formed in between. However, the number of waves tended to fluctuate in these cases as the propellant flow rate was insufficient to sustain the increased number of waves.

4.5.1 Structural Deflection in the Fuel Manifold

Due to earlier design decisions that maximized modularity of the hardware, the fuel manifold was formed by the mating of two different components. Figure 4.16 shows a section view of the mated assembly and resulting cavity that forms the fuel manifold. Semi-circular injection orifices are formed when the injector ring is seated in the injector housing. Note that while the outboard side of the manifold is sealed

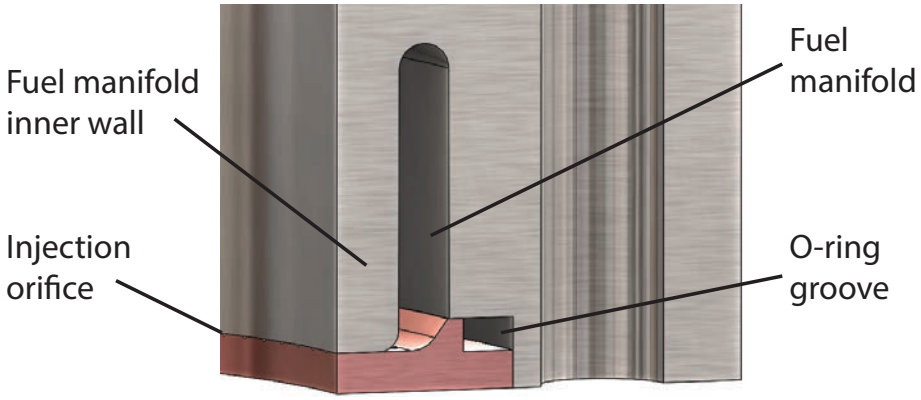

Figure 4.16. Section view of the fuel manifold and injector assembly.

using an O-ring, sealing of the injector passages solely depends on contact between two metallic surfaces.

While fuel flow was expected to favor paths of least resistance via the orifices, leak paths between orifices were almost certainly present as well. Observations from continuous testing revealed that the first tests following hardware reassembly had the tendency to display higher fuel manifold pressure levels. Significantly lower manifold pressures were recorded in subsequent tests even though fuel flow rates might have increased. Further observation of the structure surround the manifold reveals that under internal load, deformation of the manifold inner wall could cause leak paths to open up. Flexing of the wall would result in the increased impingement against the mating surface on the injector ring due to the substantial wall thickness.

Figure 4.17 shows a post-test photograph of the 011×120 injector ring. Rub marks and discoloration have been annotated on the figure. Of particular interest in this picture are the locations of the respective markings: The deepest rub marks and discoloration were separated by roughly 90°. The rub marks were likely to have been caused by the movement of stainless steel against copper while the discoloration was believed to be the result of combustion. Since the discoloration occured where the

mating surfaces should have been in contact, a gap must have opened due to structural deflection presumably from a combination of thermal and mechanical stresses.

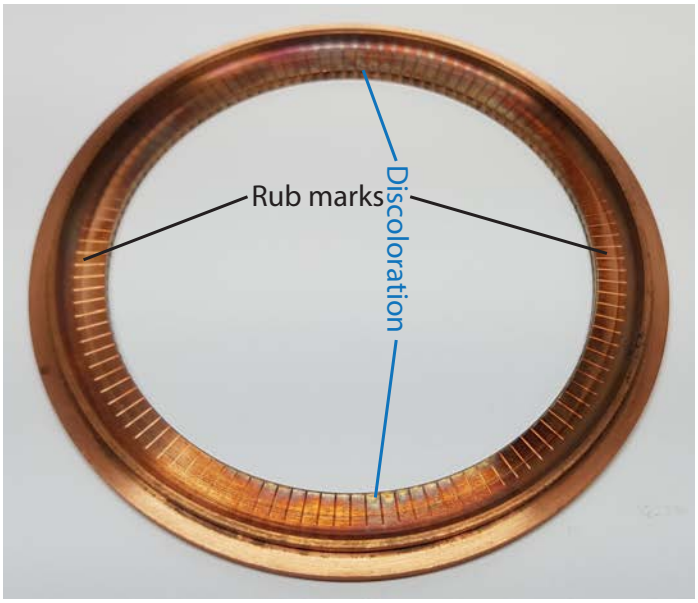

Figure 4.17. Rub marks and discoloration on the 011×120 injector ring.

Given that compression of the engine stack was achieved using bolts along the outer perimeter (vertical bolt hole visible in Fig. 4.16), it is certainly plausible that large structural deflections could have occurred where compressive loads were lower. Since decreased manifold pressures were only detected *after* the first test following engine assembly, it is believed that the deflection only occurred towards the end of the hotfire sequence. Most likely, the propellant shutdown and nitrogen purge resulted in asymmetric heat distribution that caused non-uniform expansion of the manifold wall. The manifold inner wall might have remained in the deflected position due to friction between tests. The fuel leakage might have contributed to further non-uniformity of combustion and wall deflection for subsequent tests.

The 011×120 injector happened to be the only one with such clearly-defined features; the other injectors tested at different conditions also showed similar markings, but they were not as compartmentalized. It goes to show that the current fuel man-

ifold design cannot be assumed as a rigid structure; future designs are recommended by the author to exclude unsupported walls adjacent to the combustion chamber. Additionally, fully-enclosed injection orifices will be preferred to eliminate the uncertainties pertaining to flow area; manifold conditions can be controlled more precisely when flow area is invariable to structural loading conditions. Due to the lack of clocking features on the injector ring, some uncertainty exists in the positions of the markings relative to the manifold inlets. However, in a small number of cases, matching soot deposits were found in the manifold inlet stations alongside discoloration on the injector ring.

A very significant observation from the test outcomes is the correlation between detonation stability and "goodness" of seal between the injector ring and housing. It has been noticed where information was available that the first test following hardware change and reassembly also always resulted in stable detonations and high wave speeds. When a new injector was first installed, compression by its adjacent components is expected to be effectively uniform. Therefore, fuel flow distribution is also expected to be uniform. However, in the subsequent tests that indicated leakages, distribution was probably no longer uniform. Additionally, no correlation was observed between injector configuration and detonation stability nor speed.

The significance of this finding lies in the recognition that injection uniformity also plays a major role alongside mass flux and injector stiffness in stabilizing detonations. Unfortunately, a quantitative measure of injection uniformity is unavailable based on the instrumentation employed. Nonetheless, important insights were gleaned on the design of RDE injection systems. Future designs are recommended to avoid high-tolerance, flexible components that are sensitive to geometrical distortions that can be caused by thermal stress or non-uniform pressure loads.

4.5.2 Combustion Bias Resulting from Improper Fuel Manifold Sealing

A similar trend in the azimuthal outer chamber wall temperature distribution was observed where Group 11 and 13 (12 and 6 o'clock) thermocouples began showing reduced temperature response (relative to thermocouples at other clockings around the annulus) in the same tests that registered low manifold pressure. Figure 4.18(a) shows the trace of temperatures recorded by thermocouple probes in Group 7 (head end, azimuthal distribution) for the duration of hotfire in Test 77. The azimuthal positions of the probes were 0°, 90°, 180°, and 270° in order of increasing wall depth on the plot. Similar profiles were also observed in Groups 8 and 9 (mid and aft arrays) for the same test.

For a uniformly-heated chamber, the traces would have formed a monotonically-decreasing curve such as the one depicted in Fig. 4.18(b). Test 69, which produced the temperature trace, was the first test following hardware reassembly. It was originally thought that for subsequent tests, thermal expansion effects had caused the loss of contact between the probes and wall surface, but the probability of contact failure to occur in such an organized manner was very low. The discovery of surface markings (Fig. 4.17) led to reconsideration of possible causes for the low temperatures recorded by these probes and the current working theory is that non-uniform fuel injection resulting from excessive displacement of the fuel manifold wall was also responsible for the non-uniformity in wall heating.

The fuel manifold inner wall can be approximated as a short, thick-walled cylinder fixed on one end. If non-uniform stresses are applied circumferentially, one can imagine the wall displacing inwards (towards engine centerline) at some points and outwards (away from engine centerline) at others. Because of its significant thickness, a gap between the injector insert and fuel injector housing could have opened up, or the corner of the wall could have impinged further into the copper injector insert. Where gaps had formed, fuel would have preferentially exited into the chamber via the gaps. Conversely, where flow area might have reduced, less fuel would be injected.

Unfortunately, increased fuel flow where leakage occurred could lead to two opposing effects:

1. Increased heat release due to increased reacting flow rate
2. Increased fuel film cooling due to greater fuel flow volume and reduced penetration into the GOX stream

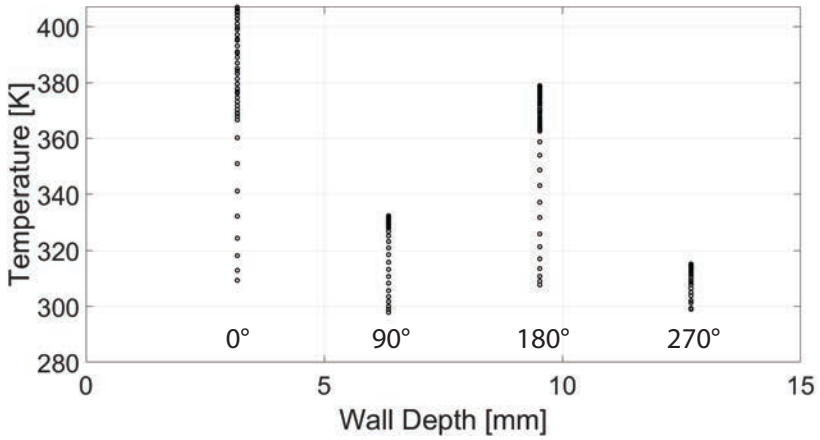

(a) Test 77, after presumed manifold leakage.

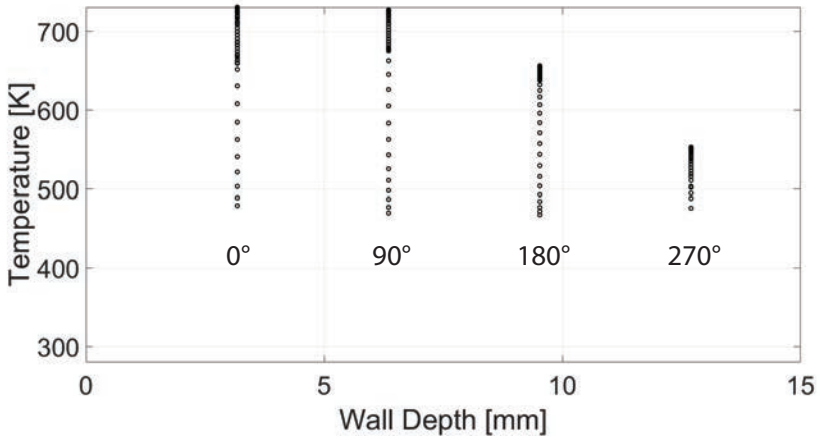

(b) Test 69, first test after hardware reassembly.

Figure 4.18. Trace of Group 7 thermocouple probe readings.

In some cases, high-speed videos revealed larger regions of combustion (based on image intensity) close to the 0° position, suggesting that the former was the more likely effect.

Another effect of the manifold wall deflection was the alteration of the GOX throat width. At a nominal width of 0.76 mm (0.030 in), any deflection of the manifold wall towards the engine centerline would significantly reduce GOX flow area and further offset the mixture ratio in the local region. Thus, the situation is further complicated. Insufficient evidence is available to ascertain the exact geometry of manifold wall deflection and the effect of propellant leakage/constriction, but there is little doubt that the deflection had been occurring throughout the tests.

4.5.3 High-frequency, High-amplitude Fluctuations in the Fuel Manifold

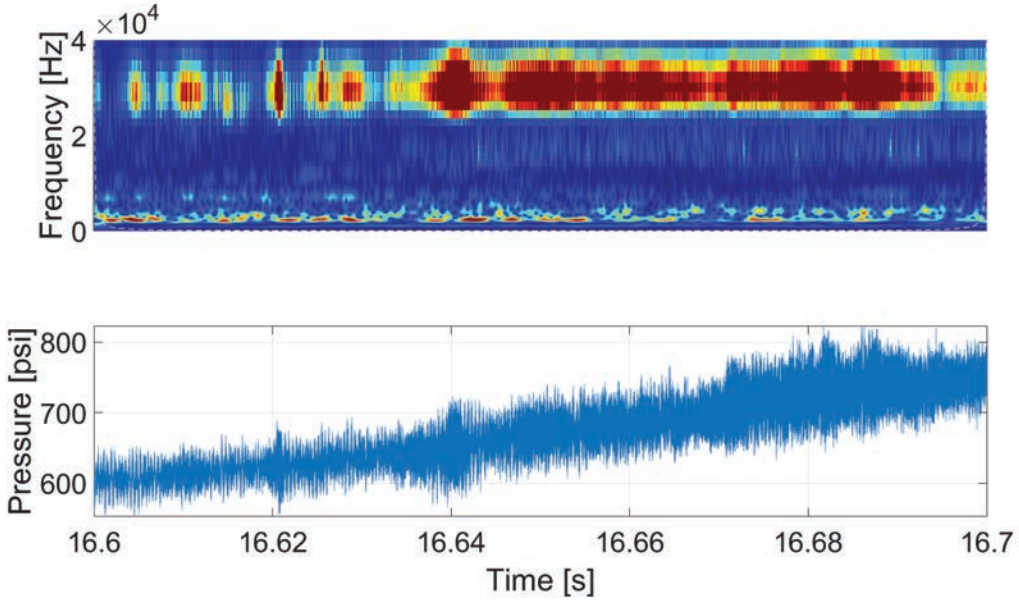

Figure 4.19. Continuous wavelet transform of high-frequency fuel manifold pressure from Test 60.

Performing continuous wavelet transform (CWT) analysis on high-frequency fuel manifold pressure data revealed that an azimuthal mode corresponding to the ro-

tational frequency of detonation waves is also present in the fuel manifold. In Fig. 4.19, a strong signal in the 30 kHz range dominates the frequency amplitude plot (top) and the corresponding peak-to-peak pressure fluctuations between 689 and 1,030 kPa (100 and 150 psi) is shown (bottom). In this test, the average recorded chamber pressure was 986 kPa (143 psia) and five stable detonation waves traveling at an average speed of 1,680 m/s (5,510 ft/s) were observed. The frequency corresponding to these measurements is 29.4 kHz – close to the observed signal.

Applying the same analysis to other test cases returns the same conclusion. Pressure fluctuations in the fuel manifold were of roughly equal magnitude to the average chamber pressure – vastly different from what one would expect in a constant-pressure combustor. While fluctuation magnitudes were high relative to average chamber pressure, they had clearly been heavily-attenuated across the injector. Earlier numerical simulations of the GOX manifold performed by Mikoshiba [67] suggested that shock reflections within the manifold could modulate mass flow rate in an annular injector. Evidently, flow associated with an RDE's injection system is highly-unsteady and much work is necessary in the optimization of manifold and injector designs.

4.6 Heat Flux

At the current stage of development, published data on rocket RDE heat transfer is still lacking. To the author's knowledge, the literature cited in Section 1.2 were the only instances where heat flux values were reported, and only two of the seven publications pertained to rocket RDEs. While the present study may contain large margins of error, it is hoped that the data and lessons learned on measurement techniques will benefit future researchers. Figure 4.20 has been reproduced here for the reader's convenience.

Before delving into the discussion, a disclaimer is necessary to inform the reader that caution is required in interpreting surface temperature measurements using thermocouple probes. Perfect thermal contact is impossible to achieve with current tech-

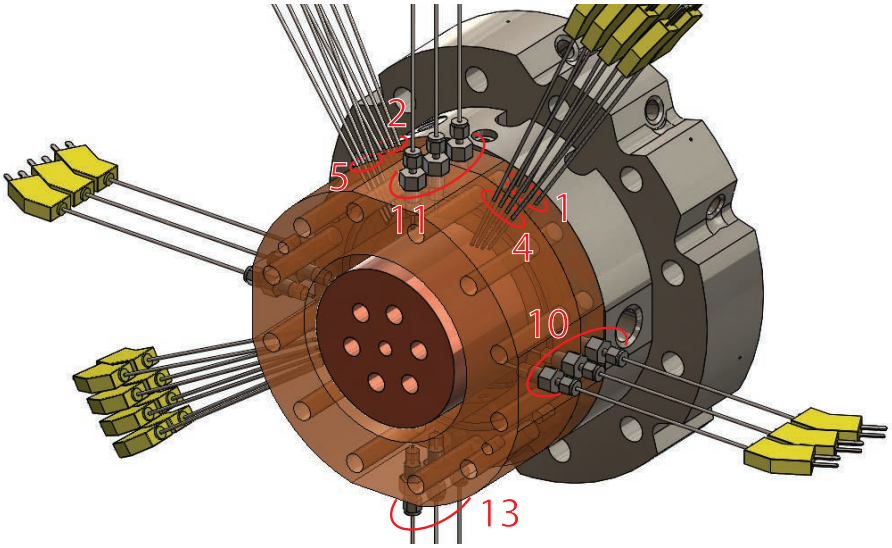

(a)

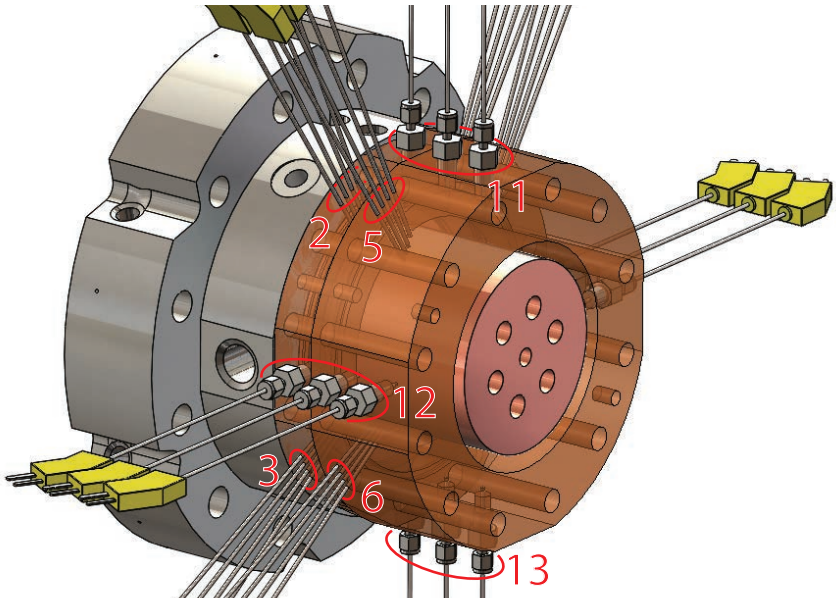

(b)

Figure 4.20. Views of chamber exterior indicating groups of thermocouple probes (reproduced from Chapter 2).

nology; there inevitably exists some amount of thermal resistance where a probe meets a solid surface whether or not a thermal compound is applied at the interface. The

extent of measurement error depends on the heat flux; a higher heat flux results in a greater deviation of measured temperature from the actual value and vice-versa. The pressure applied to the point of contact also affects the sensitivity of measurement: If a force is applied to push the probe junction against the surface to be measured, one can imagine that the material deforming ever so slightly to conform to microscopic surface imperfections on either part. Conversely, loss of contact happens when the applied force vanishes. In this case temperature change is detected indirectly through the change in temperature of the surrounding medium.

Additionally, temperature response will also be dampened by the capacitive effect of the medium surrounding the thermocouple probe. For the aforementioned reasons, wall temperature measurement and analysis presents one of the most challenging tasks in this study. Throughout the test campaign, a small number of thermocouple probes were also suspected to have lost proper contact with the wall surface due to a variety of reasons including thermal stress, engine vibration, and debonding of adhesive used in their mounting. Best efforts were employed to accommodate the affected measurements for the purpose of analysis.

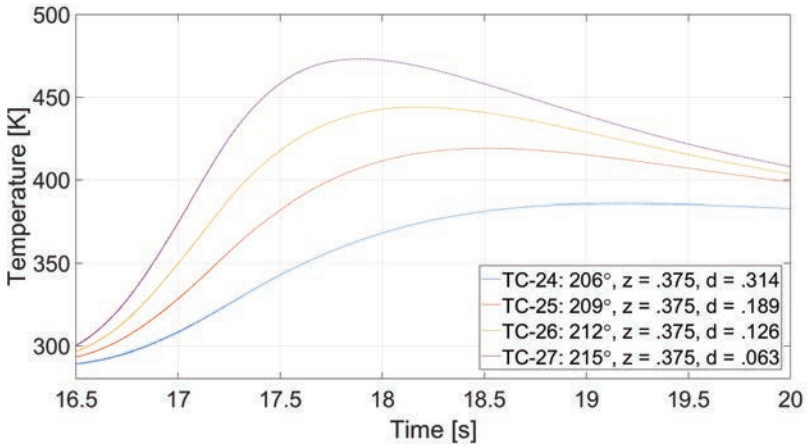

Figure 4.21. Test 78 wall temperature profile from Group 3 thermocouples. Axial station z and probe depth d are given in inches.

Figure 4.21 shows an example of wall temperature profile recorded by Group 3 thermcouple probes. In the hotfire autosequence, main chamber ignition was achieved at around 16.1 s and shutdown was complete shortly after 17 s. On the plot, recorded wall temperatures did not reach their peaks until well after 17 s. This delay is rather long considering the thermal diffusion time scale of the shallowest probe, which was calculated previously to be about 0.02 s. Undoubtedly, the long rise time of thermocouple probes (time constant of approximately 0.2 s) had a major impact on the lag in measurement.

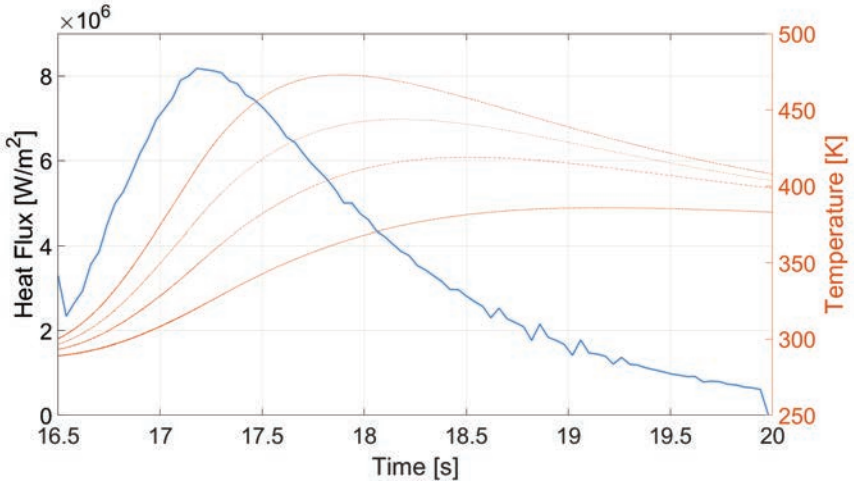

Figure 4.22. Test 78 wall heat flux profile overlayed with temperature profile from Group 3 thermocouples.

The plot in Fig. 4.22 overlays the computed heat flux with the same wall temperature profile shown in Fig. 4.21. The peak of the heat flux curve (blue), which occured at 17.2 s, coincides with the region of steepest temperature gradients in the wall (orange) as expected. Temperatures continued to rise after heat flux began decreasing until 17.9 s, when the shallowest point of measurement registered a decrease in temperature. By this time, nitrogen purge would have been flowing through the engine for roughly 1 s. However, the only heat transfer pathways that allow the thermocouple wires to cool to wall temperature were conduction back into the wall and

conduction to the quiescent air contained in the cavity, both of which possessed high resistance. Therefore, the thermocouples should respond to decrements in temperature more slowly than they would increments.

It was discovered that the contact between the thermocouple junction and wall surface varied among the probes. Consequently, some thermocouples responded less quickly and sensitively than others. However, given the large number of probes used, a good estimate of the heat flux produced during hotfire was still possible. A problem that surfaced while performing the heat flux computations was the difference between temperature gradients in the data and from 1-D conduction theory. In general, measured temperature profiles tended to be steeper than expected. Several likely explanations include

1. Surface contact resistance between thermocouple junction and wall
2. Axial and aziumuthal conduction
3. Geometrical features not included in numerical computation
4. Deviation from ideal material properties

It was understood that there would be a certain amount of contact resistance from dry contact due to surface imperfections at the microscopic level. However, even accounting for the added thermal resistance, gradient of the temperature profile was not expected to deviate significantly assuming 1-D conduction. Therefore, it is more likely that axial and azimuthal conduction were the cause of the unexpectedly steep temperature gradients. For example, if a point heat source were placed on a surface, the temperature of the surface in direct contact with the heat source would be the highest. Within the wall, conduction distributes the heat in all directions. Since the heat flux from the point source is non-uniform across the whole surface, the dissipation of heat to surrounding material in all directions causes the depth-wise temperature profile to be steeper than it would be if conduction only occurred in one dimension.

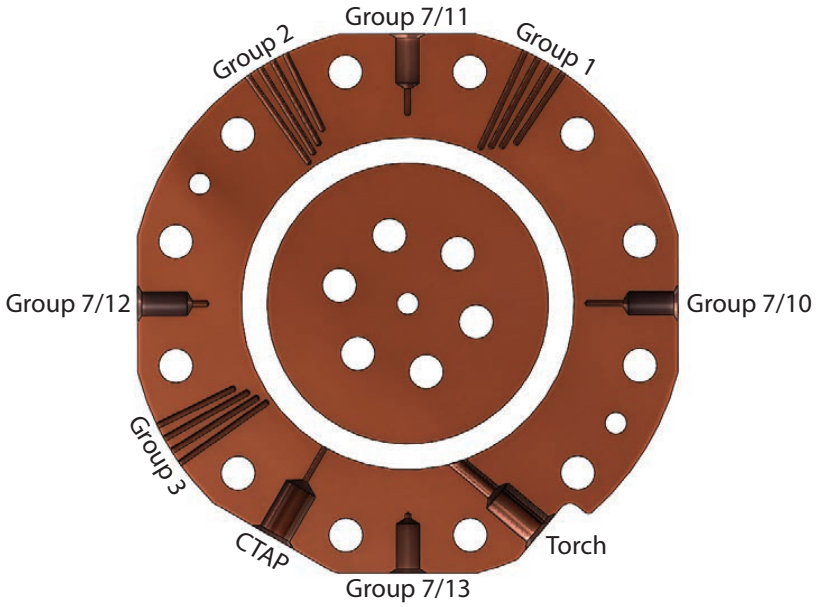

Figure 4.23. Section view of outer chamber igniter ring showing thermocouple probe locations in relation to igniter torch port (reproduced from Chapter 2).

From heat flux computations and analysis of temperature data, it was revealed that heat release in the chamber varied both axially and azimuthally. It is possible that due to transient manifold filling and mounting angle of the engine that a fuel mass flow bias was present during tests, especially so in low flow cases where manifold volume was significant relative to volumetric flow rate. During the lowest mass flow cases using the 0.20 mm (0.008 in) injector (Tests 39 through 46), head end temperature profile showed strong bias towards the 6 and 9 o'clock region. The 9 o'clock position corresponds to one of the fuel manifold inlets and the 6 o'clock position favors fuel flow due to gravity. The temperatures in these positions had the tendency to rise sooner than the other two positions although the probes were furthest away from the wall surface. There is a distinct possibility that the early temperature rise in the 6 o'clock position could be due to internal conduction from torch ignition, but

the 9 o'clock position is further from the torch passage and influence was expected to be minimal.

At similar mass flow rates utilizing the larger 0.28 mm (0.011 in) injector, head-end temperature at the 6 o'clock position actually showed *decreasing* temperature while temperature at other locations continued to increase. This would be possible only if there were a high volumetric flow of unburned propellants absorbing heat from the wall originally imparted by the torch igniter exhaust. Since the phenomenon was particularly severe for these cases, pooling of fuel at the low manifold flow speeds was very likely. Clearly, the heat flux entering the wall was non-axisymmetric. There is also evidence which suggests that the axial location of highest heat flux was influenced by the apparent stability of detonations: It appeared that decreasing stability was accompanied by a downstream shift in the peak heat release zone – this shall be discussed in more detail in a later section. This suggests that non-uniform axial heat flux also existed in the engine.

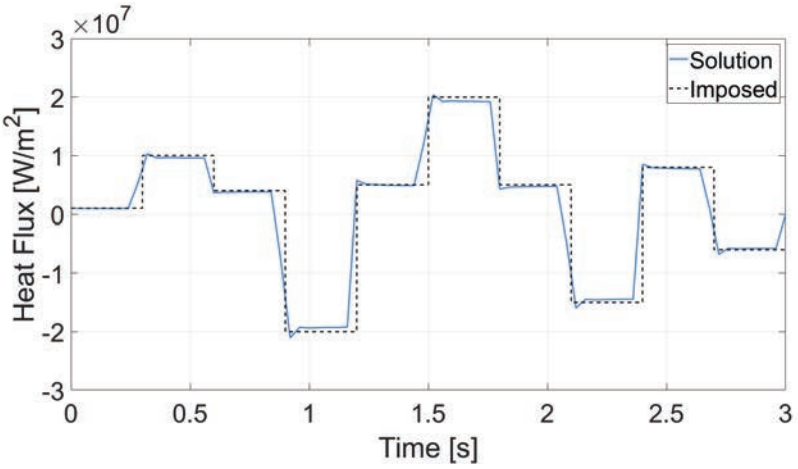

Figure 4.24. Heat flux solution with higher-than-assumed wall thermal conductivity (coefficient of 1.1).

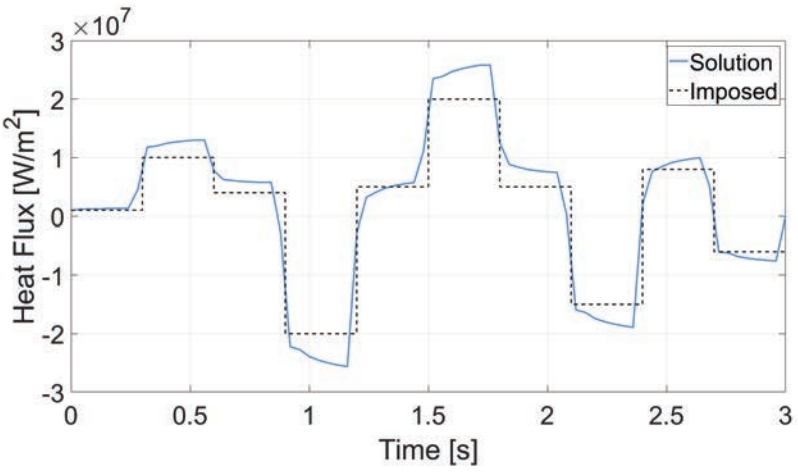

Figure 4.25. Heat flux solution with lower-than-assumed wall thermal conductivity (coefficient of 0.5).

A steeper temperature gradient implies lower-than-assumed effective heat diffusivity of the system comprising wall material, surface contact discontinuity, and thermocouple wires themselves. An investigation on the effects of actual thermal diffusivity on the heat flux solution using an assumed diffusivity value was conducted using the step change heat flux profile used to verify the inverse heat transfer solver discussed in Section 2.2.6. A coefficient was multiplied to thermal diffusivity during the creation of the target temperature profile; a value greater than unity represents thermal diffusivity that is higher than expected while a value between zero and unity signifies that it is lower than expected.

In the inverse heat transfer solution, the coefficient was set to unity to represent ideal properties. Figures 4.24 and 4.25 show the outcomes of the investigation. It is readily apparent that in both cases, the solution was unable to capture the correct value of applied heat flux. However, temporal details were still captured adequately. Most importantly, Fig. 4.25 shows that when the actual thermal diffusivity of the system is lower than assumed (as is the case with the hotfire tests), the solution overshoots actual values in both directions. This indicates that some conservatism would be added to the heat flux solutions.

4.6.1 Influence of Number of Waves on Heat Flux

One of the questions of interest at the time of writing was how the number of waves present affects wall heat flux. In an ideal detonation, the shock front is followed by its coupled reaction zone which imparts heat to the chamber walls. Since the heat release is localized, one should expect a non-uniform heat flux distribution, presumably similar in profile to the detonation wave's pressure distribution. It would follow that keeping all other conditions constant, a greater number of detonation waves would result in a higher heat flux as the chamber wall is traversed by a larger number of heat release zones per unit time.

A large majority of the tests performed throughout the test campaign resulted in four or five rotating detonation waves, therefore somewhat limiting the capacity for testing the hypothesis. However, there were several cases where the number of waves differed appreciably for similar flow rates, providing opportunities for comparison. The test pairs compared were chosen to have similar mass flow rate and apparent detonation stability so as to minimize the number of other variables that could influence heat flux. Table 4.2 highlights some of the test conditions associated with tests 59 and 80, which had the greatest difference in the number of detonation waves.

It is apparent from the table that the heat flux values vary at different engine locations for the two cases. Aside from the hot spots in Test 80 (Groups 3 and 6, which correspond to the same azimuthal station), the rest of the measurements were comparable in both tests despite the number of waves differing by a factor of 2. Two other test pairs were examined for differences in heat flux: 41 and 45, and 48 and 50. In tests 41 and 45, detonations were very unstable and numbers varied from one to five and three to seven respectively. Although the number of detonations varied throughout the data window, their computed heat flux profiles did not show significant differences from those with less variable wave counts. Peak heat flux values in both tests were also highly similar. Tests 48 and 50 produced five and four stable detonations respectively and like the other pairs examined, heat flux levels

Table 4.2. Conditions and configurations associated with tests 59 and 80.

	Test 59	Test 80
Mass flow rate [lbm/s (kg/s)]	2.96 (1.35)	3.02 (1.37)
Equivalence ratio, ϕ	1.03	1.00
Injector groove width [in (mm)]	0.011 (0.28)	0.011 (0.28)
No. of grooves	120	180
No. of waves	6	3
Group 1 peak heat flux [MW/m^2]	3.4	3.4
Group 2 peak heat flux [MW/m^2]	5.7	4.7
Group 3 peak heat flux [MW/m^2]	5.6	7.3
Group 4 peak heat flux [MW/m^2]	3.3	3.7
Group 5 peak heat flux [MW/m^2]	4.0	3.4
Group 6 peak heat flux [MW/m^2]	5.3	6.4
Group 7 peak heat flux [MW/m^2]	5.7	6.0
Group 8 peak heat flux [MW/m^2]	5.0	5.9
Group 9 peak heat flux [MW/m^2]	3.9	3.9

were essentially equal. Calorimetry measurements on a water-cooled chamber would be highly desirable here in order to assess overall heat loads given the sparcity of the thermocouple measurements.

Given this caveat, Fig. 4.26 is a plot of average specific peak heat flux against average number of waves. Head end values were computed with temperature data from Group 1, 2, and 3 thermocouple probes and chamber midsection heat fluxes were from Groups 4, 5, and 6. The average was simply calculated as the mean of the three peak values at each axial station. It was then divided by total chamber mass flow rate to give specific average heat flux. The plot shows a lack of any discernible relation between heat flux and wave count, especially given the number of variables

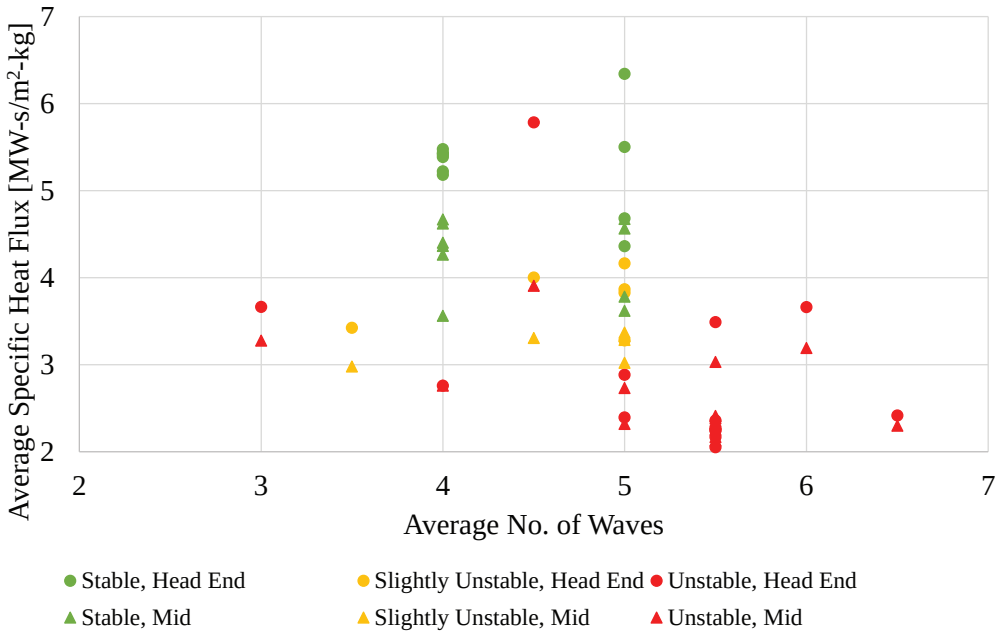

Figure 4.26. Average specific peak heat flux vs. average number of detonation waves.

and uncertainties resulting from leakages in the fuel injector. It may be tempting to claim that having four to five waves results in the highest heat fluxes, or that four to five waves were stable operating points for the engine, but there is a lack of evidence to further substantiate causality. Most of the tests that displayed unstable wave behavior were affected by non-uniform fuel injection and it is impossible to isolate those effects from the number of waves present.

4.6.2 Influence of Apparent Wave Stability on Heat Flux

The axial distribution of temperature measurements allows one to ascertain the rough location of detonation waves by computing heat flux at different axial stations. There is evidence to suggest that detonations that exhibit high speed and regular spacing are associated with highest heat flux at the head end of the chamber while lower-speed and irregularly-spaced detonations have peak heat release zones displaced

further downstream. Figure 4.27 shows wall temperature profiles of three different hotfire tests logged by Group 10 thermocouples whose axial locations and depths are indicated. The mass flow rate, equivalence ratio, number of waves, and wave stability are summarized in Table 4.3 for convenient comparison. Note that Test 89 was an auxiliary test in which a fuel additive resulted in the engine operating in deflagrative mode.

Table 4.3. Summary of operating conditions for Tests 62, 78, and 89.

Test ID	Mass flow rate [kg/s (lbm/s)]	Equivalence ratio, ϕ	No. of waves	Wave stability
62	1.35 (2.96)	1.04	5 to 6	Unstable
78	1.24 (2.72)	1.72	4	Stable
89	1.31 (2.87)	1.32	0	N/A

Beginning with Test 78 (circle markers) which displayed stable detonations, there is a clear decrease in peak temperature with increasing distance from the head end (blue > red > yellow) suggesting that the main heat release zone resided close to the chamber head. Additionally, peak temperatures were also significantly higher than the other two tests. Intermediate temperature levels were recorded in Test 62 (square markers). Unlike the axial distribution seen in Test 78, the highest temperature was recorded around the midsection of the chamber (red > blue > yellow). From the blue and yellow curves, it appears that the bulk of heat release occurred between $z = 0.375$ and $z = 1.125$ with more bias towards $z = 1.125$. Similarly, temperature distribution in Test 89 suggests combustion predominantly taking place between $z = 0.375$ and $z = 1.125$ with bias towards $z = 1.125$. The temperature curve at $z = 0.375$ (blue) may be noticed to have started at a higher temperature than the two others and could have been caused by startup transients involving flame anchoring close to the

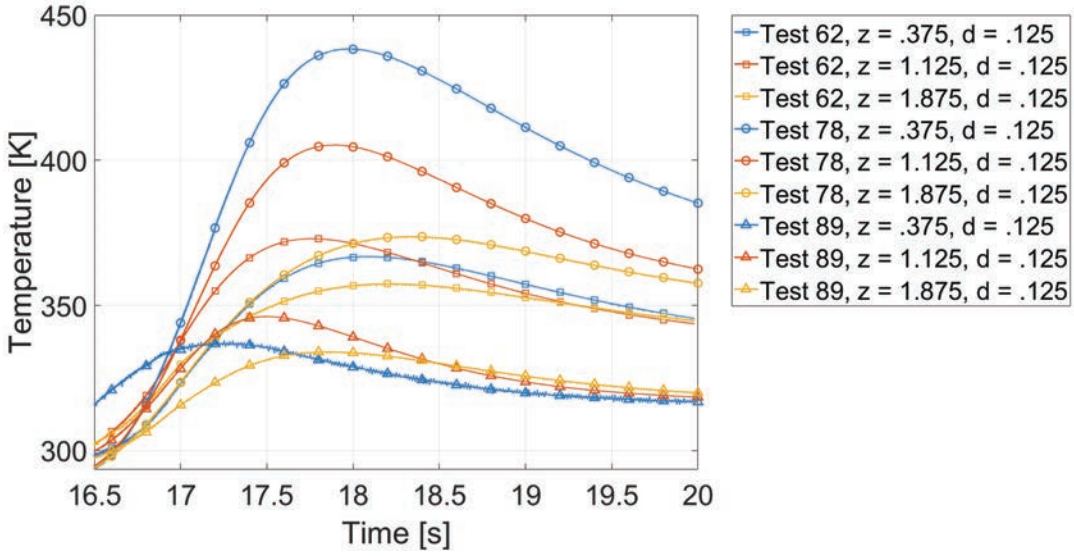

Figure 4.27. Axial distribution of wall temperature profiles for three tests exhibiting different detonation behavior. Thermocouple axial station z and depth d shown in inches.

injector. As fuel injection ramped up (unintended effect due to manifold fill), the flame front likely shifted downstream.

Considering the plot as a whole leads to two hypotheses: Firstly, that heat flux correlates with detonation stability. Test 78 produced the highest wall temperatures despite Test 62 having a higher mass flow rate and also greater number of waves. Test 89 did not produce any detonations and consequently had the lowest wall temperatures. The second hypothesis is that the axial location of highest heat flux depends on the stability of detonation, as discussed in the previous paragraph.

There is a logical reasoning to accompany the hypothesis: A stable (presumably an indicator of strength) detonation is able to cause better propellant mixing by baroclinic torque through a steep pressure gradient, therefore reducing mixing length and allowing the detonation to reside closer to the injectors. An unstable or weak detonation is unable to produce the same level of mixing, therefore additional time is required for fuel droplet breakup and vaporization before detonation can be sup-

ported. Deflagration does not produce strong pressure gradients so baroclinic torque is essentially negligible and mixing is limited by droplet breakup, vaporization, and diffusion, which causes an even further downstream shift of the main heat release region.

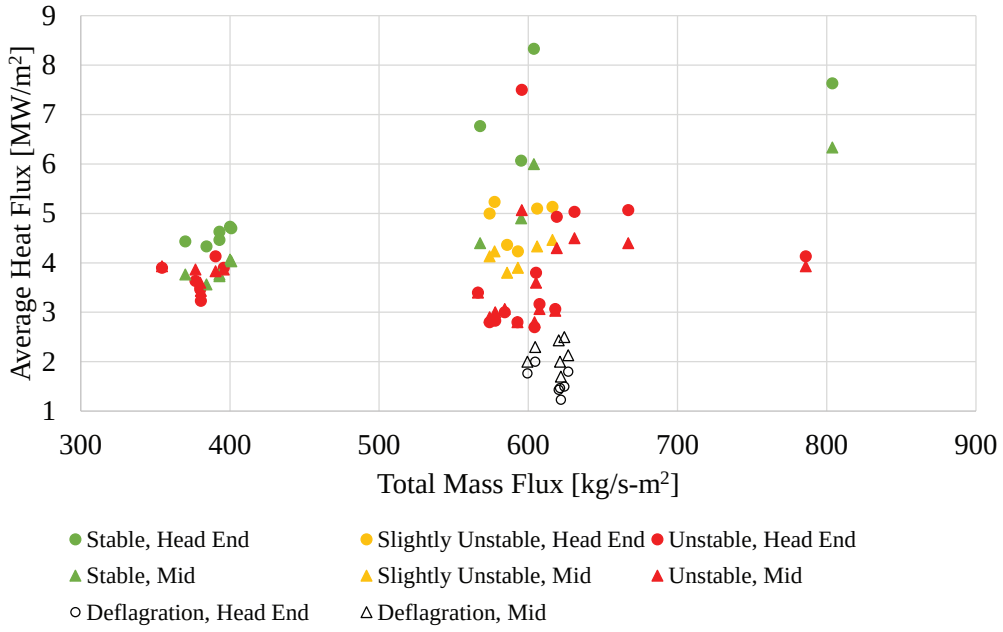

Figure 4.28. Average heat flux vs. total chamber mass flux at engine head end and midsection.

Figure 4.28 is a plot of average peak heat fluxes recorded by groups 1 through 6 thermocouple probes against total chamber mass flux. A relation between mass flux and heat flux is not readily apparent. However, the classification of data by detonation stability reveals some noteworthy features:

1. There exists a general separation between points corresponding to stable, almost stable, unstable detonation, and deflagration. For tests of similar mass flow rates, heat flux appears to increase with detonation stability, with deflagration producing the lowest recorded wall temperatures. Heat fluxes for all detonation cases (stable, slightly unstable, and unstable) greatly exceed those

for deflagrative combustion. This observation has been made empirically many times in the rocket community as numerous conventional combustors have been destroyed when tangential mode instabilities appear. The increased chamber heat loads must be accounted for in order to successfully develop RDE combustors. However, it is important to note that this applies only where gas transport properties are constant, as shall be discussed in Section 4.6.3.

2. Where stable detonation is concerned, heat flux was always highest at the head end. With decreasing detonation stability and absence of detonation, the axial temperature variation suggests that the heat release zone was displaced downstream.

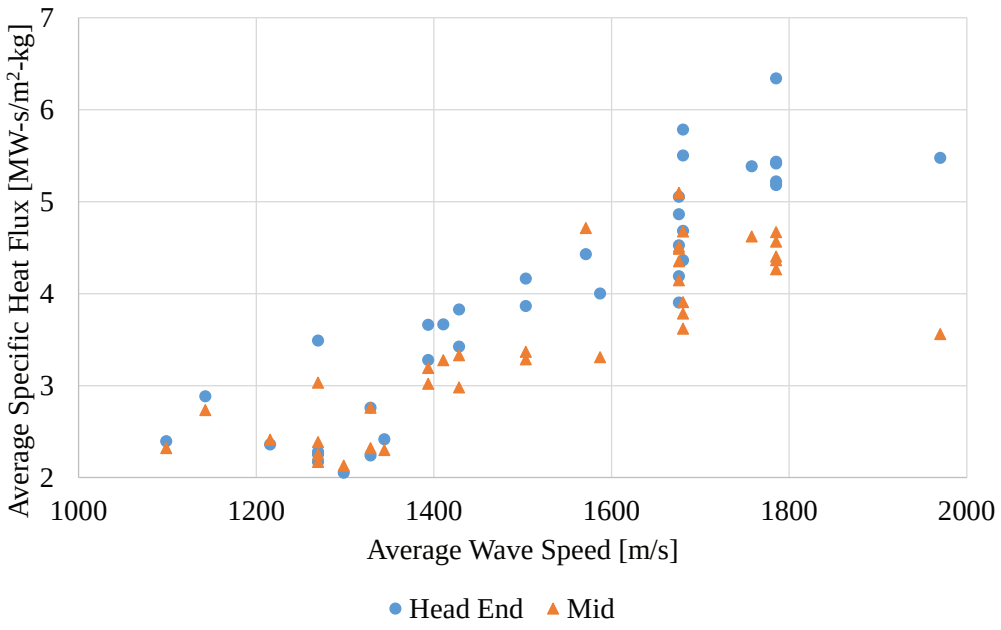

Figure 4.29. Average heat flux vs. average detonation speed at engine head end and midsection.

It was previously mentioned that detonation wave speed serves as a measure of detonation strength. In Fig. 4.29, normalized heat flux was plotted against average detonation speed for all tests. The difference between heat flux at the head end (blue

circles) and midsection (orange triangles) appears to increase with increasing wave speed. It is conceivable that the trend could be related to the rate at which propellants were mixed: When propellants mixed quickly over a short distance (relative to the injection plane), strong detonations with high velocities could be supported. On the other hand, when mixing was poor, the propellants would have traveled a further distance downstream before attaining the minimum level of mixedness required to support detonation.

The data also shows considerable linear correlation, but whether the increased heat flux was due to increased heat release by propellants or increased convection remains to be uncovered. Nevertheless, the above results are useful for designing the cooling system of an RDE. Extrapolation towards C-J velocity provides an estimate of the heat flux to be expected. Additionally, knowing the most likely location of the heat release zone allows the most aggressive cooling, which typically implies greatest pressure loss, to be targeted only at specific regions to minimize pressure loss.

4.6.3 Comparison with Bartz Relation

Prior to commencement of the RDE v1.4 hotfire test campaign, expected heat flux was estimated for a nominal flow rate of 1.3 kg/s (2.9 lbm/s) at 1.03 MPa (150 psia) using the Bartz relation for convective heat transfer. Because of the high flow speed expected in the RDE chamber, the problem was treated as nozzle throat flow ($M = 1$) in a constant-pressure combustor. Stoichiometric product gas properties were obtained from NASA CEA using the rocket problem solver. While NASA CEA is capable of performing C-J detonation calculations, the reaction zone of a detonation is thin and travels supersonically such that post-detonation gas properties only exist for a fraction of the interval between detonation waves and using these properties in a steady-flow calculation will result in gross overestimation of heat flux.

To investigate differences in gas properties between C-J detonations and constant-pressure combustion further, the appropriate equivalent inputs for NASA CEA are

required. To elaborate, if the target average chamber pressure of an RDE were to be 1 MPa, the input pressure for the detonation problem would need to be somewhat lower or gas properties will be overestimated. The method for acquiring the initial pressure for a detonation computation in NASA CEA is identical to the method discussed in Section 4.1 where minimum chamber pressure in the RDE was estimated. The equation can also be used in reverse to estimate the average pressure of a detonation wave when provided with the minimum pressure and detonation pressure ratio. Again, the reader is reminded that the assumptions hold large amounts of uncertainty.

Stoichiometric detonations and deflagrations were computed for methane, ethane, propane, and n-decyl ($C_{10}H_{21}$) with oxygen for pressures equivalent to detonation at 1 atm according to Eq. 4.1. The results have been graphed in Fig. 4.30. Orange squares and blue circles have been used to represent detonation and deflagration properties, while filled and open markers denote equilibrium and frozen conditions respectively.

While burned gas pressure and density were vastly different between detonation and deflagration, specific heat and thermal conductivity were very similar. Liquid hydrocarbons were not considered because NASA CEA has not been programmed to compute detonations when condensed phases are involved. This presents a problem since the fuel used in hotfire tests was RP-2. Chemical equilibrium programs that accept condensed phase propellants do exist, but tend to be subject to export control regulations, and are therefore not as readily accessible. Nonetheless, the similarity in detonation and deflagration properties demonstrated in Fig. 4.30 suggests that the means of obtaining gas properties from NASA CEA does not matter greatly.

Figures 4.31(a) and 4.31(b) show the vast difference in heat transfer characteristics resulting from using equilibrium and frozen product gas properties respectively. Four temperature curves are displayed on the wall temperature profile plot: The solid blue and red lines represent the head end temperature profiles of the centerbody and outer wall respectively, and dashed lines are used for the aft end. As a reference, the

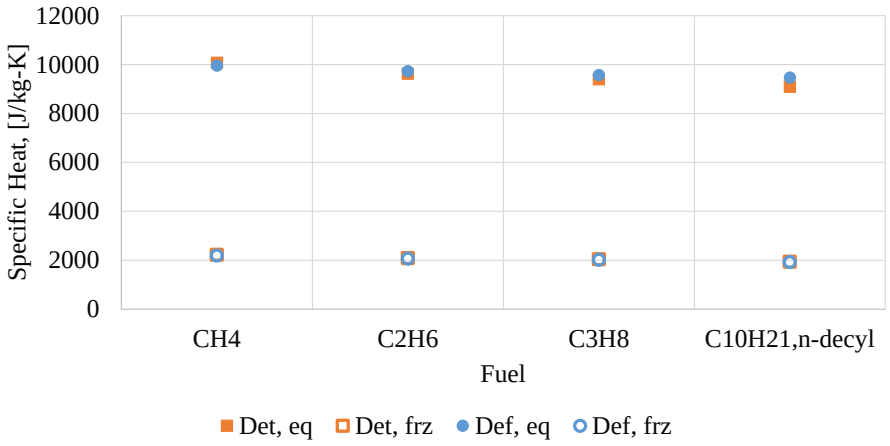

(a) Specific heat

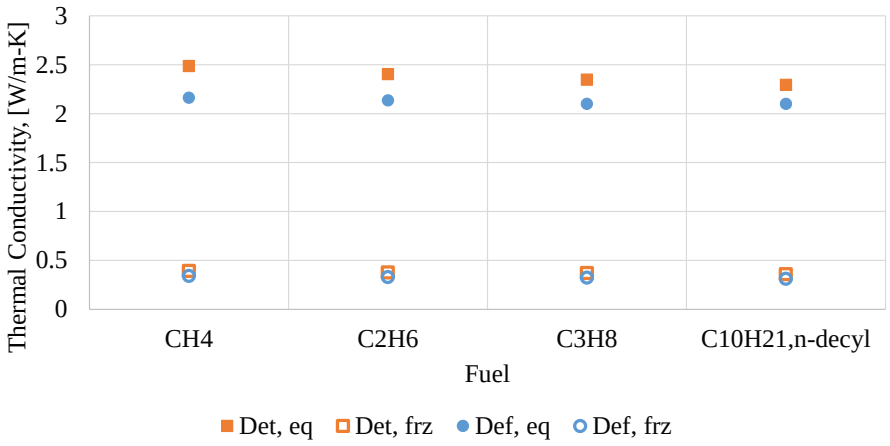

(b) Thermal conductivity

Figure 4.30. Equilibrium and frozen transport properties for detonation and deflagration of hydrocarbon fuels of various lengths with oxygen at stoichiometric ratio.

melting temperature of the copper used for engine components have been included as the black dashed line.

Using equilibrium properties (Fig. 4.31(a)), substantial portions of the chamber walls are well above the melting point of copper. Heat flux begins slightly above 100 MW/m^2 and decreases to a little over 40 MW/m^2 at the end of the one-second duration due to the decreasing temperature difference. From experimental observation,

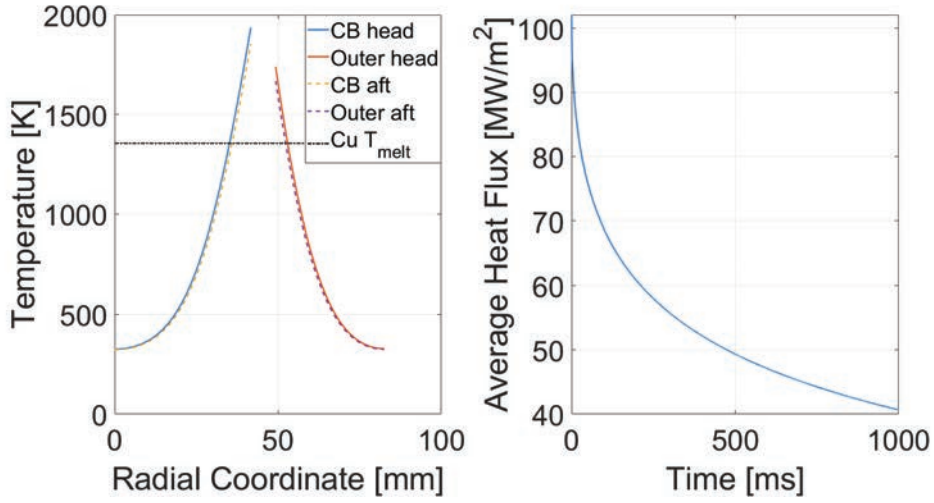

(a) Equilibrium gas properties

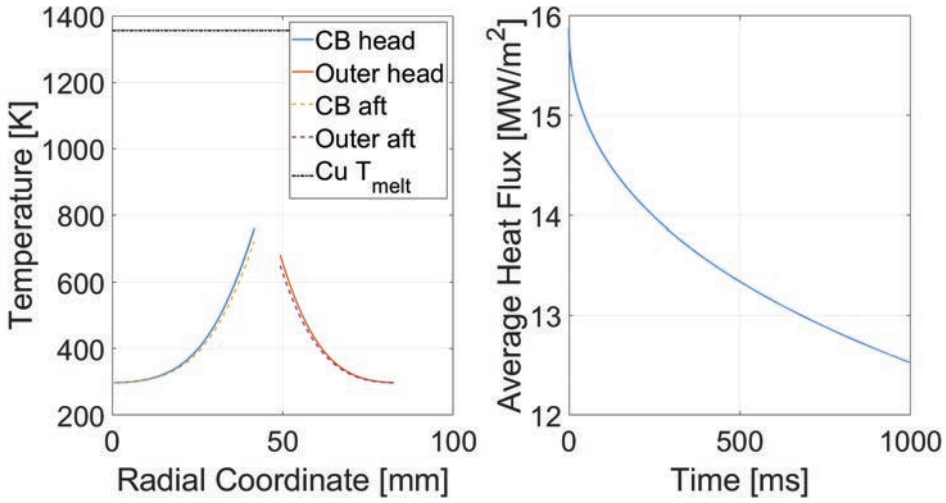

(b) Frozen gas properties

Figure 4.31. Wall temperature profile (left) and heat flux (right) for 1-s burn of stoichiometric RP-1 and oxygen at 690 kPa (100 psia).

the engine hardware incurred little visible thermal damage aside from discoloration after multiple firings in all but one test. The only instance of confirmed heat damage was Test 85, where total flow rate was increased to 3.49 kg/s (7.67 lbm/s), which re-

sulted in substantial melting of the centerbody components (Fig. 4.39(a)) and slight melting of the outer wall surface.

The heat flux computed from frozen gas properties (Fig. 4.31(b)) is three to six times lower, and wall surface temperatures are well below melting point. The highest recorded heat flux and wall temperatures from hotfire tests with similar flow rates match much more closely with the latter case. This also goes in agreement with Stechmann's use of frozen gas properties in his estimation of heat flux produced in the RDE v1.3 tests [15].

The use of frozen chemistry may be justified by the chamber residence time in the RDE: Constant-pressure engines burning oxygen and kerosene have typical characteristic length (L^*) values in the 50- to 130-centimeter range (20 to 50 in) to give reactants sufficient time to approach equilibrium for maximum performance. The RDE in discussion has an L^* of merely 7.3 cm (2.9 in) – an order of magnitude lower – so one may expect the product gas to have attributes closer to the frozen end of the spectrum by the time it reaches the exit plane. While the revelation on gas composition and properties alleviates some of the challenges associated with cooling a rocket RDE, it also implies a possible loss in combustion efficiency or specific impulse since the product gas would have left the engine before approaching chemical equilibrium.

4.7 Comparison of RDE Heat Flux with Throat Heat Flux of a Hypothetical Constant-pressure Engine

The prediction of throat heat flux in a constant-pressure combustor is commonly via the Bartz relation. The Bartz relation listed in NASA SP-125 [14] modified for use with *SI units* is given by

$$h_g = \left[\frac{0.026}{D_t^{0.2}}\left(\frac{\mu^{0.2}c_p}{Pr^{0.6}}\right)_{ns}\left(\frac{P_{c,ns}}{c^*}\right)^{0.8}\left(\frac{D_t}{R}\right)^{0.1}\right]\left(\frac{A_t}{A}\right)^{0.9}\sigma \tag{4.14}$$

where h_g is the heat transfer coefficient, D_t is the nozzle throat diameter, μ, c_p, Pr, and c^* are the dynamic viscosity, specific heat capacity, Prandtl number, and characteristic velocity of the product gas respectively, P_c is chamber pressure, R is

the mean radius of curvature at the throat, A_t is the cross sectional area of the throat, A is the cross sectional area of the engine section in question, and σ is a correction factor for property variations across the boundary layer, and is calculated as follows:

$$\sigma = \frac{1}{\left[\frac{1}{2}\frac{T_{wg}}{T_{c,ns}}\left(1+\frac{\gamma-1}{2}M^2\right)+\frac{1}{2}\right]^{0.68}\left[1+\frac{\gamma-1}{2}M^2\right]^{0.12}} \tag{4.15}$$

where T_{wg} is the local gas-side wall temperature, T_c is the chamber temperature, γ is the ratio of specific heats of the gas, and M is the flow Mach number. The subscript ns denotes nozzle stagnation conditions.

Finally, the heat flux $\dot{q}$ is calculated via

$$\dot{q} = h_g\left(T_{aw} - T_{wg}\right) \tag{4.16}$$

where adiabatic wall temperature $T_{aw} = T_{c,ns}\times$(turbulent boundary layer recovery factor ranging from 0.90 to 0.98). For simplicity, the average of the range, 0.94, will be used for calculations.

The product gas properties μ, c_p, Pr, and γ can be obtained from NASA CEA for the relavant operating parameters. Equations 4.14 and 4.15 were applied to a theoretical ideal constant-pressure combustor whose throat area is identical to the annular area of RDE v1.4, or 21.8 cm^2 (3.37 in^2). The equivalent throat diameter is 5.26 cm (2.07 in). The radius of curvature of the throat was arbitrarily made equal to the throat radius, which is 2.63 cm (1.04 in). The gas-side wall temperature was chosen to be half of copper's melting temperature, 678 K (761 °F).

Figure 4.32 shows the results of the above computation. The ideal chamber stagnation pressure on the horizontal axis is the same used in Fig. 4.10 to normalize CTAP values. It can be immediately seen that the heat flux values estimated for the RDE are approximately an order of magnitude lower than those calculated using equilibrium gas properties and about a factor of 2 different from calculated values using frozen properties. It was mentioned in Section 2.2.7 that the derived heat flux values for the RDE were expected to be close to 60% lower than true values due to long thermocouple response times. Even so, the heat flux in the RDE come nowhere

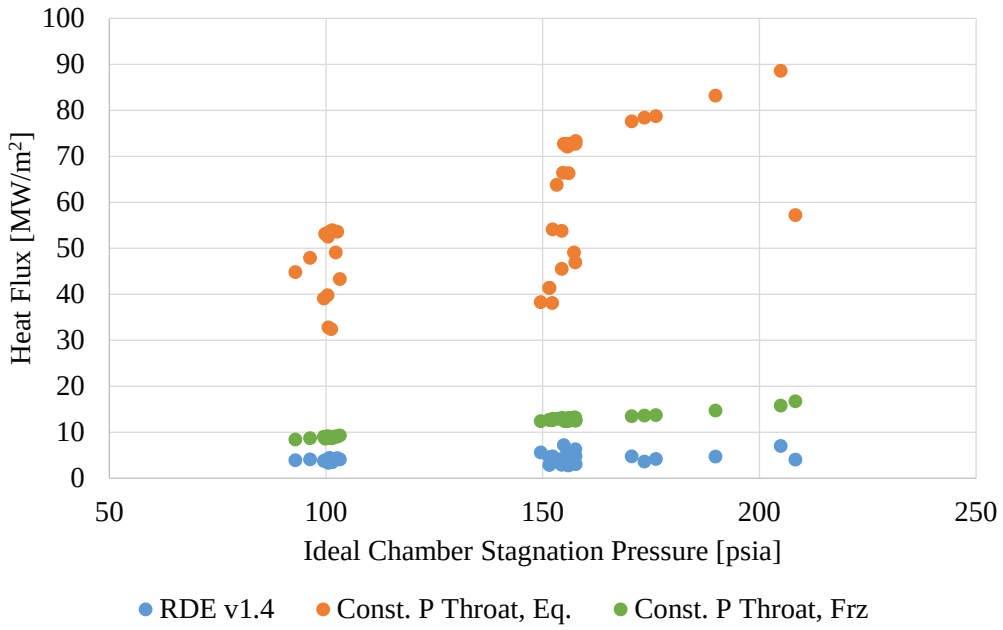

Figure 4.32. Comparison of estimated average heat flux in RDE v1.4 with computed hypothetical constant-pressure combustor throat heat flux using equilibrium and frozen gas properties.

close to the equilibrium throat values. The comparison to throat heat flux computed with equilibrium properties is more realistic since constant-pressure combustors are usually designed to allow gas composition to approach equilibrium.

However, the thermal load that the cooling system is required to remove from the wall is a function of wall surface area. To further simplify the comparison, wetted perimeter can be used to normalize thermal load in both types of engines. Although the RDE and hypothetical combustor have identical throat areas, their wetted perimeters are drastically different: RDE v1.4 has an outer wall and centerbody that require cooling, and the total wetted perimeter of both components sum to 57 cm (22.5 in). The hypothetical combustor, on the other hand, has a throat perimeter of only 16.5 cm (6.5 in). Multiplying heat flux with wetted perimeter produces a linear heat load, or heat load per chamber section length.

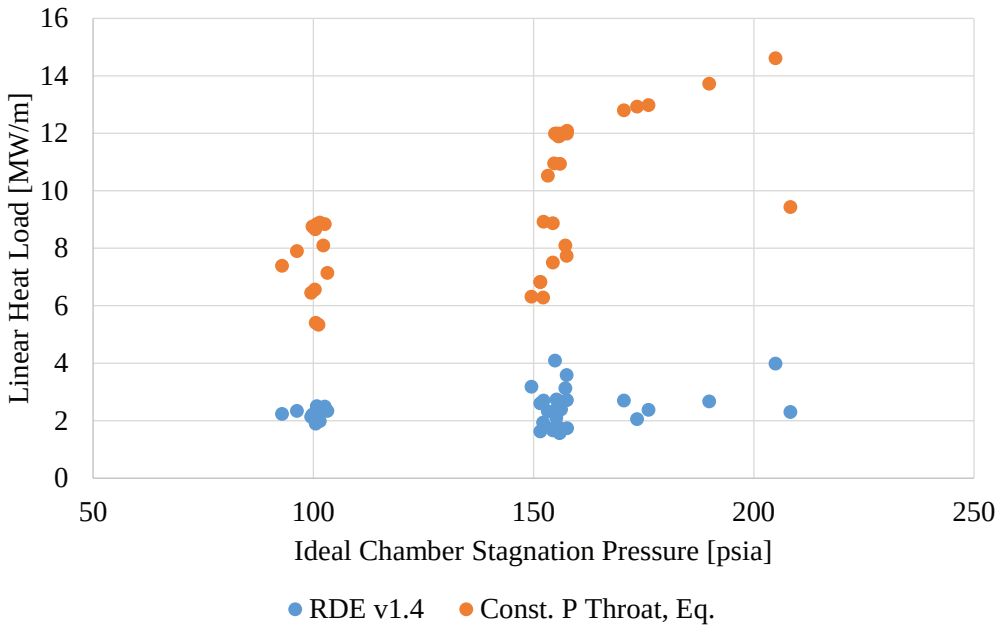

Figure 4.33. Comparison of estimated linear heat load in RDE v1.4 with hypothetical constant-pressure combustor throat using equilibrium gas properties.

Figure 4.33 compares the resultant linear heat loads for the two engine geometries. While the throat heat flux of the hypothetical combustor was an order of magnitude higher than that of the RDE, accounting for the wetted perimeter reduces that difference by half. It first appears that the RDE would be advantageous for its comparatively benign linear heat load, but the axial distance over which this linear heat load applies has yet to be accounted for. In the conventional combustor, the distance is small; only across the throat region. However, it encompasses the entire chamber length in an RDE.

In this example, the hypothetical throat has a radius of 2.6 cm. Suppose that flow area remains almost constant over 60° of the throat curvature such that heat flux or linear heat load is essentially constant. This results in a linear heating distance of 2.7 cm (1.1 in). For RDE v1.4, chamber length was 7 cm (2.75 in). The results are plotted on Fig. 4.34. After accounting for the total wetted surface area, the heat

loads in each geometry are much more similar. If a factor of 1.6 were to be applied to the values for the RDE to account for the estimated error, the RDE would end up with a higher heat load on the chart. However, the figures for the hypothetical throat only apply to the throat – the rest of the chamber has yet to be accounted for. Even though heat flux will be lower in the chamber, surface area is large. Ultimately, total heat load from chamber head to throat for the constant-pressure combustor is expected to be comparable to or higher than that of the RDE.

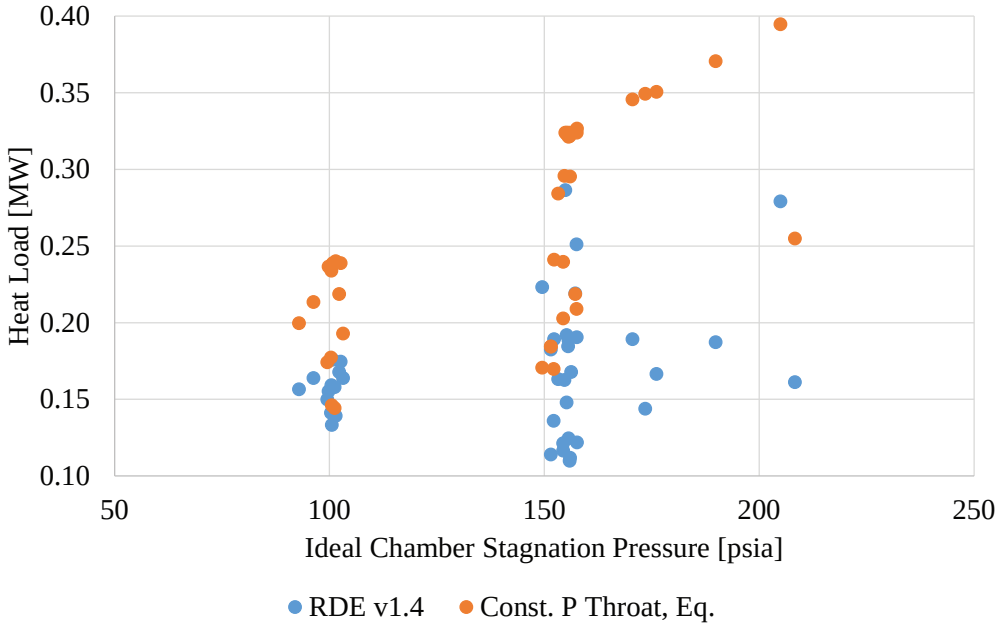

Figure 4.34. Comparison of estimated total chamber heat load in RDE v1.4 with hypothetical constant-pressure combustor throat using equilibrium gas properties.

The ratio of estimated heat flux in RDE v1.4 to that of the constant-pressure throat is shown in Fig. 4.35. The values range from 0.34 to 1.31 with a large majority being less than unity. In addition, not all tests with ratios greater than unity were ones that produced stable detonations. However, in agreement with the discussion on heat flux in prior subsections, there is some positive correlation between detonation stability and the value of this ratio.

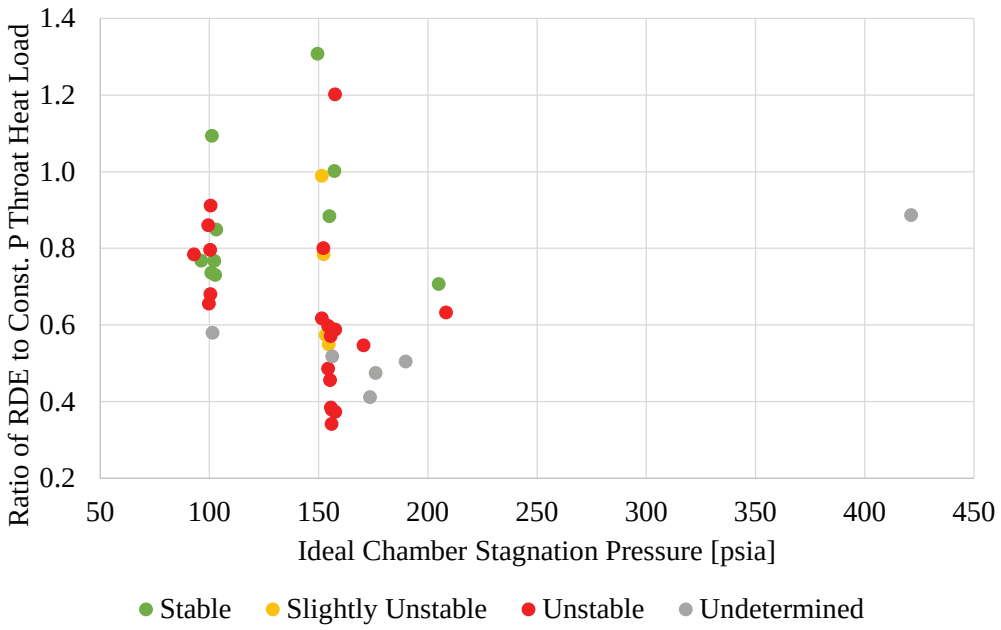

Figure 4.35. Ratio of total chamber heat load in RDE v1.4 to hypothetical constant-pressure combustor throat using equilibrium gas properties.

Since the above comparison was made between a non-ideal RDE and an ideal hypothetical combustor, the reader is advised to interpret the findings with a grain of salt. The discussion does not include cooling passage routing considerations, which will certainly be more challenging in an annular combustor. Nevertheless, the preliminary thermal load analysis places RDE thermal management in a positive light.

4.8 Hardware Damage

Test hardware was visually inspected in between hotfire tests to verify that there was no sign of critical material failure. Initial hotfire tests were performed with the 008×120 injector for its high pressure drop at very low flow rates. Aside from slight discoloration, no damage was observed on any engine component by the end of the test series involving this injector. Subsequent tests at higher mass flow rates would employ the larger injectors to reduce manifold pressure. With the larger injectors,

minor pitting damage on the injector ring and outer wall ignitor ring was observed as early as after a single test. However, it appeared to be superficial and non-critical.

Interestingly, while the heat damage documented by Stechmann during early tests with hydrogen was located directly downstream of injection orifices and associated with flameholding [15], the damaged areas on the kerosene injectors and igniter ring were within the spaces between injection slots as shown in Fig. 4.36. It is possible that the distribution of damage was related to the mixing process of the liquid fuel in oxidizer crossflow. The RP-2 spray likely turned and formed a film on the surface shortly after being injected. The emergent jet posed as an obstruction to the oxygen flow, channeling the latter towards the space between each fuel slot where the accelerated gas stripped away most of the fuel leaving a boundary layer film on the wall. Here the oxygen was able to mix with the thinned, relatively slower-moving film of RP-2 such that condensed phase detonation on the solid surface is not outside the realm of possibility.

The rough, pitted surface suggests that very localized mechanical forces were responsible for causing such a surface condition; heat damage should have resulted in a smoother surface. The lack of damage along the line of injection could be due to a combination of thicker fuel film and reduced mixing of propellants. Tests with the 008×120 injector did not result in damage possibly due to the high injection speed preventing the formation of a fuel film on the wall.

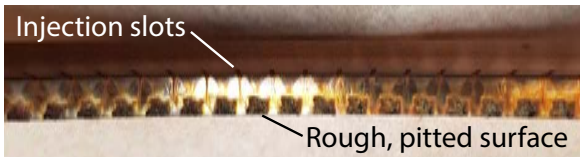

Figure 4.36. Injector ring with erosion damage on the downstream surface.

Microscope images of the original 011×120 injector before and after the hotfire tests are shown in Fig. 4.37. The microscope was focused on the bottom surface of the semicircular groove where machining using a ball end mill left overlapping

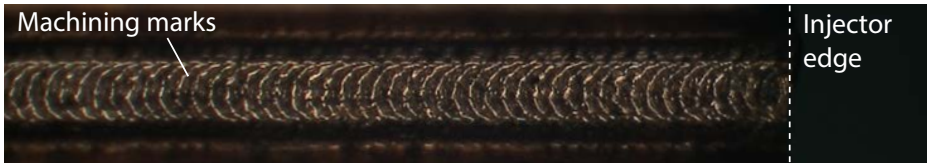

(a) Before

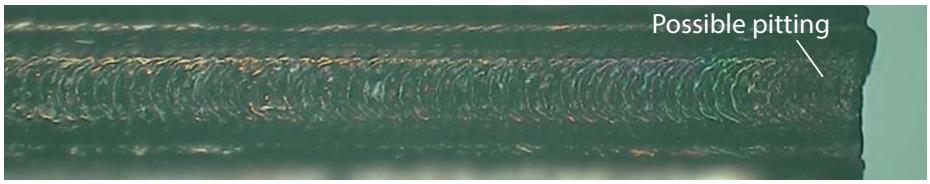

(b) After

Figure 4.37. Microscope images of a single injector element on the first 011×120 injector before and after hotfire tests.

circular surface features. The images are not of the same injector element since they were unmarked. Even though the injector had undergone 14 tests in which rotating detonations were produced, little evidence of pitting damage from cavitation can be seen, except for a small region of roughened surface near the injector exit in Fig. 4.37(b). Even so, the markings are not obvious enough to be conclusive evidence.

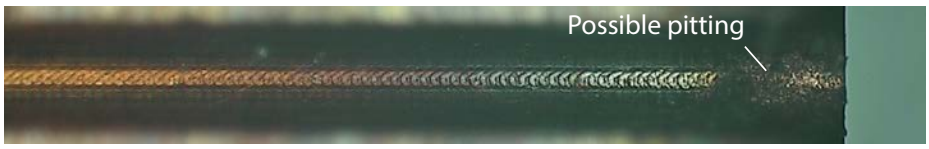

Figure 4.38. Microscope images of a single injector element on the second 011×120 injector after hotfire tests.

A second 011×120 injector was manufactured during the testing phase. Unfortunately, it had not been photographed under a microscope before testing due to time constraints. Figure 4.38 shows a post-hotfire microscope image of one of its injector elements. The near-exit region displayed what appears to be erosion damage to the extent that the circular machining marks had been completely removed. However,

whether it was due to pitting from cavitation or simply heat cannot be ascertained without further investigation.

(a) Centerbody showing extensive melting and charring. Image courtesy of Jenna Humble.

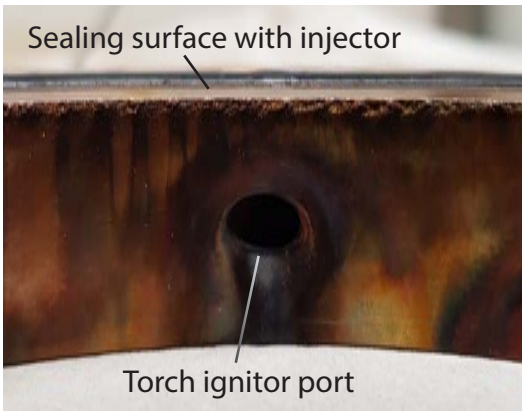

(b) Outer wall ignitor ring with erosion damage adjacent to interface with injector

Figure 4.39. Hardware damage incurred from Test 85.

The engine hardware suffered critical damage during Test 85, where mass flow rate was increased to 3.49 kg/s (7.67 lbm/s) to target a chamber pressure of 2.76 MPa (400 psia). The hardware was disassembled to assess the damage and determine the damage mechanism. The chamber centerbody assembly shown in Fig. 4.39(a) incurred the most extensive damage. The area with the greatest amount of melting was the corner formed between the aft-facing step on the injector centerbody and cylindrical wall of the inner chamber centerbody. From its location relative to the flow field, a likely cause of damage was the formation of a recirculation zone in the corner as high-speed oxidizer flow expanded around the sudden expansion. Recirculation of product gases could have provided sufficient time for the gas composition to shift towards equilibrium such that convective heat flux increased by several factors as discussed in the previous subsection and surpassed material capability.

In Fig. 4.39(b) the ignitor ring component of the outer wall displayed heavy discoloration but milder surface melting possibly due to heat diffusion being radially-outward. Along the upper edge which seals against the injector ring, the same type of pitting damage seen in Fig. 4.36 was present. In this instance the pitting was deeper than previously observed, likely the result of both increased propellant flow rate and greatly-reduced material strength close to its melting temperature. Following this outcome, high mass flow tests were discontinued and the components shown in Fig. 4.39 were replaced before testing resumed.

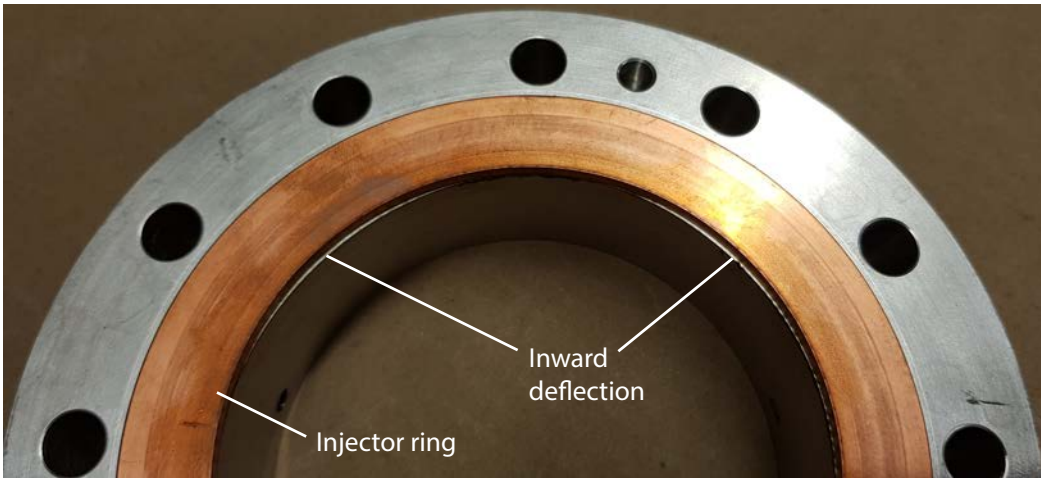

Figure 4.40. Inward warping of fuel manifold inner wall.

A final inspection of the fuel injector housing revealed that the manifold inner wall had undergone permanent deformation, although the exact point at which it happened remains unknown. Figure 4.40 shows an injector ring seated in the fuel injector housing. Under nominal condition, the inner diameters of both components would be concentric. However, due to the inward deflection in the highlighted areas, protrusion of the manifold wall is visible. Clearly, the part had experienced stresses over the course of testing that were large enough to cause plastic deformation. This also implies that some degree of deformation, elastic or otherwise, should be expected during most, if not all, tests.

In light of findings from the heat transfer analysis, it is recommended that chamber designs for future hardware exclude any aft-facing steps or features that could support formation of recirculation zones. It is vital to recognize that while the rapid ejection of combustion products reduces heat load on the engine structure, it also poses a reduction in engine performance; there exists a tradeoff between thermal management and combustion efficiency that needs to be considered during the process of designing an RDE chamber. Cooling capacity permitting, a contraction ratio could be employed to increase residence time of product gases.

Results from [15] suggest that geometrically-choking the chamber destabilized detonations of methane and oxygen. However, chamber pressures obtained in that study matched ideal constant-pressure calculations more closely than they did in the present tests. It is likely that the slot injection scheme was suboptimal for liquids and resulted in large droplets that were unable to participate in detonation readily. Chemical kinetics undoubtedly play a role in wave stability and it is conceivable that slower propellant combinations, such as ones in which liquid phases are present, may stand to gain from the introduction of a geometric throat.

4.9 Discussion on Multi-cycle Atomization and Shock Mixing

The findings of Clayton [68], Anderson [24, 30], and Bykovskii [12] pointed at the possibility of a multi-cycle atomization mechanism in liquid RDEs. Given the very short intervals between detonation waves and non-trivial time required for liquid propellants to meet at the impingement point, atomize, and mix, it seemed that liquid-liquid RDEs should not be possible. However, as all three researchers have demonstrated, a high-speed mixing mechanism was present which enabled rotating detonations to sustain. The author proposes a multi-cycle atomization process as follows:

1. Initial mode of combustion may be deflagration until pressure perturbations build up to initiate detonation. One or more detonation waves may be present.

2. The first detonation wave (Wave 1) passes over an injector, momentarily interrupting flow (not necessarily causing back-flow).

3. As injectors begin to recover, the liquid columns are met with another (or the same) detonation wave (Wave 2), which shatters them into fine mist. Baroclinic torque induces strong swirl directly behind the detonation wave and helps to mix propellants. This detonation wave may weaken as it is starved of fresh combustible propellants.

4. Injectors recover behind Wave 2 and liquid columns form.

5. Wave 3 arrives and consumes the combustible mixture while atomizing and mixing the new propellants.

6. Sustained multi-cycle atomization and rotating detonation established and steps 4 and 5 repeat for the duration of operation.

In the ideal limit of stable rotating detonation, the flow structures in the local neighborhood of any single detonation wave, and the detonation wave itself, should look similar to others. One may picture an azimuthal repeat of the structures depicted in Fig. 4.41. The solid black horizontal line represents the injector face. Individual injectors and propellants have been omitted for simplicity, but by no means implies pre-mixing or otherwise. The reader can imagine a discrete injector/manifold region upstream of the injector face. The key region is the horizontal band just above the injector face: The triangular darker blue wedge represents the recovered liquid flow ahead of the detonation wave. As the detonation wave sweeps over the liquid, it atomizes and mixes with the gaseous detonation products to form the lighter blue region which makes up the combustible mixture for the next approaching wave.

Following this logic, it is apparent that even in the case of multi-cycle atomization, the injectors would have to recover positive flow (into chamber) within the interval between successive detonation waves, or the pattern cannot repeat itself and therefore does not represent stable detonation. This would impose an upper limit on the refill

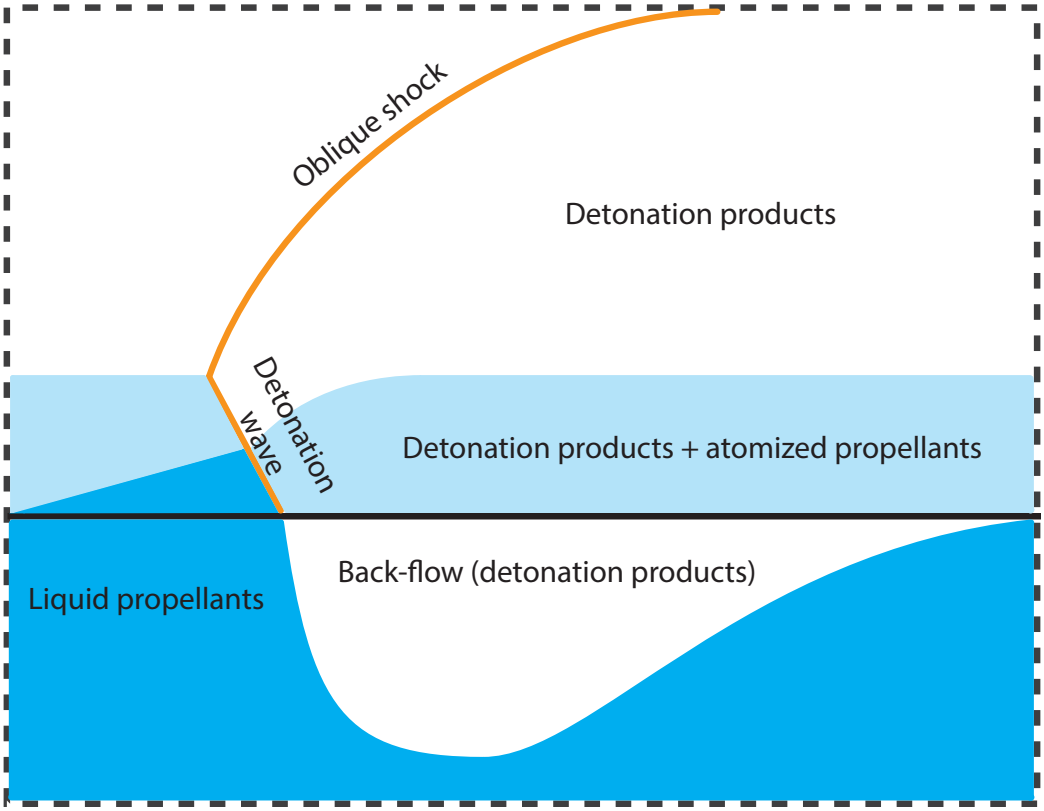

Figure 4.41. Simplified graphical representation of the multi-cycle atomization process. Combustor exit is towards the top of the diagram.

time of injectors in liquid RDEs. The experiments in [12, 24] were conducted with manifold pressures several times higher than *average* chamber pressure (similar to RDE v1.4 hotfire experiments) and from prior analysis of injector response, injector recovery had likely been almost immediate in these cases.

In [68], injector ΔP was merely half of the initial (minimum) chamber pressure, implying that injectors were very soft and would likely have back-flowed. Despite that, mixing of propellants was achieved. However, it was stated in the article that the detonation resided in the outer corner at the chamber head. Given that the chamber was of conventional design with injector elements distributed throughout the circular injector face plate, it is also possible that mixing could have occurred in the central core where pressure excursions were less severe.

5. CONCLUSIONS AND RECOMMENDATIONS FOR FUTURE WORK

5.1 On the Study of Injector Transient Response

Experimental studies have been conducted in the effort to gain fundamental understanding on the nature of liquid injection under RDE conditions. A pressure vessel was designed and built to house the test article so that experiments could be conducted at elevated pressures relevant to rocket applications. Plain orifice injectors were tested using water as the working fluid. In the first test series, hydrogen and oxygen were used as propellants to produce a single detonation that drove injector response. Three injectors of the same diameter (0.84 mm) but different L/D ratios (10, 6, and 4) were used in the tests. After completion of the first test series, a second was conducted with the intention of investigating the effects that detonation strength and geometric scaling had on injector response. For this purpose, ethylene was used as fuel, and a fourth injector configuration, which was a 1.5× scaled version of the LD6 injector, was made.

The consolidation of data from both test series revealed that the time required for an injector to back-flow and refill following the passage of a detonation wave was largely independent of injector length, and inversely-proportional to injector stiffness. Normalizing refill time by the detonation pressure ratio produced by both propellant combinations also enabled data from both test series to collapse onto the same curve. A simple curve fit with appreciable goodness of fit ($R^2 = 0.88$) was obtained from the data and used to estimate the refill time of RDE v1.4 based on its operating conditions. An important secondary product of the study was the collection of hundreds of detonation pressure profiles in benign conditions survivable by instrumentation that would otherwise have been destroyed in a full engine's operating environment. The

data allowed estimations of an engine's dynamic pressure to be made with the help of NASA CEA to enable calculation of injector stiffness that could be directly compared with injector response studies.

It was eventually realized that the pressure levels imposed on the injectors in these studies far exceeded those encountered in the RDE hotfire tests; estimated average pressure of the hydrogen-oxygen detonations ranged from 2.7 to 6.2 MPa (390 to 900 psia) while that of the ethylene-oxygen tests were 2.6 to 9.0 MPa (380 to 1300 psia). In all cases, injector manifold pressure was higher than the *minimum* pressure, but actually lower than *average* pressure for the duration of the detonation pulse. The average pressures obtained were also higher than any of the chamber average pressures achieved in the hotfire tests. Additionally, the pressure relaxation process following a detonation in an actual engine is believed to occur in a shorter time than that observed in these tests.

The cavitation observed in high-speed videos also bring to attention the possibility of erosion damage that injector passage walls could face and thus limit their lifespan. The early onset of hydraulic flip witnessed in many of the test cases also highlight the importance of injector passage geometry; straight orifices are susceptible to adverse pressure gradients along the wall that can result in hydraulic flip, which drastically decreases discharge coefficient and reduces atomization.

Although the conditions undergone by the injectors in this test campaign were not representative of those in the hotfire tests, the results acquired were beneficial nonetheless for the fundamental insights they provided. Moreover, future RDE hardware with higher chamber pressure targets may yet find utility in the data collected.

5.1.1 Recommendations

The injector refill time curve fit, while potentially useful, does not consider the role of a liquid's density and viscosity in its response to a detonation wave. The coefficient in the curve fit equation likely contains elements of the liquid's properties.

The same experiments performed with working fluids of different densities and viscosities could uncover their roles. In a similar vein, experiments with the LD6-1.5S injector suggested that boundary layer dynamics hold stronger influence over injector response than injector length and L/D ratio. Injectors of constant length with various diameters could be used to further investigate this relation.

As a general suggestion to future researchers, it is highly-recommended to minimize the number of sealing surfaces along the detonation wave's path. Peak pressures in the detonation channel can be extremely high and difficult to contain with soft materials such as those typically used for sealing purposes. While the monetary cost of replacing gaskets and seals may be cheap, the process is time consuming and introduces changes to the physical apparatus, which may result in additional uncertainties.

5.2 On the RDE v1.4 Hotfire Test Campaign

Minor modifications were made to RDE v1.3 to accommodate the use of RP-2 as a liquid fuel and expand the platform's diagnostic capability. Injector inserts with narrower grooves were designed taking into account the large increase in fuel density. The chamber outer wall was machined with 36 thermowells of different depths at various azimuthal and axial stations to permit the study of chamber heat flux. Throughout the test campaign, a single GOX injector and chamber configuration was utilized based on previous combustor performance findings by Stechmann [15], while fuel injector geometry was varied.

According to the injector transient response study, the RP-2 injectors used in the hotfire test campaign were extremely stiff and fuel flow had likely been continuous except for a brief period ($<$20 µs) of deceleration as the detonation wave traversed the orifice. A theoretical estimate of the number of waves that could be supported by the injector's recovery time while also accounting for fuel jet penetration across the GOX injector gap was at least seven, but a maximum of seven waves were observed during

the experiments. This suggests that the combustion or detonation wave formation process might have been limited by fill height and/or propellant mixing.

Throughout the test campaign, a curious phenomenon was noticed where fuel manifold pressure decreased drastically after the first test following hardware re-assembly. The low manifold pressure had immediately been recognized as leakage, but it was unclear how it had occurred and why the first test was unaffected. Analysis of high-speed videography also uncovered a correlation in which stable detonations were obtained only in cases where fuel manifold leakage did *not* occur, regardless of fuel equivalence ratio. It was only after completion of the test campaign when engine hardware had been consolidated that markings were noticed on the injector inserts which pointed towards flexing of the fuel manifold wall that had been responsible for sealing against the injectors.

It appeared that the manifold wall had deformed, although its exact geometry remains unknown. The deflection of the manifold wall had meant that fuel had become preferentially injected where leakage occurred; wall temperature data support the existence of hot and cold sectors around the annulus. The highly-nonuniform fuel distribution was also the likely cause of detonation instabilities in the same cases. The deformation is believed to be elastic even though it had been maintained between tests; the supporting evidence is the re-establishment of proper sealing with the injector insert each time the engine was reassembled. The mechanism for the deformation to persist between tests was suspected to be friction: The chamber outer wall was stacked under compression through the use of 12 $\frac{3}{8}$-in alloy steel bolts; once the deformation occurred, presumably by nonuniform thermal expansion, friction and compression prevented the manifold from returning to its original shape until compression was removed during reassembly.

Chamber heat flux was computed from wall temperature measurements using an inverse heat transfer method utilizing numerical optimization. Correlations between heat flux and detonation speed, as well as detonation stability, were observed. The number of detonations, however, did not appear to hold strong influence over chamber

heat flux. An observation relevant to the design of RDE cooling strategy is that stable detonations were associated with highest wall temperatures close to the injection plane while highest wall temperatures occured further downstream in the chamber when detonations were unstable or not present. One can envision a targeted cooling strategy similar to throat cooling in conventional engines, where much of the pressure budget is spent where heat flux is the highest. This is especially important in the cooling of a plug nozzle, whose total perimeter in contact with sonic exhaust is always greater than that of a bell nozzle.

A common benchmark for heat flux comparison with constant-pressure engines is their throat heat flux because of similarities in flow speed; the typical RDE annulus is of constant area if a geometric throat is not utilized and therefore the entire chamber encounters high-speed flow. Surprisingly, the estimated average chamber heat flux in RDE v1.4 (not considering uncertainties from thermocouple transients) was lower than the throat heat flux of an equivalent ideal constant-pressure engine. The difference may be attributed to the different gas composition in each engine: In general, constant-pressure engines are designed to maximize residence time of gases in the chamber so that equilibrium composition can be reached. Both specific heat capacity and thermal conductivity of an equilibrium mixture are higher than that of a frozen mixture (thermal conductivity can be *several factors* higher), causing heat transfer to be amplified. In contrast, the chamber design of an RDE results in a very rapid expulsion of product gas such that its composition is far from equilibrium by the time it leaves the chamber. Therefore, even though detonations produce higher local pressure and temperature, the heat transfer coefficient of the flow is far lower, greatly alleviating the heating problem.

A rough estimation of total engine heat load accounting for wall surface area was made. The results suggest that while the entirety of the RDE chamber encounters high-speed flow, the diminished thermal conductivity and heat capacity of its gas composition greatly offset the increased convective effects. The heat flux in an RDE, being an order of magnitude lower than that at the throat of a constant-pressure

engine, implies that its cooling scheme may not need to be as aggressive. The pressure loss incurred by its regenerative cooling jacket may conceivably be lower than that of a conventional engine. Consequently, the total system budget including injector pressure loss may not be as high as previously thought, and could even be comparable to that of a constant-pressure combustor.

The design of RDE v1.4 was not optimized for use with liquid propellants and difficulties with manifold sealing introduced many sources of uncertainty to the collected data. Nevertheless, it is hoped that the preliminary heat flux estimations in a rocket RDE would prove valuable to the next stage of development: building and testing actively-cooled rocket RDEs that are capable of achieving stable operating conditions. This milestone will eliminate the challenges of measuring chamber heat flux as the slow response of thermocouple probes becomes a non-issue. In addition, calorimetry could be used, as demonstrated for air-breathing engines in [35, 37], to obtain the average heat flux of a rocket RDE.

5.2.1 Recommendations

Pressure measurements in rocket RDEs remains a great challenge that needs to be overcome not only for the sake academia, but also because it is one of the simplest measurements that can be used to monitor the state of an engine. However, for it to be useful, CTAP needs to be better understood. More specifically, the nature of the pressure measured by CTAP based on its location in an engine is worth further investigation. From a fluid dynamics standpoint, it can be seen that a transient flow like that in a detonation field results in spatially-varying static pressure, and therefore the location of a CTAP port needs to be chosen with deliberation according to the measurement desired. A number of pressure measurements made at various axial stations of the chamber would be useful to improve understanding of the evolution of static pressure along the chamber.

The dynamic pressure in a rocket RDE remains an elusive measurement due to the destructive nature of detonation waves. An attempt by Stechmann [15] utilizing a used, thermal barrier-coated sensor resulted in its destruction even before the engine had attained steady-state combustion. High-frequency pressure sensors are expensive instruments and care should be taken to maximize their lifespans. Admittedly, the pre-used state of the sensor might have limited its ability to survive the harsh conditions. It is perhaps possible for a water-cooled pressure sensor coated with a thermal barrier to endure RDE chamber conditions for sufficiently long to capture the transient pressure fluctuations. It may sound like a costly endeavor to use a sensor as a consumable, but the data would be invaluable to the whole RDE research community.

Many lessons were learned throughout the hotfire test campaign, but several were especially worthy of mention. Based on the assessment of hardware damaged in Test 85, it was postulated that the formation of a recirculation zone allowed sufficient time for the gas composition to approach equilibrium and exacerbate heat transfer into the walls. Therefore, it may be prudent to avoid aft-facing steps which promote gas recirculation. From the experience gained in the use of thermocouple probes for making surface measurements, it is suggested that spring-loaded thermocouple mounts be used wherever possible to improve response time. Additionally, conductive thermal compounds may be used, but only as far as possible to fill the voids between the surface and the probe; excess thermal compound should not envelop the thermocouple wires.

A detailed study of the transient response of embedded thermocouple probes should also be carried out. Ideally, a heat source whose heat flux is known and of sufficient magnitude – of the order of 1 MW/m^2 – would be applied to on side of a wall while the other end would be insulated to approximate the adiabatic condition. Thermocouple probes embedded at different depths in the wall would be used to measure wall temperature profile. The measured profile can then be compared with a transient conduction model to calibrate the system.

Lastly, manufacturing the injector as a monolithic structure is highly recommended as discharge characteristics will be far more consistent. Flexible or cantilevered structures should be avoided as they are susceptible to uneven mechanical or thermal loads that could lead to unforeseen deviations in flow geometry. While absolute deflections might be small, relative flow areas could be significantly altered.

5.3 Closing Statement

The studies contained in this document have produced encouraging results for the future of RDEs. While there remains much to be learned before these devices can be considered for implementation, the same can be said of any emergent technology. The current rocket propulsion technology is faced with limits imposed by fundamental thermodynamics, and RDEs hold the potential to become the next step in the evolution of chemical rockets.

REFERENCES

[1] Y A Zeldovich. To the question of energy use of detonation combustion. *Journal of Propulsion and Power*, 22(3):588–592, 2006.

[2] John H S Lee. *The Detonation Phenomenon*. Cambridge, Cambridge, 2008.

[3] J Shepherd. Detonation database. `http://shepherd.caltech.edu/detn_db/html/db_121.html`, 2002. accessed: November 7, 2017.

[4] V V Mikahilov and M E Topchiyan. Study of continuous detonation in an annular channel. *Fizika Goreniya i Vzryva*, 1(4):20–23, 1965.

[5] J A Nicholls, R E Cullen, and Ragland K W. Feasibility studies of a rotating detonation wave rocket motor. *Journal of Spacecraft and Rockets*, 3(6):893–898, 1966.

[6] NASA. Space shuttle era. `https://www.nasa.gov/mission_pages/shuttle/flyout/ssme.html`. accessed: March 10, 2018.

[7] Space Exploration Technologies. Reusability, accessed July 23, 2019.

[8] Blue Origin. Our mission, accessed July 23, 2019.

[9] F A Bykovskii, S A Zhdan, and E F Vedernikov. Continuous spin detonation in annular combustors. *Fizika Goreniya i Vzryva*, 41(4):99–109, 2005.

[10] D Schwer and K Kailasanath. Numerical investigation of the physics of rotating-detonation-engines. In *Proceedings of the Combustion Institute*, volume 33, pages 2195–2202, 2011.

[11] L M Thomas, F R Schauer, J L Hoke, and A Naples. Buildup and operation of a rotating detonation engine. In *49th AIAA Aerospace Sciences Meeting*, 2011.

[12] F A Bykovskii, S A Zhdan, and E F Vedernikov. Continuous spin detonations. *Journal of Propulsion and Power*, 22(6):1204–1216, 2006.

[13] B J McBride and S Gordon. *Chemical Equilibrium with Applications*. NASA, Cleveland, OH, 1996.

[14] D K Huzel and D H Huang. *Design of Liquid Propellant Rocket Engines*. NASA, Washington, DC, 1967.

[15] D P Stechmann. *Experimental Study of High-pressure Rotating Detonation Combustion in Rocket Environments*. PhD thesis, Purdue University, 2017.

[16] Y H Wang, J P Wang, T Y Shi, and Y S Liu. Experimental research on transition regions in continuously rotating detonation waves. In *2012 Joint Propulsion Conference*, 2012.

[17] J C Shank, P I King, J Karnesky, F R Schauer, and J L Hoke. Development and testing of a modular rotating detonation engine. In *2012 Aerospace Sciences Meeting*, 2012.

[18] F A Bykovskii, S A Zhdan, and E F Vedernikov. Initiation of detonation of fuel-air mixtures in a flow-type annular combustor. *Combustion, Explosion, and Shock Waves*, 50(2):214–222, 2014.

[19] L Peng, D Wang, X Wu, H Ma, and C Yang. Ignition experiment with automotive spark on rotating detonation engine. *International Journal of Hydrogen Energy*, 40:8465–8474, 2015.

[20] V Anand, A St. George, R Driscoll, and E Gutmark. Investigation of rotating detonation combustor operation with h2-air mixtures. *International Journal of Hydrogen Energy*, 41:1281–1292, 2016.

[21] F Chacon and M Gamba. Development of an optically accessible continuous wave rotating detonation engine. In *2018 Joint Propulsion Conference*, 2018.

[22] J Kindracki. Experimental research on rotating detonation in liquid fuel-gaseous air mixtures. *Aerospace Science and Technology*, 43:445–453, 2015.

[23] J M Li, P H Chang, L Li, Y Yang, C J Teo, and B C Khoo. Investigation of injection strategy for liquid-fuel rotating detonation engine. In *2018 Aerospace Sciences Meeting*, 2018.

[24] W S Anderson, S D Heister, and C Hartsfield. Experimental study of a hypergolically ignited liquid bipropellant rotating detonation rocket engine. In *2019 AIAA Aerospace Sciences Meeting*, 2019.

[25] D T Harrje and F H Reardon. *Liquid Propellant Rocket Combustion Instability*. NASA, Washington, DC, 1972.

[26] I Reba and C Brosilow. *Combustion Instability: Liquid Stream and Droplet Behavior Part III: The Response of Liquid Jets to Large Amplitude Sonic Oscillations*. WADC, USAF, 1960.

[27] M E MacDonald, J V Canino, and S D Heister. Nonlinear response of plain-orifice injectors to nonacoustic pressure oscillations. *Journal of Propulsion and Power*, 23(6):1204–1213, 2007.

[28] B E Richards, D H Trevena, and D H Edwards. Cavitation experiments using a water shock tube. *Journal of Physics D: Applied Physics*, 13(7):1315–1323, 1980.

[29] A Benusiglio, D Quere, and C Clanet. Explosions at the water surface. *Journal of Fluid Mechanics*, 752:123–139, 2014.

[30] W S Anderson and S D Heister. Response of a liquid jet in a multiple-detonation driven crossflow. *Journal of Propulsion and Power*, 2018.

[31] H F Celebi. Transient response of tapered and angled injectors subjected to a passing detonation wave. Master's thesis, Purdue University, 2019.

[32] D Lim, H F Celebi, and S D Heister. Transient response of a liquid injector to an ethylene-oxygen detonation wave. In *2019 Aerospace Sciences Meeting*, 2019.

[33] F A Bykovskii. Thermal fluxes in combustion chamber walls in the detonation and turbulent combustion modes. *Combustion, Explosion and Shock Waves*, 27(1):66–71, 1991.

[34] F A Bykovskii and E F Vedernikov. Heat fluxes to combustor walls during continuous spin detonation of fuelair mixtures. *Combustion, Explosion and Shock Waves*, 45(1):70–77, 2009.

[35] S W Theuerkauf, F R Schauer, R Anthony, and J L Hoke. Average and instantaneous heat release to the walls of an rde. In *2014 AIAA Aerospace Sciences Meeting*, 2014.

[36] S W Theuerkauf, F R Schauer, R Anthony, and J L Hoke. Experimental characterization of high-frequency heat flux in a rotating detonation engine. In *2015 AIAA Aerospace Sciences Meeting*, 2015.

[37] C A Stevens, M L Fotia, J Hoke, and F R Schauer. Quasi-steady heat transfer measurements in an rde. In *2018 AIAA Aerospace Sciences Meeting*, 2018.

[38] C A Stevens, M L Fotia, J Hoke, and F R Schauer. An experimental comparison of the inner and outer wall heat flux in an rde. In *2019 AIAA Aerospace Sciences Meeting*, 2019.

[39] K Ishihara, J Nishimura, K Goto, S Nakagami, K Matsuoka, J Kasahara, A Matsuo, I Funaki, H Moriai, H Mukae, K Yasuda, D Nakata, and K Higashino. Study on a long-time operation towards rotating detonation rocket engine flight demonstration. In *2017 AIAA Aerospace Sciences Meeting*, 2017.

[40] D Lim. Transient response of a liquid injector to a steep-fronted transverse pressure wave. Master's thesis, Purdue University, 2015.

[41] R J Roark. *Formulas for Stress and Strain*. McGraw-Hill, 1975.

[42] W S Anderson, D Lim, M R Washington, and S D Heister. Experimental study of liquid injector elements for use in rotating detonation engines. In *2017 Aerospace Sciences Meeting*, 2017.

[43] H J C Berendsen. *A Student's Guide to Data and Error Analysis*. Cambridge, 2011.

[44] F P Incropera, D P DeWitt, T L Bergman, and A S Lavine. *Principles of Heat and Mass Transfer*. Wiley, 2013.

[45] O M Alifanov. *Inverse Heat Transfer Problems*. Springer Berlin Heidelberg, 1994.

[46] Inc. The MathWorks. Find minimum of unconstrained multivariable function. `https://www.mathworks.com/help/optim/ug/fminunc.html`, 2017. accessed: October 23, 2019.

[47] M L Huber, E W Lemmon, L S Ott, and T J Bruno. Preliminary surrogate mixture models for the thermophysical properties of rocket propellants rp-1 and rp-2. *Energy and Fuels*, 23:3083–3088, 2009.

[48] R B Stewart, R T Jacobsen, and W Wagner. Thermodynamic properties of oxygen from the triple point to 300 k with pressures to 80 mpa. *Journal of Physical and Chemical Reference Data*, 20(5):917–1021, 1991.

[49] W Wagner, J Ewers, and W Pentermann. New vapour-pressure measurements and a new rational vapour-pressure equation for oxygen. *Journal of Chemical Thermodynamics*, 8(11):1049–1060, 1976.

[50] J W Leachman, R T Jacobsen, S G Penoncello, and E W Lemmon. Fundamental equations of state for parahydrogen, normal hydrogen, and orthohydrogen. *Journal of Physical and Chemical Reference Data*, 38(3):721–748, 2009.

[51] A S Thompson. *Visualization of Cavitating and Flashing Flows Within a High Aspect Ratio Injector*. PhD thesis, Purdue University, 2014.

[52] C L Wadhwa. *High Voltage Engineering*. New Age International Publishers, 2007.

[53] M R Driels. The effect of a non-zero cavitation tension on the damage sustained by a target plate subject to an underwater explosion. *Journal of Sound and Vibration*, 73(4):533–545, 1980.

[54] Inc. The MathWorks. Continuous 1-d wavelet transform. `https://www.mathworks.com/help/wavelet/ref/cwt.html`, 2018. accessed: October 23, 2019.

[55] C F Naude and A T Ellis. On the mechanism of cavitation damage by nonhemispherical cavities collapsing in contact with a solid boundary. *Journal of Basic Engineering*, 83(4):648–656, 1961.

[56] A Sou, S Hosokawa, and A Tomiyama. Cavitation in nozzles of plain orifice atomizers with various length-to-diameter ratios. *Atomization and Sprays*, 20(6):513–524, 2010.

[57] Inc. The MathWorks. Curve fitting. `https://www.mathworks.com/help/curvefit/curvefitting-app.html`, 2018. accessed: October 23, 2019.

[58] Y Çengel and J Cimbala. *Fluid Mechanics : Fundamentals and Applications*. McGraw-Hill Higher Education, New York, 2006.

[59] F A Bykovskii, S A Zhdan, E F Vedernikov, and A N Samsonov. Scaling factor in continuous spin detonation of syngas-air mixtures. *Combustion, Explosion, and Shock Waves*, 53(2):187–198, 2017.

[60] D Lim, S D Heister, D P Stechmann, and B K Kan. Transient response of a liquid injector to a steep-fronted transverse pressure wave. *Shock Waves*, 2017.

[61] J Kindracki. Study of detonation initiation in kerosene-oxidizer mixtures in short tubes. *Shock Waves*, 24(6):603–618, 2014.

[62] I V Walters, C L Journell, A Lemcherfi, R M Gejji, S D Heister, and C D Slabaugh. Performance characterization of a natural gas-air rotating detonation engine. In *AIAA Propulsion and Energy 2019 Forum*, 2019.

[63] C A Stevens, M L Fotia, J Hoke, and F R Schauer. Comparison of transient response of pressure measurement techniques with application to detonation waves. In *2015 AIAA Aerospace Sciences Meeting*, 2015.

[64] T Gaillard, D Davidenko, and F Dupoirieux. Numerical simulation of a rotating detonation with a realistic injector designed for separate supply of gaseous hydrogen and oxygen. *Acta Astronautica*, 141:64–78, 2017.

[65] D A Schwer, R Kelso, and C M Brophy. Pressure characteristics of an aerospike nozzle in a rotating detonation engine. In *2018 Joint Propulsion Conference*, 2018.

[66] C F Lietz, Y Desai, R Munipalli, S A Schumaker, and V Sankaran. Flowfield analysis of a 3d simulation of a rotating detonation rocket engine. In *2019 Aerospace Sciences Meeting*, 2019.

[67] K Mikoshiba, S V Sardeshmukh, and S D Heister. On the response of annular injectors to rotating detonation waves. *Shock Waves*, 2019.

[68] R M Clayton, R S Rogero, and Sotter J G. An experimental description of destructive liquid rocket resonant combustion. *AIAA Journal*, 6(7):1252–1259, 1968.

A. TABLES OF DATA UNCERTAINTIES

x: Max. back-flow distance, dP: Injector pressure drop, Pc: Initial ambient pressure, dP/Pc: Injector stiffness

Table A.1. Uncertainty values of parameters associated with injector LD10 at initial ambient pressure of 100 psia utilizing hydrogen fuel.

Test No.	Resolution [in/px]	Δx [in]	Δ(dP) [psi]	ΔPmin [psi]	Δ(dP/Pmin)
2	2.87E-03	4.06E-03	7.87E-01	7.50E-01	7.90E-03
3	2.87E-03	4.06E-03	7.87E-01	7.50E-01	7.85E-03
4	2.87E-03	4.06E-03	7.87E-01	7.50E-01	7.91E-03
5	2.87E-03	4.06E-03	7.87E-01	7.50E-01	7.89E-03
6	2.87E-03	4.06E-03	7.87E-01	7.50E-01	7.86E-03
7	2.87E-03	4.06E-03	7.87E-01	7.50E-01	7.98E-03
8	2.87E-03	4.06E-03	7.87E-01	7.50E-01	7.98E-03
9	2.87E-03	4.06E-03	7.87E-01	7.50E-01	8.00E-03
10	2.87E-03	4.06E-03	7.87E-01	7.50E-01	7.99E-03
11	2.87E-03	4.06E-03	7.87E-01	7.50E-01	7.99E-03
12	2.87E-03	4.06E-03	7.87E-01	7.50E-01	8.23E-03
13	2.87E-03	4.06E-03	7.87E-01	7.50E-01	8.19E-03
14	2.87E-03	4.06E-03	7.87E-01	7.50E-01	8.22E-03
15	2.87E-03	4.06E-03	7.87E-01	7.50E-01	8.22E-03
16	2.87E-03	4.06E-03	7.87E-01	7.50E-01	8.19E-03
17	2.87E-03	4.06E-03	7.87E-01	7.50E-01	8.91E-03
18	2.87E-03	4.06E-03	7.87E-01	7.50E-01	8.82E-03
19	2.87E-03	4.06E-03	7.87E-01	7.50E-01	8.76E-03
20	2.87E-03	4.06E-03	7.87E-01	7.50E-01	8.83E-03
21	2.87E-03	4.06E-03	7.87E-01	7.50E-01	8.79E-03
22	2.87E-03	4.06E-03	7.87E-01	7.50E-01	9.21E-03
23	2.87E-03	4.06E-03	7.87E-01	7.50E-01	9.17E-03
24	2.87E-03	4.06E-03	7.87E-01	7.50E-01	9.10E-03
25	2.87E-03	4.06E-03	7.87E-01	7.50E-01	9.22E-03
26	2.87E-03	4.06E-03	7.87E-01	7.50E-01	9.14E-03
27	2.87E-03	4.06E-03	7.87E-01	7.50E-01	9.55E-03
28	2.87E-03	4.06E-03	7.87E-01	7.50E-01	9.51E-03
29	2.87E-03	4.06E-03	7.87E-01	7.50E-01	9.48E-03
30	2.87E-03	4.06E-03	7.87E-01	7.50E-01	9.49E-03
31	2.87E-03	4.06E-03	7.87E-01	7.50E-01	9.44E-03

Table A.2. Uncertainty values of parameters associated with injector LD10 at initial ambient pressure of 150 psia utilizing hydrogen fuel.

Test No.	Resolution [in/px]	Δx [in]	Δ(dP) [psi]	ΔPmin [psi]	Δ(dP/Pmin)
34	2.92E-03	4.13E-03	7.87E-01	7.50E-01	5.35E-03
35	2.92E-03	4.13E-03	7.87E-01	7.50E-01	5.36E-03
36	2.92E-03	4.13E-03	7.87E-01	7.50E-01	5.34E-03
37	2.92E-03	4.13E-03	7.87E-01	7.50E-01	5.35E-03
38	2.92E-03	4.13E-03	7.87E-01	7.50E-01	5.38E-03
39	2.92E-03	4.13E-03	7.87E-01	7.50E-01	5.44E-03
40	2.92E-03	4.13E-03	7.87E-01	7.50E-01	5.42E-03
41	2.92E-03	4.13E-03	7.87E-01	7.50E-01	5.41E-03
42	2.92E-03	4.13E-03	7.87E-01	7.50E-01	5.42E-03
43	2.92E-03	4.13E-03	7.87E-01	7.50E-01	5.43E-03
44	2.92E-03	4.13E-03	7.87E-01	7.50E-01	5.54E-03
45	2.92E-03	4.13E-03	7.87E-01	7.50E-01	5.52E-03
46	2.92E-03	4.13E-03	7.87E-01	7.50E-01	5.54E-03
47	2.92E-03	4.13E-03	7.87E-01	7.50E-01	5.50E-03
48	2.92E-03	4.13E-03	7.87E-01	7.50E-01	5.48E-03
49	2.92E-03	4.13E-03	7.87E-01	7.50E-01	5.67E-03
50	2.92E-03	4.13E-03	7.87E-01	7.50E-01	5.70E-03
51	2.92E-03	4.13E-03	7.87E-01	7.50E-01	5.66E-03
52	2.92E-03	4.13E-03	7.87E-01	7.50E-01	5.66E-03
53	2.92E-03	4.13E-03	7.87E-01	7.50E-01	5.66E-03
54	2.92E-03	4.13E-03	7.87E-01	7.50E-01	5.81E-03
55	2.92E-03	4.13E-03	7.87E-01	7.50E-01	5.83E-03
56	2.92E-03	4.13E-03	7.87E-01	7.50E-01	5.79E-03
57	2.92E-03	4.13E-03	7.87E-01	7.50E-01	5.77E-03
58	2.92E-03	4.13E-03	7.87E-01	7.50E-01	5.83E-03
59	2.92E-03	4.13E-03	7.87E-01	7.50E-01	6.07E-03
60	2.92E-03	4.13E-03	7.87E-01	7.50E-01	6.01E-03
61	2.92E-03	4.13E-03	7.87E-01	7.50E-01	5.97E-03
62	2.92E-03	4.13E-03	7.87E-01	7.50E-01	5.93E-03
63	2.92E-03	4.13E-03	7.87E-01	7.50E-01	5.93E-03
64	2.92E-03	4.13E-03	7.87E-01	7.50E-01	6.23E-03
65	2.92E-03	4.13E-03	7.87E-01	7.50E-01	6.25E-03
66	2.92E-03	4.13E-03	7.87E-01	7.50E-01	6.20E-03
67	2.92E-03	4.13E-03	7.87E-01	7.50E-01	6.19E-03
68	2.92E-03	4.13E-03	7.87E-01	7.50E-01	6.17E-03

Table A.3. Uncertainty values of parameters associated with injector LD6 at initial ambient pressure of 100 psia utilizing hydrogen fuel.

Test No.	Resolution [in/px]	Δx [in]	Δ(dP) [psi]	ΔPmin [psi]	Δ(dP/Pmin)
21	2.15E-03	3.04E-03	7.87E-01	7.50E-01	8.41E-03
22	2.15E-03	3.04E-03	7.87E-01	7.50E-01	8.41E-03
23	2.15E-03	3.04E-03	7.87E-01	7.50E-01	8.32E-03
24	2.15E-03	3.04E-03	7.87E-01	7.50E-01	8.35E-03
25	2.15E-03	3.04E-03	7.87E-01	7.50E-01	8.35E-03
26	2.15E-03	3.04E-03	7.87E-01	7.50E-01	8.64E-03
27	2.15E-03	3.04E-03	7.87E-01	7.50E-01	8.64E-03
28	2.15E-03	3.04E-03	7.87E-01	7.50E-01	8.63E-03
29	2.15E-03	3.04E-03	7.87E-01	7.50E-01	8.63E-03
30	2.15E-03	3.04E-03	7.87E-01	7.50E-01	8.64E-03
31	2.15E-03	3.04E-03	7.87E-01	7.50E-01	9.02E-03
32	2.15E-03	3.04E-03	7.87E-01	7.50E-01	9.05E-03
33	2.15E-03	3.04E-03	7.87E-01	7.50E-01	9.07E-03
34	2.15E-03	3.04E-03	7.87E-01	7.50E-01	9.04E-03
35	2.15E-03	3.04E-03	7.87E-01	7.50E-01	9.03E-03
36	2.15E-03	3.04E-03	7.87E-01	7.50E-01	9.43E-03
37	2.15E-03	3.04E-03	7.87E-01	7.50E-01	9.46E-03
38	2.15E-03	3.04E-03	7.87E-01	7.50E-01	9.41E-03
41	2.15E-03	3.04E-03	7.87E-01	7.50E-01	9.80E-03
51	2.15E-03	3.04E-03	7.87E-01	7.50E-01	1.08E-02

Table A.4. Uncertainty values of parameters associated with injector LD6 at initial ambient pressure of 150 psia utilizing hydrogen fuel.

Test No.	Resolution [in/px]	Δx [in]	Δ(dP) [psi]	ΔPmin [psi]	Δ(dP/Pmin)
4	2.91E-03	4.12E-03	7.87E-01	7.50E-01	5.75E-03
5	2.91E-03	4.12E-03	7.87E-01	7.50E-01	5.74E-03
6	2.91E-03	4.12E-03	7.87E-01	7.50E-01	5.72E-03
7	2.91E-03	4.12E-03	7.87E-01	7.50E-01	5.73E-03
8	2.91E-03	4.12E-03	7.87E-01	7.50E-01	5.73E-03
9	2.91E-03	4.12E-03	7.87E-01	7.50E-01	5.66E-03
10	2.91E-03	4.12E-03	7.87E-01	7.50E-01	5.62E-03
11	2.91E-03	4.12E-03	7.87E-01	7.50E-01	5.61E-03
12	2.91E-03	4.12E-03	7.87E-01	7.50E-01	5.57E-03
13	2.91E-03	4.12E-03	7.87E-01	7.50E-01	5.57E-03
14	2.91E-03	4.12E-03	7.87E-01	7.50E-01	5.90E-03
15	2.91E-03	4.12E-03	7.87E-01	7.50E-01	5.86E-03
16	2.91E-03	4.12E-03	7.87E-01	7.50E-01	5.85E-03
17	2.91E-03	4.12E-03	7.87E-01	7.50E-01	5.87E-03
18	2.91E-03	4.12E-03	7.87E-01	7.50E-01	5.84E-03

Table A.5. Uncertainty values of parameters associated with injector LD6 at initial ambient pressure of 150 psia utilizing hydrogen fuel, continued.

Test No.	Resolution [in/px]	Δx [in]	Δ(dP) [psi]	ΔPmin [psi]	Δ(dP/Pmin)
19	2.91E-03	4.12E-03	7.87E-01	7.50E-01	6.11E-03
20	2.91E-03	4.12E-03	7.87E-01	7.50E-01	6.02E-03
21	2.91E-03	4.12E-03	7.87E-01	7.50E-01	5.99E-03
22	2.91E-03	4.12E-03	7.87E-01	7.50E-01	6.01E-03
23	2.91E-03	4.12E-03	7.87E-01	7.50E-01	5.99E-03
24	2.91E-03	4.12E-03	7.87E-01	7.50E-01	6.23E-03
25	2.91E-03	4.12E-03	7.87E-01	7.50E-01	6.19E-03
26	2.91E-03	4.12E-03	7.87E-01	7.50E-01	6.17E-03
27	2.91E-03	4.12E-03	7.87E-01	7.50E-01	6.17E-03
28	2.91E-03	4.12E-03	7.87E-01	7.50E-01	6.18E-03
29	2.91E-03	4.12E-03	7.87E-01	7.50E-01	6.43E-03
30	2.91E-03	4.12E-03	7.87E-01	7.50E-01	6.44E-03
31	2.91E-03	4.12E-03	7.87E-01	7.50E-01	6.37E-03
32	2.91E-03	4.12E-03	7.87E-01	7.50E-01	6.31E-03
33	2.91E-03	4.12E-03	7.87E-01	7.50E-01	6.27E-03
34	2.91E-03	4.12E-03	7.87E-01	7.50E-01	6.59E-03
35	2.91E-03	4.12E-03	7.87E-01	7.50E-01	6.56E-03
36	2.91E-03	4.12E-03	7.87E-01	7.50E-01	6.58E-03
37	2.91E-03	4.12E-03	7.87E-01	7.50E-01	6.55E-03
38	2.91E-03	4.12E-03	7.87E-01	7.50E-01	6.60E-03
39	2.91E-03	4.12E-03	7.87E-01	7.50E-01	6.91E-03
40	2.91E-03	4.12E-03	7.87E-01	7.50E-01	6.87E-03
41	2.91E-03	4.12E-03	7.87E-01	7.50E-01	6.83E-03
42	2.91E-03	4.12E-03	7.87E-01	7.50E-01	6.85E-03
43	2.91E-03	4.12E-03	7.87E-01	7.50E-01	6.77E-03
45	2.91E-03	4.12E-03	7.87E-01	7.50E-01	7.25E-03
46	2.91E-03	4.12E-03	7.87E-01	7.50E-01	7.22E-03
47	2.91E-03	4.12E-03	7.87E-01	7.50E-01	7.13E-03
48	2.91E-03	4.12E-03	7.87E-01	7.50E-01	7.10E-03
49	2.91E-03	4.12E-03	7.87E-01	7.50E-01	7.24E-03
50	2.91E-03	4.12E-03	7.87E-01	7.50E-01	7.54E-03
51	2.91E-03	4.12E-03	7.87E-01	7.50E-01	7.46E-03
52	2.91E-03	4.12E-03	7.87E-01	7.50E-01	7.40E-03
53	2.91E-03	4.12E-03	7.87E-01	7.50E-01	7.52E-03
54	2.91E-03	4.12E-03	7.87E-01	7.50E-01	7.43E-03
55	2.91E-03	4.12E-03	7.87E-01	7.50E-01	7.94E-03
56	2.91E-03	4.12E-03	7.87E-01	7.50E-01	7.81E-03
57	2.91E-03	4.12E-03	7.87E-01	7.50E-01	7.80E-03
58	2.91E-03	4.12E-03	7.87E-01	7.50E-01	7.83E-03
59	2.91E-03	4.12E-03	7.87E-01	7.50E-01	7.77E-03

Table A.6. Uncertainty values of parameters associated with injector LD4 at initial ambient pressure of 100 psia utilizing hydrogen fuel.

Test No.	Resolution [in/px]	Δx [in]	Δ(dP) [psi]	ΔPmin [psi]	Δ(dP/Pmin)
11	2.16E-03	3.06E-03	7.87E-01	7.50E-01	9.84E-03
12	2.16E-03	3.06E-03	7.87E-01	7.50E-01	9.85E-03
13	2.16E-03	3.06E-03	7.87E-01	7.50E-01	9.84E-03
14	2.16E-03	3.06E-03	7.87E-01	7.50E-01	9.83E-03
15	2.16E-03	3.06E-03	7.87E-01	7.50E-01	9.83E-03
16	2.16E-03	3.06E-03	7.87E-01	7.50E-01	1.04E-02
18	2.16E-03	3.06E-03	7.87E-01	7.50E-01	1.01E-02
19	2.16E-03	3.06E-03	7.87E-01	7.50E-01	1.02E-02
20	2.16E-03	3.06E-03	7.87E-01	7.50E-01	1.01E-02
21	2.16E-03	3.06E-03	7.87E-01	7.50E-01	1.06E-02
22	2.16E-03	3.06E-03	7.87E-01	7.50E-01	1.06E-02
23	2.16E-03	3.06E-03	7.87E-01	7.50E-01	1.04E-02
24	2.16E-03	3.06E-03	7.87E-01	7.50E-01	1.04E-02
25	2.16E-03	3.06E-03	7.87E-01	7.50E-01	1.03E-02
26	2.16E-03	3.06E-03	7.87E-01	7.50E-01	1.08E-02
27	2.16E-03	3.06E-03	7.87E-01	7.50E-01	1.08E-02
28	2.16E-03	3.06E-03	7.87E-01	7.50E-01	1.07E-02
29	2.16E-03	3.06E-03	7.87E-01	7.50E-01	1.07E-02
30	2.16E-03	3.06E-03	7.87E-01	7.50E-01	1.07E-02
31	2.16E-03	3.06E-03	7.87E-01	7.50E-01	1.19E-02
32	2.16E-03	3.06E-03	7.87E-01	7.50E-01	1.20E-02
33	2.16E-03	3.06E-03	7.87E-01	7.50E-01	1.20E-02
34	2.16E-03	3.06E-03	7.87E-01	7.50E-01	1.20E-02
35	2.16E-03	3.06E-03	7.87E-01	7.50E-01	1.19E-02
36	2.16E-03	3.06E-03	7.87E-01	7.50E-01	1.24E-02
37	2.16E-03	3.06E-03	7.87E-01	7.50E-01	1.24E-02
38	2.16E-03	3.06E-03	7.87E-01	7.50E-01	1.25E-02
39	2.16E-03	3.06E-03	7.87E-01	7.50E-01	1.24E-02
40	2.16E-03	3.06E-03	7.87E-01	7.50E-01	1.25E-02
41	2.16E-03	3.06E-03	7.87E-01	7.50E-01	1.32E-02
42	2.16E-03	3.06E-03	7.87E-01	7.50E-01	1.31E-02
43	2.16E-03	3.06E-03	7.87E-01	7.50E-01	1.31E-02
44	2.16E-03	3.06E-03	7.87E-01	7.50E-01	1.30E-02
45	2.16E-03	3.06E-03	7.87E-01	7.50E-01	1.30E-02

Table A.7. Uncertainty values of parameters associated with injector LD4 at initial ambient pressure of 150 psia utilizing hydrogen fuel.

Test No.	Resolution [in/px]	Δx [in]	Δ(dP) [psi]	ΔPmin [psi]	Δ(dP/Pmin)
58	2.20E-03	3.11E-03	7.87E-01	7.50E-01	6.56E-03
59	2.20E-03	3.11E-03	7.87E-01	7.50E-01	6.58E-03
60	2.20E-03	3.11E-03	7.87E-01	7.50E-01	6.61E-03
61	2.20E-03	3.11E-03	7.87E-01	7.50E-01	6.59E-03
62	2.20E-03	3.11E-03	7.87E-01	7.50E-01	6.59E-03
63	2.20E-03	3.11E-03	7.87E-01	7.50E-01	6.94E-03
64	2.20E-03	3.11E-03	7.87E-01	7.50E-01	6.93E-03
65	2.20E-03	3.11E-03	7.87E-01	7.50E-01	6.91E-03
66	2.20E-03	3.11E-03	7.87E-01	7.50E-01	6.91E-03
67	2.20E-03	3.11E-03	7.87E-01	7.50E-01	6.92E-03
68	2.20E-03	3.11E-03	7.87E-01	7.50E-01	7.32E-03
69	2.20E-03	3.11E-03	7.87E-01	7.50E-01	7.27E-03
70	2.20E-03	3.11E-03	7.87E-01	7.50E-01	7.30E-03
71	2.20E-03	3.11E-03	7.87E-01	7.50E-01	7.29E-03
72	2.20E-03	3.11E-03	7.87E-01	7.50E-01	7.31E-03
73	2.20E-03	3.11E-03	7.87E-01	7.50E-01	7.71E-03
74	2.20E-03	3.11E-03	7.87E-01	7.50E-01	7.68E-03
75	2.20E-03	3.11E-03	7.87E-01	7.50E-01	7.64E-03
76	2.20E-03	3.11E-03	7.87E-01	7.50E-01	7.59E-03
77	2.20E-03	3.11E-03	7.87E-01	7.50E-01	7.60E-03
78	2.20E-03	3.11E-03	7.87E-01	7.50E-01	7.99E-03
79	2.20E-03	3.11E-03	7.87E-01	7.50E-01	7.87E-03
81	2.20E-03	3.11E-03	7.87E-01	7.50E-01	7.94E-03
82	2.20E-03	3.11E-03	7.87E-01	7.50E-01	7.87E-03
83	2.20E-03	3.11E-03	7.87E-01	7.50E-01	7.86E-03
84	2.20E-03	3.11E-03	7.87E-01	7.50E-01	8.37E-03
85	2.20E-03	3.11E-03	7.87E-01	7.50E-01	8.50E-03
86	2.20E-03	3.11E-03	7.87E-01	7.50E-01	8.47E-03
87	2.20E-03	3.11E-03	7.87E-01	7.50E-01	8.42E-03
88	2.20E-03	3.11E-03	7.87E-01	7.50E-01	8.59E-03
89	2.20E-03	3.11E-03	7.87E-01	7.50E-01	9.00E-03
90	2.20E-03	3.11E-03	7.87E-01	7.50E-01	8.95E-03
91	2.20E-03	3.11E-03	7.87E-01	7.50E-01	8.98E-03
92	2.20E-03	3.11E-03	7.87E-01	7.50E-01	9.02E-03
93	2.20E-03	3.11E-03	7.87E-01	7.50E-01	8.96E-03

Table A.8. Uncertainty values of parameters associated with injector LD10 at initial ambient pressure of 60 psia utilizing ethylene fuel.

Test No.	Resolution [in/px]	Δx [in]	Δ(dP) [psi]	ΔPmin [psi]	Δ(dP/Pmin)
6	3.23E-03	4.57E-03	7.87E-01	7.50E-01	1.48E-02
7	3.23E-03	4.57E-03	7.87E-01	7.50E-01	1.44E-02
8	3.23E-03	4.57E-03	7.87E-01	7.50E-01	1.46E-02
9	3.23E-03	4.57E-03	7.87E-01	7.50E-01	1.45E-02
10	3.23E-03	4.57E-03	7.87E-01	7.50E-01	1.46E-02
11	3.23E-03	4.57E-03	7.87E-01	7.50E-01	1.59E-02
12	3.23E-03	4.57E-03	7.87E-01	7.50E-01	1.56E-02
13	3.23E-03	4.57E-03	7.87E-01	7.50E-01	1.55E-02
14	3.23E-03	4.57E-03	7.87E-01	7.50E-01	1.54E-02
15	3.23E-03	4.57E-03	7.87E-01	7.50E-01	1.56E-02
16	3.23E-03	4.57E-03	7.87E-01	7.50E-01	1.53E-02
17	3.23E-03	4.57E-03	7.87E-01	7.50E-01	1.45E-02
18	3.23E-03	4.57E-03	7.87E-01	7.50E-01	1.42E-02
19	3.23E-03	4.57E-03	7.87E-01	7.50E-01	1.49E-02
20	3.23E-03	4.57E-03	7.87E-01	7.50E-01	1.46E-02
21	3.23E-03	4.57E-03	7.87E-01	7.50E-01	1.68E-02
22	3.23E-03	4.57E-03	7.87E-01	7.50E-01	1.65E-02
23	3.23E-03	4.57E-03	7.87E-01	7.50E-01	1.65E-02
24	3.23E-03	4.57E-03	7.87E-01	7.50E-01	1.65E-02
25	3.23E-03	4.57E-03	7.87E-01	7.50E-01	1.65E-02
26	3.23E-03	4.57E-03	7.87E-01	7.50E-01	1.82E-02
27	3.23E-03	4.57E-03	7.87E-01	7.50E-01	1.82E-02
28	3.23E-03	4.57E-03	7.87E-01	7.50E-01	1.80E-02
29	3.23E-03	4.57E-03	7.87E-01	7.50E-01	1.80E-02
30	3.23E-03	4.57E-03	7.87E-01	7.50E-01	1.79E-02
31	3.23E-03	4.57E-03	7.87E-01	7.50E-01	1.97E-02
32	3.23E-03	4.57E-03	7.87E-01	7.50E-01	1.96E-02
33	3.23E-03	4.57E-03	7.87E-01	7.50E-01	1.95E-02
34	3.23E-03	4.57E-03	7.87E-01	7.50E-01	1.96E-02
35	3.23E-03	4.57E-03	7.87E-01	7.50E-01	1.96E-02
37	3.23E-03	4.57E-03	7.87E-01	7.50E-01	2.26E-02
38	3.23E-03	4.57E-03	7.87E-01	7.50E-01	2.26E-02
39	3.23E-03	4.57E-03	7.87E-01	7.50E-01	2.23E-02

Table A.9. Uncertainty values of parameters associated with injector LD10 at initial ambient pressure of 100 psia utilizing ethylene fuel.

Test No.	Resolution [in/px]	Δx [in]	Δ(dP) [psi]	ΔPmin [psi]	Δ(dP/Pmin)
1	3.63E-03	5.13E-03	7.87E-01	7.50E-01	8.75E-03
2	3.63E-03	5.13E-03	7.87E-01	7.50E-01	9.02E-03
3	3.63E-03	5.13E-03	7.87E-01	7.50E-01	9.04E-03
4	3.63E-03	5.13E-03	7.87E-01	7.50E-01	9.05E-03
5	3.63E-03	5.13E-03	7.87E-01	7.50E-01	9.07E-03
6	3.63E-03	5.13E-03	7.87E-01	7.50E-01	9.51E-03
7	3.63E-03	5.13E-03	7.87E-01	7.50E-01	9.51E-03
8	3.63E-03	5.13E-03	7.87E-01	7.50E-01	9.49E-03
9	3.63E-03	5.13E-03	7.87E-01	7.50E-01	9.48E-03
10	3.63E-03	5.13E-03	7.87E-01	7.50E-01	9.52E-03
11	3.63E-03	5.13E-03	7.87E-01	7.50E-01	1.00E-02
12	3.63E-03	5.13E-03	7.87E-01	7.50E-01	1.00E-02
13	3.63E-03	5.13E-03	7.87E-01	7.50E-01	1.00E-02
14	3.63E-03	5.13E-03	7.87E-01	7.50E-01	1.00E-02
15	3.63E-03	5.13E-03	7.87E-01	7.50E-01	1.00E-02
16	3.63E-03	5.13E-03	7.87E-01	7.50E-01	1.06E-02
17	3.63E-03	5.13E-03	7.87E-01	7.50E-01	1.07E-02
18	3.63E-03	5.13E-03	7.87E-01	7.50E-01	1.07E-02
19	3.63E-03	5.13E-03	7.87E-01	7.50E-01	1.07E-02
20	3.63E-03	5.13E-03	7.87E-01	7.50E-01	1.07E-02
21	3.63E-03	5.13E-03	7.87E-01	7.50E-01	1.14E-02
22	3.63E-03	5.13E-03	7.87E-01	7.50E-01	1.14E-02
24	3.55E-03	5.02E-03	7.87E-01	7.50E-01	1.04E-02
25	3.55E-03	5.02E-03	7.87E-01	7.50E-01	1.07E-02
26	3.55E-03	5.02E-03	7.87E-01	7.50E-01	1.09E-02
27	3.55E-03	5.02E-03	7.87E-01	7.50E-01	1.14E-02
28	3.55E-03	5.02E-03	7.87E-01	7.50E-01	1.14E-02
29	3.55E-03	5.02E-03	7.87E-01	7.50E-01	1.14E-02
30	3.55E-03	5.02E-03	7.87E-01	7.50E-01	1.09E-02
31	3.55E-03	5.02E-03	7.87E-01	7.50E-01	1.08E-02
32	3.55E-03	5.02E-03	7.87E-01	7.50E-01	1.16E-02
33	3.55E-03	5.02E-03	7.87E-01	7.50E-01	1.17E-02
34	3.55E-03	5.02E-03	7.87E-01	7.50E-01	1.16E-02
35	3.55E-03	5.02E-03	7.87E-01	7.50E-01	1.17E-02
36	3.55E-03	5.02E-03	7.87E-01	7.50E-01	1.15E-02
37	3.55E-03	5.02E-03	7.87E-01	7.50E-01	1.23E-02
38	3.55E-03	5.02E-03	7.87E-01	7.50E-01	1.21E-02
39	3.55E-03	5.02E-03	7.87E-01	7.50E-01	1.23E-02
40	3.55E-03	5.02E-03	7.87E-01	7.50E-01	1.22E-02
41	3.55E-03	5.02E-03	7.87E-01	7.50E-01	1.23E-02
42	3.55E-03	5.02E-03	7.87E-01	7.50E-01	1.31E-02
46	3.33E-03	4.71E-03	7.87E-01	7.50E-01	1.26E-02
47	3.33E-03	4.71E-03	7.87E-01	7.50E-01	1.28E-02
48	3.33E-03	4.71E-03	7.87E-01	7.50E-01	1.26E-02

Table A.10. Uncertainty values of parameters associated with injector LD10 at initial ambient pressure of 100 psia utilizing ethylene fuel, continued.

Test No.	Resolution [in/px]	Δx [in]	Δ(dP) [psi]	ΔPmin [psi]	Δ(dP/Pmin)
49	3.33E-03	4.71E-03	7.87E-01	7.50E-01	1.33E-02
50	3.33E-03	4.71E-03	7.87E-01	7.50E-01	1.32E-02
51	3.33E-03	4.71E-03	7.87E-01	7.50E-01	1.32E-02
52	3.33E-03	4.71E-03	7.87E-01	7.50E-01	1.32E-02
53	3.33E-03	4.71E-03	7.87E-01	7.50E-01	1.33E-02
54	3.33E-03	4.71E-03	7.87E-01	7.50E-01	1.43E-02
55	3.33E-03	4.71E-03	7.87E-01	7.50E-01	1.42E-02
56	3.33E-03	4.71E-03	7.87E-01	7.50E-01	1.42E-02
57	3.33E-03	4.71E-03	7.87E-01	7.50E-01	1.42E-02
58	3.33E-03	4.71E-03	7.87E-01	7.50E-01	1.43E-02
59	3.33E-03	4.71E-03	7.87E-01	7.50E-01	1.53E-02
61	3.33E-03	4.71E-03	7.87E-01	7.50E-01	1.52E-02
62	3.33E-03	4.71E-03	7.87E-01	7.50E-01	1.51E-02
63	3.33E-03	4.71E-03	7.87E-01	7.50E-01	1.51E-02
64	3.33E-03	4.71E-03	7.87E-01	7.50E-01	1.64E-02
76	3.33E-03	4.71E-03	7.87E-01	7.50E-01	1.78E-02

Table A.11. Uncertainty values of parameters associated with injector LD10 at initial ambient pressure of 150 psia utilizing ethylene fuel.

Test No.	Resolution [in/px]	Δx [in]	Δ(dP) [psi]	ΔPmin [psi]	Δ(dP/Pmin)
1	3.30E-03	4.67E-03	7.87E-01	7.50E-01	6.32E-03
2	3.30E-03	4.67E-03	7.87E-01	7.50E-01	6.32E-03
3	3.30E-03	4.67E-03	7.87E-01	7.50E-01	6.25E-03
4	3.30E-03	4.67E-03	7.87E-01	7.50E-01	6.31E-03
5	3.30E-03	4.67E-03	7.87E-01	7.50E-01	6.32E-03
6	3.30E-03	4.67E-03	7.87E-01	7.50E-01	5.86E-03
7	3.30E-03	4.67E-03	7.87E-01	7.50E-01	6.33E-03
8	3.30E-03	4.67E-03	7.87E-01	7.50E-01	6.32E-03
9	3.30E-03	4.67E-03	7.87E-01	7.50E-01	6.31E-03
10	3.30E-03	4.67E-03	7.87E-01	7.50E-01	6.28E-03
11	3.30E-03	4.67E-03	7.87E-01	7.50E-01	6.72E-03
12	3.30E-03	4.67E-03	7.87E-01	7.50E-01	6.70E-03
13	3.30E-03	4.67E-03	7.87E-01	7.50E-01	6.69E-03
14	3.30E-03	4.67E-03	7.87E-01	7.50E-01	6.68E-03
15	3.30E-03	4.67E-03	7.87E-01	7.50E-01	6.70E-03
16	3.30E-03	4.67E-03	7.87E-01	7.50E-01	6.30E-03
17	3.30E-03	4.67E-03	7.87E-01	7.50E-01	6.65E-03
18	3.30E-03	4.67E-03	7.87E-01	7.50E-01	6.65E-03
19	3.30E-03	4.67E-03	7.87E-01	7.50E-01	6.32E-03
20	3.30E-03	4.67E-03	7.87E-01	7.50E-01	6.66E-03

Table A.12. Uncertainty values of parameters associated with injector LD10 at initial ambient pressure of 150 psia utilizing ethylene fuel, continued.

Test No.	Resolution [in/px]	Δx [in]	Δ(dP) [psi]	ΔPmin [psi]	Δ(dP/Pmin)
21	3.30E-03	4.67E-03	7.87E-01	7.50E-01	6.98E-03
22	3.30E-03	4.67E-03	7.87E-01	7.50E-01	6.49E-03
23	3.30E-03	4.67E-03	7.87E-01	7.50E-01	6.51E-03
24	3.30E-03	4.67E-03	7.87E-01	7.50E-01	6.79E-03
25	3.30E-03	4.67E-03	7.87E-01	7.50E-01	6.75E-03
26	3.30E-03	4.67E-03	7.87E-01	7.50E-01	7.16E-03
27	3.30E-03	4.67E-03	7.87E-01	7.50E-01	7.00E-03
28	3.30E-03	4.67E-03	7.87E-01	7.50E-01	7.01E-03
29	3.30E-03	4.67E-03	7.87E-01	7.50E-01	7.03E-03
30	3.30E-03	4.67E-03	7.87E-01	7.50E-01	6.96E-03
31	3.30E-03	4.67E-03	7.87E-01	7.50E-01	6.74E-03
32	3.30E-03	4.67E-03	7.87E-01	7.50E-01	7.14E-03
33	3.30E-03	4.67E-03	7.87E-01	7.50E-01	7.17E-03
34	3.30E-03	4.67E-03	7.87E-01	7.50E-01	7.25E-03
35	3.30E-03	4.67E-03	7.87E-01	7.50E-01	7.29E-03
36	3.30E-03	4.67E-03	7.87E-01	7.50E-01	7.42E-03
37	3.30E-03	4.67E-03	7.87E-01	7.50E-01	7.59E-03
38	3.30E-03	4.67E-03	7.87E-01	7.50E-01	7.59E-03
39	3.30E-03	4.67E-03	7.87E-01	7.50E-01	7.53E-03
40	3.30E-03	4.67E-03	7.87E-01	7.50E-01	7.57E-03
41	3.30E-03	4.67E-03	7.87E-01	7.50E-01	7.67E-03
42	3.30E-03	4.67E-03	7.87E-01	7.50E-01	7.73E-03
43	3.30E-03	4.67E-03	7.87E-01	7.50E-01	7.76E-03
44	3.30E-03	4.67E-03	7.87E-01	7.50E-01	7.67E-03
45	3.30E-03	4.67E-03	7.87E-01	7.50E-01	7.80E-03
46	3.30E-03	4.67E-03	7.87E-01	7.50E-01	8.18E-03
47	3.30E-03	4.67E-03	7.87E-01	7.50E-01	8.10E-03
48	3.30E-03	4.67E-03	7.87E-01	7.50E-01	8.27E-03
49	3.30E-03	4.67E-03	7.87E-01	7.50E-01	8.16E-03
50	3.30E-03	4.67E-03	7.87E-01	7.50E-01	8.11E-03
51	3.30E-03	4.67E-03	7.87E-01	7.50E-01	8.78E-03
52	3.11E-03	4.40E-03	7.87E-01	7.50E-01	8.63E-03
53	3.11E-03	4.40E-03	7.87E-01	7.50E-01	9.06E-03
54	3.11E-03	4.40E-03	7.87E-01	7.50E-01	8.99E-03
55	3.11E-03	4.40E-03	7.87E-01	7.50E-01	8.60E-03
56	3.11E-03	4.40E-03	7.87E-01	7.50E-01	8.97E-03
57	3.11E-03	4.40E-03	7.87E-01	7.50E-01	8.97E-03
58	3.11E-03	4.40E-03	7.87E-01	7.50E-01	9.68E-03
59	3.11E-03	4.40E-03	7.87E-01	7.50E-01	9.72E-03
60	3.11E-03	4.40E-03	7.87E-01	7.50E-01	9.73E-03
61	3.11E-03	4.40E-03	7.87E-01	7.50E-01	1.01E-02
63	3.11E-03	4.40E-03	7.87E-01	7.50E-01	9.56E-03
64	3.11E-03	4.40E-03	7.87E-01	7.50E-01	9.70E-03
65	3.11E-03	4.40E-03	7.87E-01	7.50E-01	9.49E-03
68	3.11E-03	4.40E-03	7.87E-01	7.50E-01	9.99E-03
69	3.11E-03	4.40E-03	7.87E-01	7.50E-01	1.01E-02
70	3.11E-03	4.40E-03	7.87E-01	7.50E-01	9.91E-03
75	3.11E-03	4.40E-03	7.87E-01	7.50E-01	1.06E-02
80	3.11E-03	4.40E-03	7.87E-01	7.50E-01	1.09E-02

Table A.13. Uncertainty values of parameters associated with injector LD6 at initial ambient pressure of 60 psia utilizing ethylene fuel.

Test No.	Resolution [in/px]	Δx [in]	Δ(dP) [psi]	ΔPmin [psi]	Δ(dP/Pmin)
1	3.76E-03	5.32E-03	7.87E-01	7.50E-01	1.86E-02
2	3.76E-03	5.32E-03	7.87E-01	7.50E-01	1.89E-02
3	3.76E-03	5.32E-03	7.87E-01	7.50E-01	1.84E-02
4	3.76E-03	5.32E-03	7.87E-01	7.50E-01	1.82E-02
5	3.76E-03	5.32E-03	7.87E-01	7.50E-01	1.82E-02

Table A.14. Uncertainty values of parameters associated with injector LD6 at initial ambient pressure of 100 psia utilizing ethylene fuel.

Test No.	Resolution [in/px]	Δx [in]	Δ(dP) [psi]	ΔPmin [psi]	Δ(dP/Pmin)
1	2.51E-03	3.54E-03	7.87E-01	7.50E-01	1.14E-02
2	2.51E-03	3.54E-03	7.87E-01	7.50E-01	1.14E-02
3	2.51E-03	3.54E-03	7.87E-01	7.50E-01	1.13E-02
4	2.51E-03	3.54E-03	7.87E-01	7.50E-01	1.16E-02
5	2.51E-03	3.54E-03	7.87E-01	7.50E-01	1.16E-02
6	2.51E-03	3.54E-03	7.87E-01	7.50E-01	1.19E-02
7	2.51E-03	3.54E-03	7.87E-01	7.50E-01	1.17E-02
8	2.51E-03	3.54E-03	7.87E-01	7.50E-01	1.16E-02
9	2.51E-03	3.54E-03	7.87E-01	7.50E-01	1.17E-02
10	2.51E-03	3.54E-03	7.87E-01	7.50E-01	1.19E-02
11	2.51E-03	3.54E-03	7.87E-01	7.50E-01	1.29E-02
12	2.51E-03	3.54E-03	7.87E-01	7.50E-01	1.28E-02
13	2.51E-03	3.54E-03	7.87E-01	7.50E-01	1.27E-02
14	2.51E-03	3.54E-03	7.87E-01	7.50E-01	1.27E-02
15	2.51E-03	3.54E-03	7.87E-01	7.50E-01	1.27E-02
16	2.51E-03	3.54E-03	7.87E-01	7.50E-01	1.32E-02
17	2.51E-03	3.54E-03	7.87E-01	7.50E-01	1.30E-02
19	2.51E-03	3.54E-03	7.87E-01	7.50E-01	1.34E-02
20	2.51E-03	3.54E-03	7.87E-01	7.50E-01	1.32E-02

Table A.15. Uncertainty values of parameters associated with injector LD6-1.5S at initial ambient pressure of 60 psia utilizing ethylene fuel.

Test No.	Resolution [in/px]	Δx [in]	Δ(dP) [psi]	ΔPmin [psi]	Δ(dP/Pmin)
1	2.77E-03	3.92E-03	7.87E-01	7.50E-01	1.46E-02
2	2.77E-03	3.92E-03	7.87E-01	7.50E-01	1.46E-02
3	2.77E-03	3.92E-03	7.87E-01	7.50E-01	1.45E-02
4	2.77E-03	3.92E-03	7.87E-01	7.50E-01	1.43E-02
5	2.77E-03	3.92E-03	7.87E-01	7.50E-01	1.43E-02
6	2.77E-03	3.92E-03	7.87E-01	7.50E-01	1.39E-02
7	2.77E-03	3.92E-03	7.87E-01	7.50E-01	1.36E-02
8	2.77E-03	3.92E-03	7.87E-01	7.50E-01	1.37E-02
9	2.77E-03	3.92E-03	7.87E-01	7.50E-01	1.36E-02
10	2.77E-03	3.92E-03	7.87E-01	7.50E-01	1.36E-02
11	2.77E-03	3.92E-03	7.87E-01	7.50E-01	1.35E-02
13	2.77E-03	3.92E-03	7.87E-01	7.50E-01	1.36E-02
16	2.77E-03	3.92E-03	7.87E-01	7.50E-01	1.52E-02
17	2.77E-03	3.92E-03	7.87E-01	7.50E-01	1.51E-02
18	2.77E-03	3.92E-03	7.87E-01	7.50E-01	1.48E-02
19	2.77E-03	3.92E-03	7.87E-01	7.50E-01	1.50E-02
20	2.77E-03	3.92E-03	7.87E-01	7.50E-01	1.49E-02
21	2.77E-03	3.92E-03	7.87E-01	7.50E-01	1.64E-02
22	2.77E-03	3.92E-03	7.87E-01	7.50E-01	1.60E-02
23	2.77E-03	3.92E-03	7.87E-01	7.50E-01	1.60E-02
24	2.77E-03	3.92E-03	7.87E-01	7.50E-01	1.59E-02
25	2.77E-03	3.92E-03	7.87E-01	7.50E-01	1.58E-02
26	2.77E-03	3.92E-03	7.87E-01	7.50E-01	1.80E-02
27	2.77E-03	3.92E-03	7.87E-01	7.50E-01	1.79E-02
28	2.77E-03	3.92E-03	7.87E-01	7.50E-01	1.76E-02
29	2.77E-03	3.92E-03	7.87E-01	7.50E-01	1.76E-02
30	2.77E-03	3.92E-03	7.87E-01	7.50E-01	1.76E-02
31	2.77E-03	3.92E-03	7.87E-01	7.50E-01	2.01E-02
32	2.77E-03	3.92E-03	7.87E-01	7.50E-01	1.96E-02
33	2.77E-03	3.92E-03	7.87E-01	7.50E-01	1.92E-02
34	2.80E-03	3.96E-03	7.87E-01	7.50E-01	1.94E-02
35	2.80E-03	3.96E-03	7.87E-01	7.50E-01	1.90E-02
36	2.80E-03	3.96E-03	7.87E-01	7.50E-01	2.27E-02
37	2.80E-03	3.96E-03	7.87E-01	7.50E-01	2.18E-02
38	2.80E-03	3.96E-03	7.87E-01	7.50E-01	2.15E-02
39	2.80E-03	3.96E-03	7.87E-01	7.50E-01	2.17E-02
40	2.80E-03	3.96E-03	7.87E-01	7.50E-01	2.15E-02
43	2.80E-03	3.96E-03	7.87E-01	7.50E-01	2.44E-02
45	2.80E-03	3.96E-03	7.87E-01	7.50E-01	2.46E-02

Table A.16. Uncertainty values of parameters associated with injector LD6-1.5S at initial ambient pressure of 100 psia utilizing ethylene fuel.

Test No.	Resolution [in/px]	Δx [in]	Δ(dP) [psi]	ΔPmin [psi]	Δ(dP/Pmin)
3	2.70E-03	3.82E-03	7.87E-01	7.50E-01	7.91E-03
4	2.70E-03	3.82E-03	7.87E-01	7.50E-01	7.89E-03
5	2.70E-03	3.82E-03	7.87E-01	7.50E-01	7.87E-03
6	2.70E-03	3.82E-03	7.87E-01	7.50E-01	7.85E-03
7	2.70E-03	3.82E-03	7.87E-01	7.50E-01	7.91E-03
8	2.70E-03	3.82E-03	7.87E-01	7.50E-01	8.30E-03
9	2.70E-03	3.82E-03	7.87E-01	7.50E-01	8.25E-03
10	2.70E-03	3.82E-03	7.87E-01	7.50E-01	8.26E-03
11	2.70E-03	3.82E-03	7.87E-01	7.50E-01	8.22E-03
12	2.70E-03	3.82E-03	7.87E-01	7.50E-01	8.23E-03
13	2.70E-03	3.82E-03	7.87E-01	7.50E-01	8.81E-03
14	2.70E-03	3.82E-03	7.87E-01	7.50E-01	8.81E-03
15	2.70E-03	3.82E-03	7.87E-01	7.50E-01	9.23E-03
16	2.70E-03	3.82E-03	7.87E-01	7.50E-01	8.99E-03
17	2.70E-03	3.82E-03	7.87E-01	7.50E-01	9.21E-03
18	2.70E-03	3.82E-03	7.87E-01	7.50E-01	9.68E-03
19	2.70E-03	3.82E-03	7.87E-01	7.50E-01	1.01E-02
20	2.70E-03	3.82E-03	7.87E-01	7.50E-01	1.00E-02
21	2.70E-03	3.82E-03	7.87E-01	7.50E-01	9.67E-03
22	2.70E-03	3.82E-03	7.87E-01	7.50E-01	1.00E-02
23	2.70E-03	3.82E-03	7.87E-01	7.50E-01	1.09E-02
24	2.70E-03	3.82E-03	7.87E-01	7.50E-01	1.09E-02
25	2.70E-03	3.82E-03	7.87E-01	7.50E-01	1.07E-02
26	2.70E-03	3.82E-03	7.87E-01	7.50E-01	1.08E-02
27	2.70E-03	3.82E-03	7.87E-01	7.50E-01	1.08E-02
28	2.70E-03	3.82E-03	7.87E-01	7.50E-01	1.19E-02
29	2.70E-03	3.82E-03	7.87E-01	7.50E-01	1.19E-02
30	2.70E-03	3.82E-03	7.87E-01	7.50E-01	1.18E-02
31	2.70E-03	3.82E-03	7.87E-01	7.50E-01	1.19E-02
32	2.70E-03	3.82E-03	7.87E-01	7.50E-01	1.19E-02
33	2.70E-03	3.82E-03	7.87E-01	7.50E-01	1.31E-02
34	2.70E-03	3.82E-03	7.87E-01	7.50E-01	1.29E-02
35	2.70E-03	3.82E-03	7.87E-01	7.50E-01	1.31E-02
36	2.70E-03	3.82E-03	7.87E-01	7.50E-01	1.32E-02
37	2.70E-03	3.82E-03	7.87E-01	7.50E-01	1.29E-02

Table A.17. Uncertainty values of parameters associated with injector LD6-1.5S at initial ambient pressure of 100 psia utilizing ethylene fuel, continued.

Test No.	Resolution [in/px]	Δx [in]	Δ(dP) [psi]	ΔPmin [psi]	Δ(dP/Pmin)
38	2.72E-03	3.85E-03	7.87E-01	7.50E-01	1.44E-02
39	2.72E-03	3.85E-03	7.87E-01	7.50E-01	1.44E-02
40	2.72E-03	3.85E-03	7.87E-01	7.50E-01	1.39E-02
41	2.72E-03	3.85E-03	7.87E-01	7.50E-01	1.42E-02
42	2.72E-03	3.85E-03	7.87E-01	7.50E-01	1.37E-02
43	2.72E-03	3.85E-03	7.87E-01	7.50E-01	1.50E-02
44	2.72E-03	3.85E-03	7.87E-01	7.50E-01	1.47E-02
45	2.72E-03	3.85E-03	7.87E-01	7.50E-01	1.51E-02
46	2.72E-03	3.85E-03	7.87E-01	7.50E-01	1.50E-02
47	2.72E-03	3.85E-03	7.87E-01	7.50E-01	1.49E-02
48	2.72E-03	3.85E-03	7.87E-01	7.50E-01	1.61E-02
49	2.72E-03	3.85E-03	7.87E-01	7.50E-01	1.59E-02
50	2.72E-03	3.85E-03	7.87E-01	7.50E-01	1.61E-02

Table A.18. Uncertainty values of parameters associated with injector LD6-1.5S at initial ambient pressure of 150 psia utilizing ethylene fuel.

Test No.	Resolution [in/px]	Δx [in]	Δ(dP) [psi]	ΔPmin [psi]	Δ(dP/Pmin)
58	2.72E-03	3.85E-03	7.87E-01	7.50E-01	5.99E-03
59	2.72E-03	3.85E-03	7.87E-01	7.50E-01	5.92E-03
60	2.72E-03	3.85E-03	7.87E-01	7.50E-01	6.03E-03
61	2.72E-03	3.85E-03	7.87E-01	7.50E-01	6.03E-03
62	2.72E-03	3.85E-03	7.87E-01	7.50E-01	5.52E-03

Table A.19. Uncertainty values of detonation wave speed and total mass flow rate in the RDE hotfire tests.

	Wave Speed		Total Mass Flow	
Test No.	Δv/v	Δv [m/s]	Δmdot/mdot	Δmdot [kg/s]
39	N/A	N/A	1.81E-02	2.15E-02
41	N/A	N/A	1.81E-02	2.12E-02
42	N/A	N/A	1.82E-02	1.96E-02
43	N/A	N/A	1.81E-02	2.12E-02
44	N/A	N/A	1.83E-02	2.11E-02
45	N/A	N/A	1.82E-02	2.13E-02
46	N/A	N/A	1.84E-02	2.15E-02
47	4.44E-02	7.92E+01	1.81E-02	2.14E-02
48	4.18E-02	7.02E+01	1.81E-02	2.04E-02
49	4.37E-02	7.68E+01	1.81E-02	2.17E-02
50	4.44E-02	7.92E+01	1.81E-02	2.16E-02
51	4.44E-02	7.92E+01	1.82E-02	2.19E-02
52	4.44E-02	7.92E+01	1.84E-02	2.17E-02
53	4.18E-02	7.02E+01	1.66E-02	2.95E-02
54	3.94E-02	6.26E+01	1.65E-02	2.86E-02
55	3.74E-02	5.62E+01	1.66E-02	2.85E-02
56	3.46E-02	4.83E+01	1.68E-02	2.91E-02
57	3.74E-02	5.62E+01	1.70E-02	2.96E-02
58	3.55E-02	5.07E+01	1.72E-02	2.99E-02
59	3.46E-02	4.83E+01	1.72E-02	3.00E-02
60	4.18E-02	7.02E+01	1.71E-02	3.90E-02
61	3.34E-02	4.49E+01	1.65E-02	3.90E-02
62	3.16E-02	4.01E+01	1.72E-02	3.00E-02
65	3.30E-02	4.39E+01	1.65E-02	2.85E-02
66	3.16E-02	4.01E+01	1.66E-02	2.86E-02
67	3.16E-02	4.01E+01	1.68E-02	2.91E-02
68	3.23E-02	4.19E+01	1.70E-02	2.95E-02
69	4.44E-02	7.92E+01	1.71E-02	2.93E-02
70	3.02E-02	3.67E+01	1.65E-02	2.90E-02
71	N/A	N/A	1.72E-02	3.61E-02
72	N/A	N/A	1.72E-02	3.35E-02
73	3.16E-02	4.01E+01	1.71E-02	3.24E-02
75	N/A	N/A	1.72E-02	3.30E-02
76	2.84E-02	3.25E+01	1.71E-02	2.94E-02
77	2.73E-02	3.00E+01	1.72E-02	2.95E-02
78	4.90E-02	9.65E+01	1.65E-02	2.83E-02
79	3.30E-02	4.39E+01	1.65E-02	2.82E-02
80	3.51E-02	4.95E+01	1.72E-02	3.06E-02
81	3.55E-02	5.07E+01	1.67E-02	2.88E-02
83	4.18E-02	7.02E+01	1.65E-02	2.96E-02
84	N/A	N/A	1.72E-02	3.01E-02
85	N/A	N/A	1.29E-02	5.92E-02
86	3.23E-02	4.19E+01	1.36E-02	4.92E-02
87	N/A	N/A	1.36E-02	4.89E-02
88	N/A	N/A	1.33E-02	4.59E-02

Table A.20. Uncertainty values of RP-2 mass flow rate in the RDE hotfire tests.

RP								
Test No.	EOS Δρ/ρ	NIST Δρ/ρ	Total Δρ/ρ	Δ(ρv)/(ρv)	ΔA/A	ΔCd/Cd	Δmdot/mdot	Δmdot [kg/s]
39	7.65E-03	1.00E-03	7.72E-03	3.93E-03	3.57E-02	5.00E-03	3.63E-02	7.47E-03
41	7.68E-03	1.00E-03	7.74E-03	3.95E-03	3.57E-02	5.00E-03	3.63E-02	7.22E-03
42	7.63E-03	1.00E-03	7.69E-03	3.91E-03	3.57E-02	5.00E-03	3.63E-02	7.84E-03
43	7.63E-03	1.00E-03	7.69E-03	3.91E-03	3.57E-02	5.00E-03	3.63E-02	7.84E-03
44	7.57E-03	1.00E-03	7.64E-03	3.86E-03	3.57E-02	5.00E-03	3.63E-02	9.03E-03
45	7.57E-03	1.00E-03	7.64E-03	3.85E-03	3.57E-02	5.00E-03	3.63E-02	9.07E-03
46	7.56E-03	1.00E-03	7.62E-03	3.84E-03	3.57E-02	5.00E-03	3.63E-02	9.57E-03
47	7.67E-03	1.00E-03	7.73E-03	3.95E-03	3.57E-02	5.00E-03	3.63E-02	7.36E-03
48	7.62E-03	1.00E-03	7.69E-03	3.90E-03	3.57E-02	5.00E-03	3.63E-02	7.98E-03
49	7.62E-03	1.00E-03	7.69E-03	3.90E-03	3.57E-02	5.00E-03	3.63E-02	7.98E-03
50	7.59E-03	1.00E-03	7.66E-03	3.87E-03	3.57E-02	5.00E-03	3.63E-02	8.56E-03
51	7.57E-03	1.00E-03	7.64E-03	3.85E-03	3.57E-02	5.00E-03	3.63E-02	9.14E-03
52	7.56E-03	1.00E-03	7.62E-03	3.84E-03	3.57E-02	5.00E-03	3.63E-02	9.72E-03
53	7.63E-03	1.00E-03	7.70E-03	3.92E-03	2.60E-02	5.00E-03	2.67E-02	1.07E-02
54	7.63E-03	1.00E-03	7.70E-03	3.91E-03	2.60E-02	5.00E-03	2.67E-02	1.08E-02
55	7.68E-03	1.00E-03	7.74E-03	3.96E-03	2.60E-02	5.00E-03	2.67E-02	1.00E-02
56	7.73E-03	1.00E-03	7.79E-03	4.01E-03	2.60E-02	5.00E-03	2.68E-02	9.42E-03
57	7.79E-03	1.00E-03	7.86E-03	4.07E-03	2.60E-02	5.00E-03	2.68E-02	8.83E-03
58	7.90E-03	1.00E-03	7.97E-03	4.18E-03	2.60E-02	5.00E-03	2.68E-02	8.17E-03
59	7.91E-03	1.00E-03	7.98E-03	4.18E-03	2.60E-02	5.00E-03	2.68E-02	8.11E-03
60	7.64E-03	1.00E-03	7.70E-03	3.92E-03	2.60E-02	5.00E-03	2.67E-02	1.07E-02
61	7.54E-03	1.00E-03	7.61E-03	3.83E-03	2.60E-02	5.00E-03	2.67E-02	1.43E-02
62	7.90E-03	1.00E-03	7.96E-03	4.17E-03	2.60E-02	5.00E-03	2.68E-02	8.17E-03
65	7.64E-03	1.00E-03	7.70E-03	3.92E-03	2.60E-02	5.00E-03	2.67E-02	1.07E-02
66	7.67E-03	1.00E-03	7.74E-03	3.95E-03	2.60E-02	5.00E-03	2.67E-02	1.01E-02
67	7.72E-03	1.00E-03	7.79E-03	4.00E-03	2.60E-02	5.00E-03	2.68E-02	9.48E-03
68	7.80E-03	1.00E-03	7.86E-03	4.07E-03	2.60E-02	5.00E-03	2.68E-02	8.78E-03
69	7.90E-03	1.00E-03	7.96E-03	4.17E-03	2.60E-02	5.00E-03	2.68E-02	8.14E-03
70	7.64E-03	1.00E-03	7.70E-03	3.92E-03	2.60E-02	5.00E-03	2.67E-02	1.07E-02
71	7.70E-03	1.00E-03	7.77E-03	3.98E-03	2.60E-02	5.00E-03	2.67E-02	9.66E-03
72	7.79E-03	1.00E-03	7.85E-03	4.06E-03	2.60E-02	5.00E-03	2.68E-02	8.86E-03
73	7.79E-03	1.00E-03	7.85E-03	4.06E-03	2.60E-02	5.00E-03	2.68E-02	8.88E-03
75	7.78E-03	1.00E-03	7.84E-03	4.06E-03	2.60E-02	5.00E-03	2.68E-02	8.91E-03
76	7.91E-03	1.00E-03	7.97E-03	4.18E-03	2.60E-02	5.00E-03	2.68E-02	8.11E-03
77	7.91E-03	1.00E-03	7.98E-03	4.18E-03	2.60E-02	5.00E-03	2.68E-02	8.06E-03
78	7.64E-03	1.00E-03	7.70E-03	3.92E-03	2.60E-02	5.00E-03	2.67E-02	1.08E-02
79	7.63E-03	1.00E-03	7.70E-03	3.92E-03	2.60E-02	5.00E-03	2.67E-02	1.08E-02
80	7.91E-03	1.00E-03	7.98E-03	4.18E-03	2.60E-02	5.00E-03	2.68E-02	8.11E-03
81	7.72E-03	1.00E-03	7.79E-03	4.00E-03	2.60E-02	5.00E-03	2.68E-02	9.52E-03
83	7.63E-03	1.00E-03	7.70E-03	3.91E-03	2.60E-02	5.00E-03	2.67E-02	1.08E-02
84	7.91E-03	1.00E-03	7.97E-03	4.18E-03	2.60E-02	5.00E-03	2.68E-02	8.09E-03
85	7.62E-03	1.00E-03	7.69E-03	3.90E-03	1.74E-02	5.00E-03	1.85E-02	1.70E-02
86	7.65E-03	1.00E-03	7.71E-03	3.93E-03	2.11E-02	5.00E-03	2.20E-02	1.32E-02
87	7.65E-03	1.00E-03	7.71E-03	3.93E-03	2.11E-02	5.00E-03	2.20E-02	1.31E-02
88	7.58E-03	1.00E-03	7.65E-03	3.86E-03	2.11E-02	5.00E-03	2.20E-02	1.53E-02

Table A.21. Uncertainty values of LOX mass flow rate in the RDE hotfire tests.

LOX								
Test No.	EOS Δρ/ρ	NIST Δρ/ρ	Total Δρ/ρ	Δ(ρv)/(ρv)	ΔA/A	ΔCd/Cd	Δmdot/mdot	Δmdot [kg/s]
39	1.64E-02	1.00E-03	1.65E-02	8.35E-03	1.85E-02	5.00E-03	2.09E-02	1.39E-02
41	1.64E-02	1.00E-03	1.65E-02	8.36E-03	1.85E-02	5.00E-03	2.09E-02	1.38E-02
42	1.66E-02	1.00E-03	1.67E-02	8.58E-03	1.85E-02	5.00E-03	2.10E-02	1.16E-02
43	1.65E-02	1.00E-03	1.65E-02	8.41E-03	1.85E-02	5.00E-03	2.09E-02	1.32E-02
44	1.66E-02	1.00E-03	1.67E-02	8.56E-03	1.85E-02	5.00E-03	2.10E-02	1.20E-02
45	1.66E-02	1.00E-03	1.66E-02	8.53E-03	1.85E-02	5.00E-03	2.10E-02	1.21E-02
46	1.66E-02	1.00E-03	1.67E-02	8.58E-03	1.85E-02	5.00E-03	2.10E-02	1.18E-02
47	1.64E-02	1.00E-03	1.65E-02	8.35E-03	1.85E-02	5.00E-03	2.09E-02	1.39E-02
48	1.66E-02	1.00E-03	1.66E-02	8.50E-03	1.85E-02	5.00E-03	2.10E-02	1.22E-02
49	1.65E-02	1.00E-03	1.65E-02	8.38E-03	1.85E-02	5.00E-03	2.09E-02	1.36E-02
50	1.65E-02	1.00E-03	1.66E-02	8.45E-03	1.85E-02	5.00E-03	2.10E-02	1.29E-02
51	1.65E-02	1.00E-03	1.66E-02	8.47E-03	1.85E-02	5.00E-03	2.10E-02	1.26E-02
52	1.66E-02	1.00E-03	1.67E-02	8.57E-03	1.85E-02	5.00E-03	2.10E-02	1.19E-02
53	1.63E-02	1.00E-03	1.63E-02	8.20E-03	1.85E-02	5.00E-03	2.09E-02	1.86E-02
54	1.63E-02	1.00E-03	1.63E-02	8.22E-03	1.85E-02	5.00E-03	2.09E-02	1.76E-02
55	1.63E-02	1.00E-03	1.63E-02	8.20E-03	1.85E-02	5.00E-03	2.09E-02	1.83E-02
56	1.63E-02	1.00E-03	1.63E-02	8.19E-03	1.85E-02	5.00E-03	2.09E-02	1.95E-02
57	1.63E-02	1.00E-03	1.63E-02	8.18E-03	1.85E-02	5.00E-03	2.09E-02	2.05E-02
58	1.63E-02	1.00E-03	1.63E-02	8.17E-03	1.85E-02	5.00E-03	2.08E-02	2.15E-02
59	1.63E-02	1.00E-03	1.63E-02	8.17E-03	1.85E-02	5.00E-03	2.08E-02	2.17E-02
60	1.62E-02	1.00E-03	1.63E-02	8.14E-03	1.85E-02	5.00E-03	2.08E-02	2.80E-02
61	1.62E-02	1.00E-03	1.63E-02	8.15E-03	1.85E-02	5.00E-03	2.08E-02	2.44E-02
62	1.63E-02	1.00E-03	1.63E-02	8.17E-03	1.85E-02	5.00E-03	2.08E-02	2.16E-02
65	1.63E-02	1.00E-03	1.63E-02	8.22E-03	1.85E-02	5.00E-03	2.09E-02	1.76E-02
66	1.63E-02	1.00E-03	1.63E-02	8.20E-03	1.85E-02	5.00E-03	2.09E-02	1.83E-02
67	1.63E-02	1.00E-03	1.63E-02	8.19E-03	1.85E-02	5.00E-03	2.09E-02	1.94E-02
68	1.63E-02	1.00E-03	1.63E-02	8.18E-03	1.85E-02	5.00E-03	2.09E-02	2.05E-02
69	1.63E-02	1.00E-03	1.63E-02	8.17E-03	1.85E-02	5.00E-03	2.08E-02	2.10E-02
70	1.63E-02	1.00E-03	1.63E-02	8.20E-03	1.85E-02	5.00E-03	2.09E-02	1.81E-02
71	1.62E-02	1.00E-03	1.63E-02	8.14E-03	1.85E-02	5.00E-03	2.08E-02	2.62E-02
72	1.62E-02	1.00E-03	1.63E-02	8.15E-03	1.85E-02	5.00E-03	2.08E-02	2.44E-02
73	1.62E-02	1.00E-03	1.63E-02	8.15E-03	1.85E-02	5.00E-03	2.08E-02	2.32E-02
75	1.62E-02	1.00E-03	1.63E-02	8.15E-03	1.85E-02	5.00E-03	2.08E-02	2.38E-02
76	1.63E-02	1.00E-03	1.63E-02	8.17E-03	1.85E-02	5.00E-03	2.08E-02	2.11E-02
77	1.63E-02	1.00E-03	1.63E-02	8.17E-03	1.85E-02	5.00E-03	2.08E-02	2.12E-02
78	1.63E-02	1.00E-03	1.63E-02	8.22E-03	1.85E-02	5.00E-03	2.09E-02	1.73E-02
79	1.63E-02	1.00E-03	1.63E-02	8.22E-03	1.85E-02	5.00E-03	2.09E-02	1.72E-02
80	1.63E-02	1.00E-03	1.63E-02	8.16E-03	1.85E-02	5.00E-03	2.08E-02	2.22E-02
81	1.63E-02	1.00E-03	1.63E-02	8.19E-03	1.85E-02	5.00E-03	2.09E-02	1.91E-02
83	1.63E-02	1.00E-03	1.63E-02	8.20E-03	1.85E-02	5.00E-03	2.09E-02	1.85E-02
84	1.63E-02	1.00E-03	1.63E-02	8.17E-03	1.85E-02	5.00E-03	2.08E-02	2.17E-02
85	1.62E-02	1.00E-03	1.63E-02	8.14E-03	1.32E-02	5.00E-03	1.63E-02	4.18E-02
86	1.63E-02	1.00E-03	1.63E-02	8.16E-03	1.32E-02	5.00E-03	1.63E-02	3.56E-02
87	1.63E-02	1.00E-03	1.63E-02	8.16E-03	1.32E-02	5.00E-03	1.63E-02	3.54E-02
88	1.63E-02	1.00E-03	1.63E-02	8.19E-03	1.32E-02	5.00E-03	1.64E-02	3.02E-02

Table A.22. Uncertainty values of preburner hydrogen mass flow rate in the RDE hotfire tests.

Preburner H2									
Test No.	p*	EOS Δρ*/ρ*	NIST Δρ*/ρ*	Total Δρ*/ρ*	ΔA*/A*	NIST Δa*/a*	ΔCd/Cd	Δmdot/mdot	Δmdot [kg/s]
39	4.65E+02	1.31E-02	4.00E-04	1.31E-02	5.13E-02	5.00E-03	5.00E-03	5.34E-02	1.55E-04
41	4.54E+02	1.33E-02	4.00E-04	1.33E-02	5.13E-02	5.00E-03	5.00E-03	5.35E-02	1.50E-04
42	4.34E+02	1.38E-02	4.00E-04	1.38E-02	5.13E-02	5.00E-03	5.00E-03	5.36E-02	1.45E-04
43	4.34E+02	1.37E-02	4.00E-04	1.37E-02	5.13E-02	5.00E-03	5.00E-03	5.36E-02	1.45E-04
44	3.89E+02	1.49E-02	4.00E-04	1.49E-02	5.13E-02	5.00E-03	5.00E-03	5.39E-02	1.29E-04
45	3.84E+02	1.50E-02	4.00E-04	1.50E-02	5.13E-02	5.00E-03	5.00E-03	5.39E-02	1.29E-04
46	3.84E+02	1.50E-02	4.00E-04	1.50E-02	5.13E-02	5.00E-03	5.00E-03	5.39E-02	1.29E-04
47	4.61E+02	1.32E-02	4.00E-04	1.32E-02	5.13E-02	5.00E-03	5.00E-03	5.34E-02	1.55E-04
48	4.27E+02	1.39E-02	4.00E-04	1.39E-02	5.13E-02	5.00E-03	5.00E-03	5.36E-02	1.45E-04
49	4.26E+02	1.39E-02	4.00E-04	1.39E-02	5.13E-02	5.00E-03	5.00E-03	5.36E-02	1.45E-04
50	4.06E+02	1.44E-02	4.00E-04	1.44E-02	5.13E-02	5.00E-03	5.00E-03	5.37E-02	1.34E-04
51	3.95E+02	1.47E-02	4.00E-04	1.47E-02	5.13E-02	5.00E-03	5.00E-03	5.38E-02	1.35E-04
52	3.70E+02	1.55E-02	4.00E-04	1.55E-02	5.13E-02	5.00E-03	5.00E-03	5.40E-02	1.30E-04
53	5.65E+02	1.16E-02	4.00E-04	1.16E-02	5.13E-02	5.00E-03	5.00E-03	5.31E-02	1.86E-04
54	5.67E+02	1.16E-02	4.00E-04	1.16E-02	5.13E-02	5.00E-03	5.00E-03	5.30E-02	1.86E-04
55	5.93E+02	1.13E-02	4.00E-04	1.13E-02	5.13E-02	5.00E-03	5.00E-03	5.30E-02	1.96E-04
56	6.17E+02	1.10E-02	4.00E-04	1.10E-02	5.13E-02	5.00E-03	5.00E-03	5.29E-02	2.06E-04
57	6.43E+02	1.08E-02	4.00E-04	1.08E-02	5.13E-02	5.00E-03	5.00E-03	5.29E-02	2.12E-04
58	6.82E+02	1.05E-02	4.00E-04	1.05E-02	5.13E-02	5.00E-03	5.00E-03	5.28E-02	2.27E-04
59	6.81E+02	1.05E-02	4.00E-04	1.05E-02	5.13E-02	5.00E-03	5.00E-03	5.28E-02	2.32E-04
60	9.03E+02	9.32E-03	4.00E-04	9.33E-03	5.13E-02	5.00E-03	5.00E-03	5.26E-02	2.95E-04
61	7.55E+02	1.00E-02	4.00E-04	1.00E-02	5.13E-02	5.00E-03	5.00E-03	5.27E-02	2.48E-04
62	6.85E+02	1.05E-02	4.00E-04	1.05E-02	5.13E-02	5.00E-03	5.00E-03	5.28E-02	2.27E-04
65	5.65E+02	1.16E-02	4.00E-04	1.16E-02	5.13E-02	5.00E-03	5.00E-03	5.31E-02	1.86E-04
66	6.00E+02	1.12E-02	4.00E-04	1.12E-02	5.13E-02	5.00E-03	5.00E-03	5.30E-02	1.96E-04
67	6.20E+02	1.10E-02	4.00E-04	1.10E-02	5.13E-02	5.00E-03	5.00E-03	5.29E-02	2.04E-04
68	6.51E+02	1.07E-02	4.00E-04	1.07E-02	5.13E-02	5.00E-03	5.00E-03	5.29E-02	2.17E-04
69	6.89E+02	1.04E-02	4.00E-04	1.04E-02	5.13E-02	5.00E-03	5.00E-03	5.28E-02	2.27E-04
70	5.67E+02	1.16E-02	4.00E-04	1.16E-02	5.13E-02	5.00E-03	5.00E-03	5.30E-02	1.86E-04
71	8.30E+02	9.62E-03	4.00E-04	9.63E-03	5.13E-02	5.00E-03	5.00E-03	5.27E-02	2.69E-04
72	7.59E+02	9.98E-03	4.00E-04	9.99E-03	5.13E-02	5.00E-03	5.00E-03	5.27E-02	2.48E-04
73	7.58E+02	9.99E-03	4.00E-04	1.00E-02	5.13E-02	5.00E-03	5.00E-03	5.27E-02	2.48E-04
75	7.58E+02	9.99E-03	4.00E-04	1.00E-02	5.13E-02	5.00E-03	5.00E-03	5.27E-02	2.48E-04
76	6.88E+02	1.04E-02	4.00E-04	1.05E-02	5.13E-02	5.00E-03	5.00E-03	5.28E-02	2.27E-04
77	6.88E+02	1.04E-02	4.00E-04	1.05E-02	5.13E-02	5.00E-03	5.00E-03	5.28E-02	2.27E-04
78	5.71E+02	1.15E-02	4.00E-04	1.15E-02	5.13E-02	5.00E-03	5.00E-03	5.30E-02	1.91E-04
79	5.72E+02	1.15E-02	4.00E-04	1.15E-02	5.13E-02	5.00E-03	5.00E-03	5.30E-02	1.91E-04
80	6.85E+02	1.05E-02	4.00E-04	1.05E-02	5.13E-02	5.00E-03	5.00E-03	5.28E-02	2.32E-04
81	6.23E+02	1.10E-02	4.00E-04	1.10E-02	5.13E-02	5.00E-03	5.00E-03	5.29E-02	2.12E-04
83	7.25E+02	1.02E-02	4.00E-04	1.02E-02	5.13E-02	5.00E-03	5.00E-03	5.28E-02	2.37E-04
84	8.75E+02	9.43E-03	4.00E-04	9.44E-03	5.13E-02	5.00E-03	5.00E-03	5.26E-02	2.89E-04
85	9.69E+02	9.10E-03	4.00E-04	9.11E-03	3.77E-02	5.00E-03	5.00E-03	3.95E-02	4.46E-04
86	9.66E+02	9.11E-03	4.00E-04	9.12E-03	4.26E-02	5.00E-03	5.00E-03	4.41E-02	3.88E-04
87	9.61E+02	9.13E-03	4.00E-04	9.14E-03	4.26E-02	5.00E-03	5.00E-03	4.41E-02	3.84E-04
88	8.66E+02	9.46E-03	4.00E-04	9.47E-03	4.26E-02	5.00E-03	5.00E-03	4.42E-02	3.49E-04

B. P&ID OF ZL2 TEST CELL C FACILITY

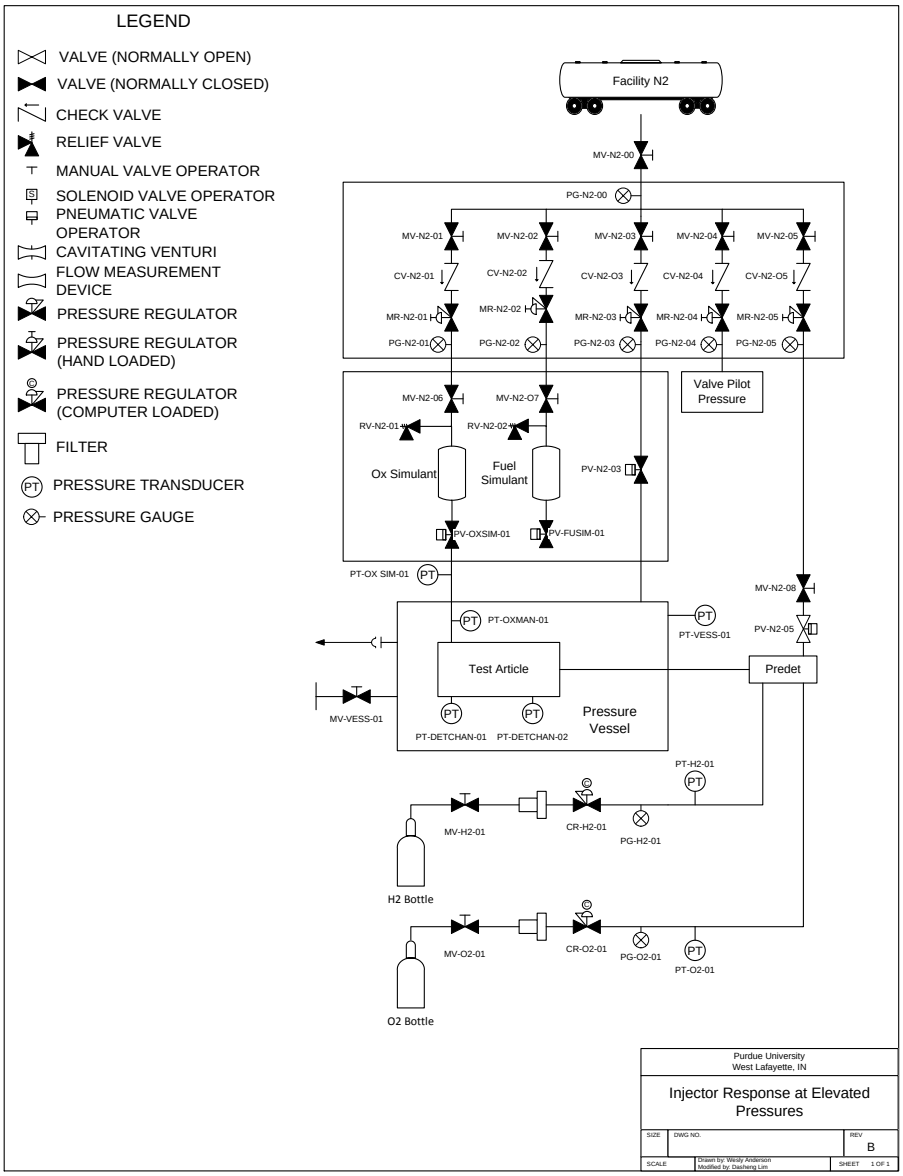

Figure B.1. P&ID of test facility in ZL2 Test Cell C.

C. ADDITIONAL FIGURES FROM INJECTOR RESPONSE EXPERIMENTS

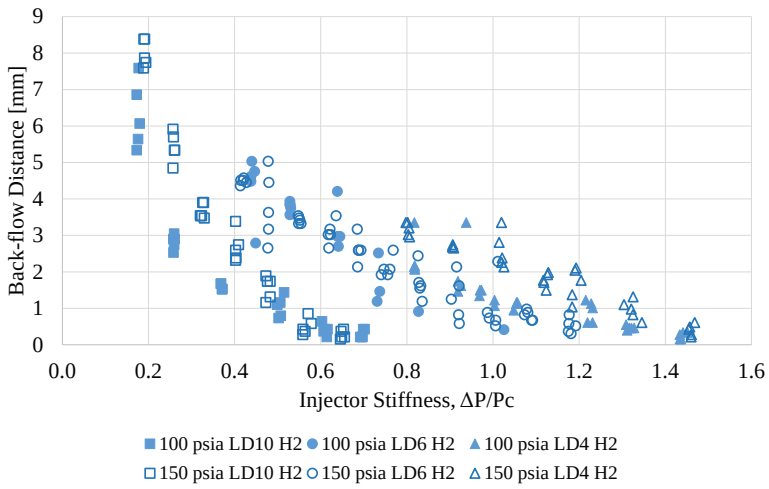

Figure C.1. Absolute back-flow distance vs. injector stiffness for tests conducted with hydrogen fuel.

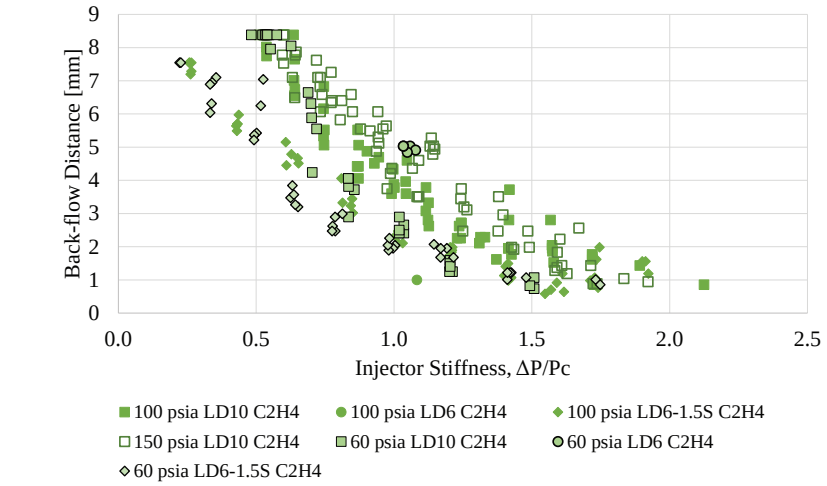

Figure C.2. Absolute back-flow distance vs. injector stiffness for tests conducted with ethylene fuel.

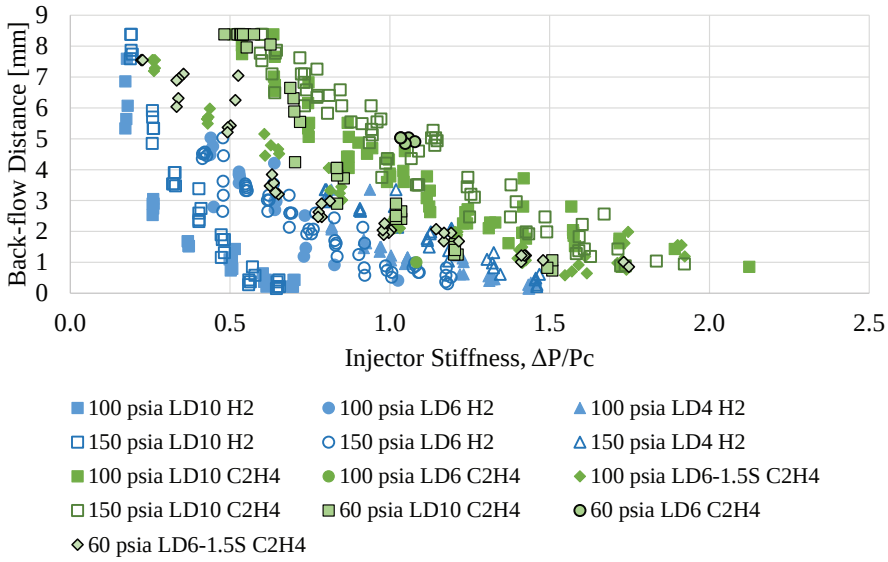

Figure C.3. Absolute back-flow distance vs. injector stiffness for all configurations tested.

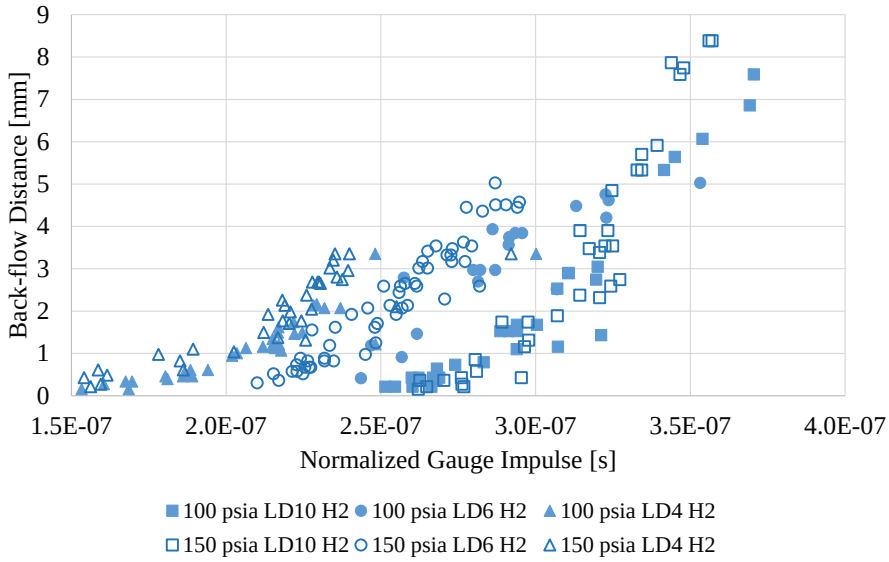

Figure C.4. Absolute back-flow distance vs. normalized gauge impulse for tests conducted with hydrogen fuel.

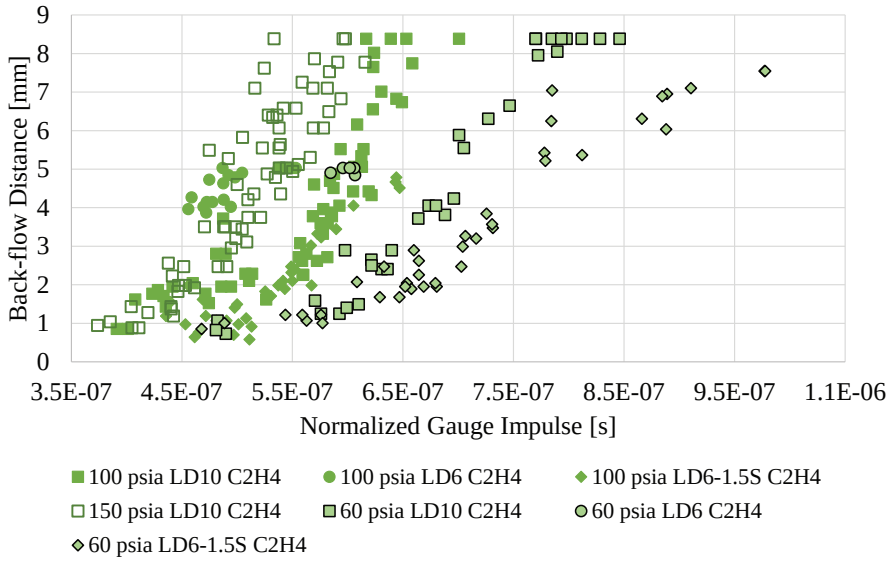

Figure C.5. Absolute back-flow distance vs. normalized gauge impulse for tests conducted with ethylene fuel.

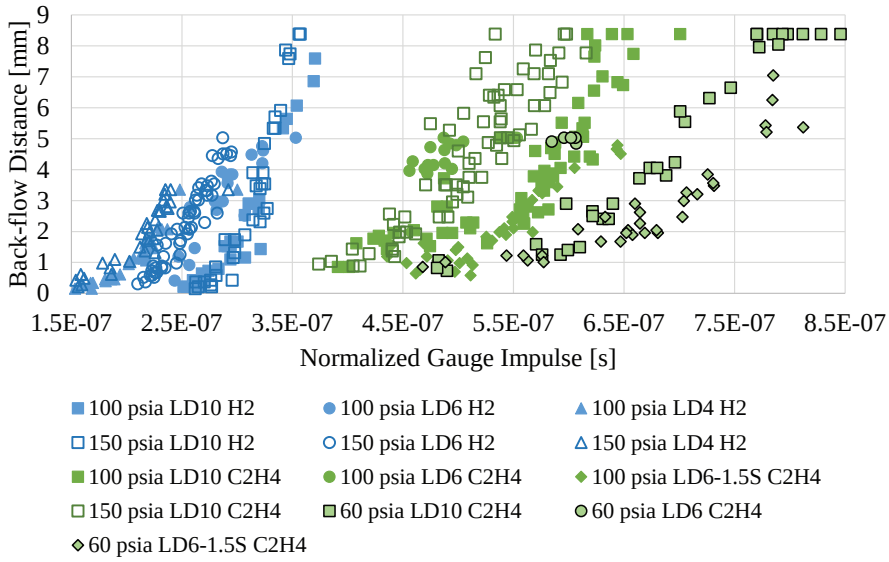

Figure C.6. Absolute back-flow distance vs. normalized gauge impulse for all configurations tested.

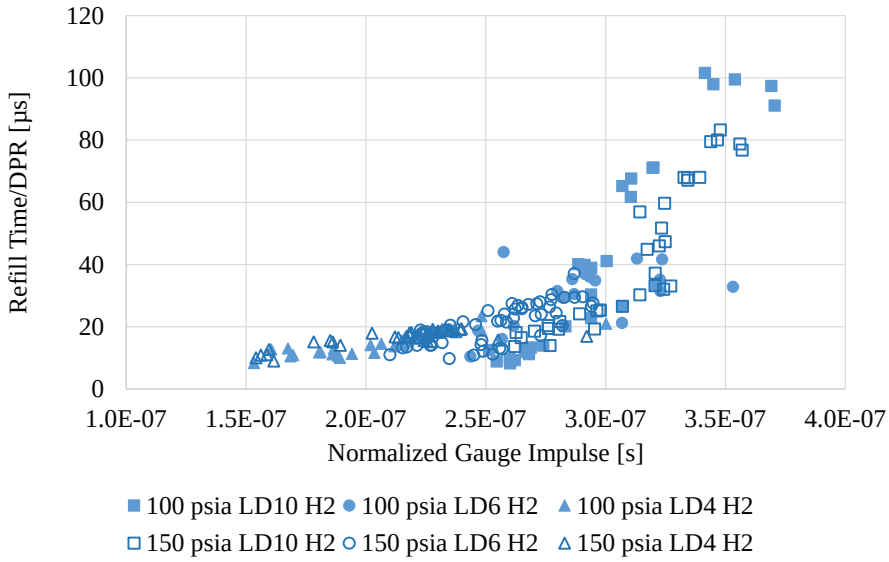

Figure C.7. Normalized refill time vs. normalized gauge impulse for tests conducted with hydrogen fuel.

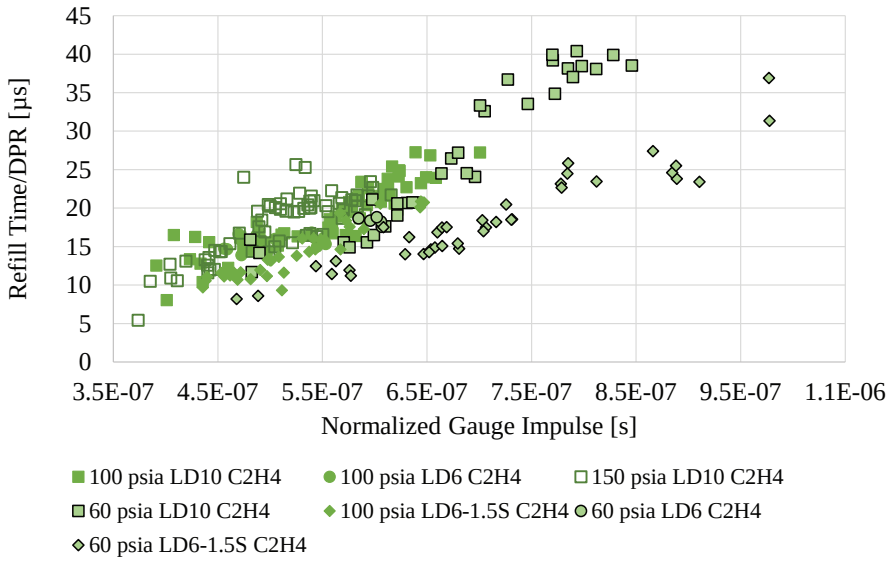

Figure C.8. Normalized refill time vs. normalized gauge impulse for tests conducted with ethylene fuel.

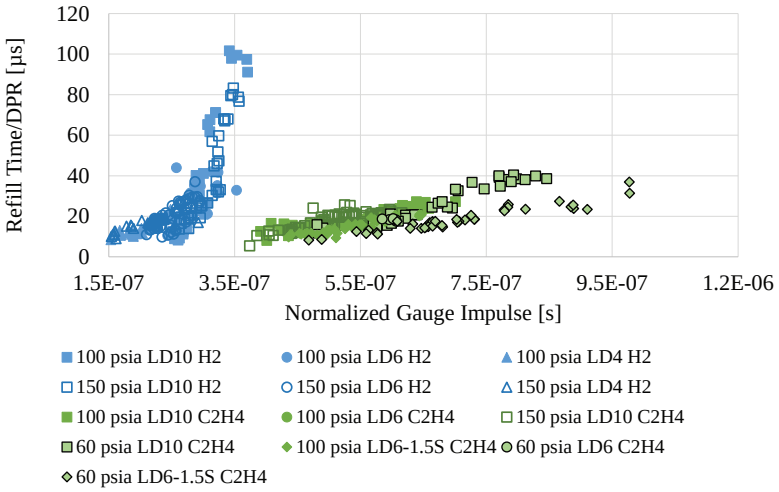

Figure C.9. Normalized refill time vs. normalized gauge impulse for all configurations tested.

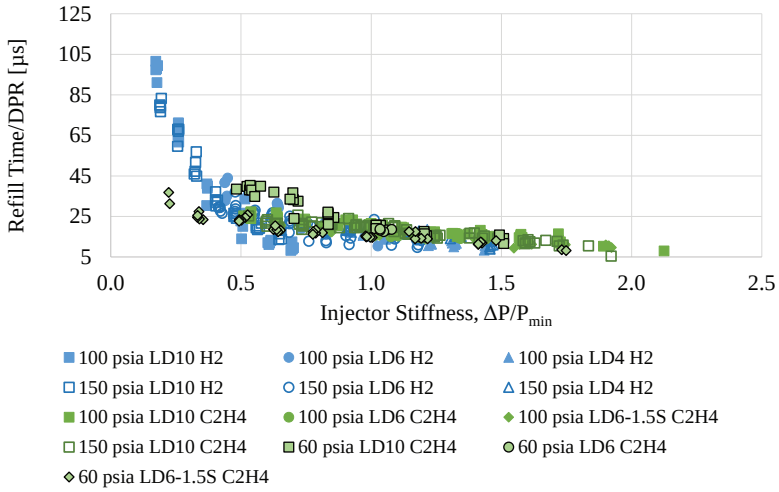

Figure C.10. Normalized refill time vs. injector stiffness for all configurations tested.

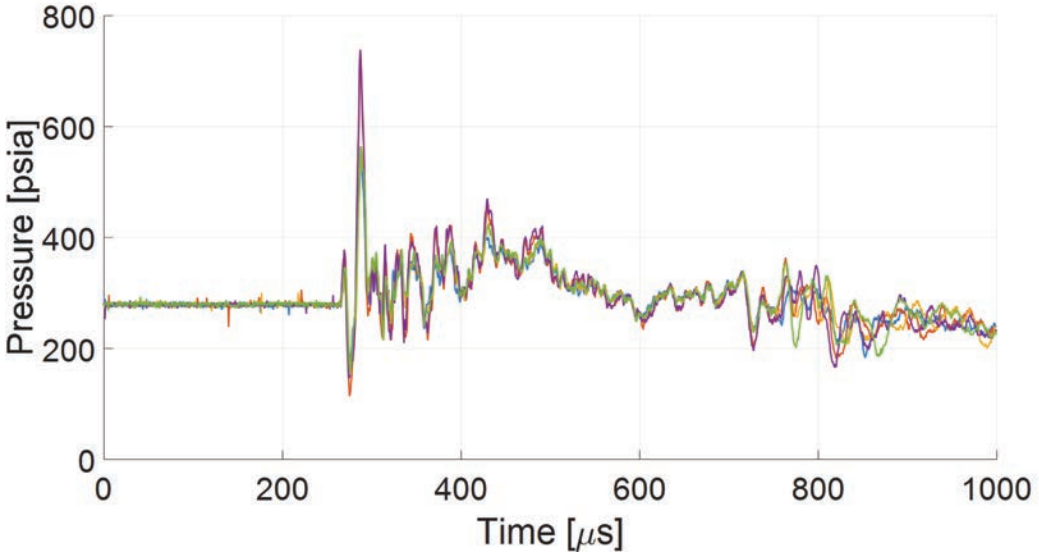

Figure C.11. Overlapping manifold pressure signals. Injector: LD6, fuel: hydrogen, initial pressure: 1,030 kPa (150 psia), ΔP: 876 kPa (127 psia).

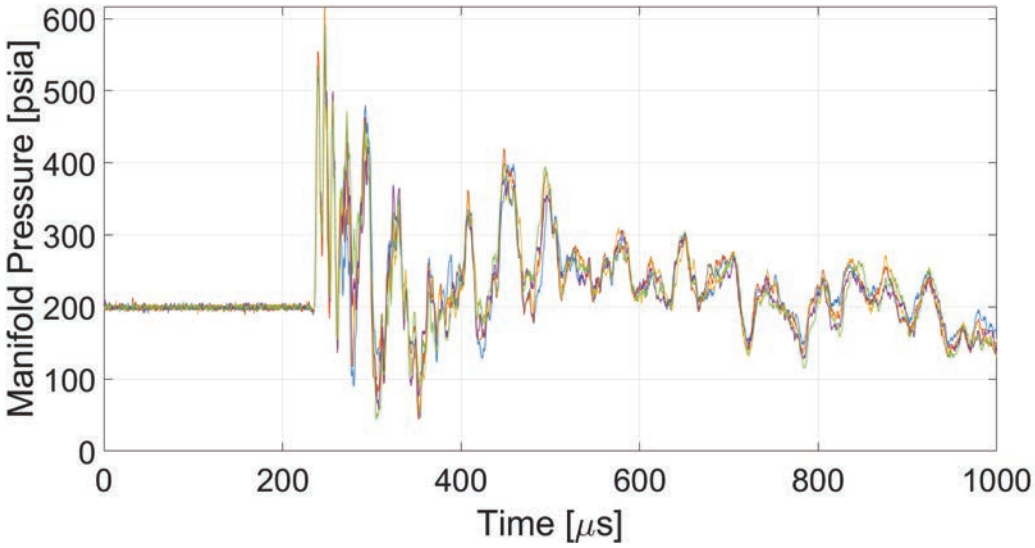

Figure C.12. Overlapping manifold pressure signals. Injector: LD10, fuel: ethylene, initial pressure: 690 kPa (100 psia), ΔP: 696 kPa (101 psia).

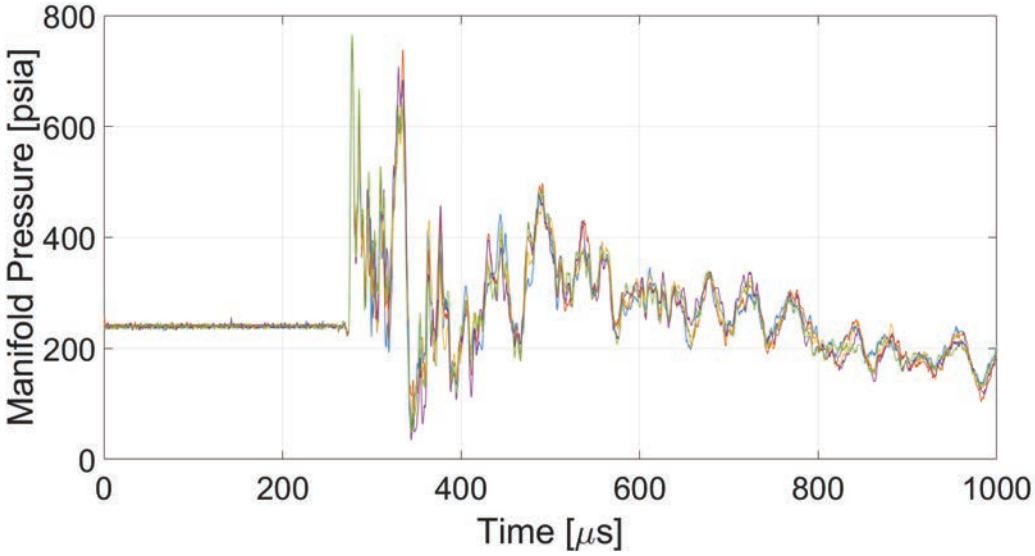

Figure C.13. Overlapping manifold pressure signals. Injector: LD10, fuel: ethylene, initial pressure: 1,030 kPa (150 psia), ΔP: 641 kPa (93 psia).

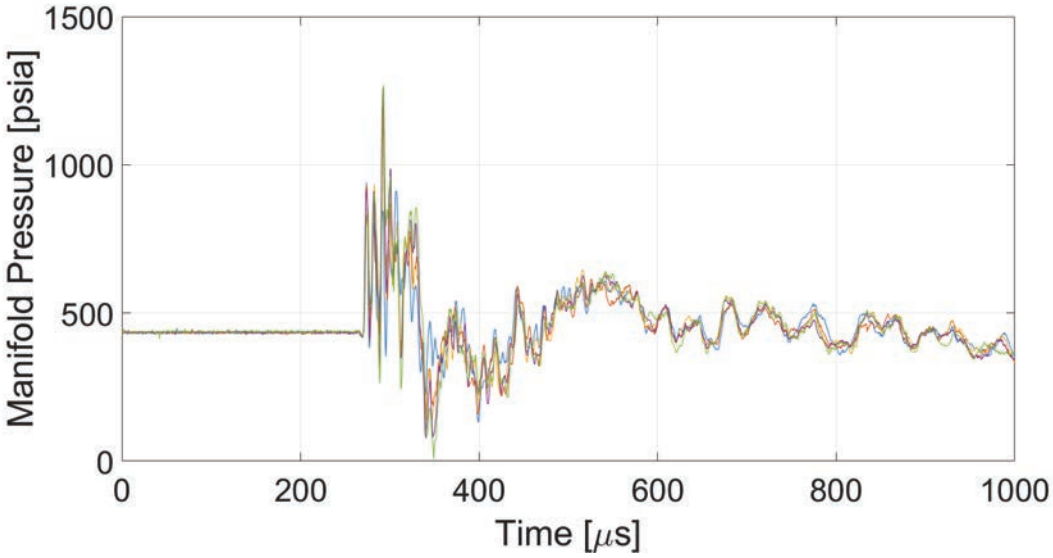

Figure C.14. Overlapping manifold pressure signals. Injector: LD10, fuel: ethylene, initial pressure: 1,030 kPa (150 psia), ΔP: 1,999 kPa (290 psia).

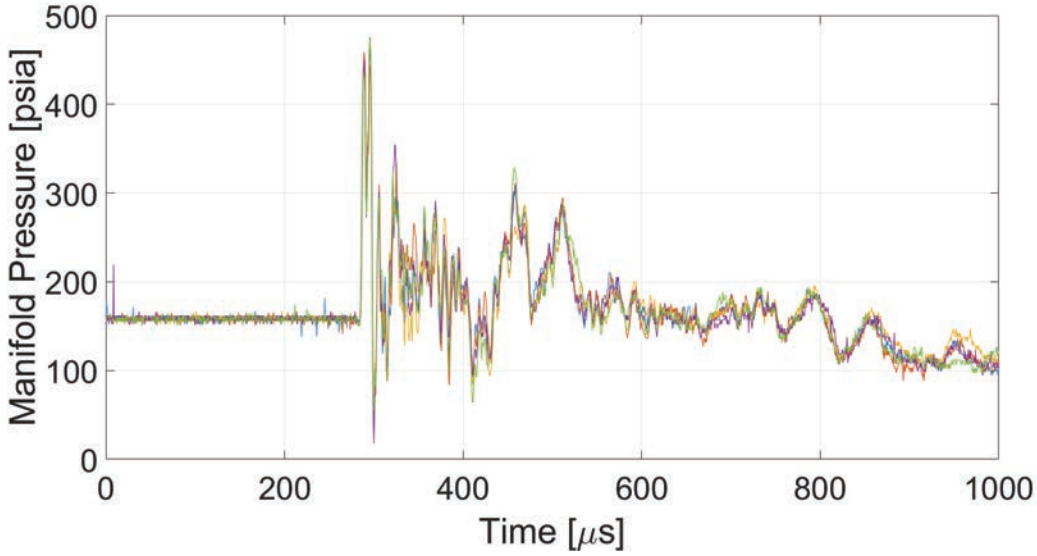

Figure C.15. Overlapping manifold pressure signals. Injector: LD6, fuel: ethylene, initial pressure: 414 kPa (60 psia), ΔP: 676 kPa (98 psia).

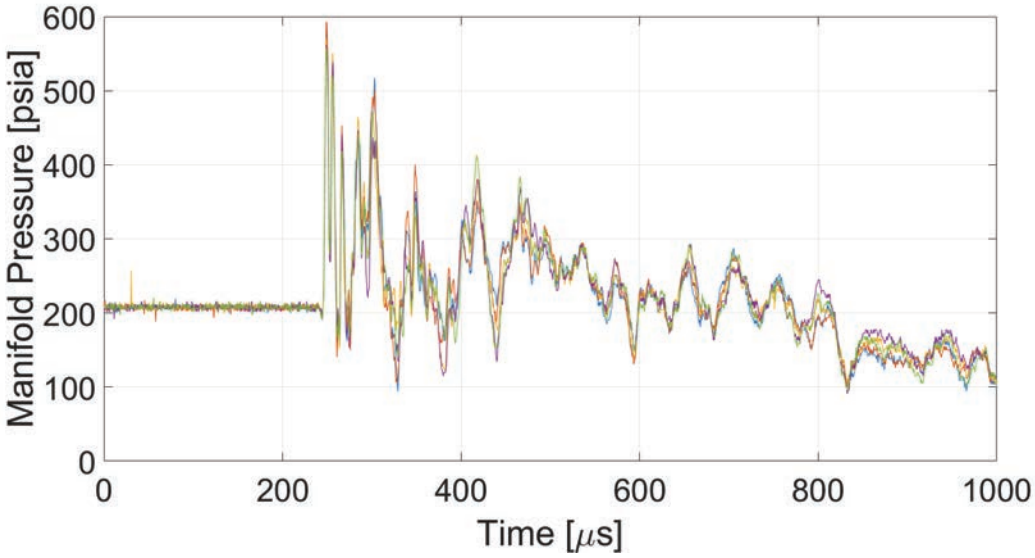

Figure C.16. Overlapping manifold pressure signals. Injector: LD6, fuel: ethylene, initial pressure: 690 kPa (100 psia), ΔP: 745 kPa (108 psia).

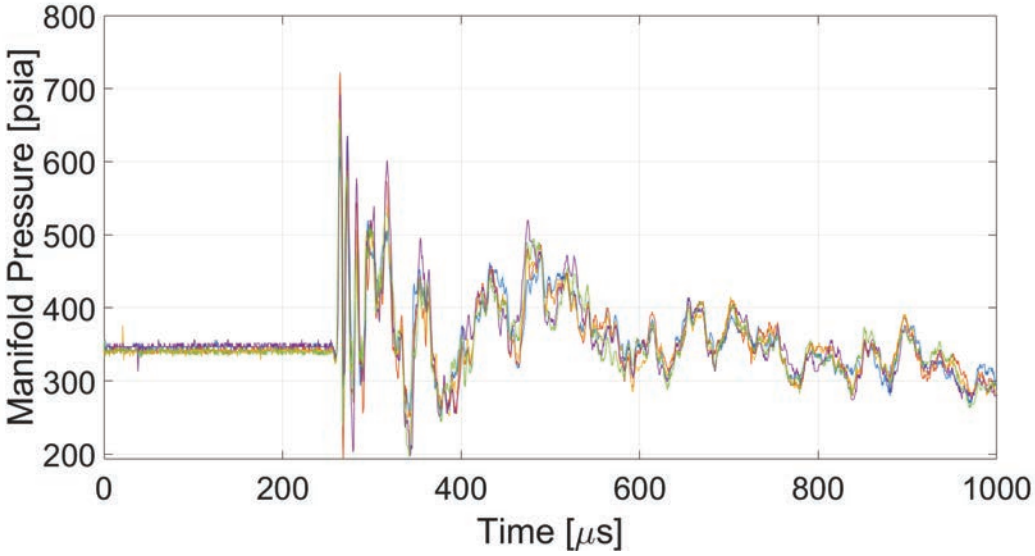

Figure C.17. Overlapping manifold pressure signals. Injector: LD6, fuel: ethylene, initial pressure: 690 kPa (100 psia), ΔP: 1,675 kPa (243 psia).

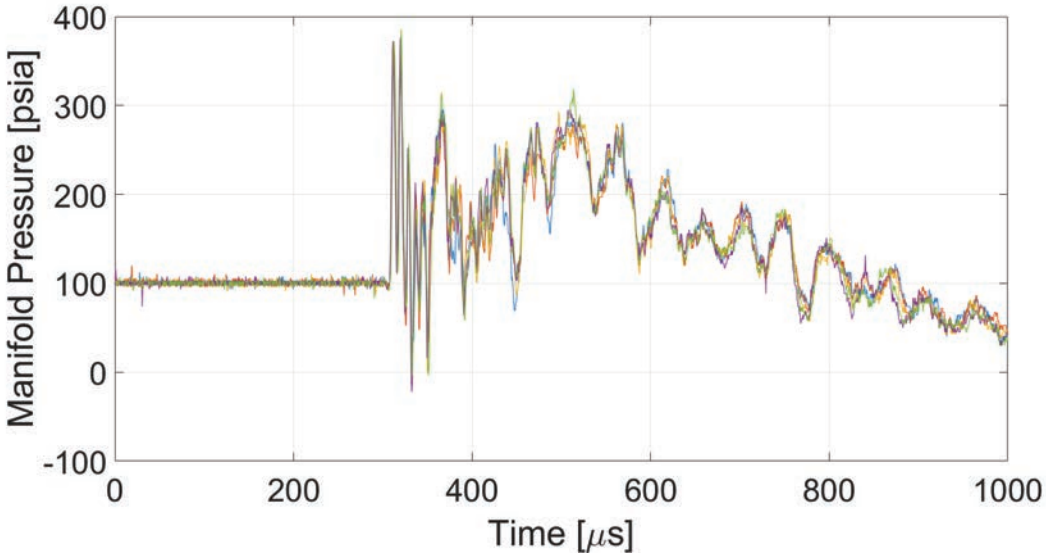

Figure C.18. Overlapping manifold pressure signals. Injector: LD6-1.5S, fuel: ethylene, initial pressure: 414 kPa (60 psia), ΔP: 269 kPa (39 psia).

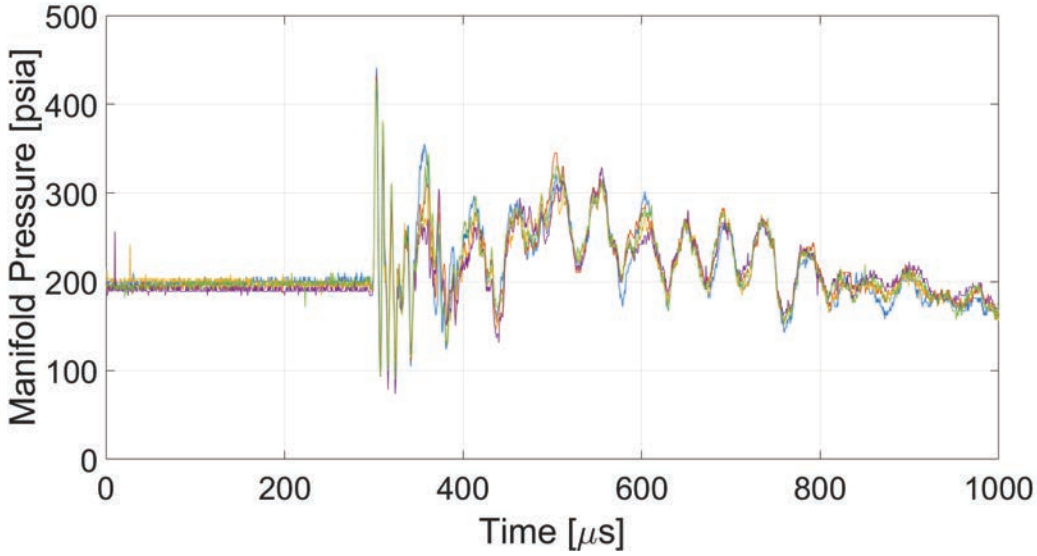

Figure C.19. Overlapping manifold pressure signals. Injector: LD6-1.5S, fuel: ethylene, initial pressure: 414 kPa (60 psia), ΔP: 910 kPa (132 psia).

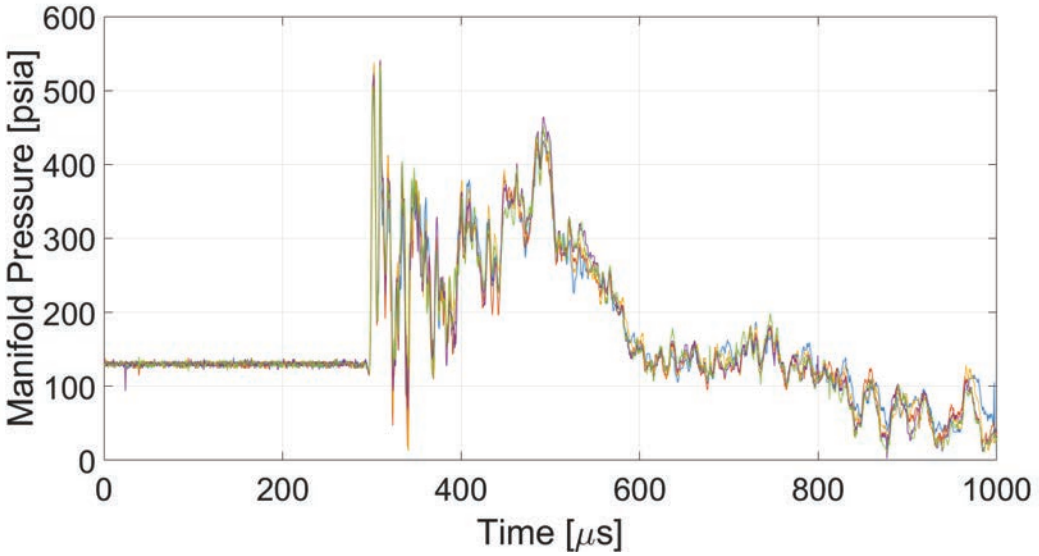

Figure C.20. Overlapping manifold pressure signals. Injector: LD6-1.5S, fuel: ethylene, initial pressure: 690 kPa (100 psia), ΔP: 186 kPa (27 psia).

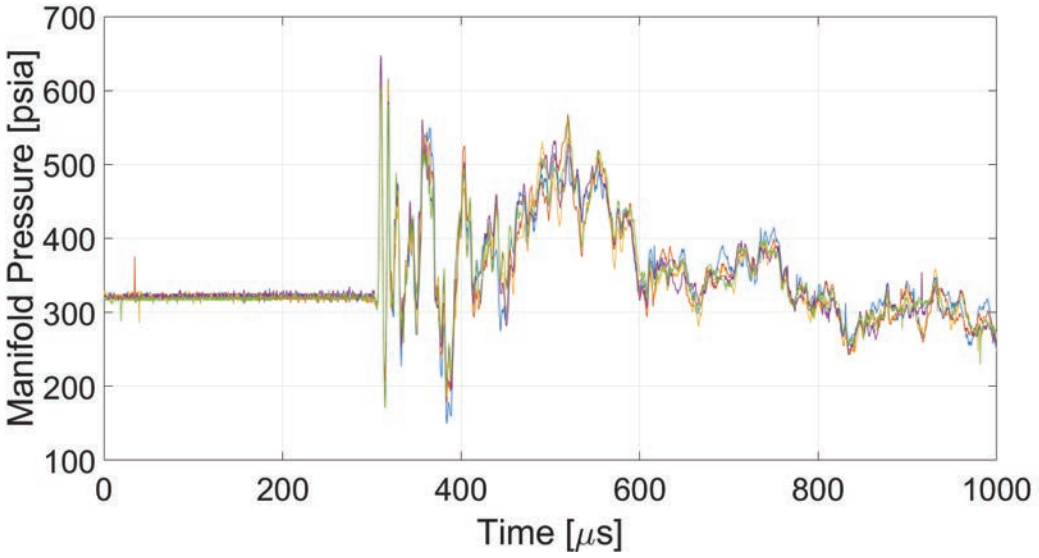

Figure C.21. Overlapping manifold pressure signals. Injector: LD6-1.5S, fuel: ethylene, initial pressure: 690 kPa (100 psia), ΔP: 1,482 kPa (215 psia).

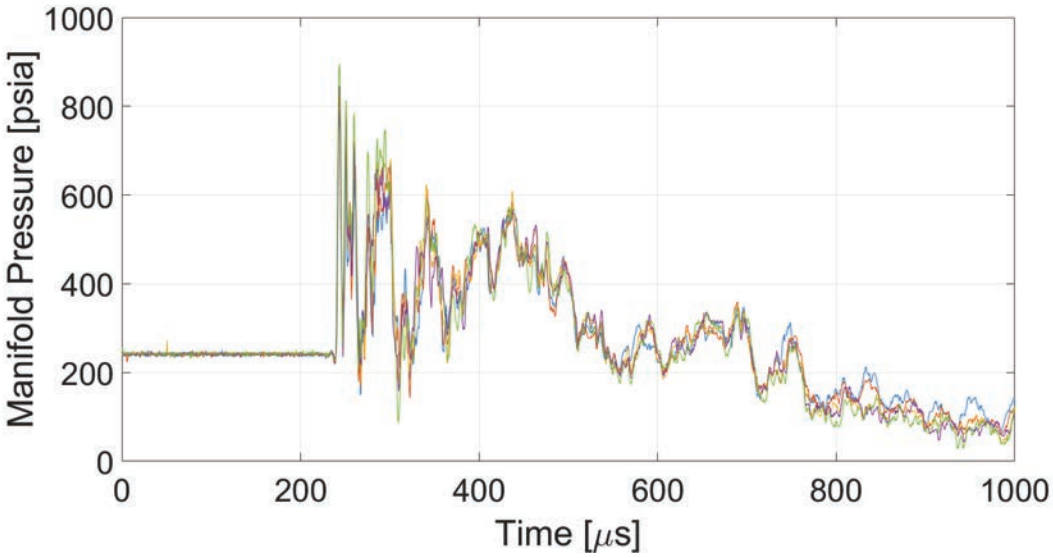

Figure C.22. Overlapping manifold pressure signals. Injector: LD6-1.5S, fuel: ethylene, initial pressure: 1,030 kPa (150 psia), ΔP: 614 kPa (89 psia).

D. RDE V1.4 OUTER WALL THERMOCOUPLE LOCATIONS

Table D.1. Angular locations, axial locations, and depths of embedded thermocouple probes.

TC channel	TC Group	Azimuthal location [°]	Axial location [in]	Depth [in]
TCTA-MC-01	7, 10	0	0.375	0.125
TCTA-MC-02	8, 10	0	1.125	0.125
TCTA-MC-03	9, 10	0	1.875	0.125
TCTA-MC-04	7, 11	90	0.375	0.25
TCTA-MC-05	8, 11	90	1.125	0.25
TCTA-MC-06	9, 11	90	1.875	0.25
TCTA-MC-07	7, 12	180	0.375	0.375
TCTA-MC-08	8, 12	180	1.125	0.375
TCTA-MC-09	9, 12	180	1.875	0.375
TCTA-MC-10	7, 13	270	0.375	0.5
TCTA-MC-11	8, 13	270	1.125	0.5
TCTA-MC-12	9, 13	270	1.875	0.5
TCTA-MC-16	1	56	0.375	0.314
TCTA-MC-17	1	59	0.375	0.189
TCTA-MC-18	1	62	0.375	0.126
TCTA-MC-19	1	65	0.375	0.063
TCTA-MC-20	2	116	0.375	0.314
TCTA-MC-21	2	119	0.375	0.189
TCTA-MC-22	2	122	0.375	0.126
TCTA-MC-23	2	125	0.375	0.063
TCTA-MC-24	3	206	0.375	0.314
TCTA-MC-25	3	209	0.375	0.189
TCTA-MC-26	3	212	0.375	0.126
TCTA-MC-27	3	215	0.375	0.063
TCTA-MC-28	4	56	1.125	0.314
TCTA-MC-29	4	59	1.125	0.189
TCTA-MC-30	4	62	1.125	0.126
TCTA-MC-31	4	65	1.125	0.063
TCTA-MC-32	5	116	1.125	0.314
TCTA-MC-33	5	119	1.125	0.189
TCTA-MC-34	5	122	1.125	0.126
TCTA-MC-35	5	125	1.125	0.063
TCTA-MC-36	6	206	1.125	0.314
TCTA-MC-37	6	209	1.125	0.189
TCTA-MC-38	6	212	1.125	0.126
TCTA-MC-39	6	215	1.125	0.063

E. ADDITIONAL FIGURES FROM RDE V1.4 HOTFIRE TESTS

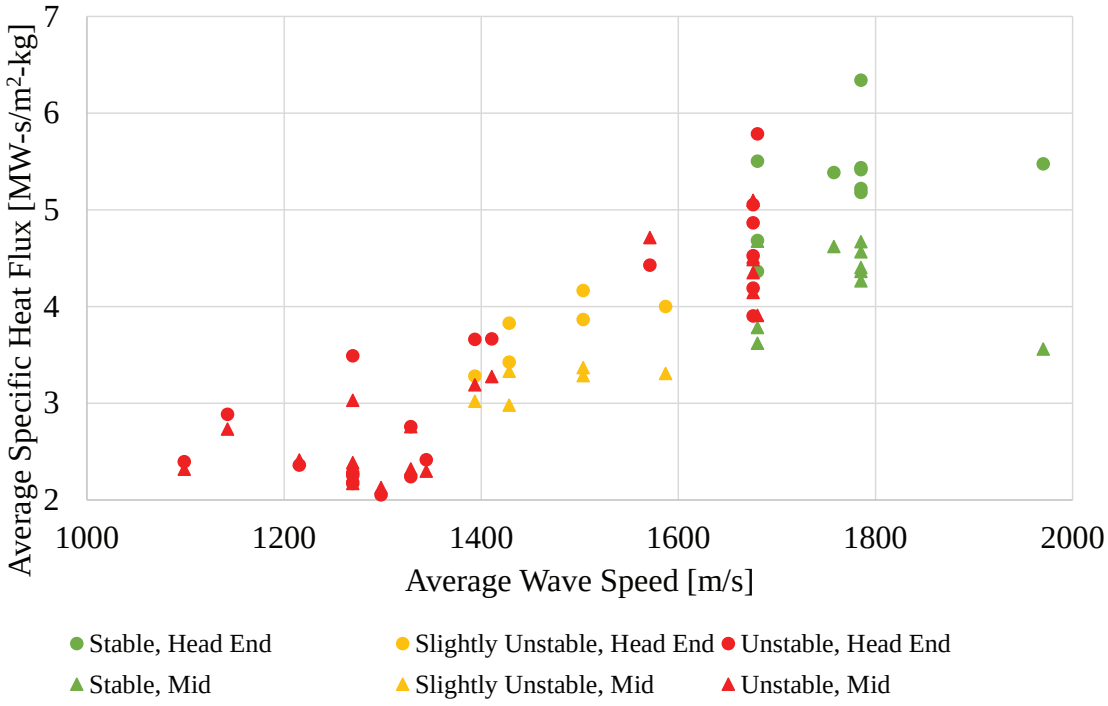

Figure E.1. Average specific heat flux vs. average detonation wave speed, colored by detonation stability.

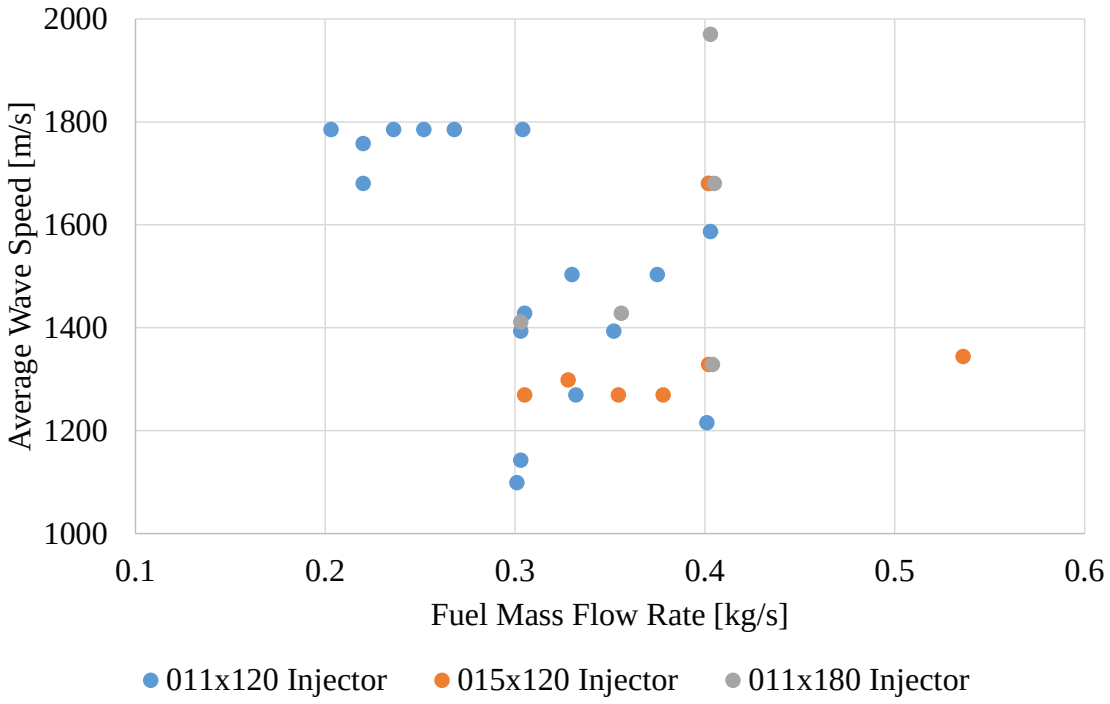

Figure E.2. Average detonation wave speed vs. fuel mass flow rate, colored by injector configuration.

VITA

Dasheng Lim was born in Singapore on the 20th of February 1986. After completing his high school education at Raffles Junior College (Singapore) in December 2004, he spent two years in the military service before beginning his college education at Nanyang Technological University (Singapore) in August 2007. While at NTU, he took part in a study abroad program at Rensselaer Polytechnic Institute (Troy, NY) during the Spring 2009 semester. In the Fall of 2009, he made the transfer to Purdue University, where he completed his Bachelor's degree in Aeronautical and Astronautical Engineering in Spring 2011. Dasheng spent the first year following graduation working as a research assistant at the Maurice J. Zucrow Laboratories, after which he took up a position of project engineer at Rolls-Royce Singapore. He returned to Purdue University in the Fall of 2013 for graduate studies and obtained his Master's degree in Fall 2015 before embarking on the journey towards a Ph.D. in Aeronautical and Astronautical Engineering in Spring 2016.